

# Imaging of material inhomogeneities with flexural waves

## PROEFSCHRIFT

ter verkrijging van de graad van doctor  
aan de Technische Universiteit Delft,  
op gezag van de Rector Magnificus prof. ir. K.C.A.M. Luyben,  
voorzitter van het College voor Promoties,  
in het openbaar te verdedigen  
op maandag 5 juli 2010 om 12:30 uur

door

**Lars HÖRCHENS**

Diplom-Ingenieur, Technische Universität Ilmenau,  
geboren te Mönchengladbach, Duitsland

Dit proefschrift is goedgekeurd door de promotor:

Prof. dr. ir. A. Gisolf

Copromotor:

Dr. ir. D. de Vries

Samenstelling promotiecommissie:

Rector Magnificus,	voorzitter
Prof. dr. ir. A. Gisolf,	Technische Universiteit Delft, promotor
Dr. ir. D. de Vries,	Technische Universiteit Delft, copromotor
Prof. dr. ir. A.J. Berkhout,	Technische Universiteit Delft
Prof. dr. ir. P.C.M. Planken,	Technische Universiteit Delft
Prof. dr. ir. D.J. Rixen,	Technische Universiteit Delft
Prof. P. Nelson, FREng,	University of Southampton
Dr. ir. M.C.M. Bakker,	Technische Universiteit Delft

ISBN 978-94-6113-010-5

Copyright ©2010, by L. Hörchens, Laboratory of Acoustical Imaging and Sound Control, Faculty of Applied Sciences, Delft University of Technology, P.O. Box 5046, 2600 GA Delft, The Netherlands.

All rights reserved. No part of this publication may be reproduced, stored in a retrieval system or transmitted in any form or by any means, electronic, mechanical, photocopying, recording or otherwise, without the prior written permission of the author.

SUPPORT

This research is supported by the Dutch Technology Foundation STW, which is the applied science division of NWO, and the Technology Programme of the Ministry of Economic Affairs (project number 06598).



Typesetting system: L<sup>A</sup>T<sub>E</sub>X.

Printed in The Netherlands by Ipskamp Drukkers, Enschede.

# Contents

---

<b>1</b>	<b>Introduction</b>	<b>1</b>
1.1	Flexural waves . . . . .	1
1.2	Acoustical imaging . . . . .	2
1.3	Nondestructive testing . . . . .	4
1.4	Coping with limitations of acoustical imaging . . . . .	5
1.5	Outline of the thesis . . . . .	5
<b>2</b>	<b>Flexural waves in beams and plates</b>	<b>7</b>
2.1	Introduction to flexural waves . . . . .	7
2.2	The flexural wave equations . . . . .	8
2.2.1	Derivation of the flexural wave equation for beams . . . . .	8
2.2.2	Historical development of the plate equation . . . . .	12
2.2.3	The flexural wave equation for plates . . . . .	13
2.2.4	The dispersion relation . . . . .	15
2.2.5	Limitations and extensions of the classical theory of flexural waves . . . . .	18
2.3	Green's function for flexural waves . . . . .	21
2.3.1	Inhomogeneous wave equation . . . . .	21
2.3.2	Green's function for the one-dimensional flexural wave . . . . .	22
2.3.3	Green's function for the two-dimensional flexural wave . . . . .	22
2.3.4	Approximation of the Green's functions . . . . .	23
2.4	Response of beams and plates to point excitation . . . . .	24
2.4.1	Point excitation of a beam . . . . .	24
2.4.2	Point excitation of a plate . . . . .	25
2.4.3	Temporal responses of beams and plates . . . . .	26
2.5	Reflected and scattered flexural waves . . . . .	27

2.5.1	Reflection from boundaries . . . . .	27
2.5.2	Reflection at cross-sectional changes . . . . .	31
2.5.3	Scattering of flexural waves . . . . .	33
2.6	Summary . . . . .	36
<b>3</b>	<b>Analysis and removal of dispersion effects</b>	<b>37</b>
3.1	Model of the flexural response . . . . .	38
3.1.1	Time-invariant reflection model for non-dispersive media . . . . .	38
3.1.2	Distance-dependent reflection model for dispersive media . . . . .	38
3.2	Dispersion removal for known source-to-receiver distance . . . . .	39
3.3	Dispersion removal by distance-dependent filtering . . . . .	41
3.4	Dispersion removal in the wavenumber-frequency domain . . . . .	42
3.4.1	Sampling and aliasing conditions for discrete signals . . . . .	47
3.5	Analysis of the dispersion removal procedure . . . . .	49
3.5.1	Influence of dispersion removal on the amplitude spectrum . . . . .	49
3.5.2	Change of the phase spectrum due to a temporal delay . . . . .	51
3.6	Limitations of the method for dispersion removal presented . . . . .	53
3.6.1	Optimal source spectrum . . . . .	53
3.6.2	The need for deconvolution of the measured signal . . . . .	55
3.7	Estimation of the dispersion model . . . . .	56
3.7.1	Estimation of the dispersion relation . . . . .	57
3.7.1.1	Extraction of the dispersion relation from the wavenumber-frequency domain . . . . .	57
3.7.1.2	Improved estimation of the dispersion relation . . . . .	58
3.8	Deconvolution . . . . .	63
3.8.1	Source signature deconvolution . . . . .	63
3.8.2	Correction of a linear phase shift . . . . .	64
3.9	Summary . . . . .	65
<b>4</b>	<b>Imaging under the Born approximation</b>	<b>67</b>
4.1	Wave field extrapolation . . . . .	67
4.1.1	The flexural wave field in the wavenumber-frequency domain . . . . .	68
4.1.2	Application of the projection-slice theorem . . . . .	70
4.1.3	Wave field extrapolation by a spatial shift . . . . .	70
4.1.4	Wave field extrapolation by mapping from frequency to wavenumber . . . . .	72
4.1.5	Wave field extrapolation of evanescent components . . . . .	75
4.1.6	Bi-directional wave field extrapolation . . . . .	75
4.1.7	From wave field extrapolation to imaging . . . . .	80
4.2	Imaging of a source distribution . . . . .	81
4.2.1	Imaging as a minimisation problem . . . . .	82
4.2.1.1	The adjoint imaging operator . . . . .	82
4.2.2	Spectral representation of the imaging problem . . . . .	83
4.2.3	Resolution analysis in the wavenumber-frequency domain . . . . .	86

4.2.4	Design and assessment of array geometries . . . . .	88
4.2.4.1	Aliasing and truncation by discrete and finite arrays in one dimension . . . . .	89
4.2.4.2	Aliasing and truncation by discrete and finite arrays in two dimensions . . . . .	91
4.2.4.3	Imaging in the near- and far-field . . . . .	94
4.2.5	Frequency and wavenumber spectra for optimal spatial res- olution . . . . .	97
4.2.6	Imaging by backpropagation . . . . .	99
4.2.7	Imaging by time shifting . . . . .	100
4.2.8	Imaging by inversion . . . . .	102
4.2.8.1	Stabilised imaging . . . . .	104
4.2.8.2	Regularised imaging . . . . .	106
4.3	Imaging of scatterers under the Born approximation . . . . .	108
4.3.1	Array setup and modes of data collection . . . . .	108
4.3.2	Forward scattering . . . . .	109
4.3.2.1	Neumann series expansion of the forward scattering operator . . . . .	111
4.3.3	Inverse scattering and the Born approximation . . . . .	111
4.3.4	Imaging by backpropagation . . . . .	112
4.3.5	Spectral analysis of the achievable resolution . . . . .	114
4.3.5.1	Coverage of the wavenumber spectrum . . . . .	116
4.3.6	Inversion . . . . .	122
4.3.6.1	Regularisation by a sparseness constraint . . . . .	123
4.3.6.2	Regularisation by a total variation constraint . . . . .	128
4.3.7	Examples . . . . .	130
4.3.8	Discussion of the imaging examples . . . . .	136
4.3.9	Towards super-resolution . . . . .	137
4.4	Imaging in finite structures . . . . .	138
4.4.1	Green's function for finite plates . . . . .	140
4.5	Summary . . . . .	145
<b>5</b>	<b>Imaging beyond the Born approximation</b>	<b>147</b>
5.1	Object and data equation . . . . .	147
5.2	Iterative linear inversion . . . . .	149
5.3	Contrast source inversion . . . . .	150
5.3.1	Update of the contrast sources . . . . .	152
5.3.2	Update of the contrast . . . . .	153
5.3.3	Regularisation by total variation . . . . .	154
5.4	Examples and discussion . . . . .	157
5.5	Modelling of finite plates . . . . .	162
5.5.1	Adaptation of the incident field . . . . .	162
5.5.2	Usage of the Green's function for finite plates . . . . .	162
5.5.3	Modelling of plate boundaries by the contrast . . . . .	163

5.5.4	Extension of contrast source inversion for an inhomogeneous background medium . . . . .	164
5.5.5	Recommendations for further research . . . . .	164
5.6	Summary . . . . .	165
<b>6</b>	<b>Conclusions and outlook</b>	<b>167</b>
6.1	Conclusions . . . . .	167
6.2	Recommendations for further research . . . . .	168
6.3	Outlook . . . . .	169
	<b>Appendices</b>	<b>171</b>
<b>A</b>	<b>Fourier transform</b>	<b>171</b>
A.1	Fourier transforms with respect to time . . . . .	171
A.2	Fourier transforms with respect to space . . . . .	171
<b>B</b>	<b>Derivation of the Green's functions</b>	<b>173</b>
B.1	Green's function for the one-dimensional wave equation . . . . .	173
B.2	Green's function for the two-dimensional wave equation . . . . .	175
B.3	Integral representation of the Hankel function of the second kind . . . . .	178
<b>C</b>	<b>Inverse Fourier transformation of a distance-dependent matched filter</b>	<b>179</b>
<b>D</b>	<b>Forward and adjoint operators for acoustical imaging</b>	<b>181</b>
D.1	Definition of the spaces . . . . .	181
D.2	Contrast source operator . . . . .	182
D.3	Measurement operator . . . . .	183
D.4	Born measurement operator . . . . .	183
D.4.1	Born measurement operator in space-frequency domain . . . . .	183
D.4.2	Born measurement operator in wavenumber-frequency domain . . . . .	184
D.4.3	Forward scattering operator . . . . .	186
<b>E</b>	<b>Estimation of the contrast</b>	<b>187</b>
<b>F</b>	<b>Conjugate gradient schemes</b>	<b>189</b>
F.1	Linear conjugate gradient scheme . . . . .	189
F.2	BI-CGSTAB . . . . .	189
F.3	Nonlinear conjugate gradient scheme . . . . .	192
<b>G</b>	<b>Experiments</b>	<b>193</b>
G.1	Measurements on a 2 mm steel plate . . . . .	193
G.2	Measurements on a 4 mm iron beam . . . . .	195
G.3	Measurements on a 3 mm aluminium plate . . . . .	196

---

<b>H Notation, symbols and acronyms</b>	<b>199</b>
H.1 Variables . . . . .	199
H.2 Special functions . . . . .	201
H.3 Mathematical operations . . . . .	202
H.3.1 Operators . . . . .	202
H.4 Indices, subscripts . . . . .	203
H.5 Representation of variables in frequency and wavenumber space . . .	203
H.6 Matrices and vectors . . . . .	203
H.7 Spaces, norms and inner products . . . . .	204
H.8 Acronyms . . . . .	204
<b>Bibliography</b>	<b>205</b>
<b>Summary</b>	<b>217</b>
<b>Samenvatting</b>	<b>219</b>
<b>Curriculum vitae</b>	<b>221</b>
<b>Acknowledgements</b>	<b>223</b>



# Introduction

*The work may be hard, and the discipline severe;  
but the interest never fails,  
and great is the privilege of achievement.*

(John William Strutt, 3rd Baron Rayleigh, 1842 – 1919)

Vibrations are an everyday phenomenon. They are often not perceived directly, but rather by the radiated sound waves they cause, either leading to enjoyment when coming from a musical instrument, for instance, or being a source of disturbance when associated with construction noise. We know from experience that different objects such as bells, bottles or baseball bats, exhibit distinct acoustical properties, simply from the different tones of their sound when struck. The characteristics of the vibrations of a body causing this radiated sound are determined by its shape and material properties. Inversely, the vibration of a structure can be expected to provide information about its geometrical and physical properties, at least to some extent [Kac 1966].

## 1.1 Flexural waves

Flexural waves, also known as bending waves, are a special type of vibrations occurring in solids of beam- or plate-like shape. These structures are relatively thin in one or two dimensions and able to act as a waveguide, i.e., transport vibrations over longer distances with relatively little damping. The flexure of a plate-like structure is mainly associated with motion normal to its surface, therefore being the main cause of radiated sound. This phenomenon is used for the construction of sound boards in musical instruments and for the development of modern loudspeakers. It can also – presumably unintentionally – be experienced when one’s neighbour is drilling a hole into the wall, causing sound radiation due to flexural motion that might make it sound as if he was trying to break through.

Due to the confinement of flexural waves in a waveguide, their propagation exhibits the special property of being dispersive, meaning that different frequencies travel at

different speeds in the medium. The effect of dispersion can also be observed for different kinds of waves, for instance surface waves in water as shown in Fig. 1.1.



---

**Figure 1.1:** *Dispersive waves caused by a stone thrown into water, shown at two different points in time.*

---

In a dispersive medium, wave fronts tend to spread out during propagation. The effect of dispersion can thus inhibit the analysis of a wave field based on local observations of arriving wave fronts. In order to analyse flexural wave fields in beams and plates, it is therefore necessary to devise ways of dealing with dispersion.

## 1.2 Acoustical imaging

Acoustical and vibrational waves can be employed to retrieve information about the medium they are propagating in, which can subsequently be used to generate an image of the properties of the medium. Despite the fact that the present work deals with imaging based on flexural waves only, it is decided to adopt the term *acoustical imaging* to emphasise the close relation to methods developed for pressure waves. Furthermore, usage of this designation underlines that a significant part of the results presented in this thesis can easily be applied to acoustical waves, thereby complementing existing methods.

The usage of acoustical waves for imaging has attractive benefits for fields such as seismics, medical diagnostics or non-destructive evaluation. In the latter two fields, acoustical methods have become an indispensable supplement to classical imaging techniques using X-rays, mainly due to the fact that an image can be formed based on the diffraction of acoustical waves using time or phase information instead of mere intensity. Furthermore, acoustical waves are not dangerous in contrast to ionising radiation.

However, with respect to the applications considered, acoustical waves and vibrations can often not be approximated by ray-theoretical approaches, which suffice to describe the propagation of radiation with shorter wavelengths. The formation of an image based on acoustical or vibrational waves is thus intrinsically more difficult than optical imaging, for instance. As an example, the reader might consider an analogy between acoustical imaging and one of the nowadays proliferated digital cameras for amateur photography: in order to mimic the conditions for acoustical imaging, it would be necessary to

- remove the lens,  
(use diffraction imaging instead of a lens system based on ray theory)
- keep less than a hundred pixels, i.e., limit the number of receivers,  
(take cost and hardware limitation into account)
- and take the picture in a medium in which white light tends to split up into different colours with increasing distance from the object to be photographed  
(include the effects of dispersion).

After this discouraging list, one might wonder how it could be possible to obtain a usable image under these circumstances and why imaging based on acoustical and vibrational waves works at all. Fortunately, there is one crucial advantage making acoustical imaging feasible: acoustical waves and vibrations propagate slowly enough to allow for the measurement of their variation in amplitude over time. This property makes all the difference: in contrast to a photographic camera, a single sensor for sound or vibration can be used to determine the time of arrival of an event.

However, the combination of several sensors enables the determination of an angle of incidence due to different times of arrival observed at different sensor positions. From a spectral point of view, the capability of measuring the time of arrival corresponds to the ability to distinguish different frequencies in the radiated spectrum. Our imaginary acoustical camera is thus able to capture significantly more different ‘colours’ (frequencies) in a more sophisticated way than its real photographic counterpart.

In order to generate a spatial image, the registered arrival times of events such as the reflection from a discontinuity must be converted to distance information. To this end, the characteristics of propagation in the medium such as the propagation velocity have to be known. At this point, dispersion plays a major role: it has to be taken into account due to the different speeds of propagation for different frequencies. If dispersion is neglected, the resulting image will be ‘blurred’ and at least difficult to interpret, if not useless.

From a single receiver, only the travel time, and accordingly only the distance to a point of interest, can be determined. This setup can be compared to a very simple form of depth sounder yielding only the distance to the ocean bottom. Hence,

information from several receivers must be combined to form an image that can be expected to bear at least some similarity to a photograph. The image quality depends to a great extent on the approach used for this combination of signals from different receivers.

In seismic exploration, the need for oil and gas has stimulated the development and improvement of imaging approaches based on a solid theoretical foundation, especially due to the lack of alternative techniques for assessment *before* drilling expensive holes. Similarly, strong progress has been made over the past three decades with respect to medical applications of ultrasound. Whereas in the 1980s a trained doctor was needed to explain to the parents-to-be that the black spot on a fuzzy picture represented their future child's head, modern ultrasonography allows for three-dimensional visualisation of the embryo's details while almost enabling the recognition of facial expressions.

### 1.3 Nondestructive testing

The practice of methods for nondestructive evaluation has not yet reached the same level of sophistication and usually requires a well-trained expert, both for taking and interpreting measurements. However, this field of research has steadily been progressing, thereby benefiting from developments in the aforementioned areas as well as other fields like radar technology, for instance.

The classical inspection of plate-like structures is carried out by performing a number of local scans on a predefined grid using bulk waves. The measured signal amplitude or travel time is represented by a certain colour, such that local changes, for instance due to an internal crack or corrosion on the far side of the plate, can easily be recognised from the generated image.

Nondestructive testing with guided waves does not require scanning of the plate. Instead, the wave is generated at a certain location and propagates along the plate. Interaction with a discontinuity causes reflection or scattering of the wave, which can be detected from a remote location, provided that the damping of the plate is not too strong. The flexural wave represents only one of many possible guided wave modes that can be used for this purpose [Alleyne 1991b].

While providing less detail, the gain in speed due to this approach is significant. This plays a very important role for the inspection of parts of industrial plants, which might have to be shut down temporarily in order to allow for testing. Therefore, it is not surprising that guided waves are often used for the detection of defects rather than for defect sizing. Imaging with guided waves can thus be regarded as a screening tool that avoids the need for time-consuming local inspection if there is no indication of a possible defect.

Present methods of imaging based on guided waves focus on the information contained in the travel time of events and are dominated by phased arrays or related techniques. Recently, there has been a tendency to apply improved imaging methods by using different approaches of combining sources and receivers well known in the field of seismics [Davies 2005], and providing a more profound theoretical background for the generation of images [Pörtzgen 2007].

Another tendency is the quest for methods achieving higher resolution by inclusion of multiple scattering, currently dominated by approaches related to eigenvalue analysis [Prada 1994] [Simonetti 2006], which are tailored to deal with point-like inhomogeneities.

## 1.4 Coping with limitations of acoustical imaging

The quality of an obtainable acoustical image depends strongly on the available samples of the wave field with respect to both time and space. The spatial sampling is restricted by factors such as accessibility, effort and hardware costs, whereas for the temporal sampling, aspects such as characteristics of available transducers, excitability of certain frequencies, material damping and required computational effort can pose limitations.

Hence, the inverse problem of generating an image from measurements can, in general, be expected to be underdetermined. It is thus necessary to devise methods for coping with little or insufficient information. The branch of mathematics dealing with inverse problems has produced a number of techniques for this purpose. Nevertheless, it remains necessary to investigate which of these common methods are suited for the imaging problem and can actually be expected to provide an improvement. In this context, sophisticated physical models can overcome the problem of non-uniqueness. Knowledge on the expected structure of a typical image can be helpful as well.

## 1.5 Outline of the thesis

Based on the equations describing the propagation of flexural waves in beams and plates, the present work seeks to derive methods for the analysis of flexural wave fields and the formation of images, from which sources of vibration and local inhomogeneities can be detected. Despite the fact that the presented approaches are derived from, and demonstrated on flexural wave fields, their applicability is not limited to this special type of waves. Whenever possible, the derivation is carried out in such a way that the transfer of the principles to other problems in imaging based on acoustical or vibrational waves is relatively straightforward.

Chapter 2 presents the equations governing flexural wave propagation in beams and plates. Different approaches to deal with dispersion are derived and compared in Chapter 3. The methods and constraints for the formation of images from measurements are presented in Chapter 4, followed by a discussion of improvements by including multiple scattering in Chapter 5. The results are summarised and evaluated in Chapter 6.

# Flexural waves in beams and plates

*ATOMYRIADES*

*Nature, it seems, is the popular name  
for milliards and milliards and milliards  
of particles playing their infinite game  
of billiards and billiards and billiards.*

(Piet Hein, 1905 – 1996)

Like for any other structure, wave fields in beams and plates can be analysed by using the three-dimensional wave equation for elastic solids. However, two dimensions of a beam are much smaller than its length. Analogously, the thickness of a plate is much smaller than the other two dimensions. It is, therefore, in many cases appropriate and more feasible to model beams as one-dimensional and plates as two-dimensional entities, using a dedicated equation to describe wave propagation within these structures.

The present chapter is structured as follows: first, the flexural mode of wave propagation is introduced, followed by the derivation of the wave equations for beams and plates. The Green's functions for both problems are presented, and models for reflection and scattering of waves are derived from the wave equations.

## 2.1 Introduction to flexural waves

The linear theory of elasticity allows for two principal modes of wave propagation in an infinite homogeneous solid medium [Graff 1975]:

- longitudinal waves associated with particles moving along the direction of propagation
- transverse shear waves exhibiting particle motion perpendicular to the direction of propagation.

However, if the extent of the medium is not infinite, boundary conditions are introduced, and reflections and scattering at the boundaries have to be taken into account. In structures such as beams and plates, waves are guided by the outer surfaces. Therefore, they can be regarded as waveguides [Auld 1973]. The superposition of waves that are incident on, and reflected from the boundaries leads to an effective propagation along the guiding surfaces that can be described by a waveguide mode. Rayleigh and Lamb were the first to derive the speeds of propagation of these modes from the exact theory of elasticity in 1889 [Graff 1975].

One of these modes is the *flexural* or *bending* mode. It is the lowest order mode of the family of guided waves with transverse displacements. Especially for plate-like structures, this mode is of considerable importance. Since it is associated with displacements normal to the vibrating structure, it can cause the generation of sound waves in a surrounding fluid [Cremer 2005]. Flexural waves are easily excited by a force acting normal to the plate, such as an impact or a vibrational source.

More than a century before Rayleigh and Lamb derived the full solution to the guided mode problem, approximate solutions for the propagation of bending waves were sought by derivation of wave equations using simplifying assumptions.

## 2.2 The flexural wave equations

### ■ 2.2.1 Derivation of the flexural wave equation for beams

The equations governing the flexural motion of beams were derived by Leonhard Euler and Daniel Bernoulli around 1750 [Graff 1975]. Essentially, the movement of the beam is modelled as rotation of infinitesimally small elements as shown in Fig. 2.1. There exists a neutral surface, which is curved in only one direction. Its length does not change when the beam is bent. Above and below this neutral surface, the beam is compressed or extended in axial direction depending on its curvature.

Euler and Bernoulli introduced hypotheses for small deflections in order to simplify the problem and allow for a one-dimensional description [Reddy 1999]:

- Plane cross-sections remain plane.
- Plane cross-sections are inextensible.
- Plane cross-sections remain normal to the neutral surface.

These assumptions have immediate consequences for the physical modelling of the problem: there is no force component along the axis of the beam, and transverse stress and strain are not included [Fahy 1985]. This assumption is only valid for thin plates and small deflections.

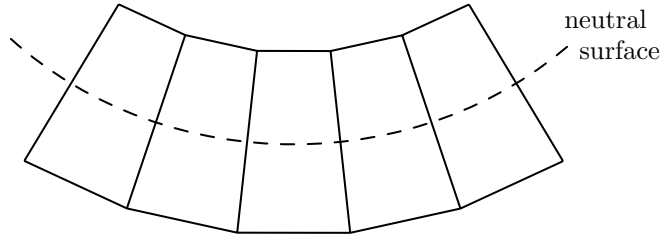


**Figure 2.1:** Euler-Bernoulli model for the bending of a beam: the beam elements are aligned along a neutral surface.

The following steps are taken according to the derivation provided by Cremer, Heckl and Petersson [Cremer 2005]. Considering a beam element rotated by an angle  $\varphi$  as shown in Fig. 2.2, it can be seen that for small angles, the following approximation can be made for an infinitesimally small transverse displacement  $u$  of an infinitesimally small beam element:

$$\frac{\partial u}{\partial x} = \tan \varphi \approx \varphi, \quad (2.2.1)$$

with  $x$  being the position in the axial direction.

In good approximation, the tensile strain  $\epsilon_x$  of the element considered is assumed to depend linearly on the distance  $z$  from the neutral axis as illustrated in Fig. 2.3.

$$\epsilon_x dx = -z d\varphi. \quad (2.2.2)$$

The tensile stress  $\sigma_x$  is related to the strain by the Young modulus  $E$ :

$$\sigma_x = E\epsilon_x = -Ez \frac{\partial \varphi}{\partial x} = -Ez \frac{\partial^2 u}{\partial x^2}. \quad (2.2.3)$$

For a beam of rectangular cross-section, the bending moment is obtained by integration over the cross-sectional area with height  $h$  and width  $b$  in the  $y$ - $z$ -plane:

$$M = \int_{-b/2}^{b/2} \int_{-h/2}^{h/2} \sigma_x z \, dy \, dz = -E \frac{\partial^2 u}{\partial x^2} \int_{-b/2}^{b/2} \int_{-h/2}^{h/2} z^2 \, dy \, dz = -EI' \frac{\partial^2 u}{\partial x^2}. \quad (2.2.4)$$

The constant  $I'$  in the above equation represents the *area moment of inertia*, which is dependent on the shape of the cross-section only and determines the resistance to bending.

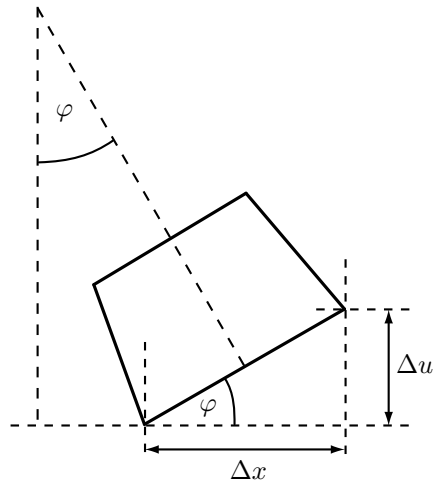


**Figure 2.2:** Rotation of a beam element

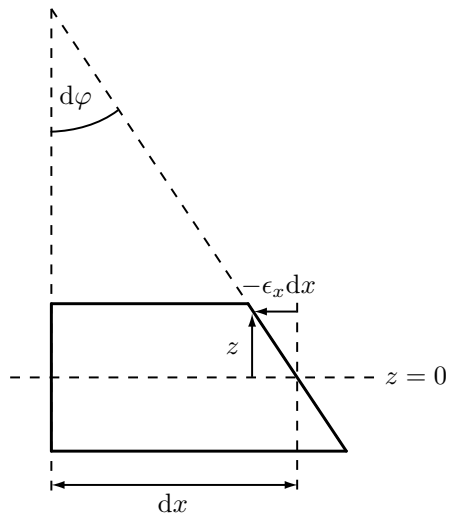


**Figure 2.3:** Strain of a beam element

The product of the Young modulus  $E$  and the area moment of inertia  $I'$  is termed the *bending stiffness* or *flexural rigidity*  $B'$ :

$$B' = EI'. \quad (2.2.5)$$

The bending stiffness depends on material parameters and cross-sectional shape of the beam. For a rectangular beam, for instance, the bending stiffness is given by

$$B' = \frac{Ebh^3}{12}. \quad (2.2.6)$$

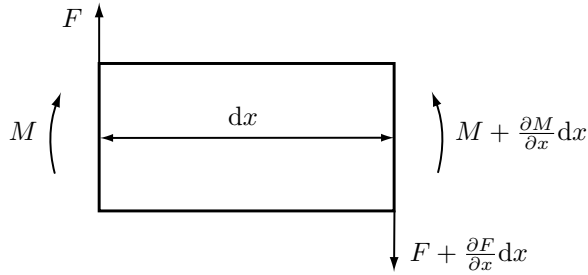
It can be seen from Eq. 2.2.4 that a lower bending stiffness leads to an increase in curvature  $\partial^2 u / \partial x^2$  for the same bending moment  $M$ .

The flexural wave equation can now be derived from the net moments and forces as shown in Fig. 2.4. The net force acting on a beam element must be equal to the mass times acceleration of the element:

$$F - \left( F + \frac{\partial F}{\partial x} dx \right) = m' dx \frac{\partial^2 u}{\partial t^2}, \quad (2.2.7)$$

with  $m'$  being the mass per unit length of the beam with given density  $\rho$ :

$$m' = \rho bh. \quad (2.2.8)$$




---

**Figure 2.4:** Moments and forces on a beam element, after [Cremer 2005].

---

For the equilibrium of moments, the rotary inertia of the element is neglected, such that the sum of moments is given by the following expression:

$$M - \left( M + \frac{\partial M}{\partial x} dx \right) - F dx = 0. \quad (2.2.9)$$

From the combination of the above equations, the bending wave equation is obtained:

$$B' \frac{\partial^4 u}{\partial x^4} + m' \frac{\partial^2 u}{\partial t^2} = 0. \quad (2.2.10)$$

Application of a temporal Fourier transform as defined in appendix A leads to the Helmholtz equation for bending waves:

$$\frac{\partial^4 \tilde{u}}{\partial x^4} - k_B^4 \tilde{u} = 0, \quad (2.2.11)$$

with  $k_B$  being the *bending wavenumber* of the beam:

$$k_B = \sqrt{\omega} \sqrt[4]{\frac{m'}{B'}}. \quad (2.2.12)$$

The phase velocity  $c_B$  is obtained as the quotient of frequency and wavenumber:

$$c_B(\omega) = \frac{\omega}{k_B} = \sqrt{\omega} \sqrt[4]{\frac{B'}{m'}}. \quad (2.2.13)$$

This result shows the dispersive nature of flexural waves: the speed of propagation depends on the frequency. Eq. 2.2.12 relating wavenumber to frequency is called the *dispersion relation*. It will be investigated in more detail in Section 2.2.4.

## ■ 2.2.2 Historical development of the plate equation

Despite their close relation, the equations describing the movement of a plate were not obtained directly along with the beam equation presented above. In fact, it took a whole century before a satisfactory answer to the plate problem was found.

Bernoulli himself tried to model plates as a gridwork of beams, based on his earlier results. However, as his approach neglected torsional resistance of the interconnected beams, he was unable to find a theory that could satisfactorily explain the results obtained by experiments [Szilard 2004].

At the beginning of the nineteenth century, it was the physicist Ernst Florens Friedrich Chladni who brought the plate problem back to the attention of the scientific community. He had discovered that sand spread out on a plate would form geometric figures when the plate was set into vibration by means of a violin bow. Although he was not the first to observe these patterns, he was the first scientist to systematically investigate the phenomenon. After several attempts to obtain a professorship had failed, he decided to earn his money by giving lecture tours, on which he presented – among self-made instruments and other experiments – the patterns on vibrating plates [Stöckmann 2007].

While being in France in 1809, he was invited by Napoleon for a personal demonstration. The emperor was impressed and offered a prize to the person that could provide the mathematical theory behind the observed patterns. However, the French Academy of Science dealing with the competition had to extend the delivery date twice due to the lack of submissions. Finally in 1811, on the last day of the extended deadline, the jury received one single paper by Sophie Germain [Szilard 2004]. Although she was denied a proper education due to the fact that she was a woman, Sophie Germain had taught herself mathematics and reached a level that allowed her to discuss problems with mathematicians such as Gauss, Lagrange and Legendre.

Unfortunately, she had made a mistake in the derivation of the flexural wave equations. Lagrange, who had witnessed Chladni's demonstration for Napoleon and was a member of the jury, was able to correct this error. Nevertheless, the subject was proposed again. In 1813, Sophie Germain submitted a paper with the corrected equation, but a definition of the wavenumber constant was left out, such that the prize was denied again. Finally, at the third attempt, she won the prize in 1816 in spite of an improper definition of the wavenumber. She had provided the correct differential equation, but the solution was still incomplete. Nevertheless, she must be regarded as the first person to derive the equations of motion for a plate.

In the following decades, scientists such as Poisson and Navier tried to find the correct wavenumber constant. The first complete theory of plate bending was not published earlier than 1850 by Gustav Kirchhoff. He had succeeded in applying the hypotheses of Bernoulli to the plate problem. For this reason, these hypotheses are usually called 'Kirchhoff hypotheses' in the context of plate problems [Reddy 1999]. The equations derived by Kirchhoff form the so-called *classical plate theory*.

### ■ 2.2.3 The flexural wave equation for plates

The derivation of the plate equations is not presented here, mainly due to the fact that the derivation itself does not provide many additional insights that are relevant in the context of this work when compared to the one-dimensional equation of a beam as presented in section 2.2.1. The reader is therefore referred to standard textbooks such as Timoshenko [Timoshenko 1959], Leissa [Leissa 1969], Graff [Graff 1975], or Cremer, Heckl and Petersson [Cremer 2005].

According to Fahy, it can be argued that a plate of infinite extent does not significantly differ from a beam [Fahy 1985], as long as only one-dimensional propagation is considered. It is then merely necessary to adapt the relation between stress and strain in axial direction. However, this is not sufficient to describe two-dimensional propagation properly. The additional dimension makes contractions of the cross sections in one direction impossible. Therefore, it is necessary to replace the Young modulus  $E$  by  $E/(1 - \nu^2)$  for the plate problem, with  $\nu$  being the Poisson ratio [Cremer 2005].

The bending stiffness of the plate  $B''$  is then given by the following expression:

$$B'' = \frac{h^3 E}{12(1 - \nu^2)}. \quad (2.2.14)$$

Furthermore, instead of the mass per unit length, the mass per unit area is included in the wave equation for the plate:

$$m'' = \rho h, \quad (2.2.15)$$

with  $h$  being the thickness of the plate.

The flexural wave equation for plates is obtained from the requirement that bending moments and forces acting on a plate element must be in equilibrium, as in the case of a beam. The two-dimensional solution arrived at is given by the following equation [Cremer 2005]:

$$B'' \nabla^4 u + m'' \frac{\partial^2 u}{\partial t^2} = 0, \quad (2.2.16)$$

in which  $\nabla^4$  represents the biharmonic operator [Graff 1975]:

$$\nabla^4 u = \left( \frac{\partial^4 u}{\partial x^4} + 2 \frac{\partial^4 u}{\partial x^2 \partial y^2} + \frac{\partial^4 u}{\partial y^4} \right) \quad (2.2.17)$$

Application of a temporal Fourier transform leads to the Helmholtz equation for bending waves:

$$\nabla^4 \tilde{u} - k_P^4 \tilde{u} = 0, \quad (2.2.18)$$

with the bending wavenumber given by

$$k_P = \sqrt{\omega} \sqrt[4]{\frac{m''}{B''}}. \quad (2.2.19)$$

Therefore, the phase velocity in the plate is obtained as:

$$c_P(\omega) = \sqrt{\omega} \sqrt[4]{\frac{B''}{m''}}. \quad (2.2.20)$$

Comparing this result to Eq. 2.2.13, it can be seen that the wavenumber and phase velocity of waves in beams and plates show exactly the same dispersive character. In the following, the indices B and P introduced above will be used whenever a distinction between beams (B) and plates (P) is required. If the index is omitted, application to both problems is possible, and the respective constants and functions can be used.

The flexural wave equation has been derived in order to describe the normal displacement of beams and plates. However, it should be noted that the wave equation

is also valid for normal velocity and normal acceleration due to the fact that calculation of the derivative with respect to time on both sides of the equation does not change its basic structure. The wave equation and the methods derived from it can thus directly be applied to flexural wave fields for which the normal velocity or normal acceleration of the plate is known. This is the case for measurements obtained using a laser vibrometer or an accelerometer, respectively.

#### ■ 2.2.4 The dispersion relation

The form of Eqs. 2.2.13 and 2.2.20 shows that the dispersion is determined by a constant factor depending on the material parameters and the geometry. For beams with rectangular cross-section and height  $h$ , this *dispersion constant*  $A_B$  is given by

$$A_B = \sqrt[4]{\frac{B'}{m'}} = \sqrt[4]{\frac{Eh^2}{12\rho}}, \quad (2.2.21)$$

showing that the width  $b$  of the beam has no influence on the speed of propagation. The corresponding constant  $A_P$  for the plate is given by the following expression:

$$A_P = \sqrt[4]{\frac{B''}{m''}} = \sqrt[4]{\frac{Eh^2}{12\rho(1-\nu^2)}}. \quad (2.2.22)$$

Comparing the results to Eq. 2.2.20, it is seen that the phase velocity increases proportionally to the square root of the thickness  $h$  for both beam and plate. Figure 2.5 presents the phase velocity curves for some typical materials.

A simulated example of a propagating wave front is presented in Fig. 2.6. The plane wave shown is chosen to have a short zero-phase pulse shape when passing the origin of the coordinate system at time  $t = 0$ . As a consequence of dispersion, the wave front spreads out over time and space during propagation.

Figure 2.7 and Fig. 2.8 show sections of the simulated flexural wave field in space and time, respectively.

Another interesting quantity for a dispersive wave field is the group velocity  $c_{gr}$ , which is the speed at which the envelope of a signal consisting of multiple frequencies propagates through space. The group velocity is defined as follows [Cremer 2005]:

$$c_{gr} = \frac{\partial\omega}{\partial k}. \quad (2.2.23)$$

For flexural waves, the group velocity depends on the frequency and is given by twice the phase velocity:

$$c_{gr} = 2c. \quad (2.2.24)$$

Hence, the envelope of a signal can travel twice as fast in a flexural wave field as a point of constant phase within this signal. This is illustrated in Fig. 2.9.

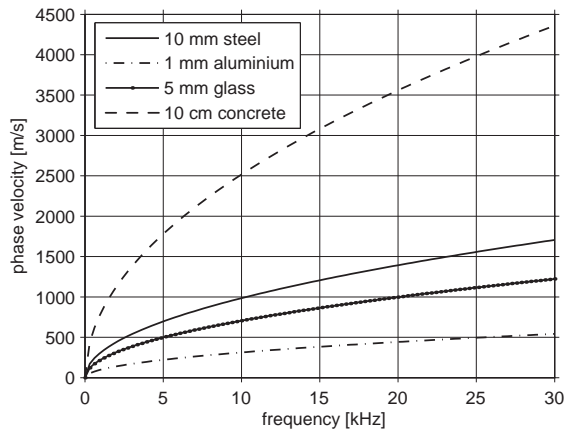


**Figure 2.5:** Phase velocity curves for some exemplary plates made of steel, aluminium, glass or concrete.

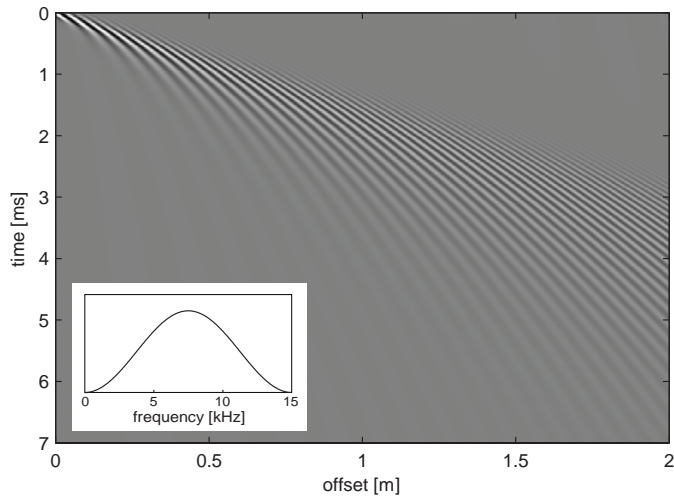


**Figure 2.6:** Simulation of a plane wave propagating in one direction in a 1 mm aluminium plate illustrating the effects of dispersion: spreading of the wave front in time and space; the magnitude of the zero-phase spectrum at the origin is shown; grey values correspond to normal velocity of the plate.

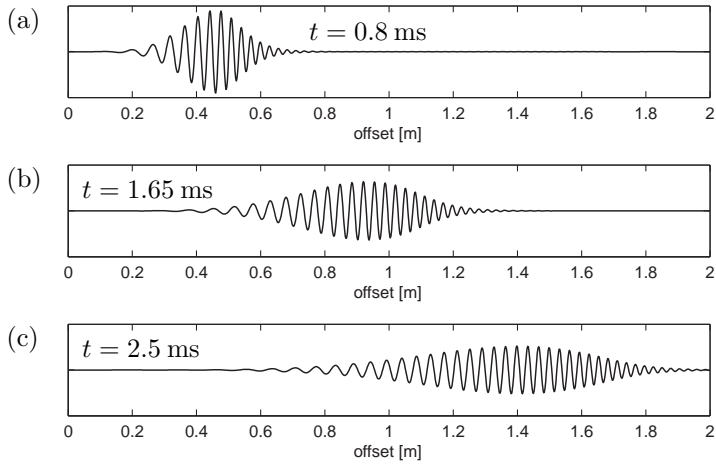


**Figure 2.7:** Spatial profile of the normal velocity of the wave field shown in Fig. 2.6 for several points in time. It can be observed that higher frequency components propagate faster than the lower frequency components, leading to increased spreading of the wave front.

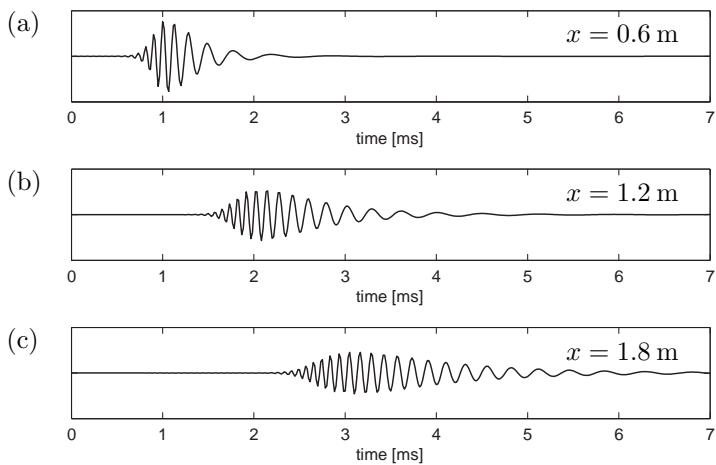


**Figure 2.8:** Temporal profile of the normal velocity of the wave field shown in Fig. 2.6 for several propagation distances  $x$  from the origin. The lower frequency components can be seen to arrive later than higher frequency components.

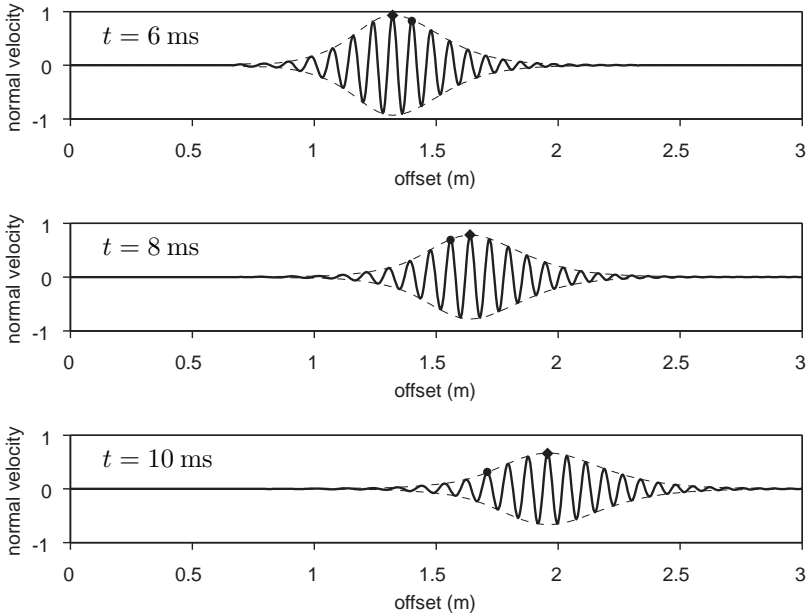


**Figure 2.9:** Normal velocity of a wave propagating in a plate with dispersion constant  $A = 1$  (normalised scale) dependent on the distance from the source shown for different points in time (6, 8 and 10 ms); a  $\cos^2$ -windowed sine tone burst with a centre frequency of 1 kHz is used; the diamond-shaped marker designates the maximum of the envelope travelling at the group velocity; the circle marks a point of constant phase travelling at the phase velocity.

The wavelength  $\lambda$  of a flexural wave is obtained as the inverse of the wavenumber:

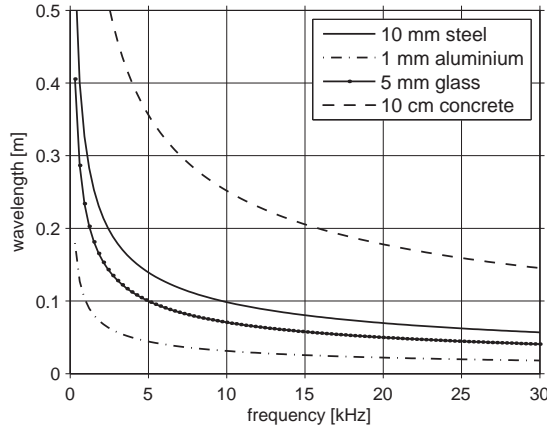
$$\lambda = \frac{2\pi}{k} = \frac{2\pi A}{\sqrt{\omega}}. \quad (2.2.25)$$

Figure 2.10 shows the frequency-dependent wavelength for the same materials as in Fig. 2.5.

The equation for the phase velocity shows that the propagation speed decreases rapidly if the frequency goes towards zero. In this case, the wavelength increases towards infinity in the theoretical limit.

## ■ 2.2.5 Limitations and extensions of the classical theory of flexural waves

The decision to neglect shear stresses leads to a maximum frequency up to which the classical equations of flexural motions can be used. Cremer, Heckl and Petersson



**Figure 2.10:** Wavelength for flexural waves in some exemplary plates made of steel, aluminium, glass or concrete.

suggest that the bending wavelength  $\lambda_P$  should exceed six times the plate thickness [Cremer 2005]:

$$\lambda_P > 6h. \quad (2.2.26)$$

This leads to the following expression for the maximum thickness given the material parameters and the maximum frequency  $f_{\max}$  to be used:

$$h < \frac{\pi \sqrt{\frac{E}{12\rho(1-\nu^2)}}}{18f_{\max}} \quad (2.2.27)$$

Figure 2.11 shows the maximum thickness as a function of the maximum frequency for steel, aluminium and concrete for the classical plate theory to be valid. For the given materials, the Kirchhoff theory is valid up to approximately 20 to 30 kHz for plates with a thickness of 1 cm, and up to more than 100 kHz for plates that are thinner than 1 mm.

If plates of higher thickness have to be investigated or if higher frequencies have to be considered, it is necessary to abandon the simplifications mentioned above. Significant extensions to the classical theory of plates published by Kirchhoff were made mainly during the first half of the twentieth century. In 1921 Stephen Timoshenko developed a theory for the motion of beams including transverse shear deformations [Timoshenko 1959]. Eric Reissner was able to solve the shear problem for plates and published his results in 1945 [Reissner 1945]. The plate model that is nowadays used as a standard in structural engineering is based on the work of Raymond

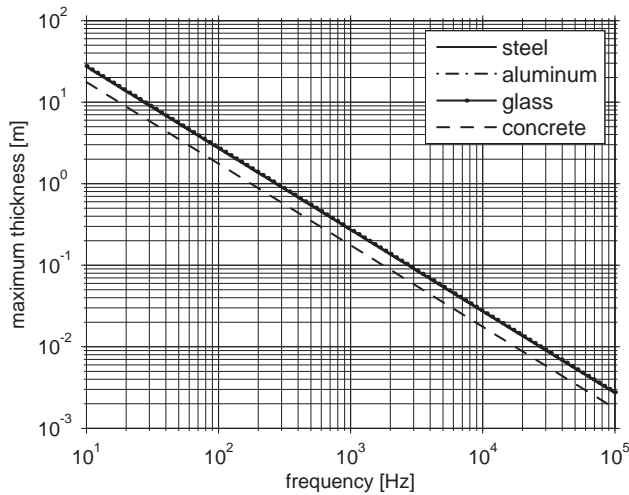


**Figure 2.11:** Maximum thickness of plates made of steel, aluminium or concrete for the Kirchhoff theory to provide a good approximation.

Mindlin, who presented an approximate plate theory including both transverse shear deformation and rotary inertia in 1951 [Mindlin 1951].

The models can be compared by the speed of propagation they predict with respect to the speed for guided waves in plates as derived by Rayleigh and Lamb [Lamb 1889]. The model for guided waves is obtained by considering the three-dimensional plate problem with longitudinal and transversal waves that have to satisfy the boundary conditions imposed by the limited thickness of the plate [Auld 1973]. Fig. 2.12 shows the different dispersion relations for a steel plate obtained from different theories, along with the frequency limit given by Eq. 2.2.27.

In this work, the classical plate theory using Kirchhoff's assumptions will primarily be used. This decision, however, should not be regarded as a limitation. On the contrary, it shows that the methods developed perform well, even if a simplified theoretical model is used. Furthermore, the approaches presented in the following chapters are based on the Green's function or the dispersion relation for the plate under investigation. By exchanging these propagation models, the methods developed can be applied even to a broader range of problems.

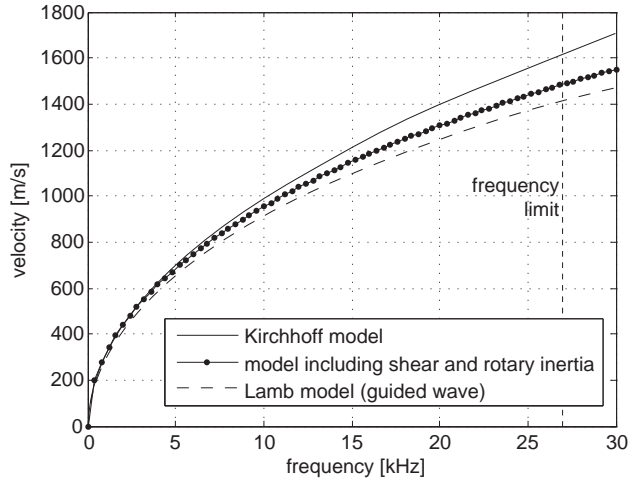


**Figure 2.12:** Phase velocity curves for a steel plate with a thickness of 1 cm: Kirchhoff bending model, corrected bending model including shear force and rotational inertia, Lamb model for guided waves. The frequency limit given by Eq. 2.2.27 is shown.

## 2.3 Green's function for flexural waves

In the previous sections, the homogeneous wave equations for one- and two-dimensional problems have been presented. As a subsequent step, it is necessary to analyse the wave equations for wave fields that contain sources.

### ■ 2.3.1 Inhomogeneous wave equation

Let us use the general term  $\tilde{S}(\underline{x}, \omega)$  to represent a source distribution in the temporal frequency domain. The inhomogeneous wave equation is given by the following expression:

$$\nabla^4 \tilde{u}(\underline{x}, \omega) - k^4 \tilde{u}(\underline{x}, \omega) = \tilde{S}(\underline{x}, \omega), \quad (2.3.28)$$

This can be written in short notation using the Helmholtz operator  $\mathcal{H}$ :

$$\mathcal{H} \tilde{u}(\underline{x}, \omega) = \tilde{S}(\underline{x}, \omega). \quad (2.3.29)$$

The Helmholtz operator  $\mathcal{H}$  relates the wave field  $\tilde{u}$  and the source distribution  $\tilde{S}$ . In order to calculate the generated wave field from a known distribution of sources, the inverse Helmholtz operator  $\mathcal{H}^{-1}$  is needed. Such an operator is called the Green operator  $\mathcal{G} = \mathcal{H}^{-1}$  [Tarantola 1988]:

$$\tilde{u}(\underline{x}, \omega) = \mathcal{H}^{-1} \tilde{S}(\underline{x}, \omega) = \mathcal{G} \tilde{S}(\underline{x}, \omega). \quad (2.3.30)$$

The Green operator carries out a spatial convolution of the source distribution and the Green's function in order to obtain the resulting field:

$$\tilde{u}(\underline{x}, \omega) = \mathcal{G}\tilde{s} = \int_{-\infty}^{\infty} \tilde{G}(\underline{x}, \underline{x}_0, \omega) \tilde{S}(\underline{x}_0, \omega) d\underline{x}_0. \quad (2.3.31)$$

The kernel of the Green operator  $\mathcal{G}$  is the Green's function  $G$ , which can be derived as solution to the inhomogeneous wave equation with a Dirac delta function as source term [Griffiths 2005]:

$$(\nabla^4 - k^4) \tilde{G}(\underline{x}, \underline{x}_0, \omega) = \delta(\underline{x} - \underline{x}_0). \quad (2.3.32)$$

This approach will be used in the following to determine the Green's functions for the one- and two-dimensional flexural wave equations. The Green's functions can then be used to determine the responses of beams and plates to a given excitation.

### ■ 2.3.2 Green's function for the one-dimensional flexural wave

The Green's function can be derived from Eq. 2.3.32. The complete derivation is presented in appendix B.1 due to its length. The Green's function for the one-dimensional case of a beam is given by the following equation:

$$\tilde{G}(x, x_0, \omega) = -\frac{1}{4k_B^3} (je^{-jk_B \Delta x} + e^{-k_B \Delta x}), \quad (2.3.33)$$

with  $\Delta x = |x - x_0|$  representing the distance to the position  $x_0$  of the source. It can be seen that the Green's function comprises a propagating and an evanescent part. The propagating part  $e^{-jk_B \Delta x}$  is phase-shifted by  $90^\circ$  with respect to the excitation; the evanescent part  $e^{-k_B \Delta x}$  rapidly dies out with increasing distance from the source.

### ■ 2.3.3 Green's function for the two-dimensional flexural wave

The two-dimensional Green's function for the plate equation is given by a combination of two Hankel functions of the second kind:

$$\tilde{G}(\underline{x}, \underline{x}_0, \omega) = -\frac{j}{8k_P^2} \left[ H_0^{(2)}(k_P \Delta x) - H_0^{(2)}(-jk_P \Delta x) \right], \quad (2.3.34)$$

with  $\Delta x = |\underline{x} - \underline{x}_0|$  representing the distance to the position  $\underline{x}_0$  of the source. The derivation can be found in appendix B.2. As in the one-dimensional case, the solution consists of a propagating and an evanescent part, which becomes more evident when an approximation to the Hankel functions is used as shown in the following section.

### ■ 2.3.4 Approximation of the Green's functions

For situations in which the product  $k\Delta x \gg 1$ , the expression for the Green's functions can be simplified:

- The evanescent part can be neglected in comparison to the propagating part.
- The Hankel function of the second kind can be approximated by an exponential function.

From the definition of the bending wavenumber in Eqs. 2.2.12 and 2.2.19 for the one-dimensional and two-dimensional case, respectively, it can be seen that the terms  $k_B\Delta x$  and  $k_P\Delta x$  increase

- with increasing distance from the source,
- with decreasing thickness of the beam or plate,
- with increasing frequency.

The one-dimensional Green's function given in Eq. 2.3.33 can be approximated by the following expression:

$$\tilde{G}(x, x_0, \omega) \approx -\frac{j}{4k_B^3} e^{-jk_B\Delta x} = \tilde{W}'(\omega) e^{-jk_B\Delta x}, \quad k_B\Delta x \gg 1. \quad (2.3.35)$$

The resulting function consists of two factors: the exponential factor  $e^{-jk_B\Delta x}$  describing the dispersive nature of the propagating waves influencing its phase spectrum, and the factor  $\tilde{W}'(\omega)$  describing a change of the amplitude spectrum of the excitation.

For the two-dimensional case, an asymptotic approximation of the Hankel function is used [Abramowitz 1964]:

$$H_0^{(2)}(k\Delta x) \approx \sqrt{\frac{2j}{\pi k\Delta x}} e^{-jk\Delta x}, \quad k\Delta x \gg 1. \quad (2.3.36)$$

Substitution of this approximation into Eq. 2.3.34 results in a description by exponential functions:

$$\tilde{G}(\underline{x}, \underline{x}_0, \omega) \approx \sqrt{\frac{1}{32j\pi k_P^5 \Delta x}} \left( e^{-jk_P\Delta x} - \sqrt{j} e^{-k_P\Delta x} \right), \quad k_P\Delta x \gg 1. \quad (2.3.37)$$

It can be seen that the term  $e^{-k_P\Delta x}$  describes an evanescent wave, which can be neglected for  $k_P\Delta x \gg 1$ . Hence, the two-dimensional Green's function can be

approximated by the following equation:

$$\tilde{G}(\underline{x}, \underline{x}_0, \omega) \approx \sqrt{\frac{1}{32j\pi k_P^5 \Delta x}} e^{-jk_P \Delta x} = \tilde{W}''(\omega) \frac{e^{-jk_P \Delta x}}{\sqrt{\Delta x}}, \quad k_P \Delta x \gg 1. \quad (2.3.38)$$

As in the one-dimensional case, the Green's function can be split into a factor describing the amplitude spectrum  $\tilde{W}''(\omega)$  and a factor representing the phase spectrum  $e^{-jk_P \Delta x}$ . Additionally, the factor  $1/\sqrt{\Delta x}$  accounts for the geometrical damping of the cylindrical wave front during propagation within the plate.

Figure 2.13 shows the accuracy of the approximations for the one- and the two-dimensional Green's functions. The phase is well approximated for distances higher than a quarter of the wavelength, the amplitude of the Green's function is well approximated for distances exceeding a wavelength.

In both the one- and the two-dimensional case, it can be seen that the essential characteristics of the Green's functions describing the dispersive nature of flexural waves are contained in the phase spectrum.

## 2.4 Response of beams and plates to point excitation

### ■ 2.4.1 Point excitation of a beam

If a force  $F$  acting in positive  $z$ -direction on a point  $x_0$  is introduced as the source term of the inhomogeneous wave equation, a formulation is obtained from which the response of the beam to the exciting force can be derived.

$$(\nabla^4 - k_B^4) \tilde{u}(x, x_0, \omega) = \frac{F}{B'} \delta(x - x_0). \quad (2.4.39)$$

Using the Green's function of the plate, the resulting vertical displacement can directly be given:

$$\tilde{u}(x, x_0, \omega) = -\frac{F}{4B'k_B^3} (je^{-jk_B \Delta x} + e^{-k_B \Delta x}). \quad (2.4.40)$$

The normal velocity  $v$  is given by multiplication by  $j\omega$ .

$$\tilde{v}(x, x_0, \omega) = j\omega \tilde{u}(x, x_0, \omega) = -\frac{j\omega F}{4B'k_B^3} (je^{-jk_B \Delta x} + e^{-k_B \Delta x}). \quad (2.4.41)$$

From this equation, the point mobility  $Y$ , i.e., the relation between force and velocity at the excitation point  $x_0 = 0$  can be derived:

$$Y = \frac{v(0, 0, \omega)}{F} = \frac{\omega(1-j)}{4B'k_B^3} = \frac{1-j}{4\sqrt{\omega^4 m'^3 B'}}. \quad (2.4.42)$$

This shows that a prescribed force exerted on a beam yields a lower velocity response if the mass density or the bending stiffness of the beam are higher.

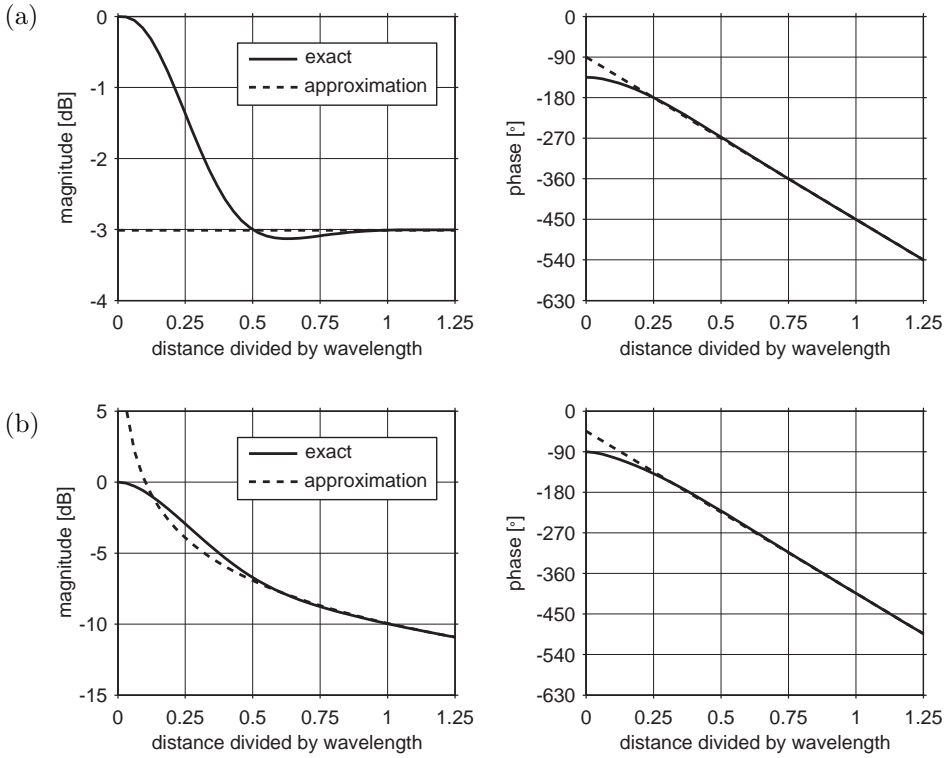


**Figure 2.13:** Magnitude and phase of the exact Green's function (solid line) and its approximation (dashed line): (a) one-dimensional case, (b) two-dimensional case; distance from the source is expressed in terms of the wavelength  $\lambda$ .

### ■ 2.4.2 Point excitation of a plate

In the following, the Green's function of the plate will be used to derive the vertical displacement due to a point force. Starting out from the inhomogeneous wave equation for the plate,

$$(\nabla^4 - k_P^4) \tilde{u}(\underline{x}, \underline{x}_0, \omega) = \frac{F}{B''} \delta(\underline{x} - \underline{x}_0), \quad (2.4.43)$$

the resulting displacement is readily obtained:

$$\tilde{u}(\underline{x}, \underline{x}_0, \omega) = -\frac{jF}{8k_P^2 B''} \left[ H_0^{(2)}(k_P \Delta x) - H_0^{(2)}(-jk_P \Delta x) \right]. \quad (2.4.44)$$

The normal velocity  $v$  is determined by multiplication by  $j\omega$  as in the one-dimensional case:

$$\tilde{v}(x, \underline{x}_0, \omega) = j\omega \tilde{u}(x, \underline{x}_0, \omega) = \frac{F\omega}{8k_P^2 B''} \left[ H_0^{(2)}(k_P \Delta x) - H_0^{(2)}(-jk_P \Delta x) \right]. \quad (2.4.45)$$

From this equation, the point mobility  $Y$  of the plate at the excitation point  $\underline{x}_0 = 0$  can be derived:

$$Y = \frac{v(0, 0, \omega)}{F} = \frac{\omega}{8k_P^2 B''} = \frac{1}{8\sqrt{B'' m''}} = \sqrt{\frac{3(1-\nu^2)}{16E\rho h^4}}. \quad (2.4.46)$$

This equation shows that the velocity obtained using a prescribed point force depends on the flexural rigidity  $B''$  and the mass density per unit area  $m''$ . The stiffer the plate, the more it resists to be set into vibration. In terms of material properties, the mobility is lower for

- higher Young's modulus  $E$ ,
- higher mass density  $\rho$ , or
- higher thickness  $h$ .

### ■ 2.4.3 Temporal responses of beams and plates

In the preceding sections, the responses of beams and plates to point excitation have been derived. The equations representing the response have been given in the temporal frequency domain. When the associated temporal response is needed, it can in most cases not directly be obtained by means of a discrete inverse Fourier transform. This is due to the dispersive nature of bending waves. The phase velocity according to Eqs. 2.2.13 and 2.2.20 tends towards zero, meaning that low frequency components arrive significantly later than components from the rest of the spectrum. As a consequence, the bending wavelet has infinite extent in the temporal domain. This poses a problem in the context of the discrete Fourier transform, which assumes periodicity for the finite time window considered. When the temporal response is calculated from an inverse discrete Fourier transform of the frequency domain equations, care has to be taken to suppress low frequency components that would arrive after the duration of the time window. If these components are not appropriately suppressed by filtering in the frequency domain, wrap-around effects can occur. The low frequency components that should appear at a later point in time can then show up at the beginning of the wavelet.

A more elegant solution is arrived at by application of the continuous Fourier transform, thereby calculating the temporal bending wavelet analytically. Temporal responses of flexural systems have first been derived by Boussinesq [Boussinesq 1885]

and have recently been presented by Büssow for the normal velocity response of beams and plates [Büssow 2008a].

For the beam, the velocity is given by the following expression:

$$v(x, x_0, t) = \frac{FH(t)}{4m'} \sqrt{\frac{2}{\pi A_B}} \sqrt{\frac{1}{t}} \sin\left(\frac{|x - x_0|^2}{4A_B t}\right), \quad (2.4.47)$$

with  $H(t)$  being the Heaviside step function.

For the plate, one arrives at the following similar representation of the normal velocity:

$$v(\underline{x}, \underline{x}_0, t) = \frac{FH(t)}{4\pi\sqrt{B''m''}} \frac{1}{t} \sin\left(\frac{|\underline{x} - \underline{x}_0|^2}{4A_P t}\right). \quad (2.4.48)$$

In both cases the phase of the response is determined by the distance to the source and the time elapsed, whereas the amplitude is determined by the time only, apart from constant factors accounting for material properties.

In the argument of the sine function, the dispersion factor  $D$  determines how fast the spectral components separate when an impulsive signal propagates in a flexural medium [Büssow 2008b]:

$$D = \frac{|\underline{x} - \underline{x}_0|^2}{4A} = \frac{(\Delta x)^2}{4A}, \quad (2.4.49)$$

with  $\Delta x = |\underline{x} - \underline{x}_0|$  being the distance from the source. The separation increases quadratically with increasing distance from the source.

## 2.5 Reflected and scattered flexural waves

Up to this point, results have been presented for homogeneous media of infinite extent. The wave field in finite beams and plates is essentially determined by the reflections occurring at the boundaries. Furthermore, the assumption that inhomogeneities in the medium scatter or reflect incident waves forms the foundation for the detection of these regions by imaging methods. Therefore, it is necessary to quantify the relation between an incident wave and the generated reflection at a boundary or inhomogeneity.

### ■ 2.5.1 Reflection from boundaries

The wave field in a semi-infinite plate ( $y > 0$ ) can be modelled by considering solutions of the following form [Graff 1975]:

$$\tilde{u}(x, y, \omega) = g(y)e^{j(k_x x - \omega t)}, \quad (2.5.50)$$

with  $g(y)$  describing the behaviour of the field in  $y$ -direction and  $k_x$  being the component of the wavenumber vector  $\underline{k}$  along the boundary. Snell's law has been used in Eq. 2.5.50, stating that incident and reflected wave at a straight boundary share the same wavenumber vector component along the boundary [Auld 1973].

Inserting Eq. 2.5.50 into the wave equation yields a quartic equation, from which four solutions can be obtained. Therefore, the wave field at the boundary can consist of the following four components [Graff 1975]:

$$\begin{aligned} \tilde{u}(x, y, \omega) = & C_1 e^{j(k_x x - k_y y - \omega t)} + C_2 e^{j(k_x x + k_y y - \omega t)} \\ & + C_3 e^{-k_{y, \text{ev}} y} e^{j(k_x x - \omega t)} + C_4 e^{k_{y, \text{ev}} y} e^{j(k_x x - \omega t)}, \end{aligned} \quad (2.5.51)$$

$$k_y = \sqrt{k_P^2 - k_x^2}, \quad (2.5.52)$$

$$k_{y, \text{ev}} = \sqrt{k_P^2 + k_x^2}. \quad (2.5.53)$$

The terms  $C_1 \dots C_4$  represent coefficients determining the strength of the respective components. The  $C_1$  and  $C_2$  terms describe propagating waves, the first one being the incident wave and the latter representing a reflected wave propagating away from the boundary. The  $C_3$  and  $C_4$  terms represent non-propagating fields. Graff rejects the field described by the  $C_4$  term “because it yields exponentially increasing waves” [Graff 1975]. However, it can be argued that it can be interpreted as an evanescent field *incident* on the boundary. In order to derive the reflection coefficients for an incident plane propagating wave, the  $C_4$  term is not neglected but chosen to be zero.

Figure 2.14 illustrates the relation between the wavenumber components along and normal to the boundary according to Snell's law. Furthermore, the damping function  $k_{y, \text{ev}}$  of the near-field represented by the  $C_4$  term is shown.

Assuming that the incident plane wave has amplitude  $C_1 = 1$ , there are two unknown reflection coefficients: the coefficient  $R = C_2/C_1$  describes the generation of a propagating wave upon reflection, the coefficient  $R_{\text{ev}} = C_3/C_1$  the generation of an evanescent field. In general,  $R$  and  $R_{\text{ev}}$  are dependent on the angle of incidence. However, in the special case of simply supported boundaries, no evanescent field is generated and  $R = -1$ ,  $R_{\text{ev}} = 0$  [Fahy 1985].

The reflection coefficients can be determined by imposing two conditions on the boundary. Table 2.1 lists the conditions for three typical cases: free, simply supported, and clamped boundaries.

Figure 2.15 shows the reflection coefficients  $R$  and  $R_{\text{ev}}$ . It can be seen that the magnitude of the reflected propagating wave is equal to one in all three cases. However, there is an additional phase shift, which is dependent on the angle of incidence for free and clamped boundaries.

The reflection coefficients for the one-dimensional beam can be obtained by setting  $k_x = 0$ , i.e., using the values for normal incidence. Table 2.2 lists the coefficients for

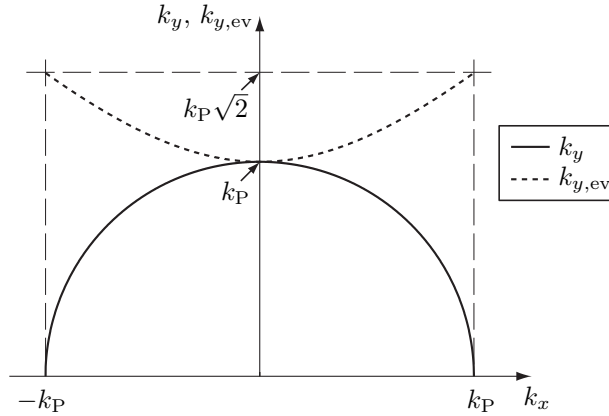


**Figure 2.14:** Relation between  $k_x$ ,  $k_y$  and  $k_{y,ev}$  according to Snell's law.

boundary condition	mathematical constraints
free	$\frac{\partial^2}{\partial y^2} \tilde{u}(x, 0, \omega) = 0$ $\frac{\partial^3}{\partial y^3} \tilde{u}(x, 0, \omega) = 0$
clamped	$\tilde{u}(x, 0, \omega) = 0$ $\frac{\partial}{\partial y} \tilde{u}(x, 0, \omega) = 0$
simply supported	$\tilde{u}(x, 0, \omega) = 0$ $\frac{\partial^2}{\partial y^2} \tilde{u}(x, 0, \omega) = 0$

**Table 2.1:** Three typical boundary conditions for plates and associated equations [Chaigne 2007].

the three aforementioned boundary conditions [Mead 1982].

The reflection coefficient  $R_{ev}$  for the evanescent wave can even take values higher than one. However, the associated field decreases rapidly with increasing distance from the boundary, such that its effect is negligible from a certain distance on. Figure 2.16 shows the damping of the near-field for free and clamped boundaries for different angles of incidence. It can be seen that the near-field effects can be neglected at distances exceeding a wavelength.

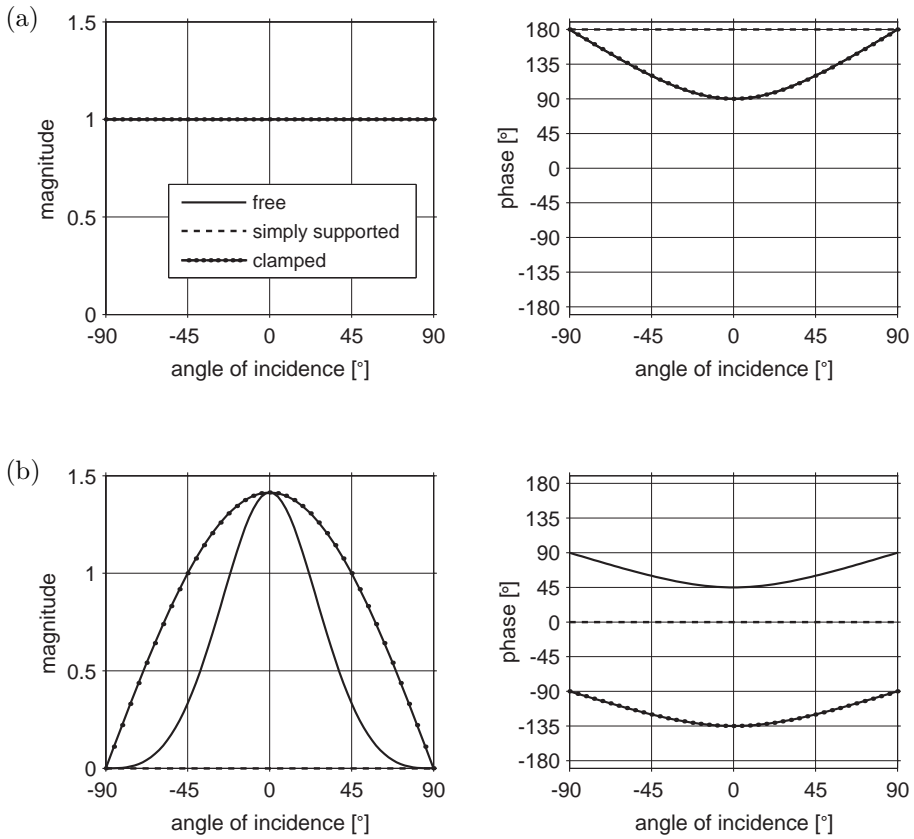


**Figure 2.15:** Magnitude and phase of the reflection coefficients (a)  $R$  and (b)  $R_{ev}$  for three typical boundary conditions.

boundary condition	$R$	$R_{ev}$
free	$j$	$1 + j$
clamped	$j$	$-1 - j$
simply supported	$-1$	$0$

**Table 2.2:** Reflection coefficients for beam ends.

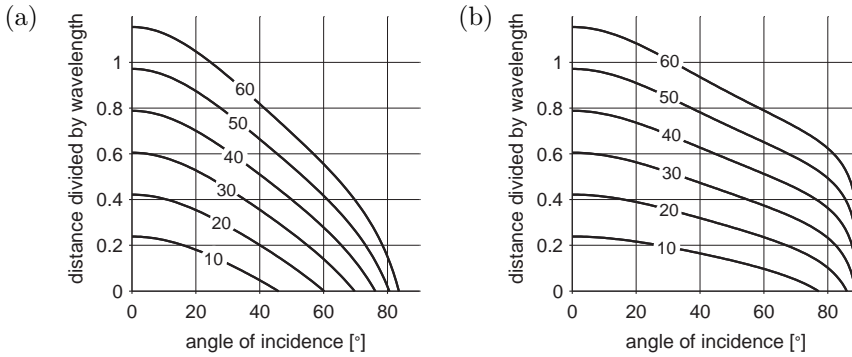


**Figure 2.16:** Damping of the near-field with increasing distance from the boundary dependent on the angle of incidence for (a) free and (b) clamped boundary conditions; contour lines show the damping from 10 to 60 dB relative to the incident wave; the distance is expressed in terms of the wavelength.

### ■ 2.5.2 Reflection at cross-sectional changes

With respect to the detection of material defects, it is interesting to analyse the reflection from a sudden change in material thickness. This coarse model of an inhomogeneity can give a first impression of the strength of the field that is reflected from a defect.

A model for the reflection and transmission of bending waves at a sudden change in material parameters is given by Cremer et al. [Cremer 2005]; only normal incidence is considered. In the present context, it is assumed that the only difference on both sides of the sudden change is given by a variation in thickness. Furthermore, the beam or plate is assumed to have a standard thickness  $h_0$ , such that the cross-sectional change can be quantified by the quotient

$$Q = \frac{h_0}{h_1}, \quad (2.5.54)$$

with  $h_1 < h_0$  representing the loss in thickness on the other side of the change. The reflection coefficient  $R$  for propagating waves is then given by the following expression:

$$R = \frac{2Q(1-Q) - j\sqrt{Q}(1-Q)^2}{\sqrt{Q}(1+Q)^2 + 2Q(1+Q)}. \quad (2.5.55)$$

For evanescent waves, the following reflection coefficient  $R_{ev}$  is obtained:

$$R_{ev} = \frac{\sqrt{Q}(1-Q^2) - j\sqrt{Q}(1-Q)^2}{\sqrt{Q}(1+Q)^2 + 2Q(1+Q)}. \quad (2.5.56)$$

Figure 2.17 shows magnitude and phase for the reflection coefficients  $R$  and  $R_{ev}$  for different values of  $Q$ . The reflection to be expected is relatively weak. For instance, the magnitude reflection coefficient  $R$  for the propagating field does not exceed 0.5 if the ‘defect’ is not thinner than approximately 10 % of the standard plate thickness.

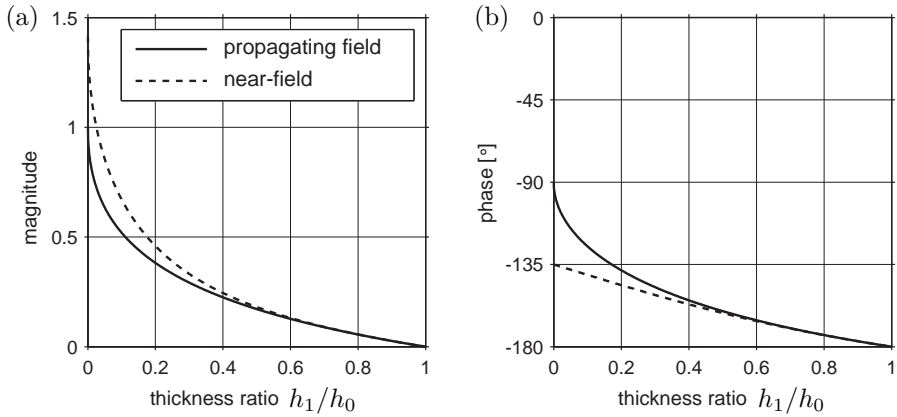


**Figure 2.17:** Magnitude (a) and phase (b) of the reflection coefficients  $R$  (solid line) and  $R_{ev}$  (dotted line) for a normal incident plane wave at a cross-sectional change.

It is thus seen that a defect has to be quite severe before it can simply be detected by looking for reflections, or alternatively, that a good signal-to-noise ratio of the measurement unit has to be maintained in order to pick up reflections from smaller changes in thickness.

### ■ 2.5.3 Scattering of flexural waves

For features of a material inhomogeneity that are in the order of magnitude of a wavelength, it does not make sense to use a reflection coefficient to describe the effect of the object on the wave field. If the object itself or parts of it, such as sharp edges, have a size comparable to the wavelength, diffraction plays a more important role [Robinson 1987]. In fact, diffraction and scattering can be seen as the more general description for the interaction of a change in medium parameters with the wave field. According to Huygens' principle, reflected wave fronts can be interpreted as the superposition of scattering effects from an aligned distribution of points at a boundary marking a change in medium properties. If this distribution of scatterers is of sufficient size with respect to the wavelength, incident waves are reflected according to Snell's law, whereas no preferred direction can be given for point-like scatterers [Gelius 2000].

Hence, it is desirable to derive the equations that describe the scattering of flexural waves. These equations will be used in Chapters 4 and 5 to obtain estimates of the material properties from measured wave fields.

There are many references that derive analytical expressions for the field scattered by a material inhomogeneity of certain geometrical shape, for example straight cracks [Porter 2007] or cylindrical inclusions [Wang 2005]. In the following, however, the more general equations describing the scattering of an incident wave field due to arbitrary inhomogeneities described by a spatial function of material properties are presented.

In order to derive the wave field caused by the scattering object, the *total* wave field is written as sum of the *incident* wave field  $\tilde{u}_{\text{inc}}(\underline{x}, \omega)$  and the *scattered* wave field  $\tilde{u}_{\text{sc}}(\underline{x}, \omega)$ :

$$\tilde{u}(\underline{x}, \omega) = \tilde{u}_{\text{inc}}(\underline{x}, \omega) + \tilde{u}_{\text{sc}}(\underline{x}, \omega). \quad (2.5.57)$$

It should be noted that this scattering model introduces the incident field  $\tilde{u}_{\text{inc}}(\underline{x}, \omega)$  and the scattered field  $\tilde{u}_{\text{sc}}(\underline{x}, \omega)$  as auxiliary fields for the mathematical description and treatment of the scattering problem. The only field that is physically observable is the total field  $\tilde{u}(\underline{x}, \omega)$ .

The incident wave field is the field caused by a source with spectrum  $\tilde{S}(\omega)$  at position  $\underline{x}_s$  if there is no scatterer present. The wave equation for this incident field is the inhomogeneous wave equation with a source term on the right hand side:

$$(\nabla^4 - k_0^4) \tilde{u}_{\text{inc}}(\underline{x}, \omega) = \tilde{S}(\omega) \delta(\underline{x} - \underline{x}_s), \quad (2.5.58)$$

with  $k_0$  being the constant wavenumber of the homogeneous background medium.

Hence, the Green's function can directly be used to calculate this field:

$$\tilde{u}_{\text{inc}}(\underline{x}, \omega) = \tilde{S}(\omega) \tilde{G}(\underline{x}, \omega). \quad (2.5.59)$$

With the scatterer present, the wave equation of the total field can be given:

$$[\nabla^4 - k(\underline{x})^4] \tilde{u}(\underline{x}, \omega) = \tilde{S}(\omega) \delta(\underline{x} - \underline{x}_s). \quad (2.5.60)$$

Since the medium with the scatterer is inhomogeneous, the wavenumber  $k(\underline{x})$  is a function of position. For reasons of simplicity, Eq. 2.5.60 has been derived using the assumption that the scattering object can be described by a change in mass density  $\rho$  only. If other material properties or the thickness of the plate are allowed to vary, the bending stiffness can no longer be regarded as constant and the flexural wave equation assumes a significantly more complicated form, see for example [Leissa 1969] or [Chaigne 2007]. The decision to assume the bending stiffness to be constant can be justified by comparison to approaches used for modelling acoustical scattering in bulk media, which often solve only the scalar field problem by taking the compressibility as variable while keeping the density constant [Abubakar 2005]. However, Van Dongen and Wright were able to show that the consideration of both density and compressibility leads to improved reconstruction results for the scattering problem in bulk media [Van Dongen 2007]. Therefore, a possible extension of the flexural scattering model including variation in the bending stiffness, albeit beyond the scope of this work, has to be kept in mind.

The wave equation for the scattered field is readily derived by subtracting the wave equation of the incident field (Eq. 2.5.58) from the wave equation of the total field (Eq. 2.5.60). After rearrangement, the following result is obtained:

$$(\nabla^4 - k_0^4) \tilde{u}_{\text{sc}}(\underline{x}, \omega) = [k(\underline{x})^4 - k_0^4] \tilde{u}(\underline{x}, \omega). \quad (2.5.61)$$

The scattered field  $\tilde{u}_{\text{sc}}(\underline{x}, \omega)$  can be modelled as a wave field caused by a source distribution. This source distribution is present within the scattering object, for which the difference between local material properties  $k(\underline{x})$  and the properties of the background  $k_0^4$  is non-zero. These distributed sources are usually referred to as the *contrast sources* [Van den Berg 1997]. The strength of the contrast sources is determined by the strength of the total field within the scatterer and the so-called scattering potential  $\tilde{\Phi}(\underline{x}, \omega)$  [Wolf 1969]:

$$\tilde{\Phi}(\underline{x}, \omega) = k(\underline{x})^4 - k_0^4. \quad (2.5.62)$$

Equation 2.5.61 shows that the scattered field is propagating in the homogeneous background medium with wavenumber  $k_0$ . The effects of the inhomogeneities are modelled by the source term on the right-hand side of this equation.

The scattering potential  $\tilde{\Phi}(\underline{x}, \omega)$  depends on the frequency. In order to model the scattering objects as changes in material parameters independent of frequency, the contrast function  $\chi(\underline{x})$  is introduced:

$$\tilde{\Phi}(\underline{x}, \omega) = k_0^4 \left\{ \left[ \frac{k(\underline{x})}{k_0} \right]^4 - 1 \right\} = k_0^4 \chi(\underline{x}). \quad (2.5.63)$$

The dimensionless contrast function  $\chi(\underline{x})$  is zero outside the scatterer. From the dispersion relation  $k(\underline{x}) = \omega/c(\underline{x}, \omega)$ , it is seen that the contrast function is positive if the phase speed  $c(\underline{x}, \omega)$  in the scatterer is lower than in the surrounding background medium, and negative if the phase speed is higher.

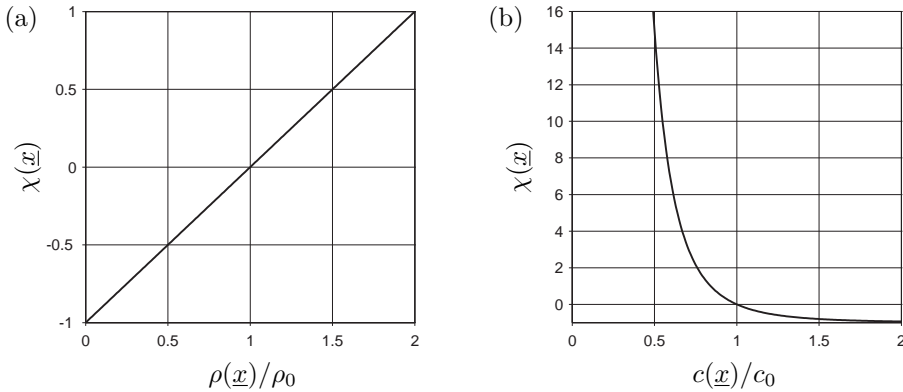


**Figure 2.18:** The dimensionless contrast depends linearly on the local change in density with respect to the background medium (a); the dependency on the local phase speed with respect to the background medium is nonlinear (b).

The source term of the scattered field described by Eq. 2.5.61 is formed by the product of the scattering potential  $\tilde{\Phi}(\underline{x}, \omega)$  and the total field  $\tilde{u}(\underline{x}, \omega)$ . It is customary to introduce the *contrast sources*  $\tilde{w}(\underline{x}, \omega)$  as a shorthand notation for this product [Van den Berg 1997]:

$$\tilde{w}(\underline{x}, \omega) = \tilde{\Phi}(\underline{x}, \omega) \tilde{u}(\underline{x}, \omega). \quad (2.5.64)$$

The scattered field can be calculated by spatial convolution of the Green's function of the background medium with the source term [Tarantola 1988]:

$$\tilde{u}_{\text{sc}}(\underline{x}, \omega) = \int_{-\infty}^{\infty} \tilde{G}(\underline{x}, \underline{x}_0, \omega) \tilde{w}(\underline{x}_0, \omega) d\underline{x}_0. \quad (2.5.65)$$

This concludes the description of the model for scattering in flexural wave fields. Summarising, the following functions have been introduced:

- The *contrast*  $\chi(\underline{x})$  represents the relative deviation of the material parameters from the background medium.

- The *scattering potential*  $\tilde{\Phi}(\underline{x}, \omega)$  is the frequency-dependent potential function describing how strong a material inhomogeneity interacts with the total wave field.
- The *contrast sources*  $\tilde{w}(\underline{x}, \omega)$  form a source distribution caused by the interaction of the wave field with material inhomogeneities. This source distribution generates the scattered field.

The scattering model for flexural waves will be used to derive the methods for imaging of inhomogeneities in Chapter 4 and 5.

## 2.6 Summary

In this chapter, the basic equations governing the flexural motion of beams and plates under the Kirchhoff plate model have been introduced. Furthermore, the Green's functions describing the reaction to an impulsive excitation of the medium have been derived. Descriptions of the reflection and scattering of flexural waves have been given. Multiple scattering is modelled by a simplified scalar scattering model.

The theory of flexural wave fields presented in this chapter will form the basis for methods used for their analysis. In the following, the just obtained theoretical background will be needed to derive techniques for the removal of the effects of dispersion and for the generation of images of sources and scatterers from measurements of the wave field.

## Analysis and removal of dispersion effects

*Everything we see hides another thing,  
we always want to see what is hidden by what we see.  
There is an interest in that which is hidden...*

(René Magritte, 1898 – 1967)

The main purpose of acoustical and vibrational imaging is the extraction of information on inhomogeneities in a medium from a measured wave field. Typical examples for these inhomogeneities are boundaries and scatterers. These inhomogeneities can be modelled by secondary sources. The contributions of all primary and secondary sources constitute the measured response of the medium under investigation.

The key information needed to obtain an image is given by the strength and the arrival times of the waves caused by secondary sources. When analysing flexural wave fields, the presence of dispersion can impede the localisation of these sources [Wilcox 2001a]. It has already been pointed out that the speed of propagation in a flexural wave field depends on the frequency. An impulsive wave travelling through the medium will thus spread out over time and space with increasing distance from the source. This has two important consequences:

- The spreading of waves impedes the accurate determination of their temporal position in the measured signal. Therefore, the localisation of the source is made difficult.
- The spreading of the waves of the contributing sources leads to overlapping events in the measured response, preventing the separation and identification of different sources.

Both effects increase over time and with increasing distance from the source. Therefore, it is desirable to remove the effects of dispersion from a measured signal to facilitate its analysis and to allow for accurate localisation and identification of events

caused by vibrational sources. The present chapter gives an overview of possible methods to perform dispersion removal. The procedures for dispersion compensation are derived from the model of a wave field in a dispersive medium. Also, methods for obtaining the dispersion properties directly from measurements are presented. It is shown that the removal of dispersion effects cannot be carried out independently from the analysis of the primary source signal, leading to a combined framework for dispersion compensation and source signature deconvolution.

## 3.1 Model of the flexural response

### ■ 3.1.1 Time-invariant reflection model for non-dispersive media

The model of a flexural response is based on the convolutional model, which is well known in the fields of seismics [Robinson 1985] and room acoustics [Berkhout 1980]. It describes a measured signal  $u(t)$  as the superposition of wavelets  $W_i(t)$  representing the signals caused by secondary sources in the medium. Examples for secondary sources are reflecting boundaries, which can be modelled by mirror image sources, and point-like diffractors and scatterers.

The superposition of all source signals with different arrival times  $t_i$  constitutes the total response:

$$u(t) = \sum_i W_i(t - t_i) + n(t), \quad (3.1.1)$$

with  $n(t)$  denoting an additive noise signal.

Assuming a simplified model in which the secondary sources share the spectrum of the source wavelet  $S(t)$  and can be characterised by their strength  $R_i$  only, the total response can be represented as a convolution of the source signal and a train of Dirac pulses:

$$u(t) = S(t) * \sum_i R_i \delta\left(t - \frac{x_i}{c}\right) + n(t), \quad (3.1.2)$$

with  $x_i$  being the distance between the secondary source  $i$  and the receiver<sup>1</sup>. It can be seen that this equation essentially represents a one-dimensional model. The signal of the primary source can be taken into account by including  $R_0 = 1$ .

### ■ 3.1.2 Distance-dependent reflection model for dispersive media

In flexural wave fields, the signal of a secondary sources is not only influenced by the primary source signal, but also determined by the dispersion characteristics and the distance between source and receiver as shown in the previous chapter. As a result

<sup>1</sup>In contrast to chapter 2,  $x_i$  is used instead of  $\Delta x_i$  as a simplified notation.

in the analysis of the approximation of the Green's function in Section 2.3.4, it was found that the dispersive nature of the Green's function is given by an exponential term describing the non-linear phase spectrum:

$$\tilde{W}(x_i, \omega) = e^{-jkx_i} = e^{-j\frac{\sqrt{\omega}}{A}x_i} \quad (3.1.3)$$

The inverse temporal Fourier transform of this expression is now defined as the *flexural wavelet*  $W(x_i, t)$ . This time signal contains the dispersive properties of a source at distance  $x_i$  from the receiver and can be used to model the measured response in a dispersive medium:

$$u(t) = S(t) * \sum_i R_i W(x_i, t) + n(t). \quad (3.1.4)$$

Note that the spectral properties of the Green's function that are not taken into account by the wavelet  $W(x_i, t)$  can be incorporated in the source signal  $S(t)$ . Likewise, the distance-dependent geometrical damping factor can be combined with the reflection coefficient  $R_i$ .

In this model, it is assumed that all source signals are produced at the same point in time  $t = 0$ , and that the strength of the dispersion is thus influenced by the distance between source and receiver. This requirement is fulfilled by the mirror image source model for reflecting boundaries, for example, as illustrated in Fig. 3.1. The boundary reflection can be replaced by a mirror image source on the opposite side of the boundary. The difference between the signals of the primary and secondary source is determined by the reflection coefficient  $R_i$ , which can be used to model a certain boundary condition. Simply supported boundaries, for instance, can be modelled by setting  $R_i = -1$  [Graff 1975].

## 3.2 Dispersion removal for known source-to-receiver distance

In the following sections, it will be investigated how the effects of dispersion can be removed if the dispersion characteristics of the material under investigation are known. Starting out from the model of the measurement  $u(t)$  taken in a dispersive wave field, a convolution filter  $F_D(t)$  is derived that can be applied to obtain a response  $q(t)$  without dispersion:

$$q(t) = F_D(t) * u(t). \quad (3.2.5)$$

In order to derive this filter, the transformation of the measurement  $u(t)$  to the frequency domain is used:

$$\tilde{u}(\omega) = \tilde{S}(\omega) \sum_i R_i \tilde{W}(x_i, \omega). \quad (3.2.6)$$

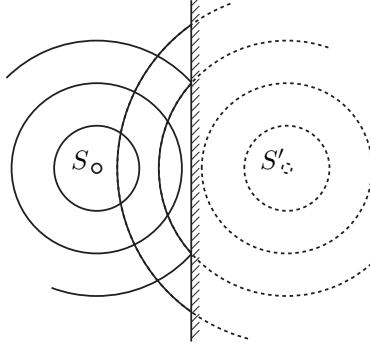


**Figure 3.1:** Illustration of the mirror image source model: the reflection of the primary source  $S$  on a boundary can be modelled by a mirror image source  $S'$ .

In this equation, the noise term  $n(t)$  has been neglected for simplicity.

If there is only one source present and the distance  $x_0$  between source and receiver is known, Eq. 3.2.6 can be simplified considerably:

$$\tilde{u}(\omega) = \tilde{S}(\omega)R_0\tilde{W}(x_0, \omega). \quad (3.2.7)$$

In this case, the matched filter to be applied to remove the effects of dispersion is the complex conjugate of the dispersive wavelet  $\tilde{W}(x_0, \omega)$ :

$$\tilde{F}_D(x_0, \omega) = \tilde{W}^*(x_0, \omega) = e^{jkx_0} = e^{j\frac{\sqrt{\omega}}{A}x_0}. \quad (3.2.8)$$

Application of this filter leads to the following result:

$$\tilde{q}(\omega) = \tilde{F}_D(x_0, \omega)\tilde{u}(\omega) = \tilde{S}(\omega)R_0. \quad (3.2.9)$$

For known source-to-receiver distance, the spectrum  $\tilde{S}(\omega)$  and strength  $R_0$  of the source are retrieved. The filtering operation can also be expressed as convolution in the time domain:

$$q(\tau) = \int_{-\infty}^{\infty} F_D(x_0, \tau - t)u(t) dt. \quad (3.2.10)$$

For discrete signals, the filtering operation can be written as matrix-vector multiplication as suggested by Berkhout et al. [Berkhout 2007]:

$$\underline{q}(\tau) = \underline{F}(\tau, t)\underline{u}(t), \quad (3.2.11)$$

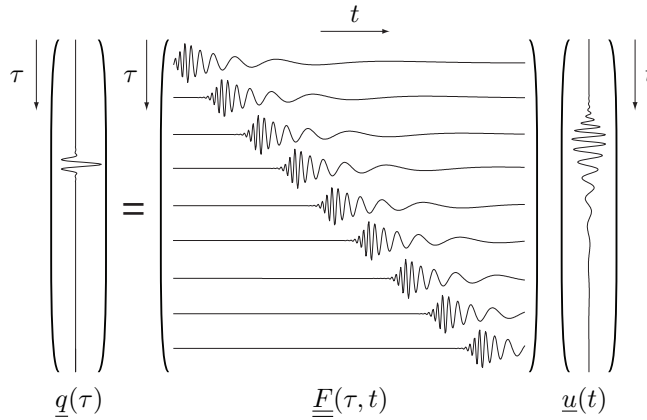


**Figure 3.2:** Illustration of dispersion removal by time-invariant convolution, after Berkhout et al. [Berkhout 2007].

with the rows of the matrix  $\underline{F}$  given by a time-sampled version of the flexural wavelet  $W(x_0, \tau - t)$  as symbolically illustrated in Fig. 3.2.

If there is a source present at a different distance  $x_1$ , for which the filter  $F_D(x_0, t)$  was not designed, its signal will show up in the output  $q(t)$  as well. The response of the filter to this input can easily be calculated:

$$\tilde{q}(x_0, \omega) = \tilde{F}_D(x_0, \omega) \tilde{S}(\omega) R_1 e^{jkx_1} = \tilde{S}(\omega) R_1 e^{-jk(x_1 - x_0)}. \quad (3.2.12)$$

Hence, signals from sources at other distances than  $x_0$  will still exhibit dispersive characteristics after the filtering operation. The strength of this dispersion is determined by the difference of the distance to the source  $x_1$  and the distance  $x_0$  the filter was designed for.

### 3.3 Dispersion removal by distance-dependent filtering

In a lot of applications, the distance between source and receiver cannot be assumed to be known beforehand. Therefore, it is desirable to develop a filter which is able to remove the effects of dispersion without prior knowledge about the position of a source. This can for example be achieved by making the matched filter  $F_D(x, \omega)$  distance-dependent as suggested by Wilcox et al. [Wilcox 2001b]. A similar concept for dispersion removal has been presented by Berkhout et al. [Berkhout 2007], proposing a dispersion compensation procedure based on time-variant convolution. The output obtained is a time signal in a non-dispersive medium for which a speed of propagation must be chosen.

The present work follows the idea of Wilcox et al. by choosing distance information as output of the dispersion removal procedure, thereby rendering the choice of an arbitrary propagation speed unnecessary. Furthermore, the distance between a secondary source and the receiver is the information of interest for obtaining an image showing the positions of secondary sources. Therefore, dispersion removal should be defined as an operation transforming a temporal signal containing dispersive wavelets to a spatial map of events associated with the observed dispersive time signal.

The filter function is no longer chosen for a fixed distance  $x_0$  as in Eq. 3.2.8, but depends on the distance  $x$  as a running variable:

$$\tilde{F}_D(x, \omega) = \tilde{W}^*(x, \omega) = e^{jkx} = e^{j \frac{\omega}{c(\omega)} x}. \quad (3.3.13)$$

The output of the filter is a function  $q$  of source-to-receiver distance  $x$ . For every distance  $x$  of interest, a matched filter corresponding to this distance is applied to the input signal:

$$q(x) = \int_{-\infty}^{\infty} \tilde{F}_D(x, \omega) \tilde{u}(\omega) d\omega. \quad (3.3.14)$$

In order to illustrate this operation and compare it to the filter for a fixed distance  $x_0$ , an inverse Fourier transform is applied to Eq. 3.3.14. This operation allows to express the filter function by time signals. The detailed derivation is presented in Appendix C and results in the following integral:

$$q(x) = 2\pi \int_{-\infty}^{\infty} W(x, t) u(t) dt. \quad (3.3.15)$$

The output for the distance  $x$  is thus determined in the time domain by the correlation of the input signal  $u(t)$  and the dispersive wavelet  $W(x, t)$  for the specific distance  $x$ . For discrete signals, this filtering operation can be written as matrix-vector multiplication:

$$\underline{q}(x) = \underline{F}(x, t) \underline{u}(t), \quad (3.3.16)$$

with the rows of the matrix  $\underline{F}$  given by a time-sampled version of the flexural wavelet  $W(x, t)$ . Fig. 3.3 illustrates the operation of dispersion removal for the distance-dependent case.

### 3.4 Dispersion removal in the wavenumber-frequency domain

An alternative and computationally simpler method for dispersion removal has been presented by Wilcox [Wilcox 2003]. This approach makes use of a representation in

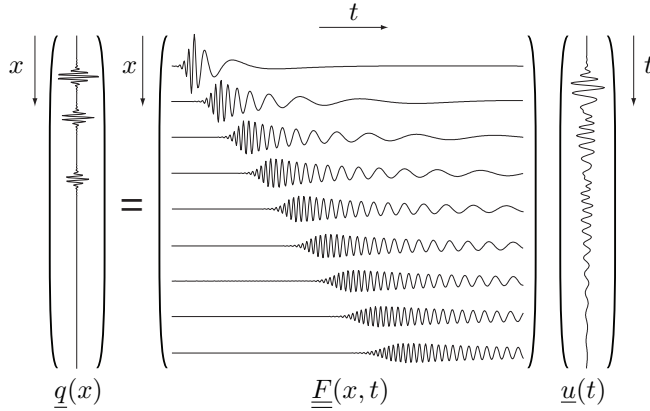


**Figure 3.3:** Illustration of the matrix multiplication needed in order to perform dispersion removal by distance-dependent convolution, after [Berkhout 2007].

the wavenumber-frequency domain, which is obtained by application of a temporal and a spatial Fourier transform. In the following, the matched filter derived above will be analysed in this domain.

A representation of the result of the distance-dependent matched filter for dispersion removal in the wavenumber-frequency domain is obtained by application of a spatial Fourier transform to Eq. 3.3.14, using  $k_x$  as the Fourier variable with respect to the distance  $x$ :

$$\tilde{q}(k_x) = \int_{-\infty}^{\infty} \int_{-\infty}^{\infty} \tilde{F}_D(x, \omega) \tilde{u}(\omega) d\omega e^{jk_x x} dx. \quad (3.4.17)$$

Under the assumption that the integrand is continuous and that the Fourier transforms converge, the order of integration can be changed:

$$\tilde{q}(k_x) = \int_{-\infty}^{\infty} \int_{-\infty}^{\infty} \tilde{F}_D(x, \omega) e^{jk_x x} dx \tilde{u}(\omega) d\omega = \int_{-\infty}^{\infty} \tilde{\tilde{F}}_D(k_x, \omega) \tilde{u}(\omega) d\omega. \quad (3.4.18)$$

The inner integral represents the filter function  $\tilde{\tilde{F}}_D(k_x, \omega)$  in the wavenumber-frequency domain, which is given by the spatial Fourier transform of Eq. 3.3.13:

$$\tilde{\tilde{F}}_D(k_x, \omega) = \int_{-\infty}^{\infty} \tilde{F}_D(x, \omega) e^{jk_x x} dx = \int_{-\infty}^{\infty} e^{j\frac{\omega}{c(\omega)}x} e^{jk_x x} dx = 2\pi\delta\left[\frac{\omega}{c(\omega)} + k_x\right]. \quad (3.4.19)$$

The Dirac delta function describes the curve of the dispersion relation for the flexural wave field:

$$k_x = -k = -\omega/c(\omega). \quad (3.4.20)$$

The negative sign arises from the fact that in the context of a transformation from a temporal to a spatial function, different exponential kernels in the definition of the Fourier transform are used (see appendix A). In a direct mapping from frequency to wavenumber in which positive time is chosen to correspond to positive distance, positive temporal frequencies have to be mapped to negative wavenumbers and vice versa. This is due to the fact that in this section, the spatial variable is chosen to designate the source position relative to the point of observation, whereas the kernels of the spatial Fourier transform are chosen with the spatial coordinate corresponding to the point of observation in a wave field.

Putting the result back into Eq. 3.4.18, the following formulation for dispersion removal in the wavenumber-frequency domain is obtained:

$$\tilde{q}(k_x) = 2\pi \int_{-\infty}^{\infty} \delta \left[ \frac{\omega}{c(\omega)} + k_x \right] \tilde{u}(\omega) d\omega. \quad (3.4.21)$$

In order to make use of the sifting property of the Dirac delta function, the following substitution is performed:

$$k = \frac{\omega}{c(\omega)}, \quad (3.4.22)$$

$$d\omega = \frac{\partial \omega}{\partial k} dk = c_{\text{gr}}(k) dk, \quad (3.4.23)$$

with  $c_{\text{gr}}$  being the group velocity defined by Eq. 2.2.23 in Section 2.2.4. Using this substitution, the argument of the Dirac delta function depends linearly on the integration variable, thereby allowing the integration to be carried out:

$$\tilde{q}(k_x) = 2\pi \int_{-\infty}^{\infty} \delta(k + k_x) \tilde{u}[k(\omega)] c_{\text{gr}}(k) dk = 2\pi \tilde{u}[k_x(\omega)] c_{\text{gr}}[k_x(\omega)]. \quad (3.4.24)$$

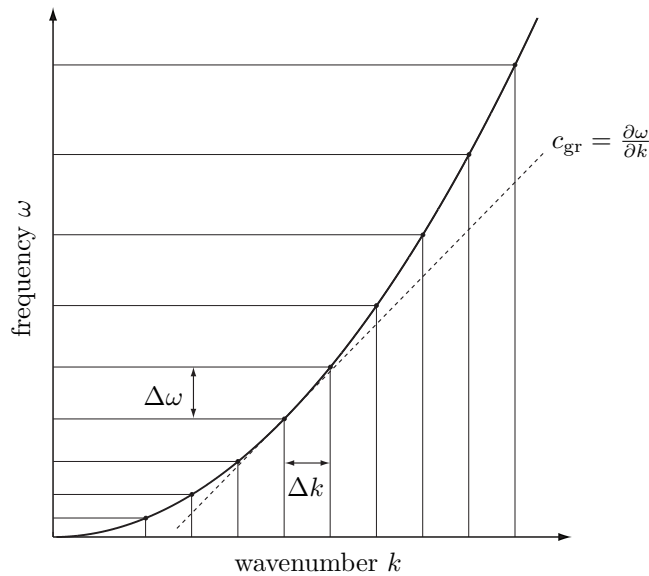
Hence, the dispersion removal operation can be interpreted as a mapping from the frequency to the wavenumber domain. For every value of  $k_x$  in the output function  $\tilde{q}(k_x)$ , the associated value of the frequency spectrum  $\tilde{u}(\omega)$  is picked using the dispersion relation.

The result in the spatial domain is then obtained by application of an inverse spatial Fourier transform:

$$q(x) = \int_{-\infty}^{\infty} \tilde{u}[k_x(\omega)] c_{\text{gr}}[k_x(\omega)] e^{-jk_x x} dk_x. \quad (3.4.25)$$

As a result of the above derivation, dispersion compensation can be performed in the wavenumber-frequency domain in a much more efficient way than in the space-time domain. Whereas in the space-time domain a distance-dependent correlation is required, the dispersion-free signal can be obtained in the wavenumber-frequency domain by a simple mapping operation. The result as a function of space is obtained by application of an inverse spatial Fourier transform to  $q(k_x)$ .

Furthermore, Eq. 3.4.24 shows that along with the mapping, the wavenumber spectrum has to be scaled by the group velocity. This corresponds to an adjustment of different spectral densities for the two spectra as illustrated in Fig. 3.4. The densities in the frequency and wavenumber spectra are related by the group velocity  $c_{gr}$ .




---

**Figure 3.4:** The densities of the wavenumber and the frequency spectra are related by the group velocity being shown as the tangent to the dispersion relation (dotted line).

---

An overview of the procedure for dispersion compensation in the wavenumber-frequency domain is given in Fig. 3.5, which illustrates the three steps:

- (1) transformation of the time signal to the frequency domain,
- (2) mapping from the frequency to the wavenumber domain using the dispersion relation, taking spectral densities and sampling criteria into account,
- (3) inverse Fourier transform to the spatial domain.

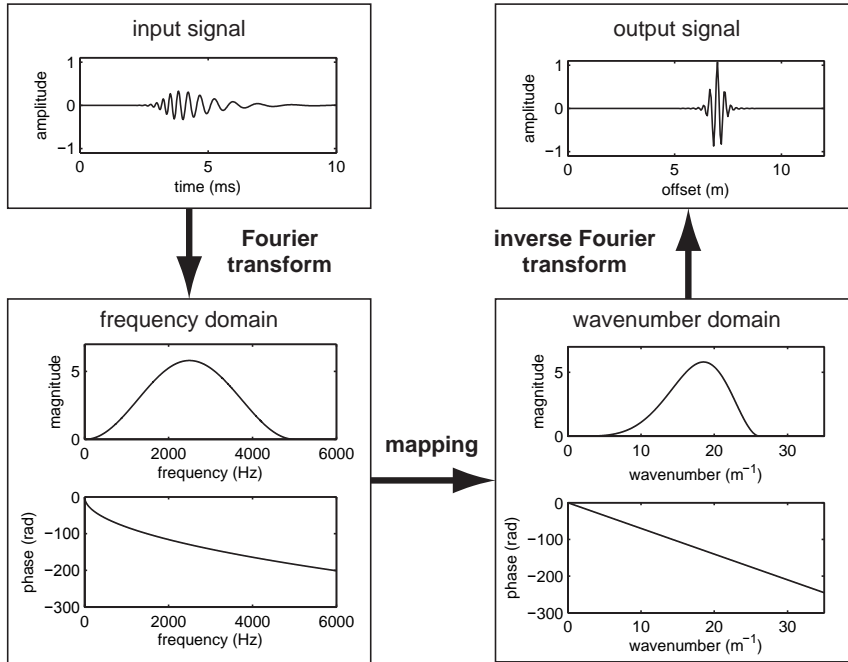


**Figure 3.5:** Schematic overview of dispersion compensation by spectral mapping.

Figure 3.5 illustrates that the method for dispersion removal transforms the phase spectrum that is nonlinearly dependent on the frequency to a phase spectrum depending linearly on the spatial Fourier variable.

Although Wilcox and his colleagues were the first to apply such a transformation in the context of dispersion removal for Lamb waves, the transformation itself originates from the work of Oppenheim, Johnson and Steiglitz [Oppenheim 1971]. They coined the term *spectral warping* [Oppenheim 1972]. In 1990, an application in the context of dispersion compensation in optical waveguides was published by Brinkmeyer et al. [Brinkmeyer 1990] [Kohlhaas 1991]. An extended and detailed description of the transformation has recently been given by Allen, Bailey and Demidenko [Bailey 2004].

An example of dispersion removal, for which the measured normal velocity of a beam has been used, is given in Fig. 3.6. The experiment is described in Appendix G.2. The dispersive impulse response is difficult to interpret. After dispersion removal, the reflections from the beam ends can clearly be identified.

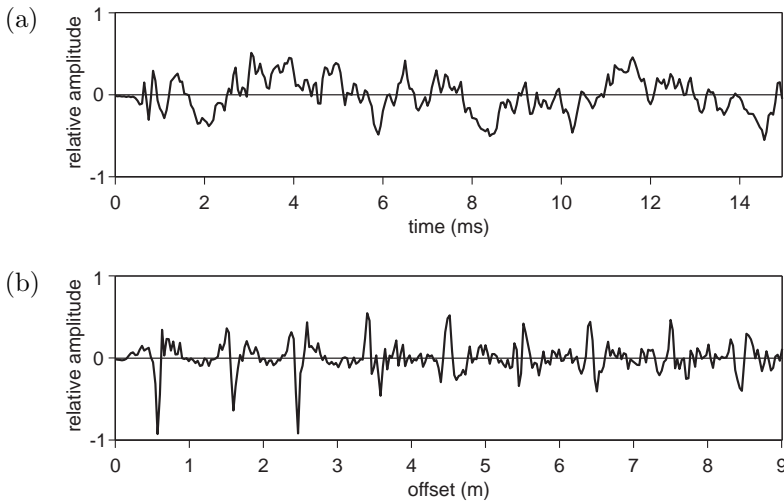


**Figure 3.6:** Impulse response showing the normal velocity of a beam measured at a single position (a); result after dispersion removal (b).

An even better insight into the wave field is gained by displaying impulse responses measured at adjacent positions next to each other. This kind of representation is typical for seismics [Berkhout 1987] and room acoustics [Kuster 2004], and allows the assessment of temporal and spatial properties of the wave field. However, Fig. 3.7(a) shows that the interpretation of the wave field is severely hampered by the effects of dispersion. After dispersion removal, travelling waves and reflections from the beam ends can clearly be recognised (see Fig. 3.7(b)).

### ■ 3.4.1 Sampling and aliasing conditions for discrete signals

In addition to the transform itself, Wilcox also investigated and described its properties with respect to an application to sampled signals. Most important, it should be realised that an equidistantly sampled frequency spectrum is connected to a wavenumber spectrum in which the samples are not equidistant, as can be seen from Fig. 3.4. This is due to the nonlinear dispersion relation used for the mapping. In order to be able to carry out fast Fourier transforms, the signals should be sampled with a regular sampling interval. It is therefore required to resample, i.e., to interpolate the wavenumber spectrum after the mapping [Wilcox 2002].

The sampling of the output signal is subject to constraints related to the sampling theorem [Wilcox 2003]. If these constraints are neglected, the signal will either be

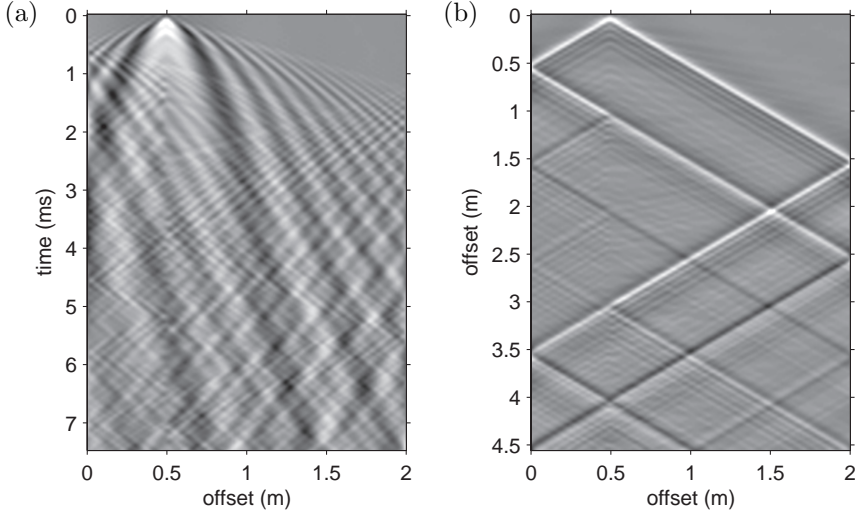


**Figure 3.7:** Normal velocity of a beam of 2 m length measured with a spatial sampling of 1 cm; the source is positioned at a distance of 0.5 m from the left end (see Appendix G.2); the image is formed by putting impulse responses next to each other (a); result after dispersion removal (b).

undersampled or corrupted by wrap-around effects. The maximum sampling interval in the wavenumber domain is limited by the sampling theorem. If the maximum frequency of the temporal spectrum is given by  $f_{\max}$ , the following limit can be given for the maximum spatial wavenumber  $k_{x,\max}$ :

$$|k_{x,\max}| \leq |k_x(f_{\max})| = \frac{\omega_{\max}}{c(\omega_{\max})}. \quad (3.4.26)$$

Furthermore, the dispersion relation as illustrated in Fig. 3.4 can be used to define the maximum sampling interval  $\Delta k_x$  in the wavenumber domain. Whereas the spatial Fourier variable  $k_x$  has opposite sign with respect to the wavenumber  $k$  due to the definitions of the Fourier transforms as shown above, the spectral densities  $\Delta k_x$  and  $\Delta k$  are equal, leading to the following limit for the sampling interval in the wavenumber domain:

$$\Delta k_x = \Delta k \leq \Delta\omega \frac{\partial k}{\partial\omega} = \frac{\Delta\omega}{c_{\text{gr}}(\omega_{\max})}. \quad (3.4.27)$$

### 3.5 Analysis of the dispersion removal procedure

In order to assess its applicability for practical purposes, the output of the dispersion removal procedure is further analysed. This analysis can be performed on either the matched filter or the mapping in the wavenumber-frequency domain since both methods are equivalent. It is chosen to make use of the matched filter and the representation of the model of the flexural wave field in the frequency domain as given by Eq. 3.2.6:

$$\tilde{u}(\omega) = \tilde{S}(\omega) \sum_i R_i e^{-j \frac{\omega}{c(\omega)} x_i}. \quad (3.5.28)$$

The ideal desired output of the dispersion removal procedure aiming to localise sources, is a series of Dirac delta pulses indicating the positions  $x_i$  and strength  $R_i$  of the sources in the spatial domain:

$$q(x) = \sum_i R_i \delta(x - x_i). \quad (3.5.29)$$

#### ■ 3.5.1 Influence of dispersion removal on the amplitude spectrum

Application of the dispersion removal filter, given by Eq. 3.3.13, to the wave field given by Eq. 3.5.28, provides a representation of the filter output:

$$q(x) = \int_{-\infty}^{\infty} e^{j \frac{\omega}{c(\omega)} x} \tilde{S}(\omega) \sum_i R_i e^{-j \frac{\omega}{c(\omega)} x_i} d\omega. \quad (3.5.30)$$

The summation describes a convergent series of continuous functions, such that the order of summation and integration can be interchanged:

$$q(x) = \sum_i R_i \int_{-\infty}^{\infty} e^{j \frac{\omega}{c(\omega)} (x - x_i)} \tilde{S}(\omega) d\omega. \quad (3.5.31)$$

The integral can be written as an inverse spatial Fourier transform by using the following substitution:

$$k_x = -\frac{\omega}{c(\omega)}, \quad (3.5.32)$$

$$d\omega = \frac{\partial \omega}{\partial k_x} dk_x, \quad (3.5.33)$$

which leads to the following equation:

$$q(x) = \sum_i R_i \int_{-\infty}^{\infty} \frac{\partial \omega}{\partial k_x} \tilde{S}[\omega(k_x)] e^{j k_x x_i} e^{-j k_x x} dk_x. \quad (3.5.34)$$

The inverse Fourier transform of the first exponential term can be carried out explicitly, such that the filter output can be written as convolution in the spatial domain:

$$q(x) = \int_{-\infty}^{\infty} \frac{\partial \omega}{\partial k_x} \tilde{S}[\omega(k_x)] e^{-jk_x x} dk_x * \sum_i R_i \delta(x - x_i). \quad (3.5.35)$$

Comparing this result with the desired output of the dispersion removal filter as defined in Eq. 3.5.29, it can be seen that the application of the filter indeed retrieves the position and strength of the sources. The resolution of this result is limited by the spatial spectrum  $S_x(k_x)$  given by the following expression:

$$\tilde{S}_x(k_x) = \frac{\partial \omega}{\partial k_x} \tilde{S}[\omega(k_x)]. \quad (3.5.36)$$

Using the point spread function  $S_x(x)$ , which is the inverse spatial Fourier transform of  $\tilde{S}_x(k_x)$ , the result of the dispersion removal procedure can be written in the following form:

$$q(x) = S_x(x) * \sum_i R_i \delta(x - x_i). \quad (3.5.37)$$

The filter output is convolved with the point spread function  $S_x(x)$ . It is, therefore, interesting to analyse the characteristics of this function and to determine the conditions under which its negative influence on the result obtained by dispersion compensation is minimised.

From Eq. 3.5.36, it can be seen that the spectrum  $\tilde{S}_x(k_x)$  consists of two parts. The frequency spectrum  $\tilde{S}[k_x(\omega)]$  of the source signal determines the spatial spectrum of the filter output. The source spectrum is mapped to the wavenumber spectrum with the mapping given by Eq. 3.5.32. This is readily understood as a limitation of the bandwidth by the source signal. The bandwidth of the source signal determines the bandwidth of the spatial spectrum.

Additionally, the spectrum is scaled by the term  $\partial \omega / \partial k_x$ . The shape of this spectral change for flexural wave fields can be expressed in terms of the spatial Fourier variable  $k_x$ , by using the dispersion relation and the dispersion constant  $A$  defined in Section 2.2.4:

$$\frac{\partial \omega}{\partial k_x} = -\frac{\partial \omega}{\partial k} = -c_{\text{gr}}(k_x) = -2A^2 |k_x|. \quad (3.5.38)$$

It is seen that the spectral scaling term represents a spatial high-pass filter, the magnitude of which increases linearly with increasing spatial frequency. This filter accounts for different spectral densities in the frequency and wavenumber spectra, as already found for the group velocity term arising for the dispersion removal in the wavenumber-frequency domain (see Eq. 3.4.24). It can be interpreted as spectral scaling that ensures the conservation of energy when transforming between frequency

and wavenumber spectra:

$$\int_{-\infty}^{\infty} |\tilde{S}(\omega)|^2 d\omega = \int_{-\infty}^{\infty} |\tilde{S}(\omega(k_x))|^2 \frac{\partial\omega}{\partial k_x} dk_x. \quad (3.5.39)$$

This energy balance resembles Parseval's theorem, which relates the energy of a time signal and its Fourier transform [Arfken 1985]. In this context, it explains the physical need for the spectral weighting by the term  $\partial\omega/\partial k_x$ .

Figure 3.8 presents an illustration of the spectral changes associated with the mapping from frequency to wavenumber. Some typical results of dispersion compensation for different source spectra are shown in Fig. 3.9. A flat amplitude spectrum as in Fig. 3.9(a) results in a more pronounced peak after dispersion removal than the shaped spectrum of Fig. 3.9(c).

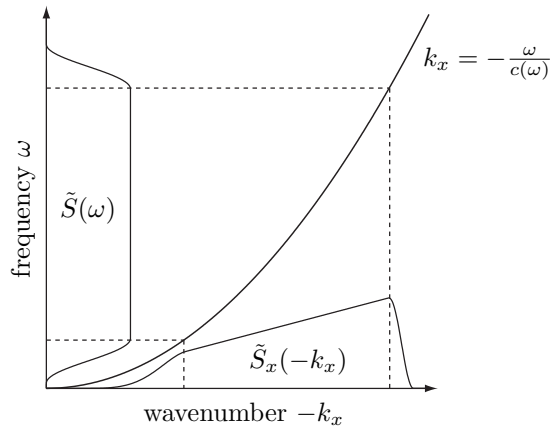


**Figure 3.8:** The wavenumber spectrum  $\tilde{S}_x(k_x)$  after dispersion removal is related to the frequency spectrum  $\tilde{S}(\omega)$  by the dispersion relation.

### ■ 3.5.2 Change of the phase spectrum due to a temporal delay

In the previous section, emphasis has been put on the effects of dispersion removal on the amplitude spectrum of the retrieved signal. It is of equal importance to investigate the changes occurring in the phase spectrum. The presented model of the flexural wave field is based on the assumption that all impulsive sources are triggered at one point in time  $t = 0$  (see Section 3.1).

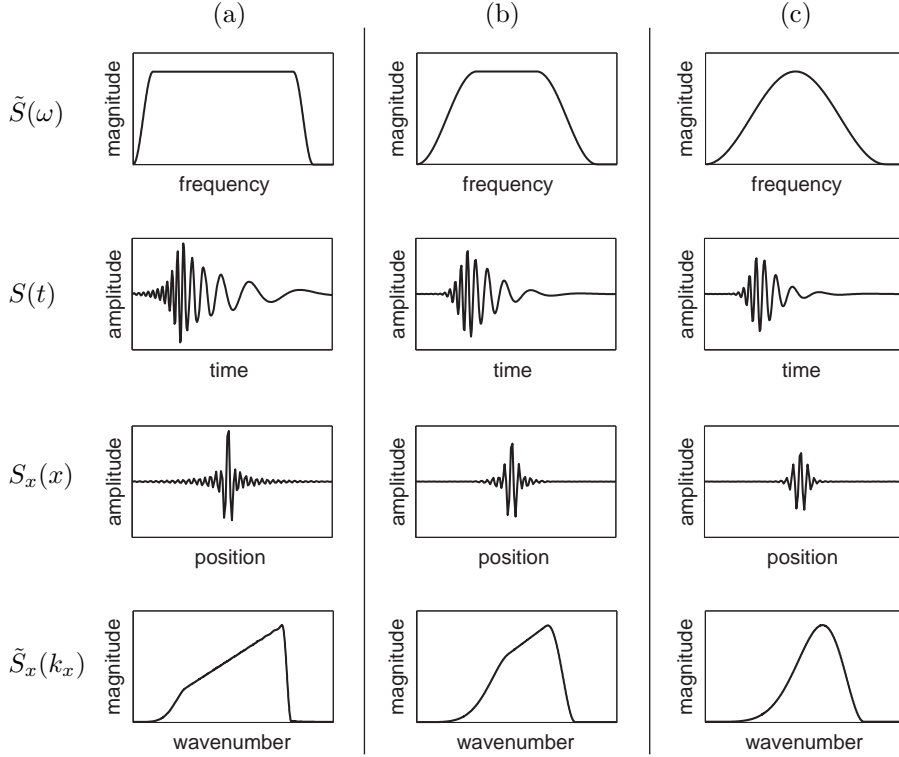


**Figure 3.9:** Dispersion compensation for three different source spectra (a, b and c) of a dispersive signal with dispersion constant  $A = 2 \text{ m} \cdot \text{s}^{-0.5}$  observed at a distance of 1 metre from the source; from top to bottom: source spectrum, associated time signal, spatial localisation after dispersion removal, wavenumber spectrum after dispersion removal.

In the following, it is investigated how the outcome of the method for dispersion compensation is influenced by a time shift, i.e., by a source signal with a linear phase spectrum. It is obvious that this case is of practical relevance. For instance, if the timing of an impact source is incorrect or a measurement system introduces an additional delay to the registered signals, the sources of the model of the flexural field will still be synchronised. However, the point in time  $t = 0$  may not be registered correctly. This condition can be modelled by a delayed source signal:

$$\tilde{S}(\omega) = e^{-j\omega t_0}. \quad (3.5.40)$$

The resulting spatial spectrum after dispersion removal can be determined using the

mapping in the wavenumber-frequency domain as given by Eq. 3.5.36:

$$\tilde{S}_x(k_x) = \frac{\partial \omega}{\partial k_x} \tilde{S}[\omega(k_x)] = -2A^2 |k_x| e^{j \operatorname{sgn}(k_x) A^2 k_x^2 t_0}, \quad (3.5.41)$$

in which the following substitutions have been used:

$$c(\omega) = A\sqrt{\omega}, \quad (3.5.42)$$

$$k_x(\omega) = -\frac{\omega}{c(\omega)}, \quad (3.5.43)$$

$$\omega(k_x) = -\operatorname{sgn}(k_x) A^2 k_x^2. \quad (3.5.44)$$

The phase of the exponential factor in Eq. 3.5.41 is proportional to  $k_x^2$ . This means that any delay  $t_0 \neq 0$  causes a nonlinear dependency of the phase spectrum of the filter output on the wavenumber  $k_x$ . Thus, a delay of the source signal introduces additional, unwanted dispersion in the result of the procedure designed to remove dispersion.

Figure 3.10 shows the result of dispersion compensation for source signals with several values of delay  $t_0$ . The effect of dispersion increases for greater delays, and the estimated position of the sources is shifted away from the correct value.

## 3.6 Limitations of the method for dispersion removal presented

The examples given in the previous sections show that there are several limitations inherent to the proposed technique for dispersion removal:

- (1) The presented approach relies on the mirror image source model, in which the primary and secondary sources are synchronised in time.
- (2) The point in time at which the sources are triggered must be known accurately in order not to introduce unwanted dispersion in the filtering process.
- (3) The bandwidth of the spectrum of the vibrational sources determines the achievable resolution for localisation.
- (4) The resolution is limited by a spatial high-pass filter.

The first item is a *model assumption*, whereas the other three are *results* of the analysis of the filter output.

### ■ 3.6.1 Optimal source spectrum

Setting optimal spatial resolution as the goal of the dispersion removal procedure, it is desirable to achieve a filter output having a flat amplitude and zero-phase

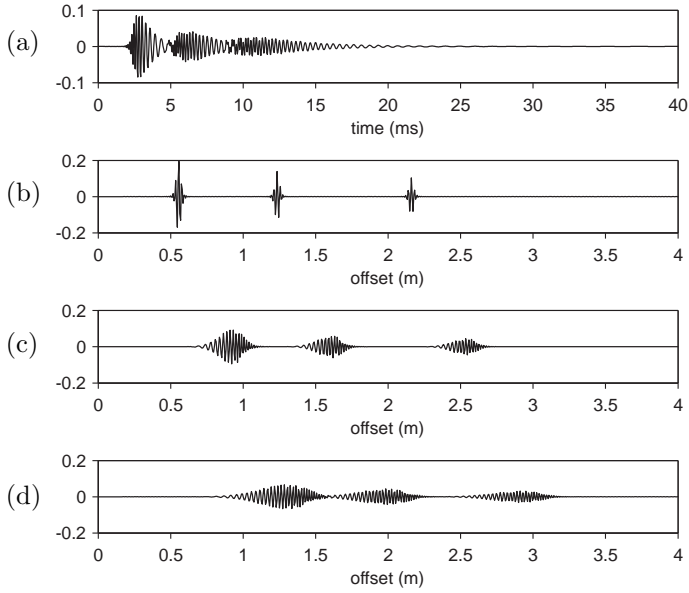


**Figure 3.10:** (a) Dispersive signal with dispersion constant  $A = 1.8 \text{ m} \cdot \text{s}^{-0.5}$ ; result after dispersion removal for different delays: (b)  $t_0 = 0 \text{ ms}$ , (c)  $t_0 = 2 \text{ ms}$ , (d)  $t_0 = 4 \text{ ms}$ .

spectrum [Berkhout 1974]. In order to satisfy this demand, a zero-phase source signal corresponding to a flat amplitude spectrum in the wavenumber domain can be chosen. The shape of its frequency spectrum is determined by the dispersion relation. The relation between frequency and wavenumber spectrum as presented in Eq. 3.5.36 can be used to derive the required frequency spectrum.

Starting out from a flat amplitude spectrum in the wavenumber domain given by

$$\tilde{S}_x(k_x) = 1, \quad (3.6.45)$$

and using the dispersion relation

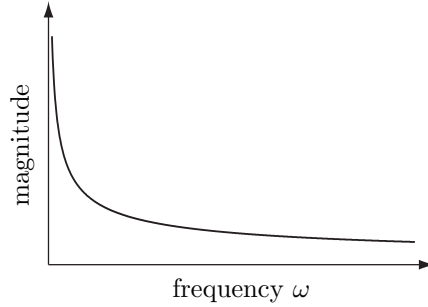
$$k_x(\omega) = -\text{sgn}(\omega) \frac{\sqrt{|\omega|}}{A}, \quad (3.6.46)$$

the following source spectrum is derived:

$$\tilde{S}(\omega) = \frac{\partial k_x}{\partial \omega} \tilde{S}_x[k_x(\omega)] = \frac{1}{2A\sqrt{|\omega|}}. \quad (3.6.47)$$

The source spectrum would need to have an amplitude distribution according to the function  $1/\sqrt{|\omega|}$  in order to achieve optimal resolution in the localisation. This

spectral shape is depicted in Fig. 3.11, showing the significant boost required for low frequencies. Since the magnitude of the spectrum tends towards infinity for  $\omega \rightarrow 0$ , it is clear that there must be a lower bound for the spectrum.




---

**Figure 3.11:** Optimal magnitude (qualitatively) of the source spectrum  $\tilde{S}(\omega)$  in order to achieve a flat wavenumber spectrum  $\tilde{S}_x(k_x)$  after dispersion removal.

---

Furthermore, it should be noted that there exists an alternative way of achieving the optimal source spectrum for discrete implementations. Instead of using the spectral shape given by Eq. 3.6.47 and depicted in Fig. 3.11, it is also possible to adjust the sampling of the input signal in the frequency domain. As can be seen from Fig. 3.4, equidistant sampling in the wavenumber domain corresponds to non-equidistant sampling in the frequency domain. It is thus possible to employ a flat frequency spectrum if the sampling in the frequency domain is chosen according to the dispersion relation, i.e., by taking the square root relation between frequency and wavenumber into account. For  $N_\omega$  frequencies  $\omega_n$  between  $\omega_{\min}$  and  $\omega_{\max}$ , equidistant sampling in the wavenumber domain corresponds to the following distribution in the frequency domain:

$$\omega_n = \left[ \sqrt{\omega_{\min}} + (n-1) \frac{\sqrt{\omega_{\max}} - \sqrt{\omega_{\min}}}{N_\omega - 1} \right]^2. \quad (3.6.48)$$

### ■ 3.6.2 The need for deconvolution of the measured signal

At this point, the question arises whether the spectral correction  $\partial\omega/\partial k_x$  has to be taken into account, given its adverse effect on the resolution. From a physical point of view, the factor has to be retained in order to ensure that energy is correctly conserved when mapping from a frequency to a wavenumber spectrum. However, if dispersion removal is understood as just a technique for signal processing, there is no need to retain an element that is detrimental to the resolution. Therefore, it is preferable to omit the spectral correction factor.

Likewise, it is not necessarily required to change the source signal physically in order to obtain optimal resolution. The measured response can be altered by deconvolving it with the source signal. This way, a signal with a flat source spectrum is obtained. Without additional knowledge about the signal characteristics, deconvolution can be performed only in the regions of the spectrum in which the signal-to-noise ratio is sufficiently high. The result of the deconvolution is, therefore, still limited in bandwidth. If a physical change of the source signal is possible, it could have the advantage of improving the signal-to-noise ratio beyond the possibilities of deconvolution.

An advantage of the deconvolution operation, however, is given by its ability to take also phase characteristics into account. Therefore, it is also possible to compensate for the effect of a time delay of the source signal as described in Section 3.5.2. This operation is feasible due to the convolutional model of the flexural wave field given by Eq. 3.1.4, in which the source spectrum and the dispersive impulse response are separable and can be treated apart.

It becomes evident that the proposed approach to dispersion removal needs to be combined with source signature deconvolution to achieve high spatial resolution and good localisation of the sources. Methods for deconvolution and their effect on the result of dispersion removal are presented in Section 3.8.

### 3.7 Estimation of the dispersion model

In the context of non-destructive testing, the properties of the medium under investigation can, in general, be assumed to be known. Nevertheless, there may be cases in which there is no available information on the material properties of the plate-like structure to be inspected, or its thickness is difficult to measure due to limited access.

The measurement does not contain direct information on properties such as density or elasticity of the material, but rather shows their combined effect on wave propagation in the dispersion relation. Knowledge of the dispersion relation is sufficient to localise secondary sources in the medium that can be interpreted as inhomogeneities.

In the following, first the estimation of the dispersion relation for general dispersive waves will be presented, followed by the special case of flexural waves leading to some simplifications and a broader range of applications.

### ■ 3.7.1 Estimation of the dispersion relation

#### 3.7.1.1 Extraction of the dispersion relation from the wavenumber-frequency domain

If a dataset is available in which the wave field is sampled in time and space, this information can be used to obtain a representation in the wavenumber-frequency domain by application of a two-dimensional Fourier transform. This domain has been shown to provide the link between frequencies and wavenumbers, which is fixed according to the dispersion relation (see Section 3.4). Therefore, significant signal components in wavenumber-frequency spectrum can be found only close to the curve describing the dispersion relation [Alleyne 1991a].

Figure 3.12(a) shows a time-space representation of a flexural wave propagating along a beam. The experiment is described in Appendix G.2. The temporal signals are measured at equidistant spatial positions. Application of a Fourier transform with respect to both time and space results in the wavenumber-frequency spectrum presented in Figure 3.12(b), in which the dispersion relation can be seen.

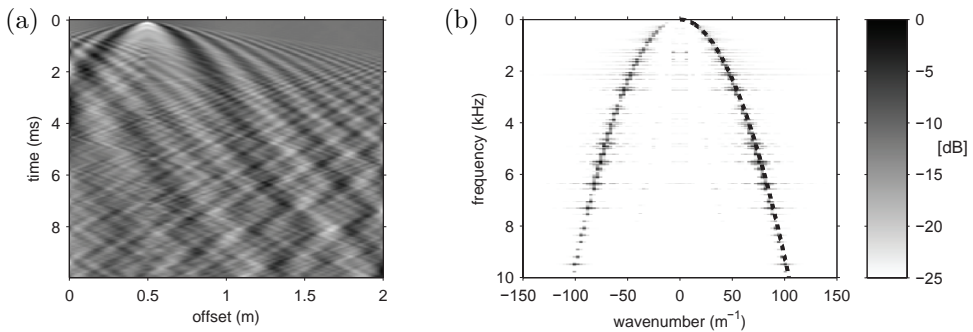


**Figure 3.12:** Flexural wave field in a beam (a) and associated representation in the wavenumber-frequency domain (b) revealing the dispersion relation (dashed).

Since it is not a problem to obtain a high number of samples in time, the applicability of this method is mainly determined by the number of available spatial samples. The resolution in the wavenumber domain is limited by the spatial aperture covered with receivers, and the maximum spacing of the receivers is dictated by the sampling criterion to avoid aliasing.

The resolution with respect to the wavenumber can be increased by application of methods that focus on high resolution. Due to the fact that only a single peak in the wavenumber spectrum needs to be retrieved for each frequency, methods for inversion with a sparseness constraint can, for example, be applied to obtain a

wavenumber-frequency spectrum with high resolution [Sacchi 1998].

In two-dimensional plates, the situation is more complicated. If a linear array of receivers is used, only contributions of waves propagating along the array can be found on the curve describing the dispersion relation. For oblique angles of incidence, the apparent speed of propagation along the array is higher, such that wavenumber components appear smaller [Berkhout 1987].

In finite structures, however, it can be assumed that reflections from the boundaries of the plate cause the presence of waves incident on the array under a high number of different angles, among which there are waves propagating along the array. In the wavenumber-frequency domain, such a wave field is represented by a spectrum with components between the outer curves of the dispersion relation for positive and negative wavenumber components.

The linear array measurement of a flexural wave field and its representation in the wavenumber-frequency domain are presented in Figure 3.13. The experiment is described in Appendix G.1.

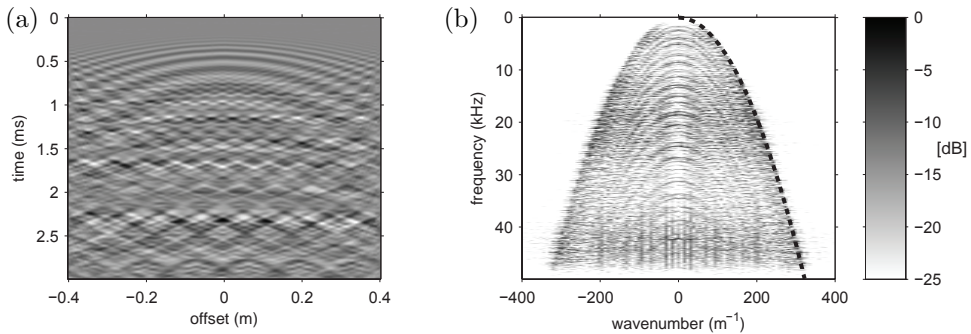


**Figure 3.13:** Flexural wave field in a plate (a) and associated representation in the wavenumber-frequency domain (b) revealing the dispersion relation (dashed).

### 3.7.1.2 Improved estimation of the dispersion relation

If there are not enough receiver positions available to extract the dispersion relation from the wavenumber-frequency domain, approaches based on the short-time Fourier transform can help to determine the travel times at different frequencies. Since the classical short-time Fourier transform can only provide limited resolution, advanced methods are often employed, such as the Wigner-Ville spectrum [Prosser 1999], the reassigned spectrogram [Niethammer 2000], or a special dispersion-oriented short-time Fourier transform [Hong 2005]. These methods are either implicitly iterative

or can be combined with iterative methods to improve the result of the obtained estimate [Zakharia 2000]. However, these approaches can only be used if the waves arriving at the receiver are not overlapping, such that a single event can be analysed.

A challenging yet interesting task is the estimation of the dispersion relation from a measurement of a wave field with reflections. In order to optimise the model given by the assumed dispersion relation, an objective function is needed. For the sake of obtaining good resolution, a function promoting sparseness of the output can be employed [Wei 2009]. Possible criteria are *maximum entropy* [Wiggins 1978] or the *L<sup>1</sup>-norm* [Donoho 2008], for instance. For the result after dispersion removal  $q(x)$ , the *L<sup>1</sup>-norm* is given by the following integral over its absolute value:

$$\|q(x)\| = \int_{-\infty}^{\infty} |q(x)| dx. \quad (3.7.49)$$

In a discrete implementation, the integration over  $x$  is replaced by a summation.

The relation between the dispersion model and the data after dispersion removal is highly nonlinear. Hence, it is not advisable to estimate the entire dispersion relation based on this objective function. Instead, it is proposed to focus on only one feature of the dispersion model that has a significant effect on the resolution of the output. Optimising for one parameter linked to the feature under consideration along with a limitation of the maximum allowed change from the standard model can render the problem well-defined and solvable. This approach will, in the following, be explained by means of an example.

Figure 3.14 shows a simulated impulse response containing several reflections in a steel plate having a thickness of 2 cm. Note that the plate is rather thick, such that the Kirchhoff plate model is not perfectly applicable (see Section 2.2.5).

The simulation is based on the more accurate model of propagating Lamb waves, whereas the simpler Kirchhoff model is used for dispersion removal. Both models are shown in Fig. 3.15 for comparison.

The example presented here represents the case in which the Kirchhoff model is not capable of accurately modelling the dispersion characteristics of the medium under investigation. The result of the dispersion removal procedure can be improved by employing a slightly modified model allowing for a deviation of the dispersion characteristics from the simple Kirchhoff model.

The strength of the dispersion is determined by the curvature of the dispersion relation. For non-dispersive wave propagation, for example, the dispersion relation exhibits zero curvature. Therefore, it is chosen to add a parameter  $\mu$  modifying the strength of dispersion to the model given by Eq. 3.6.46:

$$k_x(\omega) = -\operatorname{sgn}(\omega) \frac{\sqrt{|\omega|}}{A} \left( \frac{\omega}{\omega_{\max}} \right)^\mu, \quad (3.7.50)$$

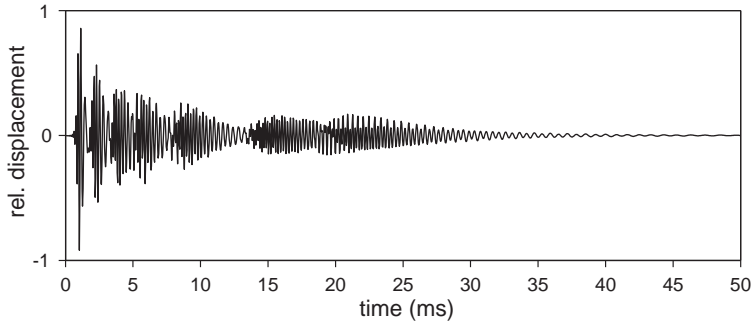


**Figure 3.14:** Simulated dispersive impulse response in a steel plate with a thickness of 2 cm containing several reflections; the Lamb model was employed to calculate the phase velocity.

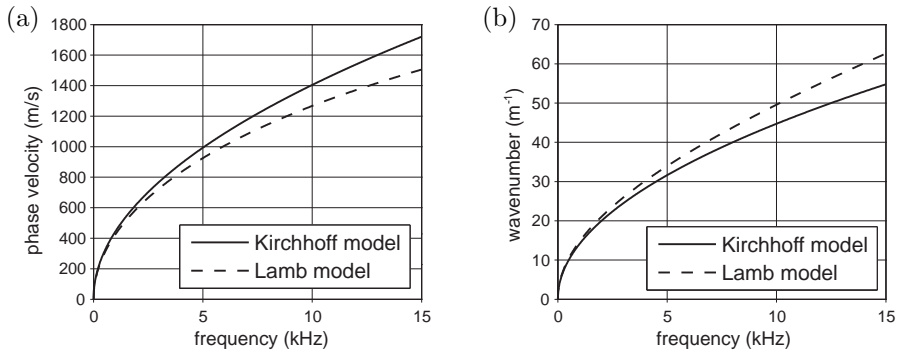
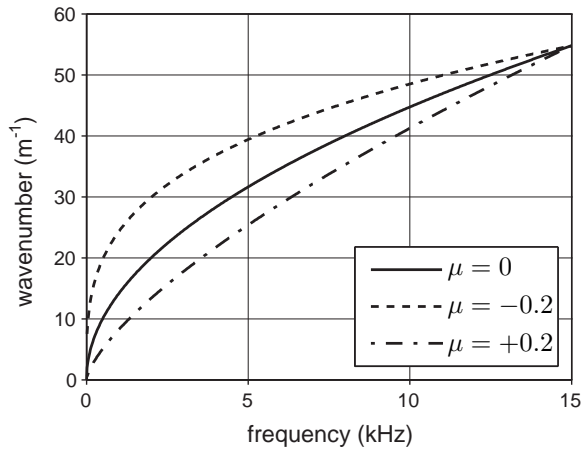


**Figure 3.15:** Comparison of phase velocity (a) and dispersion relation (b) for the Kirchhoff and the Lamb model of wave propagation in plates for the impulse response presented in Fig. 3.14.

with  $\omega_{\max}$  being the maximum frequency of the input signal.

Figure 3.16 shows how the choice of the parameter  $\mu$  changes the phase velocity curve: propagation speeds for the lowest and highest frequencies contained in the signal are not altered, whereas the region in between is modified in order to obtain variable strength of the dispersion. Using a value of zero for  $\mu$  leads to the simple Kirchhoff bending model. The modification in Eq. 3.7.50 does not directly reflect a physical model. However, it helps to correct for the major cause of error in dispersion removal: the assumption of an incorrect dispersion strength.




---

**Figure 3.16:** Illustration of the effect of the exponential parameter  $\mu$  on the phase velocity curve.

---

The modified model is then used for dispersion removal. The optimal choice of the parameter  $\mu$  is determined numerically using the  $L^1$ -norm as an optimisation criterion. To this end, Brent's algorithm for minimisation without derivatives is used [Brent 2002]. In Fig. 3.17, the result is compared with the outcome obtained using the simple Kirchhoff model. It can be seen that the adaptive dispersion model leads to an increase in resolution, a fact that can especially be observed for events at late arrival times, i.e., arriving from more distant sources.

The  $L^1$ -norm is thus indeed suitable as a measure for optimisation of the resolution of the dispersion removal result. The magnitude of the  $L^1$ -norm for different values of the parameter  $\mu$  is shown in Fig. 3.18. Despite the fact that the objective function to be minimised is nonlinear, the region around the minimum is relatively smooth.

From this example, it can be seen that there should be only one unknown parameter, and that the optimal choice of this parameter can be made by using the  $L^1$ -norm as optimisation criterion.

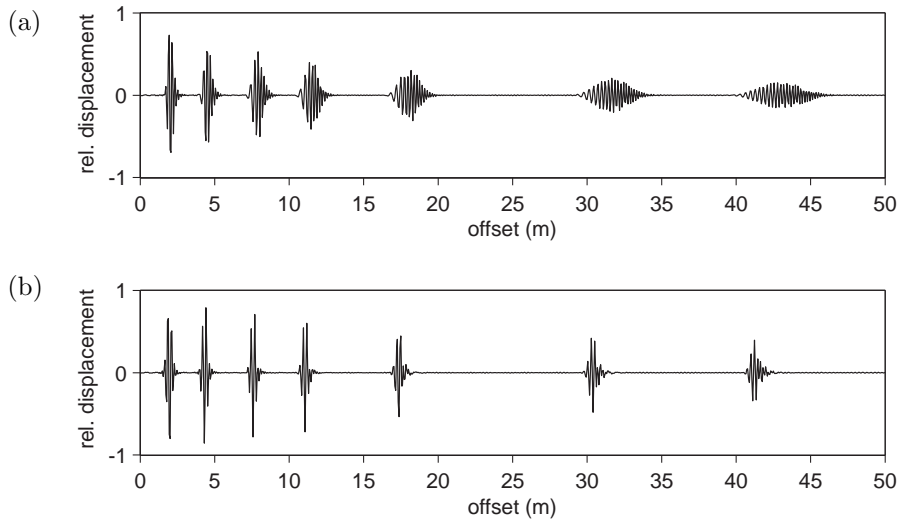


**Figure 3.17:** Result of dispersion removal for the input shown in Fig. 3.14: (a) Kirchhoff model, (b) estimate with exponential parameter and minimisation of the  $L^1$ -norm.

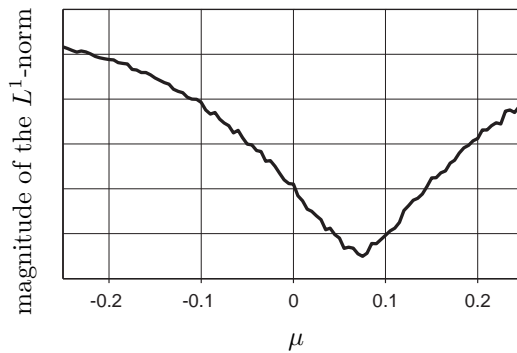


**Figure 3.18:** Magnitude of the  $L^1$ -norm for different values of the exponential tuning parameter  $\mu$ .

## 3.8 Deconvolution

In Section 3.5, the influence of the dispersion removal procedure on the spectrum has been discussed, resulting in the requirement of combining dispersion removal and deconvolution. In the following, methods for coping with a non-white source signal and a possible delay in the measurement chain will be presented.

### ■ 3.8.1 Source signature deconvolution

The removal of the imprint of the source can be achieved by standard deconvolution methods as for example discussed by Berkhout [Berkhout 1977]. It is assumed that the spectrum of the source signal is either known, or can be estimated from the measurements. The deconvolved signal can then be obtained by application of the well-known Wiener filter [Wiener 1964].

Figure 3.19 shows the result of dispersion removal with and without deconvolution for the signature of the source. It can be seen that deconvolution leads to a reduction of artefacts, thereby facilitating the interpretation of the outcome.

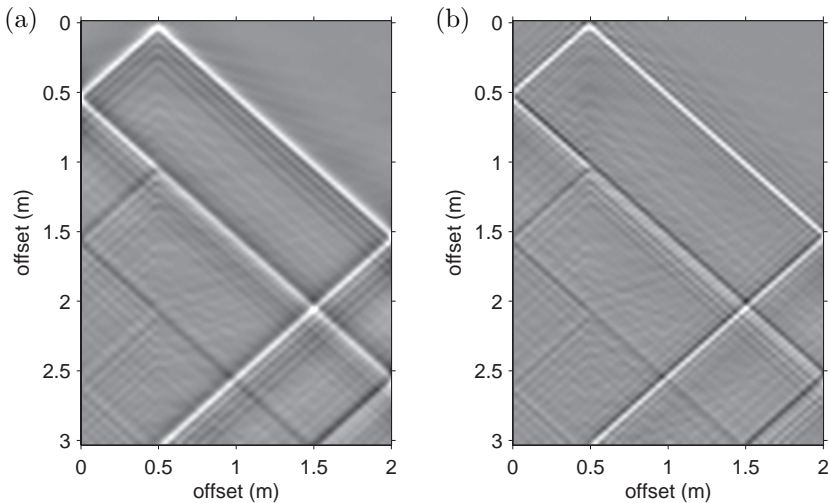


**Figure 3.19:** Result of dispersion removal for flexural waves in a beam (a) without and (b) with source signature deconvolution.

In Section 3.6.1, the optimal source spectrum corresponding to a flat wavenumber spectrum has been derived. However, the flatness of the wavenumber spectrum is not

the only criterion for optimal resolution. A sudden discontinuity of the wavenumber spectrum, for example caused by limitation of the bandwidth, leads to ringing artefacts in the spatial domain. Therefore, it is not desirable to keep the spectrum perfectly flat up to the highest wavenumber contained in it. It is rather preferable to create a smooth transition towards zero amplitude in order to reduce these artefacts. For practical applications, a compromise between flatness and smoothness has to be found [Berkhout 1984].

### ■ 3.8.2 Correction of a linear phase shift

In Section 3.5.2, it has been shown that a temporal delay, which corresponds to a linear phase shift, has significant influence on the quality of the result of the dispersion removal procedure. Therefore, it might be necessary to compensate for a delay, introduced by the measurement chain, for instance.

In this section, measurements obtained on a 2 mm steel plate excited by the impact of a small steel bullet are used. The experiment is described in Appendix G.1. Due to the mechanism of excitation, precise synchronisation was difficult to maintain during the experiment, and incorrect temporal alignment of the dataset is likely.

Figure 3.20 shows the result after applying dispersion removal to this dataset. The temporal alignment is obviously incorrect, leading to an inferior outcome.

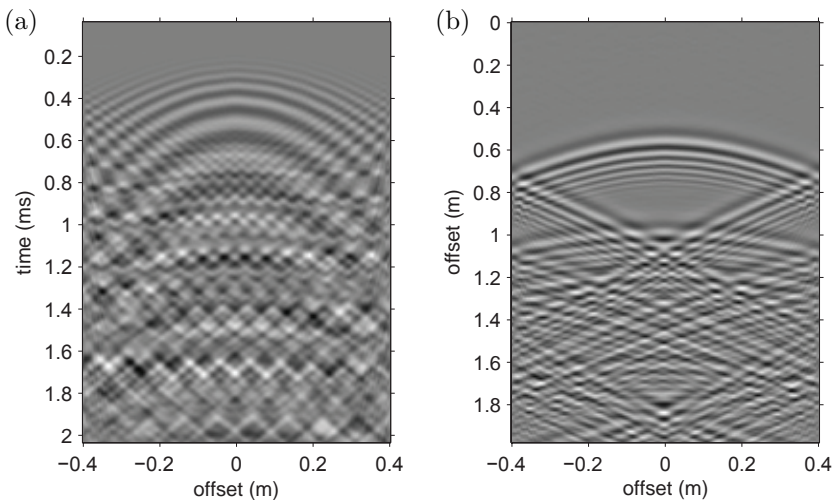
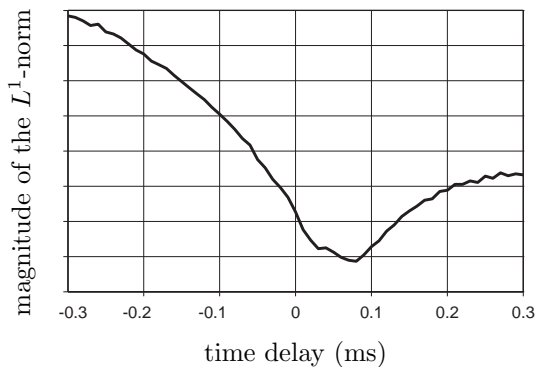


**Figure 3.20:** Wave field in a 2 mm steel plate (a); result of dispersion removal without compensation for the delay of the measured signals (b).

In this context, the methods used in Section 3.7.1.2 for the estimation of an optimal dispersion model can be used again. Once more, the  $L^1$ -norm is used as an optimisation criterion. The parameter to be estimated is the time delay before dispersion removal.

As shown in Fig. 3.21, there exists a relatively smooth minimum of the objective function. The choice of this minimum should correspond to a temporal delay that helps to improve the resolution after dispersion removal. The optimal time delay is found by application of Brent's derivative-free minimisation algorithm [Brent 2002], an implementation of which was provided by Press et al. [Press 1996], for example.



---

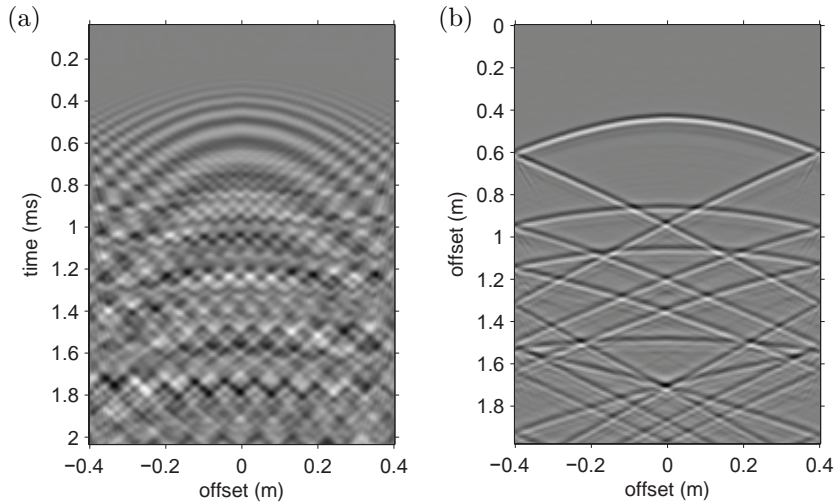
**Figure 3.21:** Magnitude of the  $L^1$ -norm for different time shifts applied before dispersion removal.

---

Figure 3.22 shows the result of dispersion removal with application of the estimated optimal time delay. Despite the fact that the applied delay is relatively small (less than 0.1 ms), the gain in resolution after dispersion removal in comparison to Fig. 3.20 is significant.

## 3.9 Summary

In this chapter, techniques for the removal of the effects of dispersion have been presented. Essentially, the effects of dispersion can be compensated for by transforming the temporal impulse response to a spatial representation. In this context, the dispersion relation does not only determine the transformation itself, but dictates the requirements for sampling and spectral shape of input and output signals as well.



---

**Figure 3.22:** Time-aligned wave field in a 2 mm steel plate (a); result of dispersion removal with optimised delay of the measured signals.

---

It has been shown that dispersion removal has to be combined with deconvolution in order to be most effective. In particular, a linear phase shift equivalent to a temporal delay has to be avoided.

Whereas dispersion removal can be applied to impulse responses measured at a single receiver location, the methods presented in the following chapters will combine information available at different receiver locations in order to obtain an image revealing the positions of primary and secondary sources in the wave field.

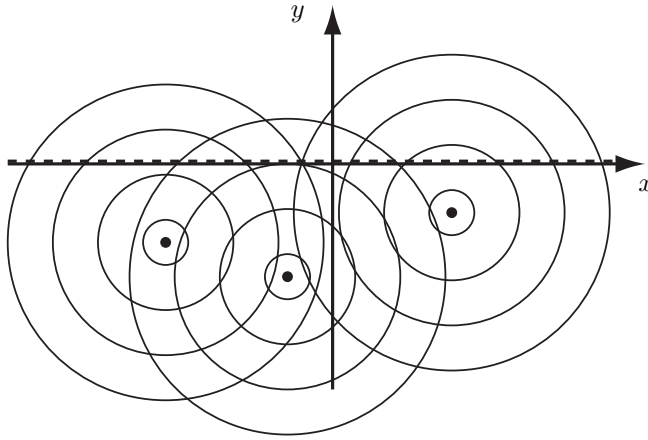
# Imaging under the Born approximation

*All science is either physics or stamp collecting.*  
(Ernest Rutherford, 1871 – 1937)

The analysis of vibrating structures is performed by measuring the wave field caused by one or more sources at a number of receiver points. The raw information obtained at these points is not sufficient to characterise the medium fully. In order to detect inhomogeneities, a map of the properties of the structure under investigation is needed. In the previous chapter, it has been shown that dispersion removal leads to a one-dimensional representation of source positions. In the present chapter, information from an array of receivers is combined to create a two-dimensional image of the medium. First, techniques for extrapolating the wave field from measured points to different points in the medium of interest are presented, followed by a discussion of methods to obtain an image of a source distribution. The derived approach is then extended to obtain an image of scatterers present in the plate under investigation. By introducing the Born approximation, an estimate of the obtainable resolution for imaging based on first-order scattering is given.

## 4.1 Wave field extrapolation

The wave equation provides temporal relationships between different spatial points in the medium. Therefore, knowledge of the wave field in a spatially limited region can be used to estimate the wave field at different locations in space. In seismics and acoustics, the Rayleigh integrals are often used for this purpose [Rayleigh 1878]. They enable the calculation of pressure or particle velocity at a point in a half space from pressure or velocity information on a plane [Berkhout 1987]. For flexural wave fields, the two-dimensional equivalent is given by extrapolation of displacement information from measurements taken on a line into a half plane as illustrated in Fig. 4.1.




---

**Figure 4.1:** Wave field with sources in the lower half space  $y < 0$ ; knowledge of the field variable at the line  $y = 0$  is sufficient to calculate the field in the upper half space  $y > 0$ .

---

The analysis of the extrapolation problem in the wavenumber-frequency domain allows geometrical illustrations of the calculations involved.

#### ■ 4.1.1 The flexural wave field in the wavenumber-frequency domain

The wave equation in the wavenumber-frequency domain is obtained by application of a spatial Fourier transform to the Helmholtz equation given by Eq. 2.2.18:

$$\left[ (k_x^2 + k_y^2)^2 - k_P^4 \right] \tilde{\tilde{u}}(k_x, k_y, \omega) = 0. \quad (4.1.1)$$

For a non-zero wave field, it can be seen that the relation between the spatial Fourier variables  $k_x$ ,  $k_y$  and the frequency  $\omega$  is determined by the dispersion relation:

$$(k_x^2 + k_y^2)^2 = k_P^4 = \left[ \frac{\omega}{c_P(\omega)} \right]^4 = \frac{\omega^2}{A_P^4}. \quad (4.1.2)$$

This means that all non-zero values can be found on the surface described by the above equation. Geometrically, it is a surface of revolution obtained by rotating the curve of the dispersion relation around the frequency axis as shown in Fig. 4.2.

For the flexural wave field, this surface is given by a paraboloid. It can easily be shown that this paraboloid is formed by all possible combinations of plane travelling waves. Considering a plane wave of a certain frequency  $\omega_0$  travelling into the

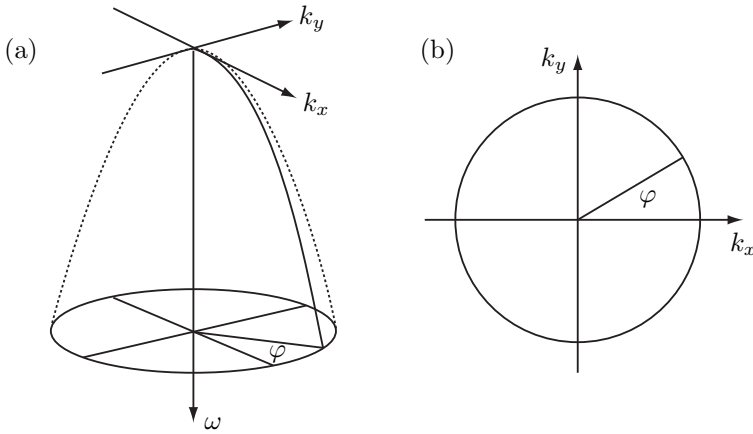


**Figure 4.2:** Illustration of the flexural wave field in the wavenumber-frequency domain: propagating plane waves can be found on the surface of revolution created by rotation of the function describing the dispersion relation around the frequency axis (a); section for a single frequency (b).

direction determined by the angle  $\varphi$ , a space-time representation is given by

$$u(x, y, t) = \cos \left\{ \omega_0 \left[ t - \frac{x \cos \varphi}{c_P(\omega)} - \frac{y \sin \varphi}{c_P(\omega)} \right] \right\}. \quad (4.1.3)$$

In the wavenumber-frequency domain, this wave field is represented by the following expression:

$$\tilde{u}(k_x, k_y, \omega) = 2\pi \delta(|\omega| - \omega_0) \delta \left[ k_x - \frac{\omega \cos \varphi}{c_P(\omega)} \right] \delta \left[ k_y - \frac{\omega \sin \varphi}{c_P(\omega)} \right]. \quad (4.1.4)$$

Thus, for a single frequency, the combination of travelling waves for all directions  $\varphi$  forms a circle with radius  $\omega/c_P(\omega)$  in the wavenumber-frequency domain as indicated in Fig. 4.2. In the same figure, it is furthermore shown that a broadband plane wave is found on the curve given by the dispersion relation and rotated to the direction of propagation  $\varphi$ .

The circle  $k_P^4 = (k_x^2 + k_y^2)^2$  of propagating waves is also known as *Ewald's circle*, named after Paul Peter Ewald who used it as a geometrical construction to derive diffraction angles in crystallography [Ewald 1969]. The paraboloid in the wavenumber-frequency domain is thus formed by the combination of Ewald's circles for multiple frequencies.

The restriction to propagating waves can be regarded as a far-field assumption: If the field is observed at a sufficient distance from the sources, the reduction of

amplitude due to geometrical damping is negligible for the region of observation. In the context of deriving approximations to the Green's functions in Section 2.3.4, it has been shown that this is the case if the distance to the sources exceeds a wavelength.

However, if the wave field is observed or calculated in the vicinity of sources, the evanescent components due to damping over distance cannot be neglected, leading to contributions to the wave field which can be found off the paraboloid in the wavenumber-frequency domain.

### ■ 4.1.2 Application of the projection-slice theorem

If the paraboloid in the wavenumber-frequency is fully known, travelling waves can be reconstructed and the wave field caused by their superposition can be calculated at all points in time and space by application of an inverse Fourier transform:

$$u(x, y, t) = \frac{1}{(2\pi)^3} \int_{-\infty}^{\infty} \int_{-\infty}^{\infty} \int_{-\infty}^{\infty} \tilde{\tilde{u}}(k_x, k_y, \omega) e^{j(\omega t - k_x x - k_y y)} dk_x dk_y d\omega. \quad (4.1.5)$$

If the wave field is known only on the line  $y = 0$ , the wavenumber-frequency spectrum at this is readily determined:

$$u(x, y = 0, t) = \frac{1}{(2\pi)^3} \int_{-\infty}^{\infty} \int_{-\infty}^{\infty} \left[ \int_{-\infty}^{\infty} \tilde{\tilde{u}}(k_x, k_y, \omega) dk_y \right] e^{j(\omega t - k_x x)} dk_x d\omega. \quad (4.1.6)$$

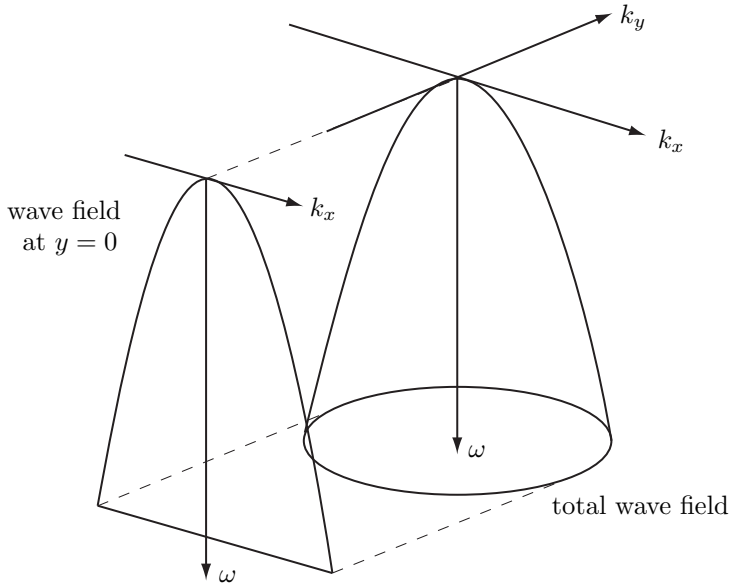
The order of integration has been changed according to Fubini's theorem [Saks 1937].

It is seen that the operation of taking a slice of the wave field at  $y = 0$  in the spatial domain is equivalent to a projection along the  $k_y$ -axis onto the  $k_x$ - $\omega$  plane in the wavenumber-frequency domain. This relation is known as the projection-slice theorem [Bracewell 2003].

The result presented in Eq. 4.1.6 shows that a spatio-temporal Fourier transform applied to a line measurement  $u(x, y = 0, t)$  of a wave field leads to a wavenumber-frequency spectrum  $\tilde{\tilde{u}}(k_x, \omega)$  being an orthogonal projection of the paraboloid representing the full wave field. This is illustrated in Fig. 4.3.

### ■ 4.1.3 Wave field extrapolation by a spatial shift

The geometrical interpretation helps to understand the need for the two assumptions introduced above:




---

**Figure 4.3:** The wavefield at the line  $y = 0$  is a projection of the full wave field taken along the  $k_y$ -axis in the wavenumber frequency domain.

---

- The wave field is assumed to be source-free in order to uniquely relate spatial Fourier variables and frequency by the dispersion relation, using only the paraboloid representing propagating plane waves.
- The reconstruction of the paraboloid from its projection is ambiguous with respect to the  $k_y$ -coordinate; it has to be mapped to one side of the line  $k_y = 0$ .

The latter result is due to the ambiguity when determining  $k_y$  from the dispersion relation in Eq. 4.1.2. Note that  $k_y$  does not represent a Fourier variable when determined from this equation. Instead,  $k_y$  must be interpreted as a wavenumber describing the propagation in  $y$ -direction. By neglecting evanescent waves,  $k_y$  is assumed to be real. The two remaining roots obtained when determining  $k_y$  from Eq. 4.1.2 reflect the fact that it cannot be resolved from which side an observed plane wave is arriving at the line  $y = 0$ . In order to resolve this ambiguity, it can, for example, be assumed that all plane waves propagate into positive half space for which  $k_y > 0$ .

Using these assumptions,  $k_y$  can uniquely be determined from  $k_x$  and  $\omega$ :

$$k_y = \sqrt{\left[\frac{\omega}{c_P(\omega)}\right]^2 - k_x^2} = \sqrt{k_P^2 - k_x^2}. \quad (4.1.7)$$

The wave field can then easily be extrapolated to a line  $y = y_0$  with  $y_0 > 0$ . The spatial shift from the line through the origin to the line at  $y = y_0$  is obtained by multiplication with an exponential function in the wavenumber domain [Sicard 2002]:

$$\tilde{u}(k_x, y_0, \omega) = \tilde{u}(k_x, 0, \omega) e^{jk_y y_0}. \quad (4.1.8)$$

#### ■ 4.1.4 Wave field extrapolation by mapping from frequency to wavenumber

Another option for wave field extrapolation is given by the direct mapping from frequency  $\omega$  to the spatial wavenumber  $k_y$ . Figure 4.4 illustrates this idea, which is known as *Stolt migration* in the context of seismic exploration [Stolt 1978]. The two-dimensional inverse Fourier transform of the wave field at the line  $y = 0$  is taken as a starting point:

$$u(x, t) = \frac{1}{(2\pi)^2} \int_{-\infty}^{\infty} \int_{-\infty}^{\infty} \tilde{u}(k_x, \omega) e^{j(\omega t - k_x x)} dk_x d\omega. \quad (4.1.9)$$

A representation of the wave field in the spatial domain is obtained by substituting  $\omega$  by  $k_y$  using Eq. 4.1.7. For the variable of integration  $\omega$ , the following substitution is obtained by differentiation of Eq. 4.1.7:

$$d\omega = \frac{k_y c_P(\omega)}{k_P - k_P^2 \frac{\partial c_P(\omega)}{\partial \omega}} dk_y, \quad (4.1.10)$$

Insertion of the phase velocity for flexural waves  $c_P(\omega) = A_P \sqrt{\omega}$  leads to the following relation for flexural wave fields:

$$d\omega = 2A_P^2 k_y dk_y. \quad (4.1.11)$$

This case is analogous to the change of variable in the context of dispersion removal presented in Section 3.5.1. The additional factor  $2A_P^2 k_y$  can be interpreted as a statement of energy conservation when transforming between two projections of the wave field in the wavenumber-frequency domain. The projection of the paraboloid representing the wave field onto the  $k_x$ - $\omega$ -plane is used to derive the projection onto the  $k_x$ - $k_y$ -plane as illustrated in Fig. 4.4

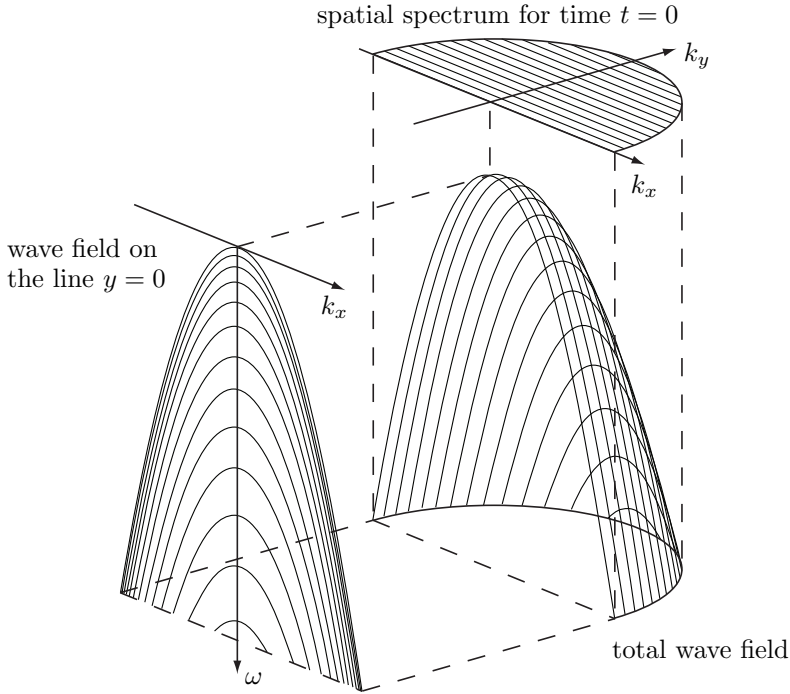


**Figure 4.4:** Knowledge of the wave field on the line  $y = 0$  can be used to reconstruct the wave field in the wavenumber-frequency domain for  $k_y > 0$ ; the projection onto the wavenumber domain provides spatial information for time  $t = 0$ .

Using the substitution of Eq. 4.1.11, the spatio-temporal Fourier transform of Eq. 4.1.9 can be rewritten as a two-dimensional spatial Fourier transform in  $k_x$  and  $k_y$ :

$$u(x, y) = \frac{A_P^2}{2\pi^2} \int_{-\infty}^{\infty} \int_{-\infty}^{\infty} \tilde{u} \left\{ k_x, k_y = \sqrt{\left| \left[ \frac{\omega}{c_P(\omega)} \right]^2 - k_x^2} \right|} \right\} e^{-j(k_x x + k_y y)} dk_x dk_y d\omega. \quad (4.1.12)$$

Information of a wave field on a line can therefore be transformed into a two-dimensional spatial representation of the field. It has already been pointed out that this image is generated by a projection onto the  $k_x$ - $k_y$ -plane in the wavenumber-frequency domain, which is equivalent to an integration along the frequency axis. Thus, it corresponds to the state of the wave field at time  $t = 0$ . In order to obtain a spatial image of the wave field for a different point in time  $t_0$ , the wavenumber-frequency spectrum can be multiplied by an exponential term  $e^{-j\omega t_0}$ . Note that this multiplication has to be carried out before  $\omega$  is substituted by  $k_y$ .

This method of producing a spatial map of the wave field can be regarded as a two-dimensional extension of the method of dispersion removal presented in Section 3.4. Equivalently, dispersion removal can thus be interpreted as a simplified form of wave field extrapolation. The processing steps are similar in both cases. As in the case of the one-dimensional dispersion removal procedure, a discrete implementation of the two-dimensional imaging requires interpolation of the wavenumber spectrum as explained in Section 3.4.1. A sampling grid that is equidistantly spaced in the  $k_x$ - $\omega$ -domain corresponds to a non-equidistantly spaced grid in the  $k_x$ - $k_y$ -plane as illustrated in Fig. 4.5.

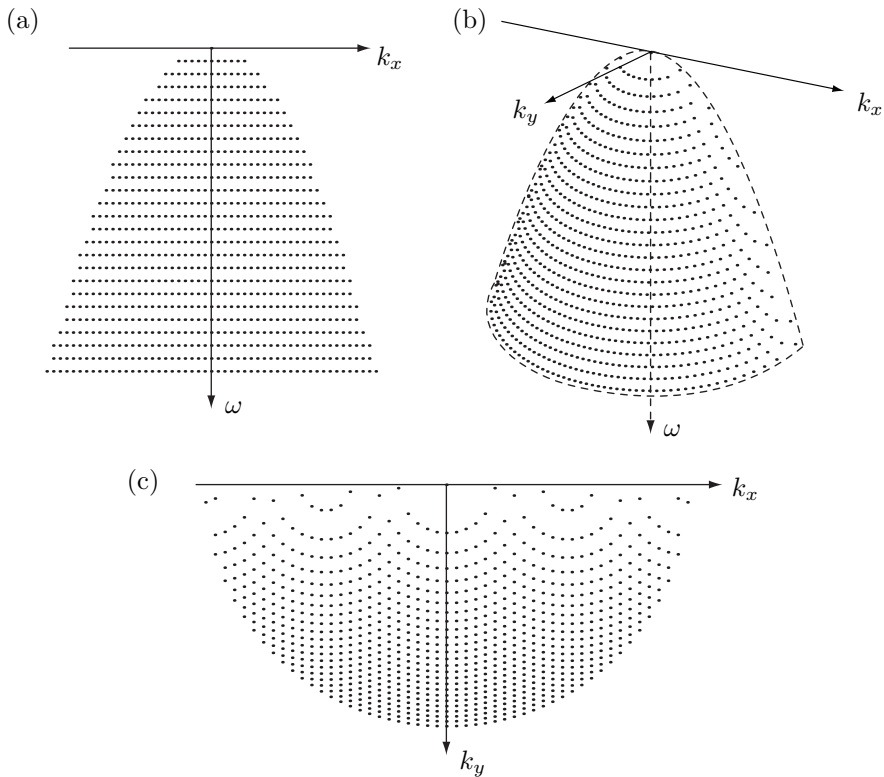


**Figure 4.5:** An equidistantly spaced sampling grid in the  $k_x$ - $\omega$  domain (a) is mapped by the dispersion relation (b) to a non-equidistant sampling grid in the  $k_x$ - $k_y$  domain (c).

### ■ 4.1.5 Wave field extrapolation of evanescent components

In general, practical measurements will not comply with the limiting condition that only propagating waves may be present in the wave field. However, it has been shown that the evanescent components are negligible if the distance to sources exceeds a wavelength.

Nevertheless, it is necessary to investigate what happens if evanescent waves are present. As stated above, any non-propagating component can be found off the paraboloid in the wavenumber-frequency domain. The mapping from frequency to wavenumber according to Eq. 4.1.7 is therefore not correct for these components. Two cases can be distinguished:

- (1) For  $|k_x| \leq k_P$ , evanescent components are mapped into the propagating field. They are projected onto the paraboloid along the  $k_y$ -axis.
- (2) For  $|k_x| > k_P$ , Eq. 4.1.7 returns positive imaginary values for  $k_y$ . With respect to the extrapolation based on mapping in the wavenumber-frequency domain, these regions should not be taken into account since no real  $k_y$  coordinate can be assigned. If the wave field is extrapolated by multiplication by an exponential function as stated in Eq. 4.1.8, the field can only be extrapolated into the positive half-plane for which  $y_0 > 0$ , i.e., away from the sources. In this case, the wave field is multiplied by a factor  $e^{-\sqrt{k_x^2 - k_P^2} y_0}$  in the wavenumber-frequency domain, such that the evanescent field decreases for increasing extrapolation distance  $y_0$ .

### ■ 4.1.6 Bi-directional wave field extrapolation

It has been shown that knowledge of the wave field on a line  $y = 0$  does not provide information about the direction of propagation normal to this line. In the above derivation, it was chosen to let all wave field components propagate into the positive half space for which  $y > 0$ .

Nevertheless, it is possible to overcome the problem of the non-uniqueness of the direction of propagation by employing more information on the wave field at the line  $y = 0$ . A classical choice is the additional usage of the normal derivative of the wave field with respect to  $y$ :  $\partial \tilde{u}(x, y = 0, \omega) / \partial y$ . The *Kirchhoff-Helmholtz theorem* states that information on the field and its normal derivative on a boundary can be used to determine the field in the source-free region enclosed by this boundary uniquely [Berkhout 1987]. In the case of a two-dimensional flexural wave field, this boundary is chosen to be an infinite line positioned at  $y = 0$ .

With respect to the representation of the wave field in the wavenumber-frequency domain, the Kirchhoff-Helmholtz theorem corresponds to the use of two different

projections of the paraboloid representing the wave field. One of them is the projection of the paraboloid as introduced above:

$$\tilde{u}(k_x, y = 0, \omega) = \frac{1}{2\pi} \int_{-\infty}^{\infty} \tilde{\tilde{u}}(k_x, k_y, \omega) dk_y. \quad (4.1.13)$$

The second projection is taken of the Fourier-transformed normal derivative of the wave field, which is obtained by a multiplication by the factor  $-jk_y$  in the wavenumber-frequency domain.

$$\frac{\partial}{\partial y} \tilde{u}(k_x, y = 0, \omega) = -\frac{j}{2\pi} \int_{-\infty}^{\infty} k_y \tilde{\tilde{u}}(k_x, k_y, \omega) dk_y. \quad (4.1.14)$$

These two projections are sufficient to reconstruct the entire paraboloid of propagating waves with positive and negative coordinates for  $k_y$ .

To this end, the wavenumber spectra of propagating waves are formed from measurements  $\tilde{u}(k_x, y, \omega)$  and  $\partial\tilde{u}(k_x, y = 0, \omega)/\partial y$  separately. At this point, the non-uniqueness is still maintained, i.e., both spectra are symmetric with respect to the  $k_x$ -axis. Denoting these two forms as  $\tilde{u}_1(k_x, k_y)$  and  $\tilde{u}_2(k_x, k_y)$ , one obtains:

$$\tilde{u}_1(k_x, k_y) = \tilde{u} \left\{ k_x, k_y = \sqrt{\left| \left[ \frac{\omega}{c_P(\omega)} \right]^2 - k_x^2} \right. \right\}, \quad (4.1.15)$$

$$\tilde{u}_2(k_x, k_y) = \frac{\partial}{\partial y} \tilde{u} \left\{ k_x, k_y = \sqrt{\left| \left[ \frac{\omega}{c_P(\omega)} \right]^2 - k_x^2} \right. \right\}. \quad (4.1.16)$$

A unique reconstruction of the field  $\tilde{u}'(k_x, k_y)$  on both sides of the array is then formed by adding these spectra in such a way that the parts placed in the incorrect half of the field cancel each other:

$$\tilde{u}'(k_x, k_y) = \frac{1}{2} \left[ \tilde{u}_1(k_x, k_y) - \frac{\tilde{u}_2(k_x, k_y)}{jk_y} \right]. \quad (4.1.17)$$

The field in the spatial domain is then obtained by an inverse Fourier transform of  $\tilde{u}'(k_x, k_y)$ .

In the following, an example will be used to illustrate the described method. Figure 4.6 shows a typical setup with two impulsive sources of equal strength both triggered at time  $t = 0$ . The wavenumber-frequency representations of the projection onto the  $k_x$ -axis of both the field and its normal derivative are shown in Fig. 4.7.

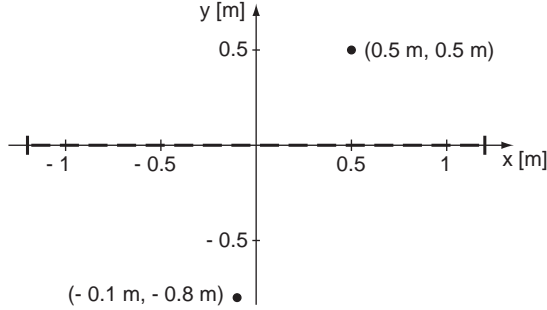


**Figure 4.6:** Simulation setup: two sources are positioned on different sides of an array (dashed) of 2.4 m length located on the  $x$ -axis; the simulations are carried out for a field with a dispersion constant  $A_P = 2 \text{ m} \cdot \text{s}^{-0.5}$ .

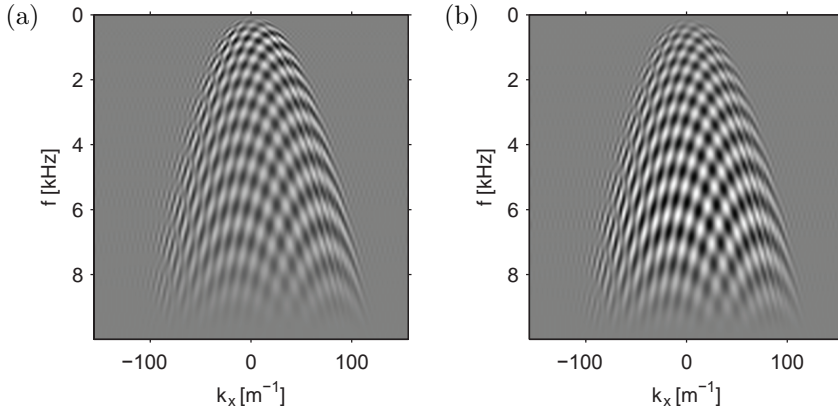


**Figure 4.7:** Projection of the wave field in the wavenumber-frequency domain obtained from (a) the field and (b) the normal derivative of the field at the array position.

The wavenumber spectra  $\tilde{u}_1(k_x, k_y)$  and  $\tilde{u}_2(k_x, k_y)$  are depicted in Fig. 4.8(a) and (c), while Fig. 4.8(b) and (d) show their spatial representations  $u_1(x, y)$  and  $u_2(x, y)$ , respectively. Clearly, both functions by themselves are non-unique as can be seen from the symmetry with respect to the  $k_x$ - or  $x$ -axis, respectively. However, these two representations of the wave field differ in their spectral content: the field derived from the normal derivative is spectrally shaped by an additional factor  $-j k_y$ . By application of Eq. 4.1.17, the unique wavenumber spectrum  $\tilde{u}'(k_x, k_y)$  shown in Fig. 4.8(e) is obtained. Its inverse Fourier transform depicted in Fig. 4.8(f) reveals the correct position of both sources.

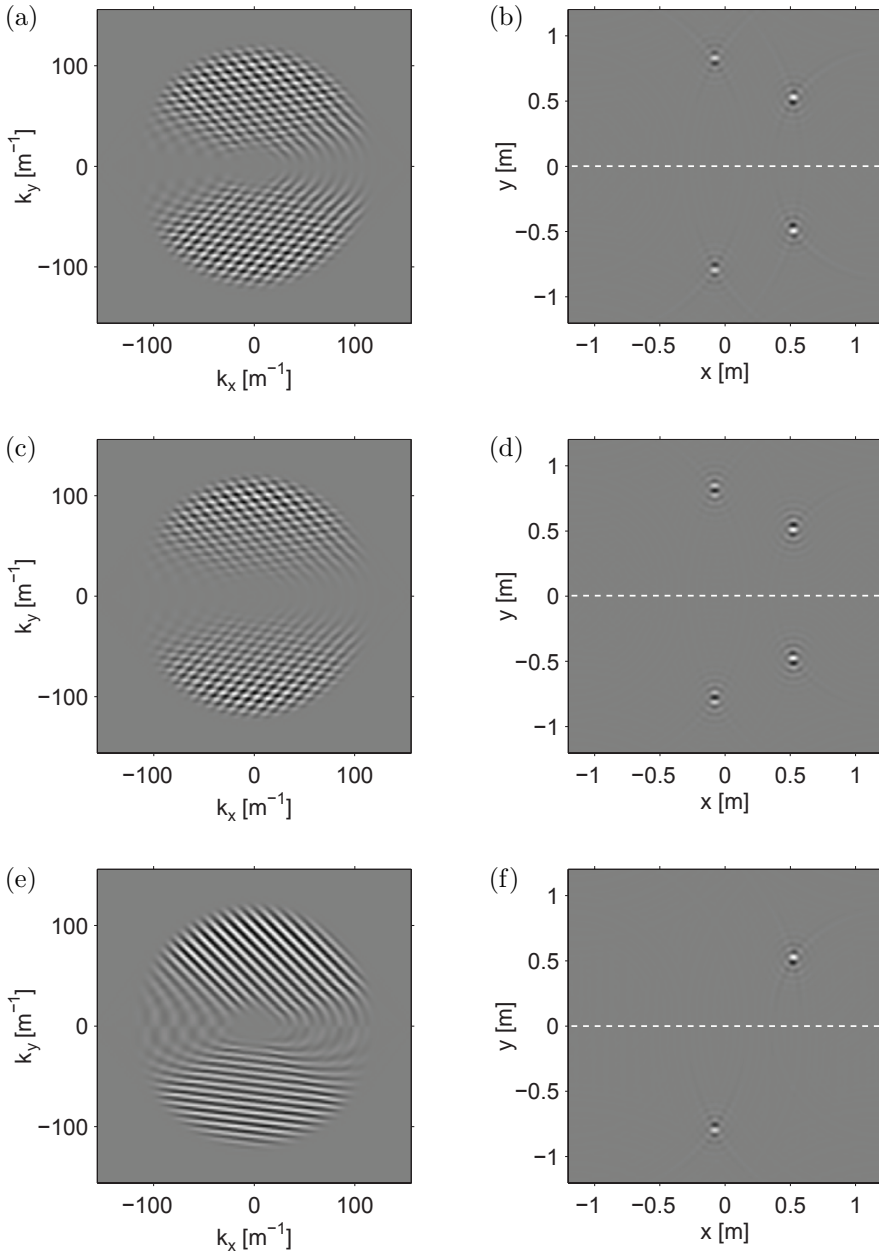


**Figure 4.8:** Wavenumber spectra and respective spatial representations obtained from the field at  $y = 0$  (a)  $\tilde{u}_1(k_x, k_y)$ , (b)  $u_1(x, y)$ , from the normal derivative of the field at  $y = 0$  (c)  $\tilde{u}_2(k_x, k_y)$ , (d)  $u_2(x, y)$ , and by combination of both: (e)  $\tilde{u}'(k_x, k_y)$ , (f)  $u'(x, y)$ .

Note that the figures obtained show the wave field at  $t = 0$ , i.e., at the moment that both sources are triggered. Snapshots at different points in time can be obtained simply by application of a positive or negative time shift to the signals recorded at the linear array. As an example, the field is reconstructed at two points in time just before and just after  $t = 0$ , see Fig. 4.9.

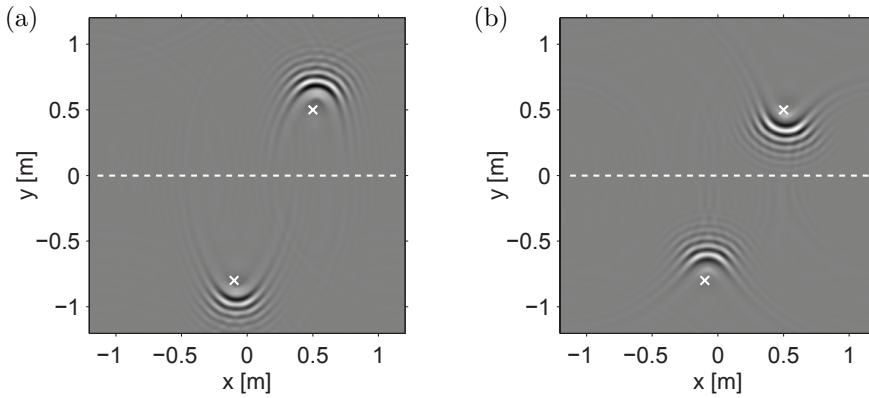


**Figure 4.9:** Reconstruction of the simulated wave field at  $t = -0.3$  ms (a) and  $t = +0.3$  ms (b) using bi-directional wave field extrapolation; the positions of the sources are indicated by the crosses.

It can be seen that the extrapolation of the wave field results in an image consisting of the propagating waves at a certain point in time. Therefore, there are no real ‘sources’ for the wave fronts in the image. The source locations observed in Fig. 4.8(f) are actually the focal points at which the propagating waves converge at the moment that the sources are triggered. From the focal points, the waves propagate towards the array. Furthermore, it should be noted that the result of the extrapolation contains only the waves for angles of propagation that can be registered by the array. Therefore, the omni-directionality of the sources cannot be retrieved.

Nevertheless, wave field extrapolation can be used as a tool to obtain insight in the wave field from snapshots at a point in time. If this point is well-chosen, the resulting image can be expected to bear sufficient information to locate primary or secondary sources. Only the case of extrapolation from a linear array of receivers has been presented here due to the fact that it can easily be used for visual illustrations of the relations between frequency and wavenumber spectra. From this point of view, wave field extrapolation can be seen as a straightforward extension of the methods for dispersion removal to two dimensions.

### ■ 4.1.7 From wave field extrapolation to imaging

It has been shown that wave field extrapolation enables the calculation of the propagating part of the wave field at arbitrary points in time and space. In order to obtain an image, it is necessary to go one step further: the observed wave field must be related to the spectra of the sources it is caused by. In this context, two types of sources can be distinguished:

- The primary sources are the *active sources* employed to generate the wave field. They are assumed to be known.
- The secondary sources can be characterised as *passive sources*. They are formed by the unknown material inhomogeneities, which are illuminated<sup>1</sup> by the primary sources.

Therefore, in order to detect changes in material properties, it is first of all necessary to be able to detect the secondary sources of an observed wave field. With respect to this application, wave field extrapolation as presented above has two main limitations: it is tailored to deal with the propagating part of the field only and requires knowledge of the wave field on a straight line. Therefore, the following issues have to be resolved:

- The restriction to propagating plane waves must be abandoned in order to be able to deal with sources present in the wave field, thereby taking geometrical damping and near-field effects into account.
- The imaging formalism has to be extended to arbitrary geometrical configurations of a finite number of sources and receivers.

Both demands can be met by using the framework of array-based imaging. Arrays of receivers are widely used in different disciplines such as mobile communication, radar tracking, seismic exploration, room acoustics, non-destructive testing, and medical imaging. This fortunate fact has led to cross-fertilisation of developments in these different areas of research. The underlying mathematical principles have extensively been studied and can be employed to assess the capabilities and limitations of an imaging system. In the following sections, the problem of determining primary and secondary sources causing a wave field is thus analysed by means of the tools of array processing.

---

<sup>1</sup>The term *illumination* is not restricted to optics, but can also refer to acoustical and vibrational sources.

## 4.2 Imaging of a source distribution

The imaging of a source distribution, also known as the *inverse source problem* [Bertero 1998] can be regarded as a prerequisite for the imaging of scatterers. Therefore, it is chosen to represent the source distribution by the variable  $w(\underline{x}, \omega)$ , already bearing in mind that it will later on be used to represent the contrast sources introduced in Section 2.5.3 when imaging a distribution of scatterers. For the problem at hand, it is sufficient to deal with an abstract distribution of sources with certain spatial and spectral properties.

The field caused by the source distribution is picked up by a collection of  $N_r$  receivers at the locations  $\underline{x}_r$  with index  $r = 1 \dots N_r$ . The signal  $\tilde{f}(\underline{x}_r, \omega)$  measured at a certain receiver  $r$  due to the source distribution can readily be determined by means of the Green's function as has been shown in Section 2.5.3:

$$\tilde{f}(\underline{x}_r, \omega) = \int_{-\infty}^{\infty} \tilde{G}(\underline{x}_r, \underline{x}, \omega) \tilde{w}(\underline{x}, \omega) d\underline{x} = \mathcal{G}_R \tilde{w}(\underline{x}, \omega). \quad (4.2.18)$$

In the above equation, the operator  $\mathcal{G}_R$  has been introduced to describe the mapping from the source space  $S$  to the receiver space  $R$ . Figure 4.10 illustrates this mapping. Besides the short notation, the usage of operators has the advantage of facilitating the treatment of problems in the framework of linear algebra. All operators presented in this work are linear operators acting on Hilbert spaces, i.e., multidimensional vector spaces on which an inner product can be defined [Riley 1997]. This property will be used below in order to derive solutions to minimisation problems.

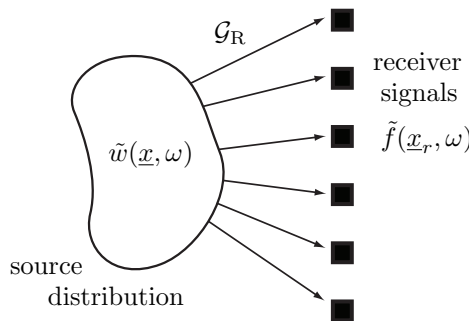


**Figure 4.10:** Mapping from the source distribution  $\tilde{w}(\underline{x}, \omega)$  to the receiver signals  $\tilde{f}(\underline{x}_r, \omega)$  by the operator  $\mathcal{G}_R$ .

Equation 4.2.18 describes the *forward problem*, i.e., the generation of the signals at

the receivers due to the source distribution. Imaging deals with the *inverse problem* of estimating a source distribution for given receiver signals. In the following sections, different methods of obtaining such estimates will be presented and analysed.

#### ■ 4.2.1 Imaging as a minimisation problem

The estimation  $\tilde{w}_{\text{est}}(\underline{x}, \omega)$  of a source distribution can be cast as a linear algebra problem by minimising the difference between the field generated by the source distribution and the observed receiver signals in a least-squares sense:

$$\tilde{w}(\underline{x}, \omega)_{\text{est}} = \arg \min_{\tilde{w}(\underline{x}, \omega)} \left\| \tilde{f}(\underline{x}_r, \omega) - \mathcal{G}_R \tilde{w}(\underline{x}, \omega) \right\|_R^2, \quad (4.2.19)$$

with  $\|\cdot\|_R^2$  denoting the  $L^2$ -norm in the receiver space  $R$ .

A solution is found by differentiating Eq. 4.2.19 with respect to  $\tilde{w}(\underline{x}, \omega)$  and setting the result equal to zero. The following *normal equations* are obtained:

$$\mathcal{G}_R^\dagger \mathcal{G}_R \tilde{w}(\underline{x}, \omega) = \mathcal{G}_R^\dagger \tilde{f}(\underline{x}_r, \omega), \quad (4.2.20)$$

with  $\mathcal{G}_R^\dagger$  representing the adjoint of the operator  $\mathcal{G}_R$ .

##### 4.2.1.1 The adjoint imaging operator

The adjoint operator  $\mathcal{G}_R^\dagger$  performs a mapping from the receiver space  $R$  to the source space  $S$  and is defined by the following inner products on these spaces:

$$\left\langle \mathcal{G}_R \tilde{w}(\underline{x}, \omega), \tilde{f}(\underline{x}_r, \omega) \right\rangle_{R, \omega} = \left\langle \tilde{w}(\underline{x}, \omega), \mathcal{G}_R^\dagger \tilde{f}(\underline{x}_r, \omega) \right\rangle_{S, \omega}. \quad (4.2.21)$$

The definition of the adjoint operators and the notation used in this work can be found in appendix D. The resulting adjoint for the operator  $\mathcal{G}_R$  is represented by the following equation:

$$\mathcal{G}_R^\dagger \tilde{f}(\underline{x}_r, \omega) = \sum_{r=1}^{N_r} \tilde{G}^*(\underline{x}_r, \underline{x}, \omega) \tilde{f}(\underline{x}_r, \omega), \quad (4.2.22)$$

with the superscript asterisk denoting complex conjugation. Besides the formal definition, the adjoint of an operator can often be given a physical interpretation. For a general convolution operator  $\mathcal{L}$ , the adjoint operator  $\mathcal{L}^\dagger$  represents a convolution with the time-reversed filtering wavelet. Hence, the adjoint operator can be used to undo the time shift of the forward operator, or equivalently, cancel the change of the phase spectrum caused by the forward operator. The amplitude spectrum is equally affected by  $\mathcal{L}$  and  $\mathcal{L}^\dagger$ .

The operator  $\mathcal{G}_R$  represents a convolution operator in space and time: it convolves the source distribution with the Green's function in order to obtain the field at the receiver points. Its adjoint  $\mathcal{G}_R^\dagger$  is known as the *backpropagation* operator [Van den Berg 1999]. The adjoint operator of the imaging problem represents a mapping from the receiver space  $R$  to the source space  $S$ . It is used to propagate the receiver signals back towards their origin. As in the case of a general convolution operator, the adjoint operator  $\mathcal{G}_R^\dagger$  undoes the time shift caused by the forward operator  $\mathcal{G}_R$ , whereas it applies the same geometrical damping, i.e., the same decrease of the amplitudes due to the spreading of the wavefronts as the forward operator  $\mathcal{G}_R$ . Hence, the amplitudes of the waves are scaled as if they would physically have propagated twice through the medium: from the source to the receiver and vice versa.

### ■ 4.2.2 Spectral representation of the imaging problem

At first sight, the introduction of operators and their adjoints might seem laborious. It is therefore important to analyse the benefits of representing the imaging problem in this form.

The least-squares solution to the imaging problem given by Eq. 4.2.20 suggests that an estimate of the source distribution can be obtained by formally inverting the operator combination  $\mathcal{G}_R^\dagger \mathcal{G}_R$ :

$$\tilde{w}_{\text{est}}(\underline{x}, \omega) = \left( \mathcal{G}_R^\dagger \mathcal{G}_R \right)^{-1} \mathcal{G}_R^\dagger \tilde{f}(\underline{x}_r, \omega) = \mathcal{R}^{-1} \mathcal{G}_R^\dagger \tilde{f}(\underline{x}_r, \omega). \quad (4.2.23)$$

The formal solution consists of the application of the backpropagation operator to the receiver signals by  $\mathcal{G}_R^\dagger$  and the application of an additional operator  $\mathcal{R} = \mathcal{G}_R^\dagger \mathcal{G}_R$  that has to be inverted. The backpropagation operator can always be applied, whereas the conditioning of the operator  $\mathcal{R}$  might prohibit its inversion. Therefore, it is important to determine the conditions under which  $\mathcal{R}$  is invertible and, in the case that inversion is not possible, to determine useful approximate solutions. To this end, the following statements about  $\mathcal{R}$  can be made:

- (1) The operator  $\mathcal{R}$  is a self-adjoint operator [Fokkema 1993].
- (2) The eigenvalue decomposition can be used in order to diagonalise  $\mathcal{R}$  and determine its spectrum, which is real and positive.
- (3) From the spectrum of  $\mathcal{R}$ , the ill-posedness of the problem can be analysed.

This means that, according to the spectral theorem for self-adjoint operators, there exists a unitary transformation operator  $\mathcal{U}$ , such that  $\mathcal{R}$  can be diagonalised:

$$\mathcal{R} = \mathcal{U}^\dagger \mathcal{S} \mathcal{U}, \quad (4.2.24)$$

with  $\mathcal{S}$  being a diagonal multiplication operator containing the eigenvalues of  $\mathcal{R}$ .

The eigenvalues form the spectrum of  $\mathcal{R}$  and indicate whether the desired inversion is possible. If the spectrum does not contain any zeros, inversion can simply be performed by using the reciprocal of the eigenvalues:

$$\mathcal{R}^{-1} = \mathcal{U}^\dagger \mathcal{S}^{-1} \mathcal{U}. \quad (4.2.25)$$

If the spectrum of the operator  $\mathcal{R}$  contains zeros, the inversion is not unique, and additional measures must be taken in order to obtain a unique solution.

In order to diagonalise the operator and analyse the spectrum, a detailed expression for  $\mathcal{R}$  is needed, which can be obtained by inserting Eq. 4.2.18 into Eq. 4.2.22:

$$\mathcal{R}\tilde{w}(\underline{x}, \omega) = \mathcal{G}_R^\dagger \mathcal{G}_R \tilde{w}(\underline{x}, \omega) = \sum_{r=1}^{N_r} \tilde{G}^*(\underline{x}_r, \underline{x}, \omega) \int_{-\infty}^{\infty} \tilde{G}(\underline{x}_r, \underline{x}, \omega) \tilde{w}(\underline{x}, \omega) d\underline{x}. \quad (4.2.26)$$

Equation 4.2.26 describes a mapping from the source space  $S$  onto itself. The analysis of this equation is simplified by re-writing it in a slightly different form:

$$\mathcal{R}\tilde{w}(\underline{x}, \omega) = \sum_{r=1}^{N_r} \tilde{G}^*(\underline{x}, 0, \omega) * \left\{ \delta(\underline{x} - \underline{x}_r) \int_{-\infty}^{\infty} \delta(\underline{x} - \underline{x}_r) \left[ \tilde{G}(\underline{x}, 0, \omega) * \tilde{w}(\underline{x}, \omega) \right] d\underline{x} \right\}, \quad (4.2.27)$$

with the asterisk denoting spatial convolution. From this equation, it can be seen that the following operations are carried out:

- (1) The source distribution is convolved with the Green's function, such that the wave field is obtained for the entire source space  $S$ .
- (2) The field is sampled at the receiver positions.
- (3) The values obtained at the receiver positions determine the strengths of a number of virtual sinks at the receiver positions.
- (4) The result of applying the operator  $\mathcal{R}$  is given by the superposition of these sinks.

The first two steps are carried out by the forward operator  $\mathcal{G}_R$ , whereas the adjoint  $\mathcal{G}_R^\dagger$  takes care of the latter two. The given description can be used to provide a physical interpretation of the operators: The forward operator  $\mathcal{G}_R$  decomposes the source distribution in terms of shifted copies of the Green's function. The receiver signals  $\tilde{f}(\underline{x}_r, \omega)$  represent the 'coefficients' of this decomposition. The adjoint operator performs a reconstruction of the source distribution by superimposing point sinks, i.e., the anti-causal equivalent of the Green's function describing circular wave

fronts propagating towards the receivers. Figure 4.11 gives an illustration of these operations. The operator  $\mathcal{R}$  performs both the decomposition and the reconstruction, thereby indicating to what extent the source distribution can be reconstructed for a given setup of receivers.

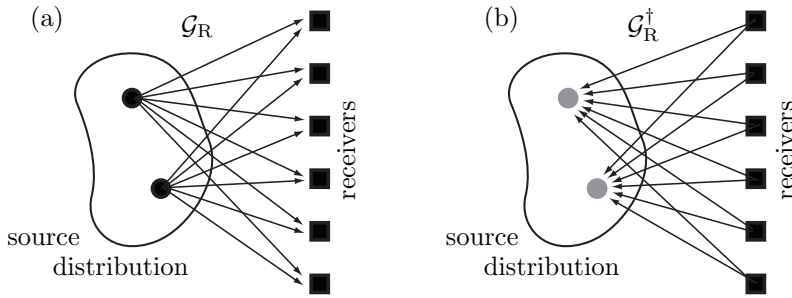


**Figure 4.11:** Mapping from the source distribution to the receivers by the operator  $\mathcal{G}_R$  (a); reconstruction of the source distribution by the operator  $\mathcal{G}_R^\dagger$  (b).

It becomes evident that  $\mathcal{R}$  must have finite rank: whereas all frequencies can be represented, the superposition of only Green's functions corresponding to sinks at the receiver locations are used to construct its result. The rank of  $\mathcal{R}$  is determined by the number of receivers. This is due to the fact that in a combination of operations, the operation with the lowest rank determines the overall rank of the operator. In the imaging problem, the operation of lowest rank is the sampling at the receiver points, the rank of which is equal to the number of receivers  $N_r$ .

Therefore, the imaging problem is not unique and ill-posed in the sense of Hadamard's definition [Hadamard 1923]. There exist different source distributions resulting in exactly the same receiver signals.

Since the non-uniqueness of the inverse problem given by the formal inversion in Eq. 4.2.23 has been established, it is necessary to devise methods that can provide approximate solutions. One of the simplest approximations has already been presented above: it is the application of the adjoint operator  $\mathcal{G}_R^\dagger$  without the additional inversion of  $\mathcal{R}$ :

$$\tilde{w}_{\text{adj}}(\underline{x}, \omega) = \mathcal{G}_R^\dagger \tilde{f}(\underline{x}_r, \omega). \quad (4.2.28)$$

If the generation of the receiver signals due to a source distribution is taken into account, it can be seen that the operator  $\mathcal{R}$  provides the result that can be obtained by backpropagation for a given source distribution:

$$\tilde{w}_{\text{adj}}(\underline{x}, \omega) = \mathcal{G}_R^\dagger \mathcal{G}_R \tilde{w}(\underline{x}, \omega) = \mathcal{R} \tilde{w}(\underline{x}, \omega). \quad (4.2.29)$$

Hence, the operator  $\mathcal{R}$  describes the quality of the image in comparison to the true source distribution. Application of this operator to a source distribution shows to what extent an image is blurred. Therefore,  $\mathcal{R}$  enables the assessment of the resolution that is obtainable by application of the adjoint operator and is called the *reproducing kernel* [Sibul 1995] or the *resolution operator* [Tarantola 2005].

### ■ 4.2.3 Resolution analysis in the wavenumber-frequency domain

Whereas the diagonalisation of the resolution operator  $\mathcal{R}$  as demanded by Eq. 4.2.24 provides information on the *operator spectrum*, it is decided to analyse how  $\mathcal{R}$  influences the *wavenumber-frequency spectrum* of a given source distribution. If the operations in the wavenumber-frequency spectrum can be expressed as a multiplication,  $\mathcal{R}$  can be described as a spectral filter. This allows for a physical interpretation of the operator: the representation in the wavenumber-frequency domain reveals how well different frequencies and related wavenumbers can be reproduced in an image. The presence or absence of wavenumber components determines the spatial resolution of the imaging technique.

Representations in the wavenumber domain for the assessment of the resolution obtained by imaging procedures have also been used by Beylkin and Oristaglio [Beylkin 1985], Berkhout [Berkhout 1987] and Bleistein et al. [Bleistein 2001]. The wavenumber domain provides an overview of the spectral content that can easily be interpreted. By establishing a link between the characteristics of the wavenumber spectrum and the choice of imaging setup, the effect of source and receiver positions as well as the choice of frequencies employed for imaging on the achievable resolution can be analysed.

The wavenumber spectrum describing the resolution is also known as the *modulation transfer function*, while its spatial counterpart, the *point spread function* describes how an ideal point-like object is reconstructed by the imaging method or system under investigation [Hendee 2002].

By application of a spatial Fourier transform, the resolution operator  $\mathcal{R}$  given by Eq. 4.2.27 is readily transformed to the wavenumber-frequency domain:

$$\mathcal{R}\tilde{w}(\underline{k}_1, \omega) = \sum_{r=1}^{N_r} \tilde{G}^*(\underline{k}_1, \omega) e^{j\underline{k}_1 \cdot \underline{x}_r} \int_{-\infty}^{\infty} e^{-j\underline{k} \cdot \underline{x}_r} \tilde{G}(\underline{k}, \omega) \tilde{w}(\underline{k}, \omega) d\underline{k}. \quad (4.2.30)$$

The influence of the receiver positions  $\underline{x}_r$  can be put into a single factor:

$$\begin{aligned} \mathcal{R}\tilde{w}(\underline{k}, \omega) &= \tilde{G}^*(\underline{k}_1, \omega) \int_{-\infty}^{\infty} \sum_{r=1}^{N_r} e^{j(\underline{k}_1 - \underline{k}) \cdot \underline{x}_r} \tilde{G}(\underline{k}, \omega) \tilde{w}(\underline{k}, \omega) d\underline{k} \\ &= \tilde{G}^*(\underline{k}, \omega) \left\{ \left( \sum_{r=1}^{N_r} e^{j\underline{k} \cdot \underline{x}_r} \right) * \left[ \tilde{G}(\underline{k}, \omega) \tilde{w}(\underline{k}, \omega) \right] \right\}, \end{aligned} \quad (4.2.31)$$

with the asterisk denoting convolution with respect to  $k_x$  and  $k_y$ . Note that the sum of exponentials in the form of  $e^{j\underline{k} \cdot \underline{x}_r}$  represents a spatial Fourier transform of the receiver geometry, for which the variable  $\tilde{\psi}(\underline{k})$  is introduced:

$$\tilde{\psi}(\underline{k}) = \sum_{r=1}^{N_r} e^{j\underline{k} \cdot \underline{x}_r}. \quad (4.2.32)$$

For an arbitrary point  $\underline{x}_P$ , the resolution operator has the following wavenumber-frequency spectrum:

$$\tilde{\tilde{R}}(\underline{k}, \underline{x}_P, \omega) = \mathcal{R}e^{j\underline{k} \cdot \underline{x}_P} = \tilde{G}^*(\underline{k}, \omega) \left\{ \tilde{\psi}(\underline{k}) * \left[ \tilde{G}(\underline{k}, \omega) e^{j\underline{k} \cdot \underline{x}_P} \right] \right\}. \quad (4.2.33)$$

This spectrum  $\tilde{\tilde{R}}(\underline{k}, \underline{x}_P, \omega)$  is formed by application of three successive operations in the wavenumber-frequency domain:

- (1) The spectrum of the source distribution is multiplied by the Green's function.
- (2) The filtered source spectrum is convolved with a spatial Fourier transform of the receiver geometry.
- (3) The result is multiplied by the complex conjugate of the Green's function.

The first and third operation represent spectral filters, i.e., multiplication operators in the wavenumber-frequency domain that perform a weighting of the spectrum by the Green's function. As shown in Appendix B.2, the Green's function for a source at the origin is given by the following expression in the wavenumber-frequency domain:

$$\tilde{\tilde{G}}(\underline{k}, \omega) = \frac{1}{(k_x^2 + k_y^2)^2 - k_P^4}. \quad (4.2.34)$$

Figure 4.12 shows a sections through this function for a single frequency. The Green's function consists of propagating and non-propagating components. The propagating components can be found on the paraboloid consisting of a combination of Ewald's

circles for multiple frequencies as introduced in Section 4.1.1. Non-propagating components decay rapidly towards the inside or outside of this paraboloid. Function values on the paraboloid tend towards infinity. However, the integral over the Green's function remains finite. Fig. 4.12 depicts the discrete spatial Fourier transform of a spatial section. The spectrum shown is thus sampled and convolved with a sinc function corresponding to the extent of the spatial domain. Therefore, the samples close to and on the Ewald's circle  $k_P^4 = (k_x^2 + k_y^2)^2$  have finite values.

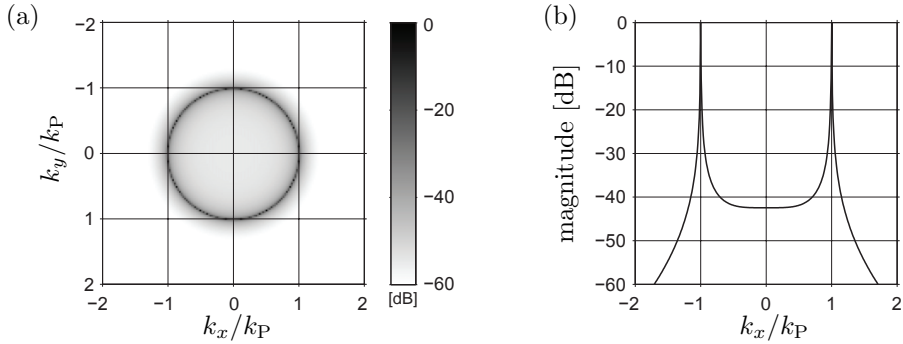


**Figure 4.12:** Section through the Green's function in the wavenumber-frequency domain for a single frequency (a); section through this axially symmetric function for  $k_y = 0$  (b).

With respect to the three operations forming the resolution operator  $\tilde{\tilde{R}}(k, \underline{x}_P, \omega)$ , the first and third operation given by the filtering with the Green's function reduce the magnitude of all non-propagating wavenumber components, i.e., components that are off the paraboloid in the wavenumber-frequency domain. Hence, the wavenumber bandwidth is effectively reduced to an annular region around the Ewald's circle of radius  $k_P$ . The width of this region is determined by the extent to which components of low magnitude can be used in the imaging process, i.e., by the signal-to-noise ratio. In many practical cases, the annular region can be approximated by the Ewald's circle of radius  $k_P$ , such that the maximum spatial resolution that can be obtained by backpropagation is in the order of the wavelength  $\lambda$  for the given frequency  $\omega$ . Whether or not this resolution limit is achieved depends on the second operation determining the spatial resolution, i.e., the Fourier transform of the array geometry.

#### ■ 4.2.4 Design and assessment of array geometries

Since it has been shown that the geometry of an array has major influence on the achievable resolution, the wavenumber spectrum of several simple array setups

is analysed. The convolution operation in Eq. 4.2.33 alters the content of spatial frequencies depending on the structure of the Fourier transform of the receiver geometry. The wavenumber content can thus be blurred, shifted, or copied to different locations in the wavenumber spectrum.

Based on these findings, two alternative desirable forms of the wavenumber spectrum for the ‘ideal’ geometry of an array of receivers can be defined:

- The wavenumber spectrum of the array geometry should resemble a Dirac delta pulse at the origin, thereby having virtually no influence on the resolution of the backpropagated field given by the resolution operator  $\mathcal{R}$  in Eq. 4.2.33.
- Alternatively, the imprint of the wavenumber spectrum of the receiver geometry should exhibit a spectral shape that is easy to compensate for by deconvolution.

The following discussion of the imaging problem will focus on the first option; the second approach is covered in Section 4.2.4.3.

It is obvious that the wavenumber spectrum of the receiver geometry can only to a limited extent resemble a Dirac delta function centred at the origin: such a spectrum would correspond to full spatial coverage with receivers – a trivial case without practical relevance. Therefore, it is necessary to investigate how a good approximation can be achieved with a finite number of receivers. First, the simple case of a one-dimensional linear array is considered, based on which rules for arbitrary two-dimensional geometries can be derived.

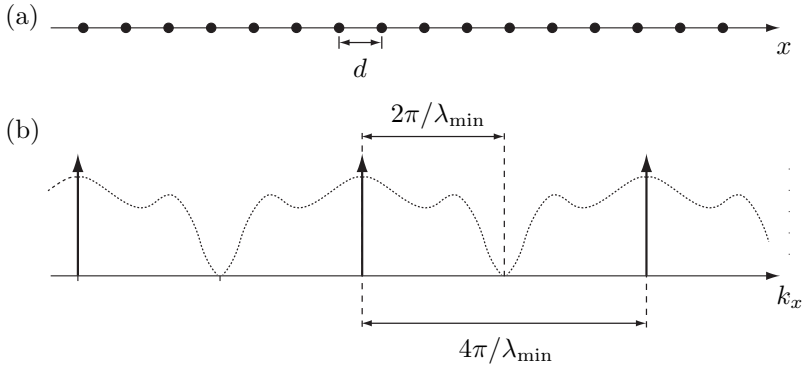
#### 4.2.4.1 Aliasing and truncation by discrete and finite arrays in one dimension

Figure 4.13(a) depicts an array of  $N_r$  receivers with a spacing distance  $d$ . The Fourier transform of this array geometry is given by a train of Dirac pulses as shown in Fig. 4.13(b). The wavenumber spectrum of the sampled wave field is convolved with these Dirac pulses, such that it is periodically repeated. According to the Nyquist-Shannon sampling theorem, the spatial distance  $d$  of the receivers should not exceed half the minimum wavelength contained in the signal in order to avoid aliasing [Shannon 1949]:

$$d_{\text{Nyquist}} \leq \frac{\lambda_{\min}}{2}. \quad (4.2.35)$$

Choosing this distance leads to repetitions of the wavenumber spectra at positions  $4\pi N/\lambda_{\min}$ ,  $N$  being an arbitrary integer. The repeated spectra of the wave field with maximum wavenumber  $2\pi/\lambda_{\min}$  do not overlap.

However, the limiting value  $d_{\text{Nyquist}}$  is only valid if an infinite number of samples is taken. Figure 4.14 depicts the case of a finite array of  $N_r$  receivers covering an aperture of  $a = N_r d$ , which is the threshold at which another receiver could just be



**Figure 4.13:** Sampling by an infinite array in the spatial domain (a) corresponds to repetition of the wavenumber spectrum of a wave field (dotted) in the wavenumber domain (b).

placed within the same aperture  $a$ . The wavenumber spectrum of a sampled wave field is not convolved by Dirac pulses as in the infinite case, but by sinc functions corresponding to the aperture  $a$  of the array as shown in Fig. 4.14(b).

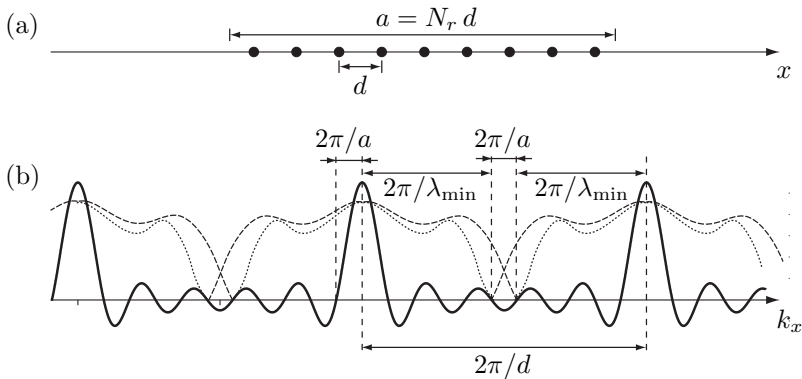


**Figure 4.14:** Sampling with a finite array of aperture  $a$  consisting of  $N_r$  receivers with distance  $d$  in the spatial domain (a); due to the finite aperture, the wavenumber spectra (dotted) are, in first approximation, extended by  $2\pi/a$  on both sides (dashed) by convolution with a sinc function (b); in order to reduce aliasing, the separation of the spectra is increased by  $2\pi/a$  in comparison to Fig. 4.13.

The wavenumber spectrum of the wave field is repeated and extended due to the convolution with the sinc function. As a consequence, the wavenumber spectra of

a wave field sampled by a finite array will overlap. Nevertheless, the impact of the aliasing can be reduced by a more rigorous sampling criterion in order to lower the extent to which the spectra overlap.

The strongest effect caused by a finite aperture is a broadening of the main lobe of the sinc function. Convolution with this main lobe extends the wavenumber spectrum by  $2\pi/a$  on both sides as depicted in Fig. 4.14(b). In order to ensure that repetitions of the wavenumber spectrum do not significantly influence the baseband with wavenumbers  $k_x \leq 2\pi/\lambda_{\min}$ , the distance between the spectra is increased by  $2\pi/a$  in comparison to the infinite array. The following condition has to be fulfilled:

$$\frac{2\pi}{d} \geq \frac{4\pi}{\lambda_{\min}} + \frac{2\pi}{a}. \quad (4.2.36)$$

The maximum distance of the receiver elements is thus given by

$$d_{\text{finite}} \leq \frac{\lambda_{\min}}{2} \frac{a}{a + \frac{\lambda_{\min}}{2}}. \quad (4.2.37)$$

If the limit towards an infinite aperture is taken,  $d_{\text{finite}}$  approaches the Nyquist-Shannon sampling interval given by Eq. 4.2.35. The maximal sampling distance can also be expressed in terms of the number of receivers  $N_r$ :

$$d_{\text{finite}} \leq \frac{\lambda_{\min}}{2} \frac{N_r - 1}{N_r}. \quad (4.2.38)$$

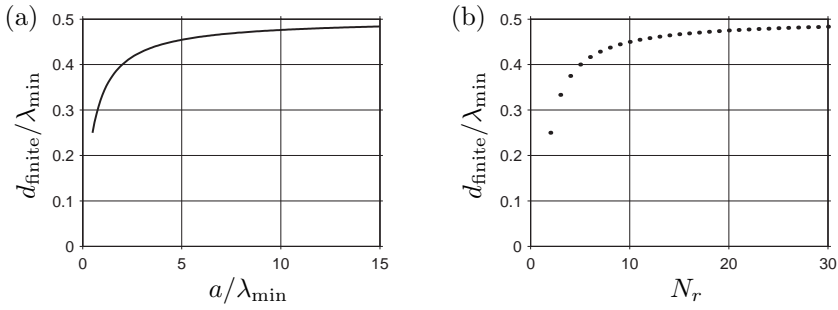
For the extreme case of only two receivers, the maximum spacing is equal to a quarter of the wavelength, which is half the interval suggested by the Nyquist-Shannon sampling theorem.

Figure 4.15 presents a plot of the maximum spatial sampling interval depending on the aperture and the number of receivers. The Nyquist-Shannon limit gives a reasonable approximation if the aperture of the array exceeds five times the wavelength, or if the linear array consists of at least ten receivers.

#### 4.2.4.2 Aliasing and truncation by discrete and finite arrays in two dimensions

The conditions derived in the one-dimensional case can also be applied to imaging in two dimensions. Figure 4.16 shows representations of a finite linear array in the spatial and the wavenumber domain, corresponding to  $\psi(\underline{x})$  and  $\tilde{\psi}(\underline{k})$ , respectively. This one-dimensional array is chosen as a first example in order to study the effects of sampling and truncation on two-dimensional imaging.

It has been shown in Eq. 4.2.33 that the resolution obtained by application of the adjoint operator is determined by three steps, the second of which is the convolution by  $\tilde{\psi}(\underline{k})$ . Furthermore, it has been pointed out that the first and the third step limit the wavenumber content to an annular region around the circle of radius  $k_P$ .



**Figure 4.15:** Maximum receiver distance expressed in terms of the minimum wavelength for a finite array with given aperture (a), and for a given number of receivers (b).

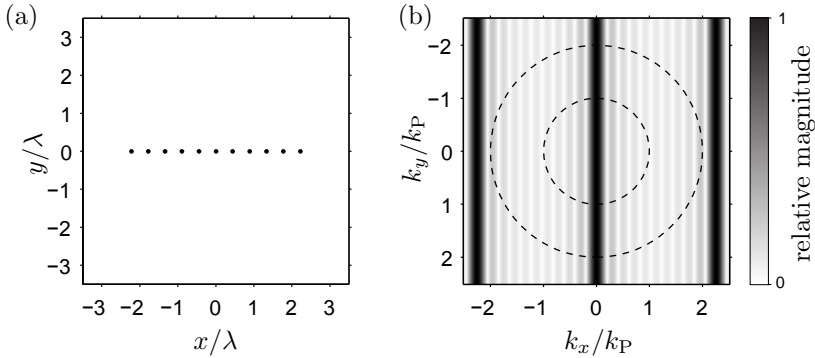


**Figure 4.16:** Representation of a finite linear array in the spatial domain (a) and in the wavenumber domain (b); two dashed circles with radius  $k_P$  and  $2k_P$  are superimposed.

From this combination of operations, it can be derived which part of the wavenumber spectrum of  $\tilde{\psi}(\underline{k})$  has an actual influence on the achievable resolution. The convolution of the incident field with  $\tilde{\psi}(\underline{k})$  can, in good approximation, be described as convolution with points on the Ewald's circle of radius  $k_P$ . The wavenumber spectrum of the receiver geometry is convolved with this circle and thus shifted by  $k_P$  into all directions. Subsequent multiplication by the Green's function, again approximated by the Ewald's circle of radius  $k_P$  reveals that only wavenumber components of  $\tilde{\psi}(\underline{k})$  inside the circle of radius  $2k_P$  can have influence on the resolution; components of the spectrum outside this circle are filtered out by the subsequent multiplication with the Green's function in Eq. 4.2.33.

This insight provides a tool which can be used to design and assess array setups. The following two design criteria have to be met by an array of receivers:

- The Fourier transform  $\tilde{\psi}(\underline{k})$  of an array geometry should resemble a Dirac pulse at the origin.
- Apart from this pulse,  $\tilde{\psi}(\underline{k})$  should be zero inside the circle of radius  $2k_P$ .

The spacing of the array elements in Fig. 4.16 is chosen according to Eq. 4.2.38. The repetitions of the main lobe of the spectrum are outside the circle of radius  $2k_P$ . Hence, significant effects of aliasing are avoided.

It has been shown that a finite aperture leads to a broadening of the lobe at the origin of  $\tilde{\psi}(\underline{k})$ . An extreme case is found in the two-dimensional representation of the one-dimensional linear array: the aperture in  $y$ -direction is zero, corresponding to infinite extent in the  $k_y$ -direction in the wavenumber domain. The resolution function  $\tilde{R}(\underline{x}, \underline{x}_P, \omega)$  is therefore symmetric with respect to the  $y$ -axis. As already seen in the context of wave field extrapolation, the linear array does not discriminate between positive and negative  $y$ -coordinates.

This ambiguity can be resolved by extending the array in the  $y$ -direction. Figure 4.17(a) shows a curved array. From the representation in the wavenumber domain shown in Fig. 4.17(b), it can be seen that the extent of the main lobe at the origin of  $\tilde{\psi}(\underline{k})$  is limited in the  $y$ -direction.

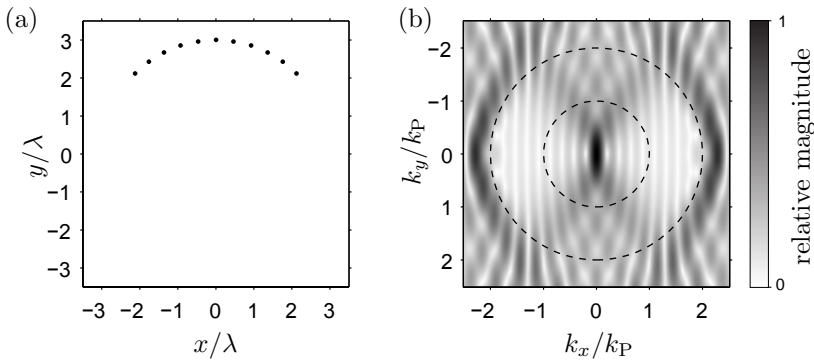


**Figure 4.17:** Representation of a curved array (quarter of a circle) in the spatial domain (a) and in the wavenumber domain (b).

The aperture in the  $y$ -direction can further be increased by employing a semi-circular array as shown in Fig. 4.18(a). The sampling distance is chosen in such a way that

interference from spectral repetitions is mainly found outside the circle of radius  $2k_P$ . Note the main lobe at the origin in the wavenumber domain, the extent of which in the  $k_y$ -direction becomes smaller with increasing aperture of the array in  $y$ -direction.

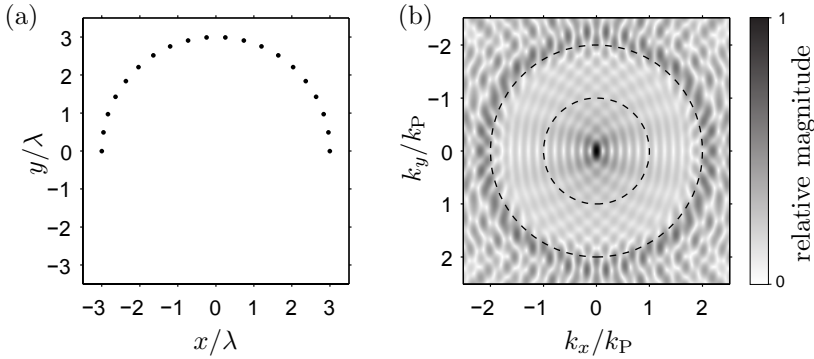


**Figure 4.18:** Representation of a curved array (semi-circle) in the spatial domain (a) and in the wavenumber domain (b).

The main lobe of the Fourier transform of the array geometry can be narrowed further by using a circular setup, thereby making  $\tilde{\psi}(\underline{k})$  axially symmetric with respect to the origin as shown in Fig. 4.19(b). For a given number of receivers, the circular array provides an efficient way of achieving a relatively high aperture while limiting the interference due to aliasing.

The two criteria for array setups introduced above can be employed for the analysis of arbitrary geometries. The transition from the linear array to the circle has been chosen as a simple example. For more complex geometries, the two criteria enable the assessment and optimisation of the array design. For instance, it can be decided whether the placement of another receiver can actually give an improvement in resolution, and where the receiver should be placed to give the best improvement.

#### 4.2.4.3 Imaging in the near- and far-field

As a generalisation of the example of a circular setup of receivers, the imaging of a source distribution in the near- and far-field is considered. The setup shown in Fig. 4.19(a) is modified towards continuous sampling on a circle of radius  $\Delta x$ , such that effects of aliasing do not have to be taken into account. To this end, the wavenumber spectrum of the receiver geometry  $\tilde{\psi}(\underline{k})$  is expressed in terms of angular

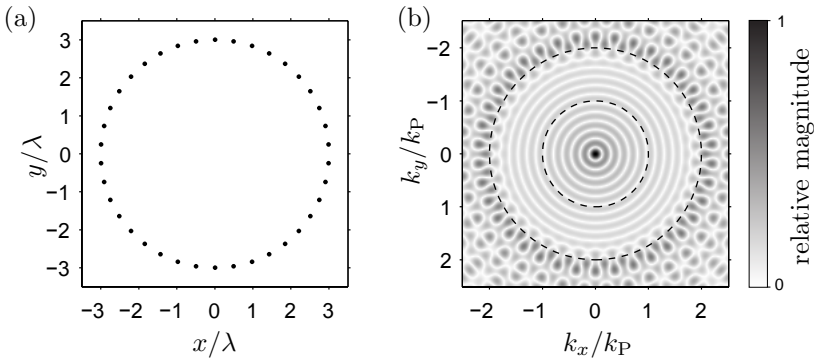


**Figure 4.19:** Representation of a circular array in the spatial domain (a) and in the wave-number domain (b).

position  $\theta_r$  and distance from the origin  $\Delta x$ :

$$\tilde{\psi}(\underline{k}) = \sum_{r=1}^{N_r} e^{j|\underline{k}|\Delta x \cos \theta_r}. \quad (4.2.39)$$

For continuous sampling, the Fourier transform of the receiver geometry is then given by integration over all angles  $\theta$  of the representation in polar coordinates:

$$\tilde{\psi}(\underline{k}) = \int_0^{2\pi} e^{j|\underline{k}|\Delta x \cos \theta} d\theta = 2\pi J_0(|\underline{k}|\Delta x), \quad (4.2.40)$$

with  $J_0$  representing the zeroth order Bessel function of the first kind. This Bessel function has a peak of unit magnitude at the origin of the wavenumber domain and side lobes extending in radial direction as shown in Fig. 4.20. In comparison to Fig. 4.19(b), it can be seen that aliasing effects are not present in the case of continuous sampling as expected.

For different values of the radius  $\Delta x$ , the wavenumber spectrum of the circular receiver geometry is scaled in the radial direction. As the radius  $\Delta x$  is taken towards infinity, the far-field approximation is obtained:

$$\lim_{\Delta x \rightarrow \infty} J_0(|\underline{k}|\Delta x) = \begin{cases} 1, & |\underline{k}| = 0 \\ 0, & |\underline{k}| > 0 \end{cases} \quad (4.2.41)$$

This asymptotic result represents the ideal case of a wavenumber spectrum having only a peak of magnitude 1 at the origin, which is close to the desired spectrum

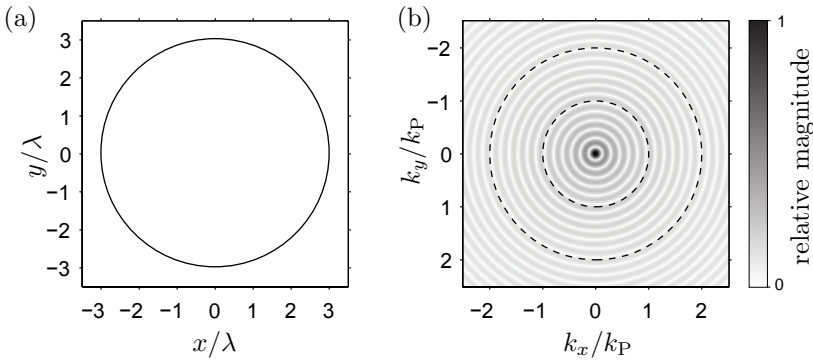


**Figure 4.20:** Representation of an ideal continuous circular array in the spatial domain (a) and in the wavenumber domain (b).

having a Dirac delta pulse at the origin as derived at the beginning of Section 4.2.4. Hence, by measuring in the far-field all around a source distribution, where the radiated wave field can be received for all angles separately, the influence of the receiver array on the achievable resolution can virtually be eliminated.

Another case of interest is obtained for low values of the radius  $\Delta x$ , i.e., for imaging in the near-field of the source distribution. For lower  $\Delta x$ , the peak at the origin of the Bessel function increases, such that the circles of zero magnitude are shifted outwards in radial direction. Since the first zero crossing of  $J_0(|\underline{k}| \Delta x)$  can be found for  $|\underline{k}| \Delta x \approx 2.405$ , imaging at a radial distance equal to a wavelength  $\lambda$ , for instance, leads to the first circle of zero magnitude at  $|\underline{k}| \approx 0.38k_P$ .

The increase of the width of the main peak of  $J_0(|\underline{k}| \Delta x)$  seems to have an adverse effect the obtainable resolution according to Eq. 4.2.33 because of the blurring effect of the Fourier transform of the receiver geometry  $\tilde{\psi}(\underline{k})$  on the wavenumber spectrum. However, with respect to inversion, the broadening of the main peak can actually be shown to have a positive influence on the obtainable resolution. The feasibility of inversion can be determined by the ability to divide by the spectrum of the resolution operator  $\tilde{R}(\underline{k}, \underline{x}_P, \omega)$ . Inversion is hindered by zeros in this spectrum. The convolution of the Green's function by  $\tilde{\psi}(\underline{k})$  in Eq. 4.2.33 introduces zeros to wavenumber components inside and outside the Ewald's circle of radius  $k_P$ . If the width of the main peak of  $J_0(|\underline{k}| \Delta x)$  increases, the distance of these zeros from the Ewald's circle is increased as well, leading to a bigger part of the wavenumber spectrum that is not affected by zeros. In the inversion, higher wavenumber components outside the Ewald's circle can thus be reconstructed. Hence, it is possible to obtain an image with *superresolution*, i.e., an image with a spectrum having wavenumber components above the resolution limit, if the receivers are positioned in the near-field.

This principle is extensively used in near-field acoustic holography [Williams 1999] or near-field microscopy [Greffet 1997].

The advantages of imaging in the near-field are mentioned mainly for the sake of completeness. With respect to the purpose of the present work, its possibilities can be regarded as a special case that can only be exploited if the receiver setup is explicitly chosen. The restriction to an image region extending only a few centimetres from the receivers is not considered useful for the imaging of plate-like structures using flexural waves. For this limited range, the benefit in comparison to classical scanning techniques, i.e., a combination of local measurements of the plate thickness, becomes negligible.

The possibilities of inversion will further be investigated in Section 4.2.8. First, the backpropagation approach will be presented in the case that information at multiple frequencies is available.

#### ■ 4.2.5 Frequency and wavenumber spectra for optimal spatial resolution

In the previous section, the setup of the receivers has been analysed with respect to the available information represented in the wavenumber-frequency domain. Significant improvement of the obtained image can be achieved by including information available at different frequencies in the imaging process. Different frequencies are directly related to different wavenumbers by the dispersion relation and correspond to information at annular rings of different radii in the wavenumber domain. Combination of rings in the wavenumber domain as the one shown in Fig. 4.12 helps to fill the wavenumber spectrum, leading to an increase in resolution.

The question how information at different frequencies should be employed in the imaging process is directly related to the optimisation of the resolution of the image. In optics, an empirical resolution criterion postulated by Rayleigh is often used: two peaks can just be resolved when the maximum of the image of the first peak coincides with the first minimum of the image of the second peak [Born 1999]. Optimal resolution is thus achieved by minimising the width of the point spread function of the imaging process. Hence, the resolution of an image is improved if the following demands are met by the wavenumber spectrum:

- (1) The wavenumber spectrum should have a high bandwidth.
- (2) In the discrete case, the spectrum should be sampled equidistantly.
- (3) All wavenumbers should be present with equal strength, i.e., the wavenumber spectrum should be flat.

These requirements can be translated to the frequency spectrum by means of the dispersion relation  $k = \sqrt{\omega}/A$ . The bandwidth of the wavenumber spectrum can

directly be extended by employing more frequencies. For bending waves, it should be noted, however, that a downward extension of the frequency spectrum results in a relatively large extension of the wavenumber spectrum, whereas the bandwidth must significantly be extended towards higher frequencies in order to achieve the same relative extension on the high end of the wavenumber spectrum. This is due to the square root characteristics of the dispersion relation.

Similarly, the requirement of equal sampling distance in the wavenumber domain corresponds to non-equidistant sampling the frequency domain as illustrated in Fig. 3.4 in the context of dispersion removal in Section 3.4. There are two alternative possibilities of dealing with this issue:

- Non-equidistant samples are taken from a flat frequency spectrum, or,
- equidistant samples are taken from a frequency spectrum, the shape of which is adapted in such a way that the corresponding wavenumber spectrum is flat.

Both options have been presented in the context of deriving an optimal input frequency spectrum for the dispersion removal procedure in Section 3.6.1. The latter option requires an amplitude content proportional to  $1/\sqrt{\omega}$  as derived in Eq. 3.6.47. Nevertheless, the first option of using non-equidistant samples is to be preferred since it requires less effort for additional calculations in order to achieve the optimal spectral content by deconvolution. Equation 3.6.48 can thus be used to calculate the optimal distribution of a discrete number of frequencies applied for the formation of the image.

The demands derived above assume that the wave field caused by the sources exhibits a flat wavenumber spectrum. If this is not the case, additional deconvolution procedures can be applied to the receiver signals to improve the resolution. Furthermore, it becomes once more evident that the optimal source spectrum and the sampling conditions for imaging are essentially determined by the medium itself. The wavenumber spectrum dictates the criteria for optimal resolution, which can be transferred to the frequency spectrum of the sources via the dispersion relation. In addition, it has to be kept in mind that the spectral content for optimal resolution should not only exhibit a flat, but also a smooth amplitude spectrum as pointed out in Section 3.8.1 [Berkhout 1984].

Based on the detailed discussion of the resolution operator  $\mathcal{R}$  in the previous section, it is possible to present and analyse several methods for imaging. So far, the imaging problem has been presented for a single frequency. The criteria for optimal spectra have been established in this section, such that different imaging approaches can be reviewed under the assumption that information is available at multiple frequencies.

### ■ 4.2.6 Imaging by backpropagation

In Section 4.2.2, it has been shown that the imaging problem consists essentially of backpropagation of the receiver signals, i.e., the application of the adjoint operator  $\mathcal{G}_R^\dagger$ . In addition, an inversion of the resolution operator  $\mathcal{R}$  is needed as derived in Eq. 4.2.23. Omission of the inversion provides a simple, approximate solution to the imaging problem. The resolution that can be obtained by backpropagation for a single frequency is given by the resolution operator  $\mathcal{R}$  as shown in Eq. 4.2.29.

The backpropagated source distribution  $\tilde{w}_{\text{adj}}(\underline{x}, \omega)$  for a single frequency is obtained by application of the adjoint operator to the receiver signals  $\tilde{f}(\underline{x}_r, \omega)$  as shown in Eq. 4.2.28. The correct frequency-dependent weighting  $\alpha(\omega)$  for the adjoint operator can then be determined by minimising the difference between the receiver signals corresponding to  $\tilde{w}_{\text{adj}}(\underline{x}, \omega)$  and the measured receiver signals [Van den Berg 1999]:

$$\begin{aligned} \alpha(\omega) &= \arg \min_{\alpha(\omega)} \left\| \alpha(\omega) \mathcal{G}_R \tilde{w}_{\text{adj}}(\underline{x}, \omega) - \tilde{f}(\underline{x}_r, \omega) \right\|_R^2 \\ &= \arg \min_{\alpha(\omega)} \left\| \alpha(\omega) \mathcal{G}_R \mathcal{G}_R^\dagger \tilde{f}(\underline{x}_r, \omega) - \tilde{f}(\underline{x}_r, \omega) \right\|_R^2 \\ &= \frac{\left\| \mathcal{G}_R^\dagger \tilde{f}(\underline{x}_r, \omega) \right\|_S^2}{\left\| \mathcal{G}_R \mathcal{G}_R^\dagger \tilde{f}(\underline{x}_r, \omega) \right\|_R^2}. \end{aligned} \quad (4.2.42)$$

From the approximate representation of the Green's functions derived in Section 2.3.4, it can be seen that the amplitude spectrum of Green's function for beams is proportional to  $k_B^{-3}$ , whereas the Green's function for plates is proportional to  $k_P^{-2.5}$ . The frequency-dependent weighting factor  $\alpha(\omega)$  for beams exhibits the following characteristics:

$$\alpha(\omega) \propto k_B(\omega)^6 \propto \omega^3, \quad (4.2.43)$$

whereas the following spectral dependency is valid for plates:

$$\alpha(\omega) \propto k_P(\omega)^5 \propto \omega^{2.5}. \quad (4.2.44)$$

Therefore, the weighting factors compensate for the influence of the forward and backward propagation on the frequency spectrum. This operation can be interpreted as deconvolution: the weighting factor equalises the frequency weighting introduced by the Green's function.

The source distribution estimated by backpropagation is obtained by the following expression:

$$\tilde{w}_{\text{est}}(\underline{x}, \omega) = \alpha(\omega) \mathcal{G}_R^\dagger \tilde{f}(\underline{x}_r, \omega). \quad (4.2.45)$$

The achievable resolution can be expressed in terms of the resolution operator. In contrast to Eq. 4.2.29, the weighting by  $\alpha(\omega)$  is taken into account in case of multiple

frequencies. The following relation between the imaged distribution  $\tilde{w}_{\text{est}}(\underline{x}, \omega)$  and the true source distribution  $\tilde{w}(\underline{x}, \omega)$  is obtained:

$$\tilde{w}_{\text{est}}(\underline{x}, \omega) = \alpha(\omega) \mathcal{G}_R^\dagger \mathcal{G}_R \tilde{w}(\underline{x}, \omega) = \alpha(\omega) \mathcal{R} \tilde{w}(\underline{x}, \omega). \quad (4.2.46)$$

By deriving  $\alpha(\omega)$  as the minimum of an error functional (Eq. 4.2.42), a step is already taken from pure backpropagation towards inversion. In this simple form, merely the compensation for different strength of the field at different frequencies is taken into account.

Figure 4.21 shows a typical simulation setup with two sources of equal strength positioned at a distance of 0.5 m from an array of 12 receivers. The medium is chosen to be an aluminium plate of 3 mm thickness. Information at ten different frequencies between 1 kHz and 12 kHz distributed according to Eq. 3.6.48 is used for the formation of an image. In order to make the simulation more realistic, 10 % noise is added to the receiver signals. Only the domain marked by the dashed line is used for imaging.

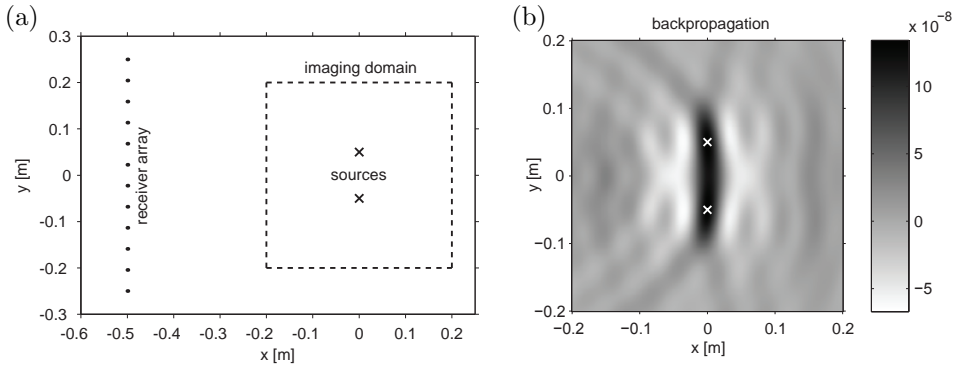


**Figure 4.21:** Simulation setup for the imaging of two sources marked by crosses (a); image obtained by backpropagation (b).

Despite the fact that the sources have a distance of 10 cm, which is approximately two times the smallest wavelength used, they cannot be resolved due to the limited aperture covered by the array and the simplicity of backpropagation.

#### ■ 4.2.7 Imaging by time shifting

It has already been pointed out that the adjoint operator  $\mathcal{G}_R^\dagger$  does not only cancel the time shift introduced by the forward operator, it also introduces additional

damping. The reconstructed amplitude decreases with increasing distance from the receivers, just as if a real source at the receiver position had been used. A viable alternative is given by application of an operator  $\mathcal{T}$  that only performs an inverse time shift without affecting the signal amplitudes. In order to apply this operator, it is sufficient to know the dispersion relation, or equivalently, the frequency-dependent phase velocity. Knowledge of the frequency-dependent amplitude characteristics of the Green's function is not required.

This approach can be qualified as a ray-theoretical approximation [Bleistein 2001]. With respect to the approximate expressions for the Green's functions in beams and plates presented in Section 2.3.4, it can be seen that this approximation is essentially valid for high frequencies. Similar approaches for which only the direction and speed of propagating wave fronts are considered are also used for seismic modelling [Robinson 2008]. The methods for dispersion removal presented in the previous chapter are also based on this kind of approximation, such that a correct determination of the position can be expected, whereas the estimated amplitude might only partially reflect the actual strength of a detected source.

Analogously to the adjoint of  $\mathcal{G}_R$  as given by Eq. 4.2.22, the operator  $\mathcal{T}$  can be defined as superposition of the time-shifted receiver signals:

$$\mathcal{T}\tilde{f}(\underline{x}_r, \omega) = \sum_{r=1}^{N_r} e^{jk \cdot (\underline{x} - \underline{x}_r)} \tilde{f}(\underline{x}_r, \omega). \quad (4.2.47)$$

In contrast to the adjoint operator  $\mathcal{G}_R^\dagger$ , the operator  $\mathcal{T}$  does not affect the amplitude of the frequency spectrum. The frequency-dependent weighting factor  $\alpha(\omega)$  has to take only the forward propagation from the source to the receivers into account and needs to be adapted:

$$\begin{aligned} \alpha(\omega) &= \arg \min_{\alpha(\omega)} \left\| \alpha(\omega) \mathcal{G}_R \mathcal{T} \tilde{f}(\underline{x}_r, \omega) - \tilde{f}(\underline{x}_r, \omega) \right\|_R^2 \\ &= \frac{\left\langle \mathcal{G}_R \mathcal{T} \tilde{f}(\underline{x}_r, \omega), \tilde{f}(\underline{x}_r, \omega) \right\rangle_R}{\left\| \mathcal{G}_R \mathcal{T} \tilde{f}(\underline{x}_r, \omega) \right\|_R^2}. \end{aligned} \quad (4.2.48)$$

For this reason, the frequency-dependent weighting factor  $\alpha(\omega)$  has to be taken as the square root of the values obtained in Eq. 4.2.43 and 4.2.44. The spectral shape for beams is therefore given by:

$$\alpha(\omega) \propto k_B(\omega)^3 \propto \omega^{1.5}, \quad (4.2.49)$$

For plates, the following expression is obtained analogously:

$$\alpha(\omega) \propto k_P(\omega)^{2.5} \propto \omega^{1.25}. \quad (4.2.50)$$

The resolution achieved by application of the operator  $\mathcal{T}$  is described by the following expression relating the true source distribution to its estimate:

$$\tilde{w}_{\text{est}}(\underline{x}, \omega) = \alpha(\omega) \mathcal{T} \mathcal{G}_R \tilde{w}(\underline{x}, \omega). \quad (4.2.51)$$

It should be noted that the weighting factor  $\alpha(\omega)$  depends strongly on the frequency as shown by Eq. 4.2.43 and 4.2.44, as well as its counterparts 4.2.49 and 4.2.50. For practical applications, the signal-to-noise ratio might limit the extent to which  $\alpha(\omega)$  can be used for amplification of the higher frequencies in order to achieve the optimal resolution. Application of the described amplification might introduce noise, whereas limiting of the amplification by  $\alpha(\omega)$  leads to inferior resolution.

Figure 4.22 shows the result of imaging by time shifting for the simulation example described in Section 4.2.6. For the presented case, only a small qualitative difference in comparison to imaging by backpropagation can be observed.

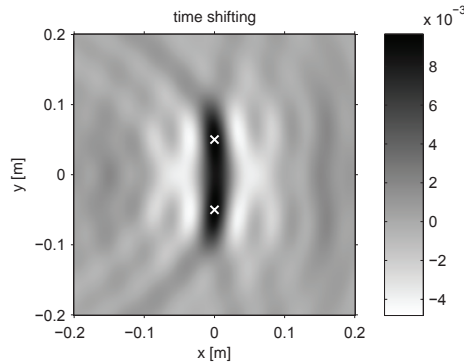


**Figure 4.22:** Image of two sources obtained by time shifting; the qualitative difference to the result obtained by backpropagation and shown in Fig. 4.21 is negligible.

### ■ 4.2.8 Imaging by inversion

It is to be expected that further improvements in resolution can be obtained only by abandoning the limitation to backpropagation or simple time reversal, and including the inversion of the resolution operator as demanded by Eq. 4.2.23.

In Section 4.2.3, the operations carried out by the resolution operator have been investigated in detail (see for instance Eq. 4.2.33). Inversion of this operator requires the application of the following three operations in the wavenumber-frequency domain:

- (1) multiplication by an inverse filter  $\tilde{\tilde{F}}_1(\underline{k}, \omega)$  in order to compensate for the multiplication by the complex conjugate of the Green's function due to the adjoint operator:

$$\tilde{\tilde{F}}_1(\underline{k}, \omega) = \frac{\tilde{\tilde{G}}(\underline{k}, \omega)}{\left| \tilde{\tilde{G}}(\underline{k}, \omega) \right|^2}, \quad (4.2.52)$$

- (2) deconvolution of the result with the spatial Fourier transform of the receiver geometry  $\tilde{\tilde{\psi}}(\underline{k})$ ,

- (3) multiplication by an inverse filter  $\tilde{\tilde{F}}_2(\underline{k}, \omega)$  in order to compensate for the multiplication by the Green's function due to the forward propagation:

$$\tilde{\tilde{F}}_2(\underline{k}, \omega) = \frac{\tilde{\tilde{G}}^*(\underline{k}, \omega)}{\left| \tilde{\tilde{G}}(\underline{k}, \omega) \right|^2}. \quad (4.2.53)$$

The feasibility of carrying out the first and third operation is limited by the signal-to-noise ratio. Division by the Green's function is only possible for a frequency-dependent annular region close to the Ewald's circle as shown in Fig. 4.12. Outside this region, the Green's function decays rapidly, such that multiplication by the reciprocal of its squared magnitude as required by Eq. 4.2.52 or 4.2.53 leads to strong amplification that would boost any noise present in the measured signals [Aster 2005]. Only wavenumber components which correspond to frequencies present in the source signal can be reconstructed, indicating once more the theoretical resolution limit of one wavelength derived in Section 4.2.3. Effectively, the filters given by Eq. 4.2.52 and 4.2.53 perform the compensation for the frequency-dependent amplitude of the Green's function. Essentially, they correspond to the weighting factor  $\alpha(\omega)$  introduced in Section 4.2.6 in the case of backpropagation. However, the additional effect of equalisation within the annular region around the Ewald's circle by these two filters slightly increases the range of wavenumber components present in the image.

The second operation described above, i.e., the deconvolution in the wavenumber-frequency domain, corresponds to the necessity to compensate for the spatial sampling of the wave field by the receivers. Such a compensation is possible to full extent if spatial interpolation of the receiver signals can yield the full wave field, a requirement that is fulfilled only if the wave field is sampled with an infinite array and a spacing according to the Nyquist-Shannon sampling theorem as discussed in Section 4.2.4. A finite array has a smoothing effect on the wavenumber spectrum of the wave field that can at least partially be compensated for by deconvolution in the wavenumber domain, thereby trying to remove the imprint of the array geometry as shown in Figs. 4.16 to 4.19 for several examples.

Hence, inversion of the resolution operator can be expected to yield an improvement in resolution compared to backpropagation. Since it has been established that full inversion is not possible due to the ill-posedness of the problem, the question arises how an approximate inversion can be performed. Possible solutions are described in the following section.

#### 4.2.8.1 Stabilised imaging

Strategies for approximate solutions to the present inversion problem can be found by closer inspection of the eigenvalues of the resolution operator  $\mathcal{R}$ , formally given by the diagonalisation of the operator presented in Eq. 4.2.24.

If the imaging problem was well-posed, the operator  $\mathcal{R}$  could be inverted according to Eq. 4.2.25, repeated here for convenience:

$$\mathcal{R}^{-1} = \mathcal{U}^\dagger \mathcal{S}^{-1} \mathcal{U}, \quad (4.2.54)$$

with  $\mathcal{U}$  being a unitary operator performing the diagonalisation and  $\mathcal{S}^{-1}$  representing a diagonal operator containing the reciprocals of the eigenvalues  $\sigma_i$ .

Eigenvalues equal to zero have to be neglected since their reciprocal is not defined. From the spectral analysis of the problem, it is evident that zero eigenvalues can be caused only by the sampling of the wave field by the receivers, not by forward or backward propagation. The sampling of the wave field has been shown to correspond to a convolution of the Fourier transform of the array geometry  $\tilde{\psi}(\mathbf{k})$  with the wave field in the wavenumber-frequency domain. The inverses of the forward and backward propagation, however, represented by the filters given by Eq. 4.2.52 and 4.2.53, do not contain zeros in the wavenumber-frequency domain. Nevertheless, they are ill-conditioned, which means that they contribute to a large spread of the eigenvalues.

The inverse problem requires *stabilisation*, i.e., the exclusion of eigenvalues close or equal to zero and the corresponding eigenfunctions from the inversion. Hence, a necessary step is the removal of zero eigenvalues, which is achieved by using the pseudo-inverse operator  $\mathcal{R}^+$  [Strang 1988]. The pseudo-inverse is given by the following expression:

$$\mathcal{R}^+ = \mathcal{U}^\dagger \mathcal{S}^+ \mathcal{U}, \quad (4.2.55)$$

with  $\mathcal{S}^+$  being a diagonal operator containing the reciprocal of the eigenvalues  $\sigma_i$  for  $\sigma_i > 0$ , and zeros for  $\sigma_i = 0$ . Out of the multitude of non-unique solutions to the original problem, the application of pseudo-inverse returns the solution with the smallest  $L^2$ -norm. From a physical point of view, the obtained solution has minimum energy since all eigenfunctions belonging to zero eigenvalues that could also contribute to a possible solution are excluded.

The rough assessment of the eigenvalues of the filters  $\tilde{\tilde{F}}_1(\mathbf{k}, \omega)$  and  $\tilde{\tilde{F}}_2(\mathbf{k}, \omega)$  has been carried out for the sake of illustration and clarification. In practice, it is not efficient to obtain the eigenvalues of a computationally large problem before even starting to solve it. Instead, it is proposed to make use of an iterative minimisation scheme, such as the *conjugate gradient* (CG) method, which is the approach of choice in the present work. Conjugate gradient methods can be used for solving linear and non-linear systems of equations. A comprehensive overview of the origin of the CG approach was presented by Golub and O’Leary [Golub 1989]. A more recent summary of its development and refinement is given by Van der Vorst [Van der Vorst 2003].

The error functional to be minimised has already been presented in Eq. 4.2.19 at the beginning of Section 4.2.1. Minimisation of this functional in a least-squares sense can be performed by solving the normal equations (Eq. 4.2.20). This can be achieved by a simplified conjugate gradient scheme for self-adjoint operators such as  $\mathcal{G}_R^\dagger \mathcal{G}_R$  [Fokkema 1993]. Both the forward operator  $\mathcal{G}_R$  and the adjoint operator  $\mathcal{G}_R^\dagger$  needed have been presented above and can be found, along with a derivation of the adjoint operator, in Appendix D.3. The linear conjugate gradient scheme used is given in Appendix F.1.

Figure 4.23 shows the result of imaging by unstabilised inversion for the simulation example described in Section 4.2.6. If we know where to expect the sources, their position and extent are significantly better resolved. However, the presence of noise in the receiver data causes artefacts that prohibit the easy detection of the true sources and render this method useless for practical applications.

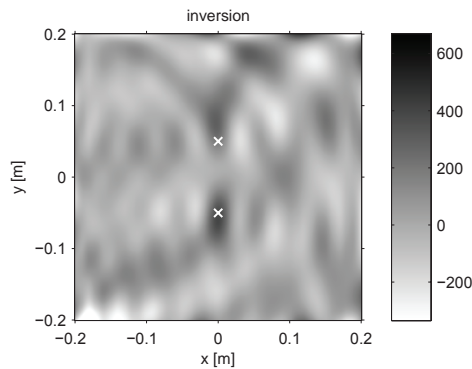


**Figure 4.23:** Image of two sources obtained by straightforward inversion; the noise present in the data is amplified and leads to the creation of severe artefacts in the image.

### 4.2.8.2 Regularised imaging

A useful property of a linear CG scheme in the context of the present problem is the fact that the scheme converges to the pseudo-inverse solution if the algorithm is started with zero as the first guess for the solution [Hestenes 1975]. The usage of a conjugate gradient scheme excludes the eigenvalues that are equal to zero from the inversion of the operator. Nevertheless, the problematic combination of relatively small eigenvalues and noisy data remains unresolved. Additional measures have to be taken to avoid the excessive amplification of noise. The choice of how to deal with the small eigenvalues marks the transition from *stabilisation* of the inversion towards *regularisation*. Straightforward calculation of the inversion is possible. However, it cannot be expected to produce a useful result.

Therefore, it is necessary to add some a priori information about the properties that a ‘useful result’ should have. This formulation is as vague as the range of possible choices is broad. A standard method is given by further limiting the energy of the solution by simply excluding small eigenvalues from the inversion. This method is usually known as *truncated singular value decomposition* (TSVD) [Hansen 1987]. Noise in the solution is avoided by excluding more eigenfunctions corresponding to small eigenvalues from contributing to the estimated solution. A similar result can be achieved by premature stopping of a conjugate gradient scheme [Ertürk 2002]. The motivation behind this choice is, again, the concurrent minimisation of energy of the estimated solution.

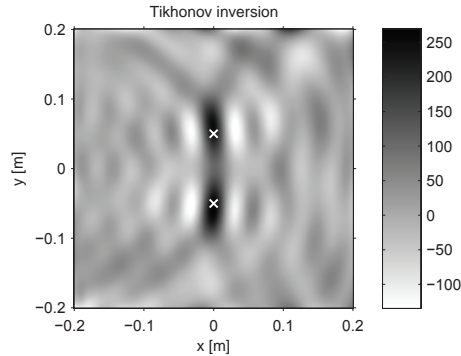
Another common choice for a regularising functional is *Tikhonov regularisation*, which is based on minimising the following error functional:

$$\tilde{w}(\underline{x}, \omega)_{\text{est}} = \arg \min_{\tilde{w}(\underline{x}, \omega)} \left\| \tilde{f}(\underline{x}_r, \omega) - \mathcal{G}_R \tilde{w}(\underline{x}, \omega) \right\|_R^2 + \gamma \|\mathcal{L} \tilde{w}(\underline{x}, \omega)\|_S^2, \quad (4.2.56)$$

with  $\gamma$  being a regularisation parameter and  $\mathcal{L}$  representing a general operator, for which often the identity operator  $\mathcal{I}$  is used [Aster 2005]. This type of regularisation is also known as *damped least squares* or *ridge regression*.

Tikhonov regularisation can also be applied to the singular value decomposition by adding a small constant value to the eigenvalues of the operator to be inverted [Hansen 1998]. This kind of regularisation is often chosen due to its simplicity. The eigenfunctions corresponding to small eigenvectors are thereby chosen to contribute to the solution only to a limited extent. Both truncated singular value decomposition and Tikhonov regularisation provide solutions with a small  $L^2$ -norm, i.e., minimum energy. These types of regularisation tend to smooth the estimated solution, which might not be desired in general [Sacchi 1998]. This problem will be covered in depth when dealing with the imaging of material inhomogeneities in Section 4.3.6.

The imaging result obtained by inversion with Tikhonov regularisation is shown in Fig. 4.24. The two sources can clearly be resolved, and the noise level in the image is acceptable.




---

**Figure 4.24:** Image of two sources obtained by inversion with Tikhonov regularisation.

---

However, it has already been shown that there are different ways of manipulating the eigenvalues of an operator before inverting it. For multiplicative manipulation, these choices are known as *filter functions* [Nagy 2003]. There are two issues to be considered:

- Which filter function suits the problem at hand?
- How are the parameters of this function chosen?

The first question refers to the decision of truncating or merely damping small singular values. The latter one refers to the even more crucial question *at which level* of the eigenvalues cutting or damping should be applied. The decision can be made relatively easily if all eigenvalues are available and their distribution can be analysed. However, when using a conjugate gradient scheme, the optimal point of stopping is difficult to pick [Hanke 1995]. Methods such as *generalised cross validation* [Bertero 1998] or the *L-curve criterion* [Calvetti 2000] usually require the solution of the problem for several different parameter values before the optimal one can be picked, thereby increasing the computational effort considerably.

Instead of focusing on the choice of optimal regularisation parameters, this discussion is postponed to Section 4.3.6, which deals with methods for imaging of a scattering distribution by inversion. In this context, two more regularisation methods that are relevant in the context of imaging will be presented: regularisation based on a *sparseness* constraint and regularisation based on a *total variation* constraint. Similar to truncated singular value decomposition or Tikhonov regularisation, these methods can be applied to both the imaging of a source distribution or the imaging of a scattering object.

The present section can be understood as an introduction to regularisation, with

minimum norm regularisation as a simple method applicable to general inversion problems. Advanced methods of regularisation, however, require more knowledge on the expected inversion result to be used. Hence, a good regularisation technique appropriate to the imaging problem must be chosen. Therefore, the two additional methods will be presented after the analysis of the second imaging problem, i.e., the problem of imaging a passive scattering distribution.

### 4.3 Imaging of scatterers under the Born approximation

Based on the results obtained for the imaging of a source distribution, the problem of imaging material inhomogeneities can be addressed. A local deviation from an otherwise homogeneous background medium causes scattering of the incident field as described in Section 2.5.3. The inhomogeneity can be described as a scattering distribution by using the contrast in material parameters  $\chi(\underline{x})$  and the frequency-dependent scattering potential  $\tilde{\Phi}(\underline{x}, \omega)$ . A scattering object can be regarded as a secondary source distribution that has to be illuminated by primary sources. In the following, it will be investigated how illumination from different directions and at different frequencies can be used to create an image of the scattering distribution.

#### ■ 4.3.1 Array setup and modes of data collection

In order to derive the principles of imaging using a number of sources and a number of receivers, the setup shown in Fig. 4.25 is considered. The embedding background medium is given by an infinite homogeneous plate of known material properties.

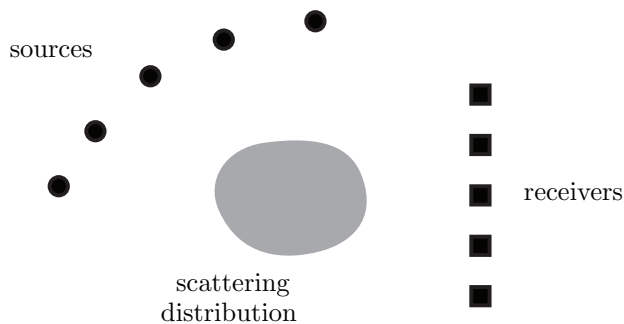


**Figure 4.25:** Setup for the imaging of a distribution of scatterers: a number of sources and receivers are positioned in a homogeneous background medium.

For reasons of simplicity, the sources at positions  $\underline{x}_s$  and receivers at positions  $\underline{x}_r$  are assumed to be omni-directional. Different experiments can be performed in order to measure the wave field and obtain information on the scatterer. Depending on the availability of receiver and sources, different configurations are possible:

- **Common receiver method**

The fields caused by a number of sources are measured at one receiver point.

- **Common source method**

The field caused by one source is measured at a number of receivers.

- **Zero-offset method**

One transducer or a closely spaced source-receiver pair is repositioned in the medium under investigation.

- **Total matrix method**

For a number of sources triggered successively, measurements are taken at a number of receivers.

The different possibilities of combining sources and receivers for imaging are illustrated in Fig. 4.26. Note that the principle of reciprocity applies, such that interchanging source and receivers provides exactly the same information on the wave field [Pierce 1989]. Different information is obtained only by measuring different paths of propagation. The *common source method* is therefore equivalent to the *common receiver method* if sources and receivers are swapped.

For the *total matrix method*, it is seen that some combinations of sources and receivers are redundant if the locations of sources and receivers coincide, thereby reducing the necessary number of measurements to be taken [Davies 2005]. On the other hand, the total matrix method retrieves less information on the wave field than a method using separate sources and receivers.

### ■ 4.3.2 Forward scattering

The basic equations describing the scattering of flexural waves have been introduced in Section 2.5.3. From Eq. 2.5.65, it can be seen that the scattered field at the receiver positions  $\underline{x}_r$  is given by the convolution of the Green's function and the contrast sources  $\tilde{w}(\underline{x}, \underline{x}_s, \omega)$ :

$$\begin{aligned} \tilde{f}(\underline{x}_r, \underline{x}_s, \omega) &= \tilde{u}_{sc}(\underline{x}_r, \underline{x}_s, \omega) = k_0^4 \int_{-\infty}^{\infty} \tilde{G}(\underline{x}_r, \underline{x}, \omega) \tilde{w}(\underline{x}, \underline{x}_s, \omega) d\underline{x} \\ &= k_0^4 \int_{-\infty}^{\infty} \tilde{G}(\underline{x}_r, \underline{x}, \omega) \tilde{u}(\underline{x}, \underline{x}_s, \omega) \chi(\underline{x}) d\underline{x}. \end{aligned} \quad (4.3.57)$$

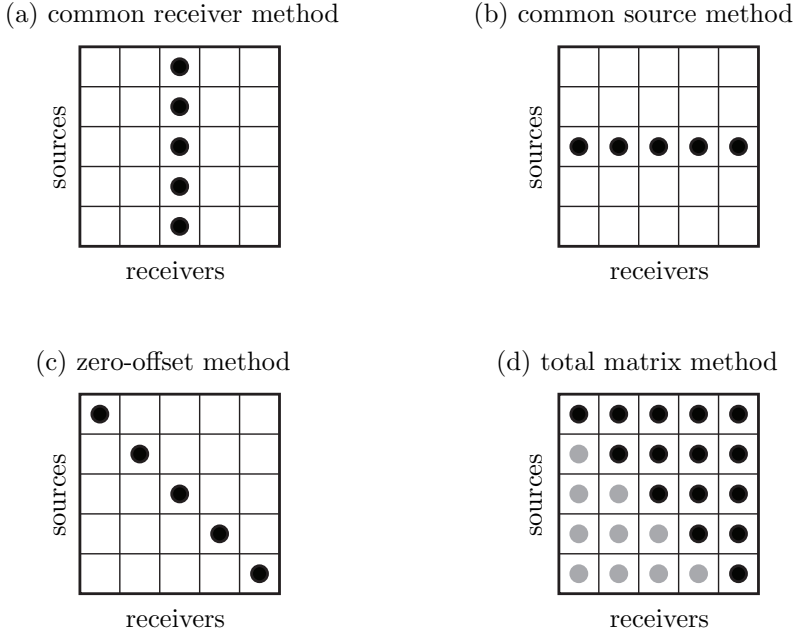


**Figure 4.26:** Different methods of using sources and receivers in order to obtain an image with acoustical or vibrational waves. For the total matrix method (d), some combinations (shown in grey) are redundant if source and receiver positions coincide.

The source position  $\underline{x}_s$  has been introduced in order to discriminate between fields and observations caused by illumination from different sources.

The scattered field is determined by both the contrast  $\chi(\underline{x})$  and the total field  $\tilde{u}(\underline{x}, \underline{x}_s, \omega)$ . The total field, in turn, is by definition the sum of the incident and the scattered field:

$$\tilde{u}_{\text{inc}}(\underline{x}, \underline{x}_s, \omega) + \mathcal{G}_D \mathcal{X} \tilde{u}(\underline{x}, \underline{x}_s, \omega) = \tilde{u}(\underline{x}, \underline{x}_s, \omega). \quad (4.3.58)$$

Here, two operators have been introduced:

- The operator  $\mathcal{G}_D$  describes a mapping from the source space  $S$  onto itself; it calculates the field caused by a given source distribution by convolution with the Green's function:

$$\mathcal{G}_D \tilde{w}(\underline{x}, \omega) = \int_{-\infty}^{\infty} \tilde{G}(\underline{x}, \underline{x}_0, \omega) \tilde{w}(\underline{x}_0, \omega) d\underline{x}_0. \quad (4.3.59)$$

- The contrast operator  $\mathcal{X}$  performs a multiplication by the scattering potential:

$$\mathcal{X}\tilde{u}(\underline{x}, \underline{x}_s, \omega) = \tilde{\Phi}(\underline{x}, \omega)\tilde{u}(\underline{x}, \underline{x}_s, \omega). \quad (4.3.60)$$

This leads to the following equation for the total field  $\tilde{u}(\underline{x}, \underline{x}_s, \omega)$ :

$$(\mathcal{I} - \mathcal{G}_D \mathcal{X}) \tilde{u}(\underline{x}, \underline{x}_s, \omega) = \tilde{u}_{\text{inc}}(\underline{x}, \underline{x}_s, \omega). \quad (4.3.61)$$

If the incident field and the contrast are known, Eq. 4.3.61 can be solved for  $\tilde{u}(\underline{x}, \underline{x}_s, \omega)$  by application of a conjugate gradient scheme, for instance. The adjoint operator for application of the CG scheme to the normal equations is given in Appendix D.4.3.

#### 4.3.2.1 Neumann series expansion of the forward scattering operator

The forward scattering operator shown in Eq. 4.3.61 can be expanded into a Neumann series [Debnath 2005]:

$$\tilde{u}(\underline{x}, \underline{x}_s, \omega) = (\mathcal{I} - \mathcal{G}_D \mathcal{X})^{-1} \tilde{u}_{\text{inc}}(\underline{x}, \underline{x}_s, \omega) = \sum_{n=0}^{\infty} (\mathcal{G}_D \mathcal{X})^n \tilde{u}_{\text{inc}}(\underline{x}, \underline{x}_s, \omega). \quad (4.3.62)$$

In this representation, it can easily be seen that an infinite order of scattering due to the contrast represented by  $\mathcal{X}$  is taken into account. However, Eq. 4.3.62 must be interpreted as a formal solution: the inverse may not exist, and the Neumann series does not necessarily converge.

If the medium under investigation is strongly damped, it might be sufficient to include only a few orders of scattering in the model. In the general case, however, the full scattering problem has to be solved.

### ■ 4.3.3 Inverse scattering and the Born approximation

In the inverse scattering problem, it is desired to estimate the contrast function  $\chi(\underline{x})$  based on knowledge of the incident field  $\tilde{u}_{\text{inc}}(\underline{x}, \underline{x}_s, \omega)$  and the receiver signals  $f(\underline{x}_r, \underline{x}_s, \omega)$ . In this case, both the contrast and the total field are unknown. The implicit relation between the total field and the contrast makes the inverse problem nonlinear. In the present chapter, it is chosen to use a linearised approximation for imaging of the scattering distribution. Chapter 5 will deal with techniques for solving the full nonlinear problem.

If the scattering is weak, the amplitude of the scattered field can be expected to be significantly lower than the amplitude of the incident field. Therefore, a common linearisation is given by the *Born approximation*, which assumes that the total field inside the scattering object can be approximated by the incident field [De Hoop 1995]:

$$\tilde{u}(\underline{x}, \underline{x}_s, \omega) \approx \tilde{u}_{\text{inc}}(\underline{x}, \underline{x}_s, \omega). \quad (4.3.63)$$

Equation 4.3.58 is then adapted to include only first-order scattering:

$$\tilde{u}_{\text{inc}}(\underline{x}, \underline{x}_s, \omega) + \mathcal{G}_D \mathcal{X} \tilde{u}_{\text{inc}}(\underline{x}, \underline{x}_s, \omega) \approx \tilde{u}(\underline{x}, \underline{x}_s, \omega). \quad (4.3.64)$$

It becomes evident that the Born approximation establishes a linear relation between the contrast and the receiver signals for a given incident field. The receiver signals can be expressed in terms of the *Born measurement operator*  $\mathcal{G}_X$ :

$$\tilde{f}(\underline{x}_r, \underline{x}_s, \omega) = \mathcal{G}_X \chi(\underline{x}) = k_0^4 \int_{-\infty}^{\infty} \tilde{G}(\underline{x}_r, \underline{x}, \omega) \tilde{u}_{\text{inc}}(\underline{x}, \underline{x}_s, \omega) \chi(\underline{x}) \, d\underline{x}. \quad (4.3.65)$$

Thus, the incident field is scattered once by the material inhomogeneities, and the resulting field is picked up by the receivers. The contrast function can formally be obtained by inversion of this equation:

$$\chi(\underline{x}) = \left( \mathcal{G}_X^\dagger \mathcal{G}_X \right)^{-1} \mathcal{G}_X^\dagger \tilde{f}(\underline{x}_r, \underline{x}_s, \omega). \quad (4.3.66)$$

The problem of imaging a distribution of scatterers can, in many aspects, be approached as the problem of imaging of a source distribution presented in Section 4.2.2. For instance, a resolution operator  $\mathcal{R}_X$  for imaging of the contrast function can be defined analogously to Eq. 4.2.23:

$$\mathcal{R}_X = \mathcal{G}_X^\dagger \mathcal{G}_X. \quad (4.3.67)$$

#### ■ 4.3.4 Imaging by backpropagation

A first approximation to the solution is obtained by backpropagation, i.e., the application of the adjoint operator  $\mathcal{G}_X^\dagger$  to the receiver signals. The derivation of the adjoint operator is presented in Appendix D.4.1 and leads to the following expression:

$$\chi(\underline{x})_{\text{adj}} = \mathcal{G}_X^\dagger \tilde{f}(\underline{x}_r, \underline{x}_s, \omega) = \int_{-\infty}^{\infty} k_0^4 \sum_{s=1}^{N_s} \tilde{u}_{\text{inc}}^*(\underline{x}, \underline{x}_s, \omega) \left[ \sum_{r=1}^{N_r} \tilde{G}^*(\underline{x}_r, \underline{x}, \omega) \tilde{f}(\underline{x}_r, \underline{x}_s, \omega) \right] \, d\omega. \quad (4.3.68)$$

Note that the inner part of this equation in square brackets represents the adjoint of the problem of imaging a source distribution as shown in Eq. 4.2.22. This means that the problem of imaging an inhomogeneity in the material actually consists of two subproblems:

- (1) The receiver signals are used to estimate the distribution of contrast sources.
- (2) The contrast sources are related to the incident field in order to determine the contrast.

For the first problem, the results from Section 4.2.6 can be used in order to determine an estimate of the contrast sources  $\tilde{w}_{\text{est}}(\underline{x}, \underline{x}_s, \omega)$  using the appropriate frequency-dependent weighting function  $\alpha(\omega)$ . The adjoint of the operator  $\mathcal{G}_X$  is then given by the following expression:

$$\chi(\underline{x})_{\text{adj}} = \int_{-\infty}^{\infty} k_0^4 \sum_{s=1}^{N_s} \tilde{u}_{\text{inc}}^*(\underline{x}, \underline{x}_s, \omega) \tilde{w}(\underline{x}, \underline{x}_s, \omega) d\omega. \quad (4.3.69)$$

This equation represents the *imaging condition*, i.e., it describes how the image of the contrast is generated from the known incident field  $\tilde{u}_{\text{inc}}(\underline{x}, \underline{x}_s, \omega)$  and the estimated contrast sources  $\tilde{w}(\underline{x}, \underline{x}_s, \omega)$ . An interpretation can be given in time domain: in the case of backpropagation, the image is obtained by performing a cross-correlation of contrast sources and incident field, from which the sample at time  $t = 0$  is retained [Sava 2006].

This result can be improved further. According to the Born approximation, the contrast sources are formed by multiplication of the contrast function and the incident field:

$$\tilde{w}(\underline{x}, \underline{x}_s, \omega) = k_0^4 \tilde{u}_{\text{inc}}(\underline{x}, \underline{x}_s, \omega) \chi(\underline{x}). \quad (4.3.70)$$

Equation 4.3.69 represents the adjoint of this operation, which is also derived in Appendix D.2. A better estimate of the contrast can be obtained by inverting the equation by minimising the following functional [Van den Berg 1999]:

$$\chi(\underline{x})_{\text{est}} = \arg \min_{\chi(\underline{x})} \left\| \tilde{w}(\underline{x}, \underline{x}_s, \omega) - k_0^4 \tilde{u}_{\text{inc}}(\underline{x}, \underline{x}_s, \omega) \chi(\underline{x}) \right\|_{S, \omega}^2. \quad (4.3.71)$$

If there is a significant variation in the amplitude of the field or contrast sources for different frequencies, the above approach will yield suboptimal results since frequencies present with high strength will have a stronger influence on the optimisation. Therefore, it is advisable to divide by the magnitude of the incident field, assuming that all frequencies considered can equally contribute to a solution:

$$E[\chi(\underline{x})] = \int_{-\infty}^{\infty} \int_{-\infty}^{\infty} \frac{\sum_{s=1}^{N_s} |\tilde{w}(\underline{x}, \underline{x}_s, \omega) - k_0^4(\omega) \tilde{u}_{\text{inc}}(\underline{x}, \underline{x}_s, \omega) \chi(\underline{x})|^2}{\sum_{s=1}^{N_s} |k_0^4(\omega) \tilde{u}_{\text{inc}}(\underline{x}, \underline{x}_s, \omega)|^2} d\underline{x} d\omega \quad (4.3.72)$$

The result of this least-squares problem is derived in Appendix E and given by Eq. E.5:

$$\chi(\underline{x})_{\text{est}} = \frac{1}{\Omega} \int_{-\infty}^{\infty} \frac{\sum_{s=1}^{N_s} \tilde{w}(\underline{x}, \underline{x}_s, \omega) \tilde{u}_{\text{inc}}^*(\underline{x}, \underline{x}_s, \omega)}{k_0^4(\omega) \sum_{s=1}^{N_s} |\tilde{u}_{\text{inc}}(\underline{x}, \underline{x}_s, \omega)|^2} d\omega, \quad (4.3.73)$$

with  $\Omega$  representing the spectral bandwidth:

$$\Omega = \int_{-\infty}^{\infty} d\omega. \quad (4.3.74)$$

In this case, it can be seen that the imaging condition of cross-correlation has been replaced by deconvolution. The intention behind the deconvolution is the removal of the imprint of the spectrum of the incident field. Effectively, the source spectrum is whitened, leading to a compact source signal in the time domain. This is advantageous for improving the resolution of the resulting image.

Instead of showing results for the different imaging methods separately, it is chosen to present images obtained using different methods in Section 4.3.7 for comparison.

### ■ 4.3.5 Spectral analysis of the achievable resolution

Analogously to Section 4.2.2, the operator  $\mathcal{G}_X$  can be analysed in the wavenumber-frequency domain in order to assess the spatial resolution that can be obtained by imaging. In this domain, the forward operator  $\mathcal{G}_X$  is given by the following equation:

$$\tilde{f}(\underline{x}_r, \underline{x}_s, \omega) = \mathcal{G}_X \tilde{\chi}(\underline{k}) = k_0^4 \int_{-\infty}^{\infty} e^{-j\underline{k} \cdot \underline{x}_r} \tilde{\tilde{G}}(\underline{k}, \omega) \left\{ \left[ \tilde{S}(\omega) \tilde{\tilde{G}}(\underline{k}, \omega) e^{j\underline{k} \cdot \underline{x}_s} \right] * \tilde{\chi}(\underline{k}) \right\} d\underline{k}, \quad (4.3.75)$$

with the asterisk denoting convolution in the wavenumber-frequency domain and the incident field being expressed in terms of the Green's function, the source spectrum and the position of the sources:

$$\tilde{u}_{\text{inc}}(\underline{k}, \underline{x}_s, \omega) = \tilde{S}(\omega) \tilde{\tilde{G}}(\underline{k}, \omega) e^{j\underline{k} \cdot \underline{x}_s}. \quad (4.3.76)$$

Equation 4.3.75 can be rearranged to have the following preferred form for analysis of the wavenumber-frequency spectrum, see Appendix D.4.2:

$$\tilde{f}(\underline{x}_r, \underline{x}_s, \omega) = \mathcal{G}_X \tilde{\chi}(\underline{k}) = k_0^4 \tilde{S}(\omega) \int_{-\infty}^{\infty} \tilde{\chi}(\underline{k}) \left\{ \left[ \tilde{\tilde{G}}(\underline{k}, \omega) e^{-j\underline{k} \cdot \underline{x}_r} \right] * \left[ \tilde{\tilde{G}}(\underline{k}, \omega) e^{-j\underline{k} \cdot \underline{x}_s} \right] \right\} d\underline{k}. \quad (4.3.77)$$

As can be seen, the received signal is thus determined by the expression in curly brackets representing a filter in the wavenumber-frequency domain, for which a new variable is introduced:

$$\tilde{\Psi}(\underline{k}, \underline{x}_r, \underline{x}_s, \omega) = \left[ \tilde{\tilde{G}}(\underline{k}, \omega) e^{-j\underline{k} \cdot \underline{x}_r} \right] * \left[ \tilde{\tilde{G}}(\underline{k}, \omega) e^{-j\underline{k} \cdot \underline{x}_s} \right]. \quad (4.3.78)$$

From a physical point of view, this filter describes a combination of the incident and the received field for a certain combination of source, receiver and frequency.

The corresponding adjoint operator  $\mathcal{G}_X^\dagger$  is derived in Appendix D.4.2 and given by the following expression:

$$\begin{aligned}
 & \mathcal{G}_X^\dagger \tilde{f}(\underline{x}_r, \underline{x}_s, \omega) \\
 &= \int_{-\infty}^{\infty} k_0^4 \tilde{S}^*(\omega) \sum_{s=1}^{N_s} \sum_{r=1}^{N_r} \tilde{f}(\underline{x}_r, \underline{x}_s, \omega) \left\{ \left[ \tilde{G}^*(\underline{k}, \omega) e^{j\underline{k} \cdot \underline{x}_r} \right] * \left[ \tilde{G}^*(\underline{k}, \omega) e^{j\underline{k} \cdot \underline{x}_s} \right] \right\} d\omega \\
 &= \int_{-\infty}^{\infty} k_0^4 \tilde{S}^*(\omega) \sum_{s=1}^{N_s} \sum_{r=1}^{N_r} \tilde{f}(\underline{x}_r, \underline{x}_s, \omega) \tilde{\Psi}^*(\underline{k}, \underline{x}_r, \underline{x}_s, \omega) d\omega.
 \end{aligned} \tag{4.3.79}$$

Based on this result, the resolution operator  $\mathcal{R}_X$  being the composition of the forward operator and the adjoint operator can be written in compact form:

$$\begin{aligned}
 \mathcal{R}_X &= \mathcal{G}_X^\dagger \mathcal{G}_X \\
 &= \int_{-\infty}^{\infty} k_0^8 \left| \tilde{S}(\omega) \right|^2 \sum_{s=1}^{N_s} \sum_{r=1}^{N_r} \tilde{\Psi}^*(\underline{k}_1, \underline{x}_r, \underline{x}_s, \omega) \int_{-\infty}^{\infty} \tilde{\Psi}(\underline{k}, \underline{x}_r, \underline{x}_s, \omega) \tilde{\chi}(\underline{k}) d\underline{k} d\omega.
 \end{aligned} \tag{4.3.80}$$

Note that the structure of this result is similar to Eq. 4.2.30 describing the achievable resolution for the imaging of a source distribution.

Hence, the imaging of a scattering distribution using backpropagation can be described by the following steps, analogue to the imaging of a source distribution as derived in Section 4.2.2:

- (1) The wavenumber spectrum of the scattering distribution  $\tilde{\chi}(\underline{k})$  is decomposed in terms of spectral filters  $\tilde{\Psi}(\underline{k}, \underline{x}_r, \underline{x}_s, \omega)$  formed by certain combinations of source, receiver and frequency.
- (2) The receiver signals  $\tilde{f}(\underline{x}_r, \underline{x}_s, \omega)$  form the ‘coefficients’ of this decomposition.
- (3) The reconstruction by the adjoint operator is performed by superposition of the spectral filters  $\tilde{\Psi}(\underline{k}, \underline{x}_r, \underline{x}_s, \omega)$  weighted by the receiver signals.

Furthermore, Eq. 4.3.80 shows that there are two frequency-dependent terms having particular influence on the achievable resolution: the source spectrum  $\tilde{S}(\omega)$  and the wavenumber of the background medium  $k_0$ . By performing a deconvolution with respect to the source spectrum and application of a frequency-dependent weighting

to compensate for the influence of  $k_0$ , the resolution can be improved – independently of the position of sources and receivers.

Therefore, the filter set  $\tilde{\Psi}(k, \underline{x}_r, \underline{x}_s, \omega)$  for a certain source-receiver setup can be interpreted as basis functions of a decomposition and can thus be referred to as *image decomposition filter*. Analysis of a given set of filters can be expected to provide information on the ability to reconstruct a certain scattering distribution from the measured receiver signals. The obtainable resolution in imaging depends on the position of the sources and receivers, as well as on the frequencies used for imaging.

#### 4.3.5.1 Coverage of the wavenumber spectrum

One of the most important limitations in imaging under the Born approximation can directly be derived from the structure of the image decomposition filter. As can be seen from Eq. 4.3.78, the filter is formed by the convolution of the Green's function with itself, yet under different modulations of the phase due to the exponential functions. Assuming the optimal case in which only constructive interference between the two convolved parts is given, it can be seen that the maximum theoretical range of wavenumbers considered in the imaging process is given by the auto-convolution of the Green's function in the wavenumber domain.

In Section 4.2.3, it has been shown that wavenumber components outside the circle of radius  $k_P$  are so small that they cannot contribute to the image. Hence, for the auto-convolution of the Green's function, all wavenumbers with relevant contribution can be found inside the circle of radius  $2k_P$ , which is the Ewald's circle for the scattering field as illustrated in Figure 4.27. The maximal spatial resolution that can be obtained under the Born approximation is thus limited to about half a wavelength [Wolf 1969]. Note that this resolution is twice as high as the resolution achievable for the imaging of a source distribution.

There are some special configurations of sources and receivers that are interesting to analyse in this context. For zero-offset imaging, for instance, the locations of source and receiver coincide:

$$\underline{x}_r = \underline{x}_s = \underline{x}_{r,s}. \quad (4.3.81)$$

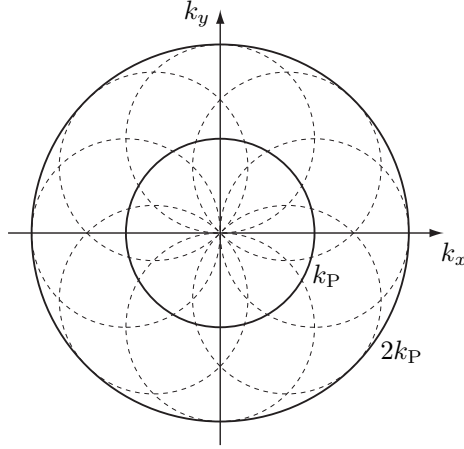


**Figure 4.27:** The auto-convolution of a spectrum with maximum wavenumber  $k_P$  leads to a spectrum with maximum wavenumber  $2k_P$ .

The image decomposition filter  $\tilde{\tilde{\Psi}}(\underline{k}, \underline{x}_r, \underline{x}_s, \omega)$  can thus be simplified:

$$\begin{aligned}
 \tilde{\tilde{\Psi}}_{\text{zero-offset}}(\underline{k}, \underline{x}_r, \underline{x}_s, \omega) &= \left[ \tilde{\tilde{G}}(\underline{k}, \omega) e^{-j\underline{k} \cdot \underline{x}_{r,s}} \right] * \left[ \tilde{\tilde{G}}(\underline{k}, \omega) e^{-j\underline{k} \cdot \underline{x}_{r,s}} \right] \\
 &= \int_{-\infty}^{\infty} \tilde{\tilde{G}}(\underline{k}_1 - \underline{k}, \omega) e^{-j(\underline{k}_1 - \underline{k}) \cdot \underline{x}_{r,s}} \tilde{\tilde{G}}(\underline{k}, \omega) e^{-j\underline{k} \cdot \underline{x}_{r,s}} d\underline{k} \\
 &= e^{-j\underline{k} \cdot \underline{x}_{r,s}} \left[ \tilde{\tilde{G}}(\underline{k}, \omega) * \tilde{\tilde{G}}(\underline{k}, \omega) \right].
 \end{aligned} \tag{4.3.82}$$

This representation of the filter confirms the wavenumber limit derived above: the maximum wavenumber components are determined by the auto-convolution of the Green's function in the wavenumber domain and can be found inside the circle of radius  $2k_P$ . Since the strongest spectral components of the Green's function belonging to propagating waves can be found on the circle of radius  $k_P$ , the simplified image decomposition filter derived in Eq. 4.3.82 has the strongest spectral components on the Ewald's circle of radius  $2k_P$ .

The filter is modulated by an exponential function according to the position of source and receiver. Different directions of illumination and reception provide a set of basis functions in the wavenumber domain that decompose the spectrum of

the contrast function  $\tilde{\chi}(\underline{k})$ . A combination of these decompositions is required to reconstruct the contrast function with sufficient accuracy. This illustrates the need for *measurement diversity* in order to obtain information on different parts of the wavenumber spectrum [Langenberg 2002].

The requirement of diversity can best be derived from the far-field expressions of the incident and the received field. For high distance of source and receiver from the scattering object, the modulated Green's functions in Eq. 4.3.78 can be replaced by plane waves with directions dependent on the location of source or receiver. The vectors  $\underline{k}_r$  and  $\underline{k}_s$  are introduced to represent the wavenumber vectors associated with plane waves for certain directions of incidence and reception:

$$\underline{k}_r = k_P \frac{\underline{x}_r}{|\underline{x}_r|}, \quad \underline{k}_s = k_P \frac{\underline{x}_s}{|\underline{x}_s|}. \quad (4.3.83)$$

Furthermore, for coincident source and receiver location, the following wavenumber vector for the far-field approximation is defined:

$$\underline{k}_{r,s} = k_P \frac{\underline{x}_{r,s}}{|\underline{x}_{r,s}|}. \quad (4.3.84)$$

A far-field expression for the image decomposition filter is then readily derived:

$$\begin{aligned} \tilde{\Psi}_{\text{far-field}}(\underline{k}, \underline{x}_r, \underline{x}_s, \omega) &= \delta(\underline{k} + \underline{k}_r) * \delta(\underline{k} + \underline{k}_s) \\ &= \delta(\underline{k} + \underline{k}_r + \underline{k}_s). \end{aligned} \quad (4.3.85)$$

The filter  $\tilde{\Psi}_{\text{far-field}}(\underline{k}, \underline{x}_r, \underline{x}_s, \omega)$  is represented by a single Dirac delta pulse in the wavenumber domain, meaning that one combination of angle of incidence and angle of reception for a certain frequency can only provide information on a single point in the wavenumber spectrum if the scattering object is imaged from the far-field.

The range of obtainable wavenumber components is determined by the addition of the wavenumber vectors for the incident and the receiving wave field; the maximum wavenumber components of radius  $2k_P$  are obtained only for zero offset between source and receiver as illustrated in Fig. 4.28(a). In this case, the image decomposition filter is given by the following expression:

$$\tilde{\Psi}_{\text{zero-offset, far-field}}(\underline{k}, \underline{x}_r, \underline{x}_s, \omega) = \delta(\underline{k} + 2\underline{k}_{r,s}). \quad (4.3.86)$$

Increasing the angle between incident and received field results in an image decomposition filter containing lower wavenumber components. For a single direction of incidence  $-\underline{k}_s$ , the figure shows that the wavenumber components that can be received from different directions in the far-field are found on the Ewald's sphere of radius  $k_P$  centred at  $-\underline{k}_s$  [Langenberg 2002].

Hence, in the case of common source or common receiver imaging from the far-field, all wavenumber components are found on a circle of radius  $k_P$  passing through the

origin of the wavenumber spectrum. This illustrates the fact that for one direction of incidence, only little information on the wavenumber spectrum of the scattering object can be obtained. The usage of different frequencies, for instance, can then help to improve the coverage of the wavenumber spectrum.

Examples for incident fields from different angles are shown in Fig. 4.28(b). The angle  $\varphi$  between the directions of incidence and reception is kept constant, a mode of imaging that exhibits a constant angular offset between source and receiver. Two typical cases are shown: for an angle of  $\varphi = 90^\circ$  between incident and scattered plane wave, only wavenumber components of fixed magnitude  $\sqrt{2} k_P$  can be imaged in the far-field.

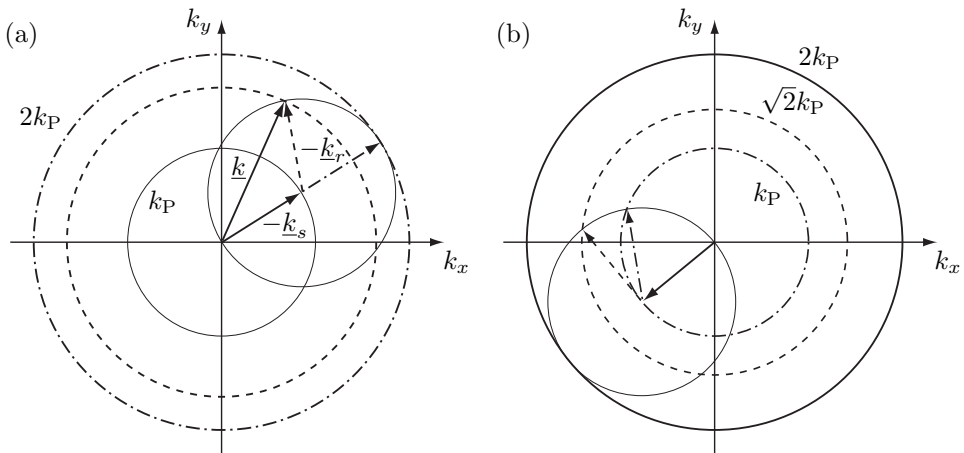


**Figure 4.28:** Wavenumber components obtained by imaging in the far-field; (a) comparison between arbitrary angle between incident and receiving field (dashed) and zero-offset imaging (dash-dot line); (b) special cases with angles of  $\varphi = 90^\circ$  (dashed) and  $\varphi = 120^\circ$  (dash-dot line) between the direction of incidence and reception providing wavenumber components with absolute value  $\sqrt{2} k_P$  and  $k_P$ , respectively.

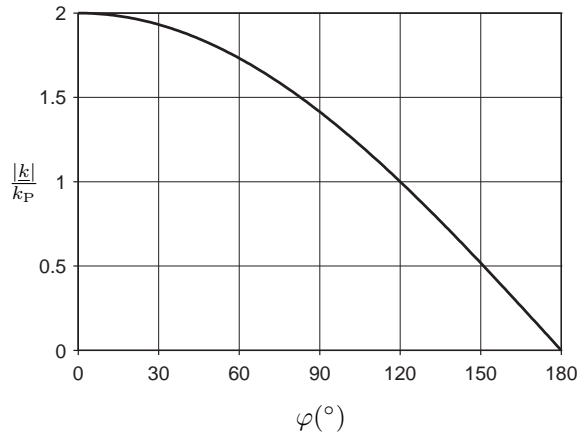
Furthermore, the geometrical construction of Fig. 4.28 shows that the magnitude  $|\underline{k}|$  of a wavenumber component for a certain angle  $\varphi$  between incident and scattered plane wave is given by the following equation:

$$|\underline{k}| = 2k_P \cos \frac{\varphi}{2}. \quad (4.3.87)$$

Hence, the angular difference  $\varphi$  between  $\underline{k}_r$  and  $\underline{k}_s$  needed for a wavenumber component of desired magnitude  $|\underline{k}|$  can easily be determined:

$$\varphi = 2 \arccos \frac{|\underline{k}|}{2k_P}. \quad (4.3.88)$$

As an example, Fig. 4.28(b) shows the circle of wavenumber components with magnitude  $k_P$  obtained for  $\varphi = 120^\circ$  from the above equation. The general relation between the angular offset  $\varphi$  and the magnitude  $|\underline{k}|$  of wavenumber components in the image decomposition filter is depicted in Fig. 4.29.




---

**Figure 4.29:** Relation between the angle  $\varphi$  between incident and scattered plane wave for imaging in the far-field and the magnitude  $|\underline{k}|$  of the wavenumber components covered by the image decomposition filter.

---

It can be seen that for a small angular offset  $\varphi$  between source and receiver, only high wavenumber components are involved in the imaging process, whereas for source and receiver on opposite sides of a scattering object, wavenumber components of low magnitude can be reconstructed. This result is well-known in the field of seismic imaging [Berkhout 1987].

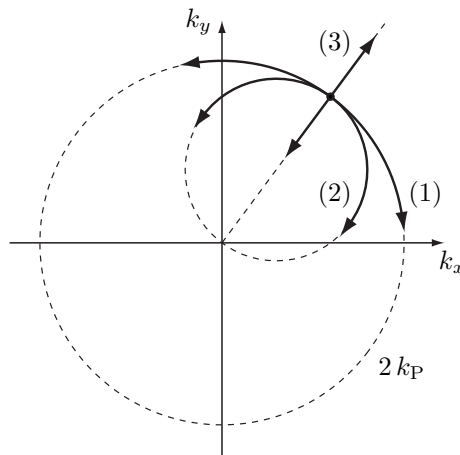
With respect to the coverage of the wavenumber spectrum, several conclusions can be drawn:

- (1) Different directions of illumination and detection are needed for sufficient coverage in the angular direction of the wavenumber domain.
- (2) Different angular offsets between source and receiver can be used to cover both different angular and different radial positions in the wavenumber domain.
- (3) Different frequencies can be used to cover different radial positions in the wavenumber domain.

For a given coincident source-receiver pair in zero-offset mode, for instance, there are three options for obtaining an image decomposition filter with different wavenumber content, corresponding to the above conclusions:

- (1) Both source and receiver are moved by the same angular offset.
- (2) The angular position of the source or receiver is changed while keeping the other fixed.
- (3) The frequency is changed.

Figure 4.30 illustrates the corresponding changes in the wavenumber domain.




---

**Figure 4.30:** Shift of the peak in the far-field spectral decomposition filter due to three different changes of the imaging setup: (1) equal shift of the angular position of source and receiver, (2) shift of the angular position of source or receiver, (3) shift of the frequency; the change is shown in comparison to the zero-offset situation.

---

For practical applications, it is usually advisable to combine the above strategies, i.e., to

- use a large angular aperture,
- combine sources and receivers with different angular offsets, and
- make use of information available at different frequencies.

Furthermore, the array setup can be chosen to achieve optimal sensitivity for a certain type of inhomogeneity. For the detection of smooth variations in material properties, for instance, the inclusion of the low wavenumber spectrum is essential. From the above derivation, it can be seen that a tomographic setup, i.e., sources and receivers at opposite sides of the imaging region, can help to improve the coverage of the lower part of the spectrum in this case. For the detection of sharp transitions in material parameters, on the other hand, the higher part of the wavenumber spectrum plays an important role. In this case, a transducer setup with both sources and receivers at the same side of the imaging region facilitates the formation of a well-resolved image.

The findings presented in this section can serve as a tool to estimate the benefit of different array setups with respect to the coverage of the wavenumber spectrum. It is, of course, to be expected that there arise situations in which the choice of the array and imaging setup is limited by factors such as hardware costs and size, frequency-dependent damping, or processing time. Under all these circumstances, a compromise degrading the resolution of the image might be required.

#### ■ 4.3.6 Inversion

Having established the equations describing the maximum resolution that can be obtained for the imaging of a scattering distribution, it is necessary to deal with methods that can fully utilise this potential. The resolution operator  $\mathcal{R}_X$  derived above describes the resolution obtainable by backpropagation, as well as the approximate range of the wavenumber spectrum above the noise level, i.e., the range that can be used for inversion.

As in the case of imaging of a source distribution, an iterative method such as a conjugate gradient scheme can be used to obtain an estimate of the contrast function. The error functional to be minimised is given by the difference of the measured receiver signals and the result of applying the forward operator to the estimate of the contrast:

$$\chi_{\text{est}}(\underline{x}) = \arg \min_{\chi(\underline{x})} \left\| \tilde{f}(\underline{x}_r, \underline{x}_s, \omega) - \mathcal{G}_X \chi(\underline{x}) \right\|_{R, \omega}^2. \quad (4.3.89)$$

From the analysis of the operator  $\mathcal{G}_X$  in the wavenumber-frequency domain, it is clear that application of a conjugate gradient scheme cannot provide a perfect physical reconstruction as suggested by the formal inversion of the problem (Eq. 4.3.66). Instead, it is necessary to tackle an ill-posed problem that has to be stabilised and regularised to deal with small eigenvalues of the operator  $\mathcal{G}_X$  and obtain a useful solution.

The idea behind regularisation methods related to the energy or  $L^2$ -norm of the solution, such as the standard Tikhonov regularisation, has already been discussed

in Section 4.2.8.2. In the following, two other methods of regularisation that are suitable for the imaging problem will be introduced.

It has been established that there are regions in the wavenumber spectrum of the unknown contrast function  $\tilde{\chi}(\underline{k})$  that cannot be retrieved from the data: spectral components in these regions have marginal influence on the receiver signals and are usually masked by noise, which makes their reconstruction impossible. Hence, these values of the unknown function cannot be estimated from the data. Minimum norm regularisation neglects these values by setting them to a low level to avoid disturbance of the estimated solution. Another approach, however, is to fill in these regions with values that complement the known part of the solution. Since there is no reliable information from the *data* available, the solution has to be complemented with values that fit a certain *model*, i.e., a priori knowledge on the structure of the solution. Examples of such methods for regularisation suitable for imaging are presented in the following two sections.

#### 4.3.6.1 Regularisation by a sparseness constraint

One of the possible modelling assumptions for image formation has already been presented in Section 3.7.1.2 in the context of estimating the dispersion relation from measured data: the sparseness assumption. This model can also be applied as an imaging constraint if it can be justified that the unknown contrast function contains only a few significant values at a limited number of positions. Especially with respect to the detection of defects, this assumption seems to be reasonable. The usage of sparseness constraints has a long history in the field of seismic data processing, in which measures and methods to introduce sparseness have been developed and refined for several decades.

Ideally, the sparseness of a discrete vector or matrix is determined by the  $L^0$ -norm, i.e., the number of non-zero entries. However, direct minimisation of the number of non-zero entries leads to an intractable nonconvex optimisation problem [Donoho 2006]. Fortunately, other constraints promoting sparseness such as the  $L^1$ -norm can be shown to achieve almost equal performance [Donoho 2008]. Classical norms for sparse regularisation include the  $L^p$ -norm for  $p < 1$ , as well as norms related to signal entropy [Karvanen 2003]. Entropy norms have successfully been used for seismic data processing in the context of deconvolution [Wiggins 1978] and velocity estimation [De Vries 1984]. An overview of different penalty functions for sparse regularisation was given by Zwartjes [Zwartjes 2005].

The difference between the minimum energy norm and sparse regularisation can easily be illustrated by comparing the regularisation constraints for the unknown contrast function  $\chi(\underline{x})$  using the  $L^2$ - and the  $L^1$ -norm.

The error functionals are given by the following expressions:

$$E_{L^2} [\chi(\underline{x})] = \int_{-\infty}^{\infty} |\chi(\underline{x})|^2 \, d\underline{x} \quad (4.3.90)$$

$$E_{L^1} [\chi(\underline{x})] = \int_{-\infty}^{\infty} |\chi(\underline{x})| \, d\underline{x}. \quad (4.3.91)$$

The gradient of the error functionals known as the *influence function* shows how the contrast  $\chi(\underline{x})$  has to be modified in order to get closer to a minimum, since a minimisation step is taken in the direction of the negative gradient:

$$\frac{\partial E_{L^2}(\chi)}{\partial \chi} = 2\chi(\underline{x}) \quad (4.3.92)$$

$$\frac{\partial E_{L^1}(\chi)}{\partial \chi} = \text{sgn } \chi(\underline{x}). \quad (4.3.93)$$

For the  $L^2$ -norm, the influence function is proportional to the contrast  $\chi$ , meaning that its elements are affected by the minimisation according to their magnitude: high values are pulled towards zero with higher strength than low values. The  $L^1$ -norm, on the contrary, exhibits equal influence for values of all magnitudes, such that small levels of  $\chi$  are driven faster towards zero than high ones [Bishop 2006]. Figure 4.31 illustrates this difference for a typical distribution.

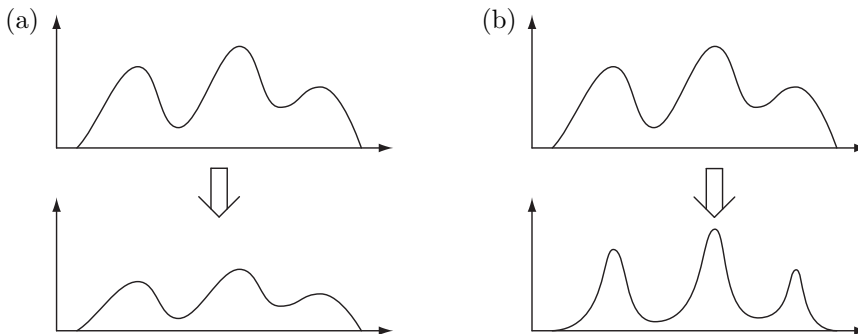


**Figure 4.31:** Influence of  $L^2$ -norm regularisation (a) and  $L^1$ -norm regularisation (b) on an arbitrary distribution; the  $L^2$ -norm regularisation scales the distribution in its entirety to minimise the energy, the  $L^1$ -norm regularisation emphasises peak values.

This idea forms the basis of norms promoting sparseness: the gradient of the penalty function should either be independent of the magnitude of the contrast function  $\chi(\underline{x})$  as for the  $L^1$ -norm, or, to force sparseness on the result, take higher values when the contrast is small. In the following, the Cauchy norm complying with the latter condition will be used. This norm has the advantage of being continuously differentiable, in contrast to the  $L^1$ -norm.

The Cauchy regulariser was introduced by Sacchi and Ulrych in order to obtain a sparse result for the Radon transform [Sacchi 1995]. It was derived by assuming the variable to be estimated to obey a Cauchy distribution, i.e., a probability distribution of the following form:

$$p(\chi, \sigma_\chi) \propto \frac{1}{1 + \frac{|\chi(\underline{x})|^2}{2\sigma_\chi^2}}, \quad (4.3.94)$$

with  $\sigma_\chi$  being a parameter determining the shape of the tail of the distribution.

The regularising penalty term is given by the following expression:

$$E_{\text{sparse}}(\underline{x}) = \int_{-\infty}^{\infty} \ln \left[ 1 + \frac{|\chi(\underline{x})|^2}{2\sigma_\chi^2} \right] d\underline{x}. \quad (4.3.95)$$

For the imaging of a contrast function, the following error functional can be used to perform optimisation including the additive penalty of the Cauchy regulariser  $E_{\text{sparse}}(\underline{x})$ :

$$E = \frac{1}{2\sigma_n^2} \left\| \tilde{f}(\underline{x}_r, \underline{x}_s, \omega) - \mathcal{G}_X \chi(\underline{x}) \right\|_{R, \omega}^2 + \gamma \int_{-\infty}^{\infty} \ln \left[ 1 + \frac{|\chi(\underline{x})|^2}{2\sigma_\chi^2} \right] d\underline{x}, \quad (4.3.96)$$

with  $\gamma$  being a regularisation parameter. The measurement noise is assumed to obey a normal distribution with zero mean and variance  $\sigma_n^2$ . The parameter  $\sigma_\chi$  can be used to control the desired level of sparseness in the solution.

Derivation of the error functional  $E$  with respect to the contrast and equating to zero yields the following solution for the contrast:

$$\chi_{\text{est}}(\underline{x}) = \left[ \mathcal{G}_X^\dagger \mathcal{G}_X + \gamma \mathcal{Q}(\underline{x})^{-1} \right]^{-1} \mathcal{G}_X^\dagger \tilde{f}(\underline{x}_r, \underline{x}_s, \omega), \quad (4.3.97)$$

with  $\gamma = \sigma_n^2 / \sigma_\chi^2$ , and  $\mathcal{Q}(\underline{x})$  being the diagonal sparseness operator:

$$\mathcal{Q}(\underline{x}) = 1 + \frac{|\chi(\underline{x})|^2}{2\sigma_\chi^2}. \quad (4.3.98)$$

There are two problems associated with this formal solution:

- Since the operator  $\mathcal{Q}(\underline{x})$  depends on the solution  $\chi(\underline{x})$ , Eq. 4.3.97 cannot be solved in closed form.
- Furthermore, it is not obvious how the two parameters  $\gamma$  and  $\sigma_\chi$  have to be chosen in order to obtain the desired result.

In order to tackle the first problem, Eq. 4.3.97 is solved by application of an *iteratively reweighted least-squares* (IRLS) scheme in which the current estimate of the sparseness operator is held fixed while the contrast is updated [Scales 1988]. Further simplification can be achieved by application of a few operator identities, details of which are given by Sacchi and Ulrych [Sacchi 1998], in order to rewrite Eq. 4.3.97:

$$\chi_{\text{est}}(\underline{x}) = \mathcal{Q}(\underline{x})\mathcal{G}_X^\dagger \left[ \mathcal{G}_X \mathcal{Q}(\underline{x})\mathcal{G}_X^\dagger + \gamma\mathcal{I} \right]^{-1} \tilde{f}(\underline{x}_r, \underline{x}_s, \omega). \quad (4.3.99)$$

In this form, the imaging problem with sparseness constraint can be split into two parts:

- A linear conjugate gradient scheme applied to the normal equations is used to determine the auxiliary variable  $\tilde{\zeta}(\underline{x}_r, \underline{x}_s, \omega)$  (CGNE update):

$$\tilde{\zeta}(\underline{x}_r, \underline{x}_s, \omega) = \left[ \mathcal{G}_X \mathcal{Q}(\underline{x})\mathcal{G}_X^\dagger + \gamma\mathcal{I} \right]^{-1} \tilde{f}(\underline{x}_r, \underline{x}_s, \omega). \quad (4.3.100)$$

- After convergence of the scheme, the contrast is updated (IRLS update):

$$\chi_{\text{est}}(\underline{x}) = \mathcal{Q}(\underline{x})\mathcal{G}_X^\dagger \tilde{\zeta}(\underline{x}_r, \underline{x}_s, \omega). \quad (4.3.101)$$

Note that the additive term  $\gamma\mathcal{I}$  corresponds to the well-known Tikhonov regularisation with minimum  $L^2$ -norm constraint. As pointed out in Section 4.2.8.2, minimum norm regularisation can be achieved by early stopping of the conjugate gradient scheme. The explicit regularisation can thus be replaced by only performing a few conjugate gradient steps after every update of  $\chi$  and  $\mathcal{Q}(\underline{x})$ , which helps to dispose of the parameter  $\gamma$  [Zwartjes 2005]. Trad et al. suggest the usage of generalised cross-validation in order to determine the number of necessary iterations [Trad 2003]. However, diverse simulation experiments carried out in this work have shown the empirical choice of about five to ten CGNE iterations to be sufficient. Likewise, the necessary number of IRLS iterations can empirically be determined. About two to five iterations are found to be adequate, which is in accordance with the findings of Zwartjes [Zwartjes 2005].

For the determination of the remaining parameter  $\sigma_\chi$ , different suggestions can be found in the literature. On the one hand, general methods such as the L-curve

criterion [Hansen 1998] introduced in Section 4.2.8.2 can be used. However, these methods require the calculation of the problem for several values of  $\sigma_\chi$ , which is not desirable. Another option is the tuning of  $\sigma_\chi$  based on the noise level, if this level can be determined [Sacchi 1998].

In the present work, however, it is decided to pursue yet another strategy based on interpreting Eq. 4.3.97 as a spatially dependent Tikhonov regularisation. The definition of the sparseness operator in Eq. 4.3.98 shows that the regulariser reaches its maximum value where the contrast is low, and its minimum for high values of the contrast. The result of the inversion is thus stronger regularised for regions in which the contrast exhibits low magnitude. Based on this view of the sparse regularisation, the parameter  $\sigma_\chi$  determines to what extent the regularisation is relaxed for peaks of the contrast function with respect to regions in which the contrast function is close to zero.

For a conservative approach, it is suggested to choose  $\sigma_\chi$  in such a way that the regularising term  $\mathcal{Q}(\underline{x})^{-1}$  in Eq. 4.3.97 is half as strong for the maximum absolute value of the contrast as for regions of the contrast equal to zero:

$$\sigma_\chi = \frac{1}{2} \max |\chi(\underline{x})|^2. \quad (4.3.102)$$

The regularisation is thus relaxed for the peaks of the contrast functions. Setting  $\sigma_\chi$  to lower values can be used in order to force sparseness, i.e., apply even less regularisation to the peaks of the contrast function. For the examples presented in this work, the empirical rule of Eq. 4.3.102 has proved to be sufficient to automatically determine values for  $\sigma_\chi$  dependent on the current estimate of the contrast.

The proposed scheme for imaging by sparse inversion is obtained by the combination of the components derived above:

- A first estimate of the contrast and the sparseness operator is obtained by application of the adjoint operator:

$$\chi_0(\underline{x}) = \mathcal{G}_X^\dagger \tilde{f}(\underline{x}_r, \underline{x}_s, \omega), \quad (4.3.103)$$

$$\sigma_{\chi,0} = \frac{1}{2} \max |\chi_0(\underline{x})|^2, \quad (4.3.104)$$

$$\mathcal{Q}_0(\underline{x}) = 1 + \frac{|\chi_0(\underline{x})|^2}{2\sigma_{\chi,0}^2}. \quad (4.3.105)$$

- Then, a number of IRLS iterations are carried out, with the  $n$ -th iteration consisting of two steps:

- (1) The auxiliary variable  $\tilde{\zeta}(\underline{x}_r, \underline{x}_s, \omega)$  is calculated using a few conjugate gradient iterations:

$$\tilde{\zeta}_n(\underline{x}_r, \underline{x}_s, \omega) = \left[ \mathcal{G}_X \mathcal{Q}_{n-1}(\underline{x}) \mathcal{G}_X^\dagger \right]^{-1} \tilde{f}(\underline{x}_r, \underline{x}_s, \omega). \quad (4.3.106)$$

- (2) Contrast and sparseness operator are updated from the obtained auxiliary variable:

$$\chi_n(\underline{x}) = \mathcal{Q}_{n-1}(\underline{x}) \mathcal{G}_X^\dagger \tilde{\zeta}_n(\underline{x}_r, \underline{x}_s, \omega), \quad (4.3.107)$$

$$\sigma_{\chi,n} = \frac{1}{2} \max |\chi_n(\underline{x})|^2, \quad (4.3.108)$$

$$\mathcal{Q}_n(\underline{x}) = 1 + \frac{|\chi_n(\underline{x})|^2}{2\sigma_{\chi,n}^2}. \quad (4.3.109)$$

Examples of imaging results based on inversion with a sparseness constraint can be found in Section 4.3.7.

#### 4.3.6.2 Regularisation by a total variation constraint

As pointed out in the previous section, sparseness might not be the appropriate regularisation constraint if there are different magnitudes of contrast and spatially extended regions of non-zero contrast to be expected. Therefore, another type of regularisation will be discussed that is expected to be useful for a broader range of applications: minimum *total variation*. This type of constraint has first been introduced by Rudin et al. in the context of image denoising problems [Rudin 1992].

The total variation functional seeks to minimise the absolute value of the gradient of a function, in contrast to the  $L^1$ -norm, for example, which minimises the absolute value of the function itself. For the contrast function to be estimated, the total variation penalty term  $E_{\text{TV}}[\chi(\underline{x})]$  is given by the following expression:

$$E_{\text{TV}}[\chi(\underline{x})] = \int_{-\infty}^{\infty} |\nabla \chi(\underline{x})| \, d\underline{x}. \quad (4.3.110)$$

Whereas regularisation with a sparseness constraint leads to ‘spiky’ estimates, the total variation constraint favours results exhibiting a smooth or ‘blocky’ structure, i.e., with limited regions of strong transitions.

In this work, the weighted  $L^2$ -norm being a slightly modified version of the total variation regulariser is used:

$$E_{\text{weighted } L^2}[\chi(\underline{x})] = \int_{-\infty}^{\infty} b_{\text{TV}}^2(\underline{x}) [|\nabla \chi(\underline{x})| + \beta^2] \, d\underline{x}, \quad (4.3.111)$$

with  $b_{\text{TV}}(\underline{x})$  being a positive weight and  $\beta^2$  being a positive steering parameter to ensure that the functional is continuously differentiable.

Van den Berg et al. presented an inversion algorithm using the weighted  $L^2$ -norm as a multiplicative regularisation constraint, having the advantage that  $b_{\text{TV}}(\underline{x})$

and  $\beta^2$  can automatically be chosen. Furthermore, the inclusion of the regularisation as a multiplicative factor does away with the regularisation parameter  $\gamma$  [Van den Berg 1999]. A comprehensive overview of this multiplicative regularisation approach with some refinements is given by Abubakar et al. [Abubakar 2004]. In the following, only the essentials of the proposed algorithms are presented.

The error functional is given by the multiplication of the data error and the regularisation error:

$$E[\chi(\underline{x})] = \left\| \tilde{f}(\underline{x}_r, \underline{x}_s, \omega) - \mathcal{G}_X \chi(\underline{x}) \right\|_{R, \omega}^2 E_{\text{weighted L}^2}[\chi(\underline{x})]. \quad (4.3.112)$$

The weighting factor  $b_{\text{TV}}(\underline{x})$  is chosen in such a way that that  $E_{\text{weighted L}^2}(\underline{x})$  is close to one to ensure that the data error is minimised and not only the regularisation term:

$$b_{\text{TV}}^2(\underline{x}) = \left\{ V \left[ |\chi(\underline{x})|^2 + \beta^2 \right] \right\}^{-1}, \quad (4.3.113)$$

with  $V$  being the area of the imaging domain:

$$V = \int_{-\infty}^{\infty} d\underline{x}. \quad (4.3.114)$$

There are different ways of determining values for  $\beta^2$ . Abubakar et al. provide a lower bound in order for the regularisation functional to be convex [Abubakar 2004]:

$$\beta^2 \geq \frac{\|b_{\text{TV}}(\underline{x}) \nabla \chi(\underline{x})\|_S^2}{2 \|b_{\text{TV}}(\underline{x})\|_S^2}. \quad (4.3.115)$$

The following equation for determining  $\beta^2$  is used for the examples presented in this work; it can be shown to minimise the arc length of the contrast function in x- and y-direction [Van den Berg 2010]:

$$\beta^2 = \frac{1}{V} \int_{-\infty}^{\infty} |\nabla \chi(\underline{x})|^2 d\underline{x}. \quad (4.3.116)$$

With all parameters and auxiliary variables determined, the inversion with total variation constraint can be performed by means of a nonlinear conjugate gradient scheme as described in Appendix F.3. The gradient of the error functional  $E(\underline{x})$  in the  $n$ th iteration is readily determined:

$$\begin{aligned} \frac{\partial E[\chi_n(\underline{x})]}{\partial \chi_{n-1}(\underline{x})} = & -2E_{\text{weighted L}^2}[\chi_{n-1}(\underline{x})] \mathcal{G}_X^\dagger \left[ \tilde{f}(\underline{x}_r, \underline{x}_s, \omega) - \mathcal{G}_X \chi_{n-1}(\underline{x}) \right] \\ & - 2E[\chi_{n-1}(\underline{x})] \left\{ \nabla [b_{\text{TV}}^2(\underline{x}) \nabla \chi_{n-1}(\underline{x})] \right\}. \end{aligned} \quad (4.3.117)$$

In this form, it can be seen that the error of the regularisation determines how strong the minimisation of the data error is carried out, thereby showing why  $E_{\text{weighted L}^2}[\chi(\underline{x})]$  is kept close to one. The data error  $E[\chi(\underline{x})]$ , on the other hand, determines the strength of the regularisation, the influence of which decreases as the algorithm approaches the final solution.

After determination of the search direction from the gradient, the step size for the conjugate gradient scheme can be derived in closed form. A detailed description of the required calculations was given by Abubakar et al. [Abubakar 2004] and is omitted here for the sake of brevity.

Examples of images obtained with the total variation constraint are presented in the following section, which allows for the comparison of different imaging methods.

### ■ 4.3.7 Examples

The capabilities of the different imaging methods are presented by means of a few examples. These simulations are carried out for a 3 mm aluminium plate at four different frequencies between 500 Hz and 4 kHz distributed according to Eq. 3.6.48. The first setup depicted in Fig. 4.32 consists of a few scattering structures of equal strength surrounded by a circle of sources and receivers.

In the following, three different experiments related to this dataset will be presented: in addition to the setup shown, the effect of limiting the aperture of the array of sources and receivers will be investigated. The imaging results for the full circular array are shown in Fig. 4.34. For the images depicted in Fig. 4.35, only the left half of sources and receivers is used. Figure 4.36 presents the images obtained with only a quarter of a circle on the right side being used. The robustness of the different imaging and regularisation methods with respect to the angular aperture can thus be compared.

The second imaging setup considered is shown in Fig. 4.33. Two scatterers are positioned relatively close together in order to be able to assess the ability of imaging algorithms to resolve small structures.

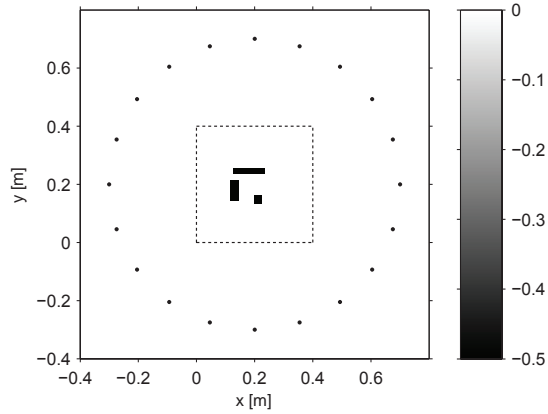


**Figure 4.32:** Setup for imaging simulation containing a few scattering objects.

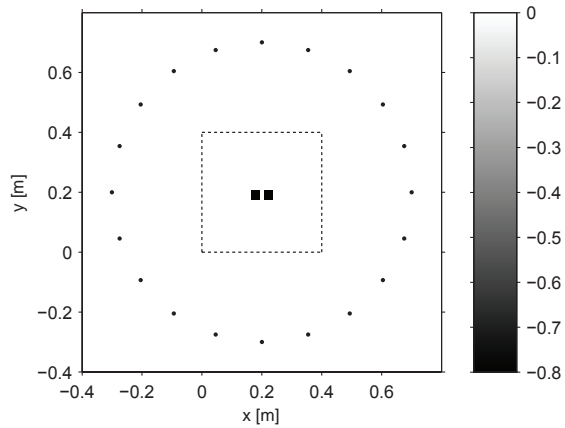


**Figure 4.33:** Setup for imaging simulation containing two closely spaced scatterers.

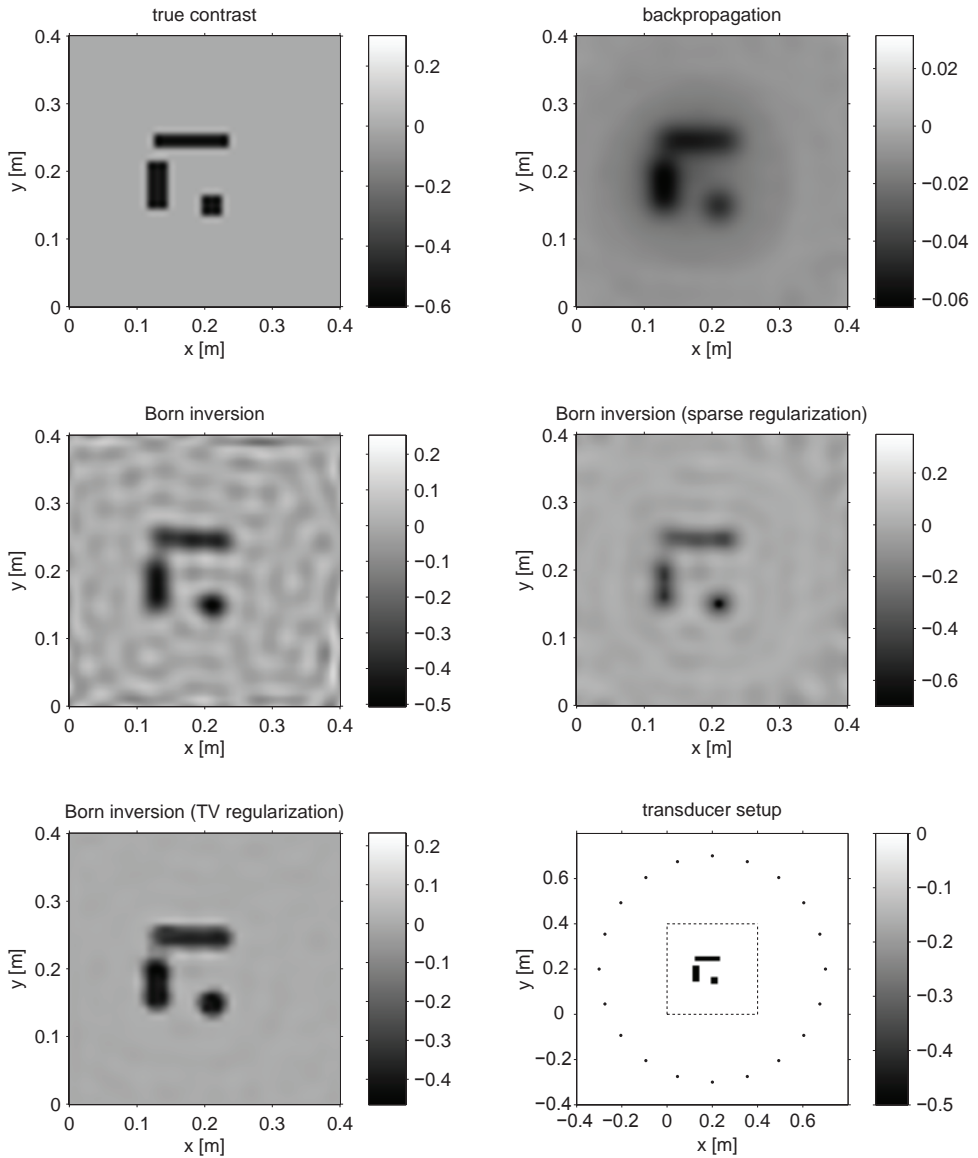


**Figure 4.34:** Imaging results for the setup shown in Fig. 4.32 with full circular coverage by sources and receivers.

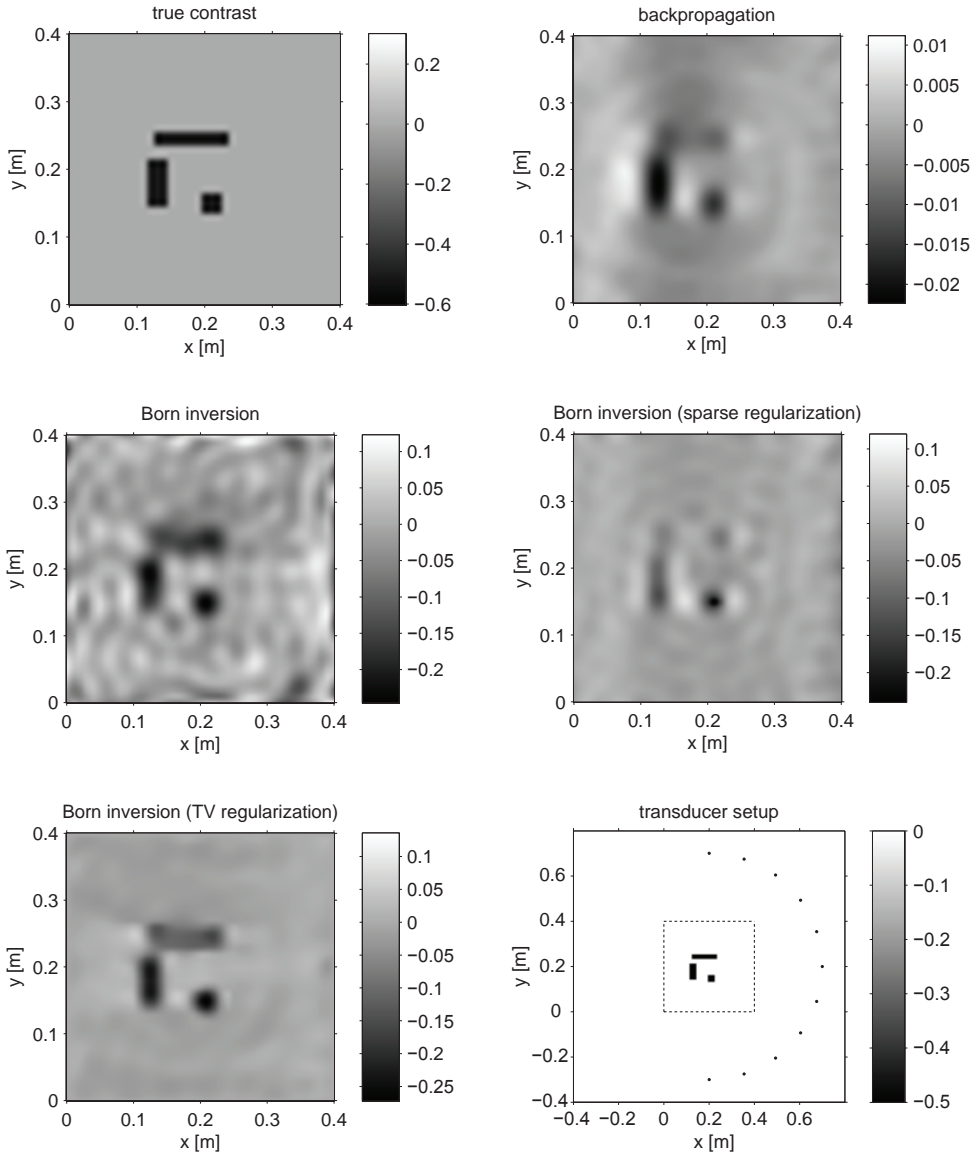


**Figure 4.35:** Imaging results for the setup shown in Fig. 4.32 with only sources and receivers on the right-hand side used.

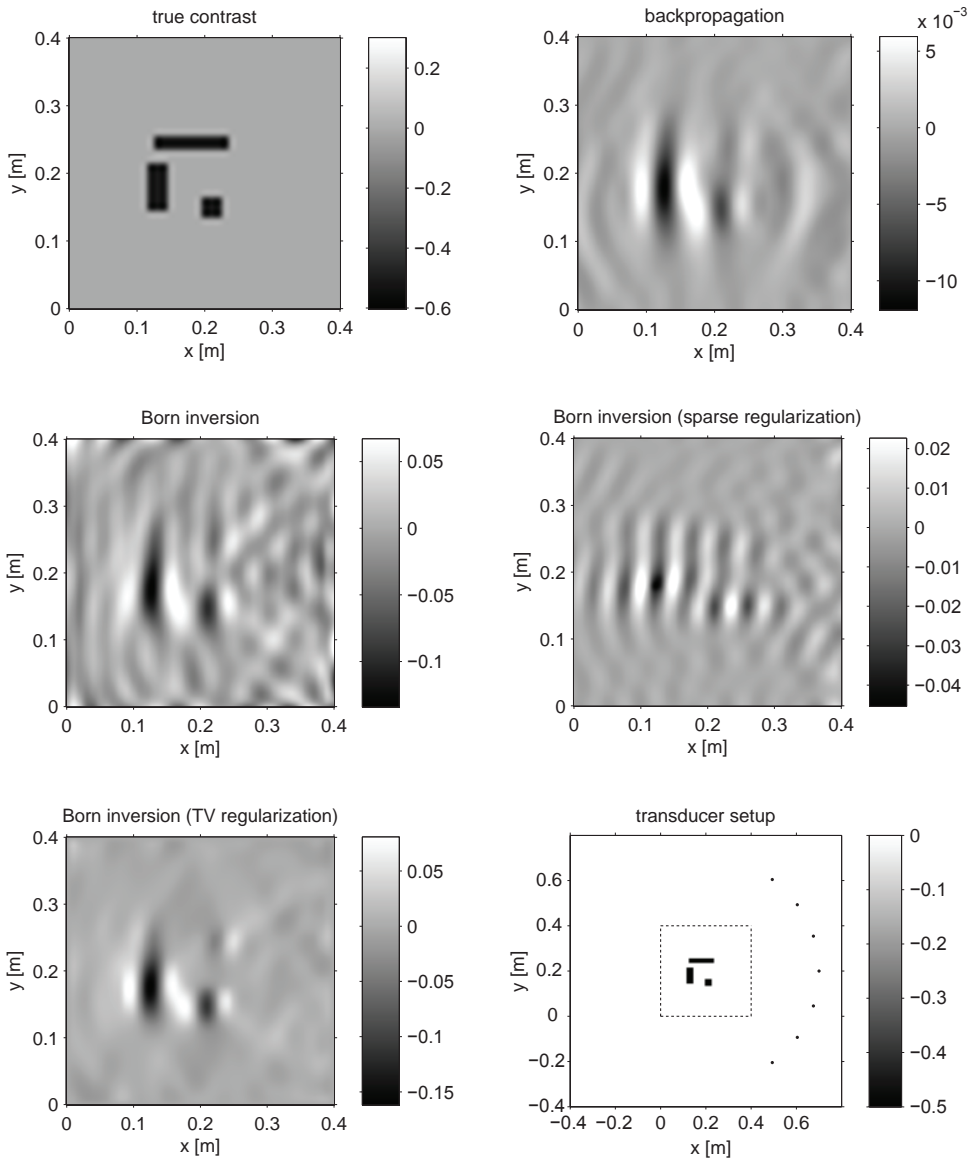


**Figure 4.36:** Imaging results for the setup shown in Fig. 4.32 with only sources and receivers positioned within a quarter of a circle to the right of the object.

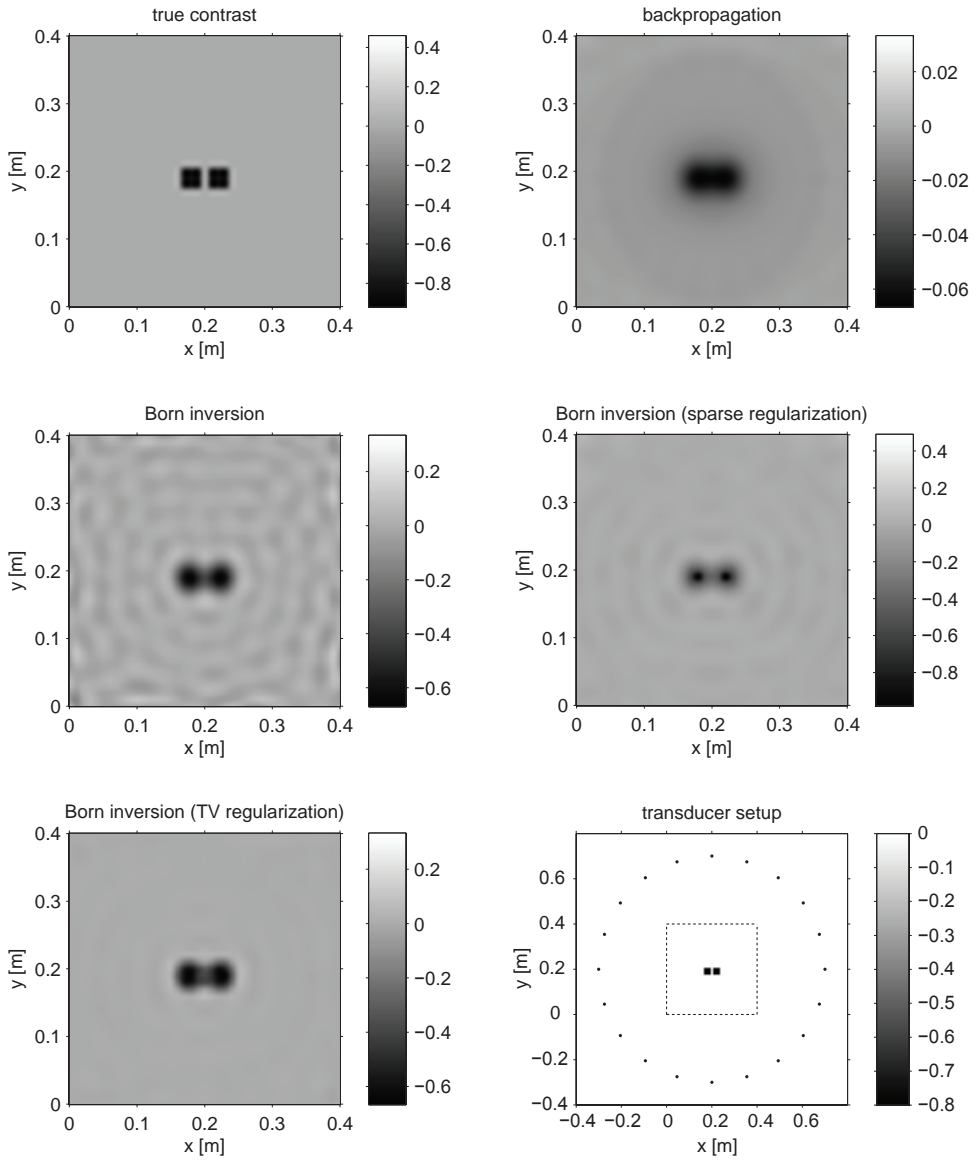


**Figure 4.37:** Imaging results for the setup shown in Fig. 4.33 with two scattering objects surrounded by a full circle of sources and receivers.

### ■ 4.3.8 Discussion of the imaging examples

In the context of this work, the presented imaging methods have been tested on simulations of several transducer setups and constellations of defects. Based on this experience, the examples shown are chosen in such a way that the characteristic properties of the different approaches are brought out.

- First of all, it can be stated that *backpropagation*, which is the only non-iterative method presented, yields a very robust, indicative image of the inhomogeneities. The resolution is rather low in comparison to the other methods, despite the fact that the individual strength of the four frequencies employed for imaging is taken into account as discussed in Section 4.3.4. The robustness and ease-of-use of backpropagation can serve as an explanation for the attractiveness of this approach in current industrial applications.
- *Born inversion* with simple Tikhonov regularisation can be seen to achieve significantly better resolution than backpropagation in the case of full coverage with transducers (Fig. 4.34). It is even more important to note that inversion can retrieve certain features better than backpropagation: in Fig. 4.35, only the tips of the upper defect are visible in the image obtained by backpropagation. This is due to the fact that this inhomogeneity is only illuminated from the right hand side, such that the receivers can only pick up the field scattered by the tips, and no reflection from the broad side of this object. In this setup, inversion is still able to retrieve the full inhomogeneity.

On the other hand, it can clearly be seen that the images obtained by inversion with Tikhonov regularisation are relatively noisy and contain undesirable artefacts. The number of iterations can be used as a regularisation parameter in order to find a trade-off between resolution and noise level, see Section 4.2.8.2. In general, a more appropriate form of regularisation, i.e., a form which is motivated by the type of inhomogeneity to be expected, is to be preferred.

- Inversion with a *sparse regularisation* constraint can achieve superior resolution, which can best be seen from the example of two point-like scatterers presented in Fig. 4.37. On the other hand, it must be stated that this regularisation technique favours point-like defects. In the case of limited illumination in Fig. 4.35 discussed above, inversion with sparse regularisation is able to recover the tips of the defect on the top, but suppresses the information in between due to its weak presence in the receiver signals. Furthermore, it can be seen from Fig. 4.36 that sparse regularisation can actually worsen the imaging result if used in combination with insufficient illumination due to a limited aperture.

This behaviour can be critical if defects should be detected that do not comply with the presumed sparse structure: if sparse regularisation is applied to the detection of a slowly varying change in material properties as for example a

shallow corrosion defect, it could actually suppress this type of inhomogeneity in the generated image, which is not acceptable for the application in mind.

- Inversion with *total variation regularisation* makes fewer assumptions about the shape of features in the image; it accepts both smooth variations and sudden local discontinuities. In all results shown in Fig. 4.34 to 4.37, regularisation by minimum total variation achieves a good resolution while suppressing noise and imaging artefacts. Only in the case of a restricted aperture, shown in Fig. 4.36, the defect for which there is not sufficient data available is not fully imaged. Nevertheless, the image obtained by inversion with regularisation by minimum total variation is the best of all results presented and shows the positions of the tips of the elongated defect on the top.

Summarising, imaging by inversion has to be preferred to backpropagation due to the gain in resolution. The combination with regularisation is inevitable in order to achieve stabilisation and robustness to noise. Furthermore, regularisation can serve as a tool to fill gaps for which there is not sufficient information from the measured data. Hence, the regularisation method has to be chosen carefully, not to force the image to obey a model which does not comply with the structure of typical defects to be expected. With respect to this requirement, regularisation by minimum total variation has to be regarded as the most promising of the presented methods.

#### ■ 4.3.9 Towards super-resolution

In Section 4.2.4.3, the advantage of measurements in the near-field with respect to the achievable resolution have briefly been discussed. In the present work, however, it is chosen to neglect possible applications of near-field techniques in combination with flexural waves due to the restricted imaging range.

In the previous section, it has been shown that regularisation of the imaging problem can help to increase the resolution slightly. The observed improvement is due to the incorporation of a priori assumptions on the structure of the image. Despite the fact that regularisation criteria such as minimum total variation can also be justified from a physical point of view, it is desirable to obtain an increase in resolution based on improved physical modelling of the underlying problem rather than an advanced method of ‘guessing’ the outcome.

The key to super-resolution lies in the usage of the evanescent components of the wave field. Since the possibility of probing the near-field is not considered in the context of this work, the evanescent field is not utilised as in the case of near-field acoustic holography, for instance. At higher distances from the object to be imaged, however, the magnitude of the evanescent field is too small as to be measured [Wolf 1998].

Nevertheless, it has been established that the placement of a scattering object smaller

than the diffraction limit in the near field can lead to a conversion of evanescent waves to propagating waves. This approach is used for scanning microscopy [Courjon 1994]. This basic idea can be extended: it is not necessary to place a small passive probe close to the object of interest to achieve the conversion of the evanescent field to propagating waves. Instead, multiple scattering in the inhomogeneous object itself makes the propagating wave field contain information on the evanescent field, information with resolution above the diffraction limit [Chen 1998].

However, the high resolution information which is ‘encoded’ in the propagating field can be extracted only by methods which unravel the effects of multiple scattering, i.e., methods beyond the Born approximation [Simonetti 2006]. While this result has *qualitatively* been established for several years, it remains difficult to make general *quantitative* statements on the gain in resolution to be expected. Experimental verification of the improvement in resolution by taking multiple scattering into account has, among others, been given by Chen and Chew [Chen 1998], Blomgren et al. [Blomgren 2002] and Cui et al. [Cui 2004].

In Chapter 5, the possibilities of including multiple scattering for imaging using flexural waves are investigated.

## 4.4 Imaging in finite structures

Up to this point, the imaging problem has been treated under the simplifying assumption that measurements are taken in an infinite medium. For real media of finite extent, reflections from the boundaries have to be expected. Depending on the size of the structure under investigation, these reflections can possibly be removed from the measured impulse responses by simple filtering in time domain. This approach is chosen by many researchers, for instance Simonetti [Simonetti 2006], probably because of the fact that it can easily be achieved in a controlled experiment, for which the size of the plate and the position of the defect can arbitrarily be chosen. Another option is the artificial creation of anechoic boundary conditions by application of damping to the boundary regions [Francoeur 2008].

In the previous chapter, it has been shown that the temporal and spatial extent of a dispersive wavelet increases with increasing distance from the source. Therefore, overlapping between primary and reflected events constitutes a typical feature of dispersive wave fields, especially in structures being relatively small in comparison to the wavelength. The method for dispersion removal can then be used to separate different events and, for instance, filter out reflections from the boundaries.

Typical imaging results obtained by this approach are shown in Fig. 4.38. An aluminium plate of 3 mm thickness with an artificial defect of 1 mm depth is used; the experiment is described in Appendix G.3. The correct location of the pit is shown in Fig. 4.38(a); the images obtained by backpropagation, inversion with  $L^2$ -norm

constraint and inversion with total variation constraint are shown in the subfigures (b) to (d), respectively.

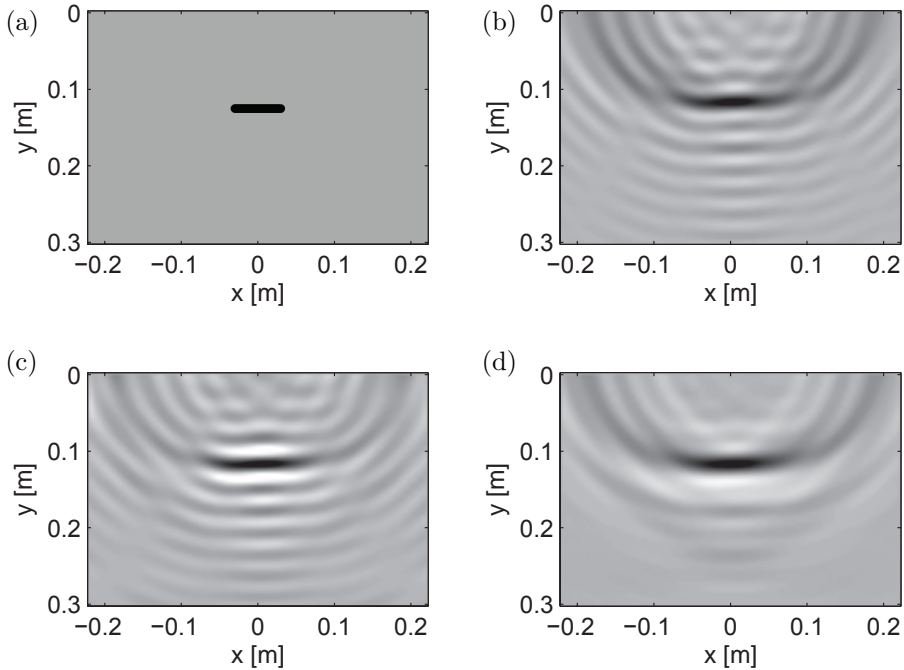


**Figure 4.38:** Location of an artificial defect in a 3 mm aluminium plate (a); imaging results obtained by backpropagation (b), minimum  $L^2$ -norm inversion (c), and inversion with total variation constraint (d).

It can be seen that all three methods suffice to detect the presence of the pit. However, inversion achieves slightly higher resolution than backpropagation, and the additional total variation constraint helps to suppress side lobes and imaging artefacts.

However, if material properties are to be imaged in the vicinity of the plate boundaries, separation of the boundary reflections from the field scattered by an inhomogeneity might be difficult. Therefore, another method of dealing with reflections is presented in the following section.

### ■ 4.4.1 Green's function for finite plates

The suppression of unwanted reflections is not the only way of dealing with finite structures. An alternative is given by the usage of a finite plate model in the imaging procedure. In plates of limited extent, the Green's function is determined by both the material properties as well as the the positions and conditions of the boundaries. By using this Green's function for the methods derived in this chapter, the finite nature of the medium can be taken into account.

The displacement field of a plate subject to boundary conditions can assume only certain modal shapes  $\xi_m(\underline{x})$ . These modal shapes have to fulfill both the homogeneous wave equation and the boundary conditions [Cremer 2005]. From a mathematical point of view, the modal shapes are the eigenfunctions of the plate, and the associated eigenfrequencies represent the eigenvalues.

If the plate is harmonically excited at a certain point  $\underline{x}_0$  with frequency  $\omega$ , the Green's function  $\tilde{G}(\underline{x}, \underline{x}_0, \omega)$  can be determined by weighted superposition of the modal shapes  $\xi_m$  [Cuenca 2009]:

$$\tilde{G}(\underline{x}, \underline{x}_0, \omega) = \sum_{m=1}^{\infty} \frac{\xi_m(\underline{x})\xi_m(\underline{x}_0)}{\rho h(\omega_m^2 - \omega^2)}, \quad (4.4.118)$$

with  $h$  being the thickness of the plate and  $\rho$  its mass density. The variable  $\omega_m$  represents the eigenfrequency associated with the modal shape  $\xi_m$ .

In the ideal case without damping, the plate can be excited only at its eigenfrequencies. In practical applications, damping can be taken into account by assuming the bending stiffness  $B''$  of the plate to be complex:

$$B''_{\text{damped}} = B''(1 + j\eta), \quad (4.4.119)$$

with  $\eta$  determining the strength of the damping. This modification requires the eigenfrequencies to be complex as well, and  $\omega_m^2$  in Eq. 4.4.118 has to be replaced by  $\omega_m^2(1 + j\eta)$  [Cremer 2005]. In the damped plate, a modal shape can be excited by frequencies other than its eigenfrequency. Nevertheless, a mode is only excited to a significant extent if the excitation frequency is close to its eigenfrequency.

It is important to realise that the excitability of a mode depends on the point of excitation  $\underline{x}_0$ . A mode cannot be excited at its nodal points. It can be concluded that imaging in finite plates requires the usage of different points of excitation in order to achieve sufficient illumination of the region to be imaged, from both a spatial and spectral point of view.

A simulation example is used to investigate the potential and possible pitfalls of this approach. Figure 4.39 shows the setup of the simulation.

The receiver signals due to excitation at different source positions are determined for 20 frequencies between 500 Hz and 5 kHz. To this end, a finite element analysis

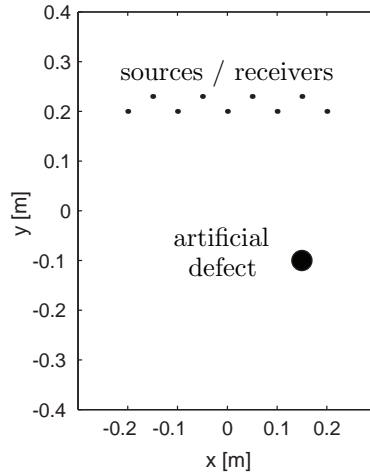


**Figure 4.39:** Simulation setup for a finite aluminium plate (3 mm thickness) of 60 by 80 cm; a circular defect with a diameter of 4 cm and a depth of 2 mm is simulated.

based on the Mindlin plate model is used. Furthermore, the plate response according to the Kirchhoff plate model applied in this thesis is calculated. A comparison of both models is shown in Fig. 4.40.

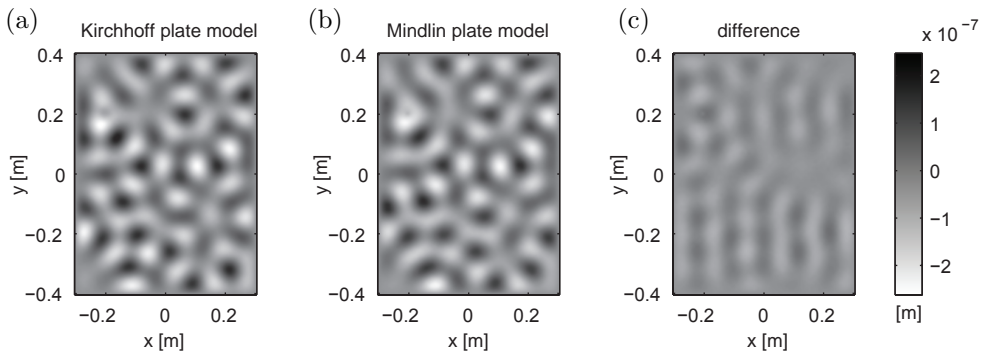


**Figure 4.40:** Displacement of the plate for the leftmost source position at 2.5 kHz in the absence of the defect: Kirchhoff plate model (a), Mindlin plate model (b), difference between both models (c) shown on the same scale.

It can be seen that, even at the rather low frequency of 2.5 kHz for which the Kirchhoff approximation should be valid, there is a significant difference between the Kirchhoff and the Mindlin plate model. This effect is due to the boundary conditions: relatively small differences in the propagation velocity can lead to a large difference in the predicted modal shapes of a finite plate. The deviation increases with increasing frequency as shown in Fig. 4.41.

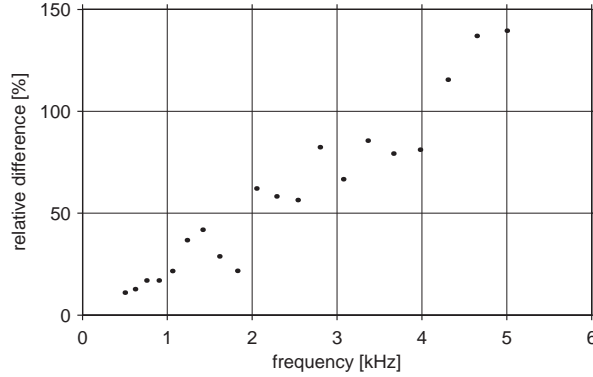


**Figure 4.41:** Relative difference of the modal shapes of the Kirchhoff and the Mindlin plate model with respect to the average amplitude at different excitation frequencies between 500 Hz and 5 kHz.

As a consequence, the simplified Kirchhoff model is only partially useful for the determination of the modal shapes of a finite plate. In order to obtain an image of inhomogeneities, the incident field at the receiver position has to be known with sufficient accuracy.

In contrast to images obtained in infinite plates, the presence of modal patterns has an adverse influence on the image obtained. For a certain frequency, nodal lines are present at which the plate cannot be excited. Hence, the incident field can be zero at certain locations, and the imaging procedure has to be stabilised. In the case of backpropagation, Eq. 4.3.73 has to be replaced by the following expression:

$$\chi(\underline{x})_{\text{back}} = \frac{1}{\Omega} \int_{-\infty}^{\infty} \frac{\sum_{s=1}^{N_s} \tilde{w}(\underline{x}, \underline{x}_s, \omega) \tilde{u}_{\text{inc}}^*(\underline{x}, \underline{x}_s, \omega)}{k_0^4(\omega) \sum_{s=1}^{N_s} |\tilde{u}_{\text{inc}}(\underline{x}, \underline{x}_s, \omega)|^2 + \epsilon} d\omega, \quad (4.4.120)$$

with  $\epsilon$  being a stabilisation constant to avoid division by zero, and  $\Omega$  representing

the bandwidth of the spectrum used:

$$\Omega = \int_{-\infty}^{\infty} d\omega. \quad (4.4.121)$$

Figure 4.42(a) presents the image obtained under the assumption that the incident field is accurately known, i.e., by using the Mindlin plate model for both the simulation of the receiver signals and the calculation of the incident field.

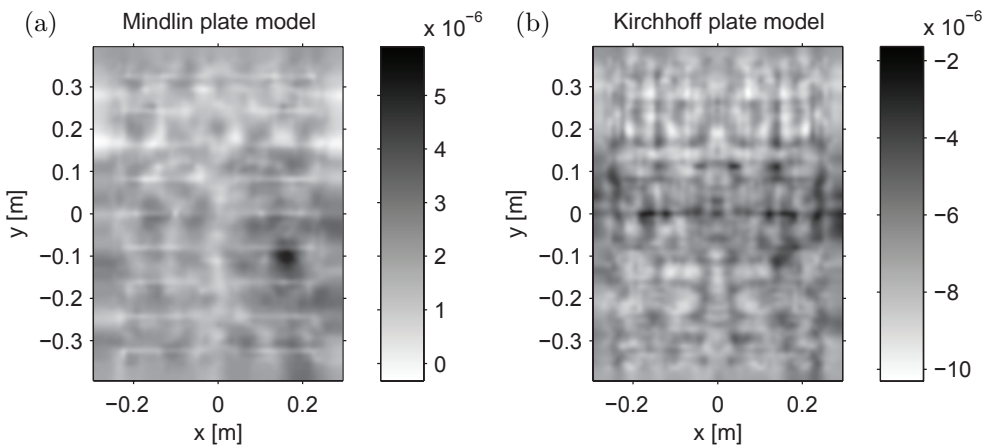


**Figure 4.42:** Images of the simulated defect obtained by using the Mindlin plate model (a) and the Kirchhoff plate model (b) at 20 frequencies between 500 Hz and 5 kHz.

The simulated defect can clearly be seen. However, even when combining different frequencies and different points of excitation, the images obtained by this approach look slightly ‘noisy’ due to the influence of different modal patterns.

If the simple Kirchhoff bending model is used for the calculation of the modal shapes and the incident field, the result depicted in Fig. 4.42(b) is obtained. It can be seen that the difference between the simplified model and the simulation based on the Mindlin model is too high to obtain a reliable image. The result can be improved by lowering the maximum frequency used for imaging, i.e., using only modes for which the Kirchhoff model provides a rather good prediction of the incident wave field.

Figure 4.43 shows the imaging results obtained by using only frequencies up to 2.5 kHz. The image obtained using the Mindlin model is almost equal to Fig. 4.42(a). However, the image based on the Kirchhoff plate model is improved with respect to

Fig. 4.42(b). The defect can be detected, despite the fact that there are still a lot of interfering artefacts present.

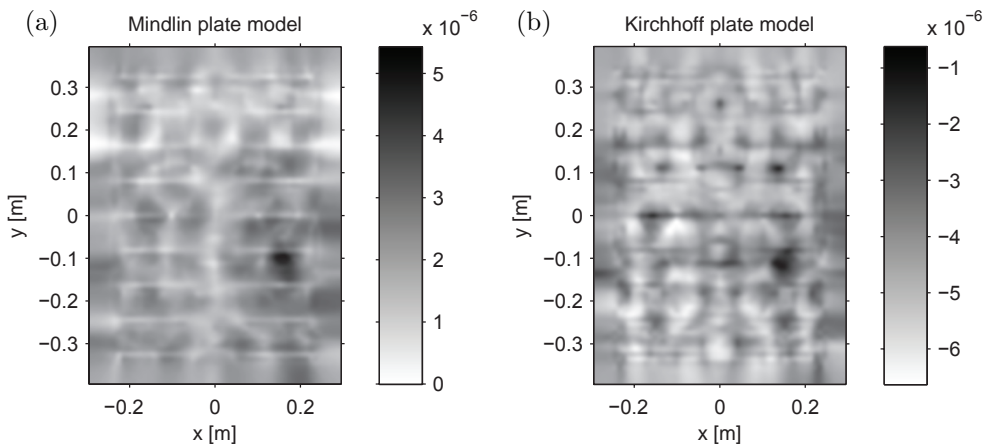


**Figure 4.43:** Images of the simulated defect obtained by using the Mindlin plate model (a) and the Kirchhoff plate model (b) at 10 frequencies between 500 Hz and 2.5 kHz.

From this example, it can be concluded that imaging in finite plates based on wave fields including the boundary reflections requires high accuracy in comparison to imaging in infinite plates. The Kirchhoff plate model cannot be assumed to predict the modal shapes with sufficient accuracy. Therefore, it is necessary to limit the maximum frequency or use a more sophisticated plate model, such as Mindlin's theory.

Further research is needed to investigate if it is possible to estimate the propagation velocity and the boundary conditions from the measurements itself, such that the modal shapes can be reconstructed. However, the complexity of this task is beyond the scope of this work.

From the point of view of currently available techniques, it is most promising to either remove the boundary reflections from the measured data before calculating the image as done in Section 4.4, or rely on accurate knowledge of the incident field. The latter option, for example, is given if a reference measurement of the finite structure is available, i.e., if an object is monitored regularly and only a change in the reflection pattern due to a newly developing defect has to be detected.

## 4.5 Summary

In this chapter, methods for wave field extrapolation and imaging of source distributions and scatterers under the Born approximation have been presented. Different approaches for imaging have been derived by posing the calculation of an image as a least-squares optimisation problem. Standard approaches such as backpropagation and inversion have been compared both theoretically and by means of examples. The application of regularised inversion has produced promising results. However, it should be noted that the kind of regularisation has to be chosen carefully in order not to introduce inappropriate assumptions leading to a loss of available information. In addition, approaches of applying the presented techniques to beams and plates of finite extent have been outlined.



# Imaging beyond the Born approximation

*Problems worthy  
of attack  
prove their worth  
by hitting back.*

(Piet Hein, 1905 – 1996)

In the previous chapter, it has been shown how the resolution of acoustical and vibrational images is limited if the Born approximation is applied. A model based on the Born approximation is not able to explain the received signals to full extent. The disregard of multiple scattering can cause artefacts that hinder the interpretation of an image severely.

Hence, there are two interconnected purposes of extending imaging procedures beyond the Born approximation:

- obtaining *qualitatively* better images by increasing the achievable resolution,
- obtaining *quantitatively* better estimates of the material inhomogeneities by using an improved model for the explanation of the measured signals.

In the first part of this chapter, a general approach for imaging in plates based on *contrast source inversion* is derived, followed by extensions of the method for structures with reflecting boundaries.

## 5.1 Object and data equation

In the case of multiple scattering, the relation between the contrast describing the material inhomogeneities and the receiver signals is no longer linear. In fact, there are two equations that have to be dealt with simultaneously: the *object* equation and

the *data* equation. Both equations have already been introduced and are repeated here for convenience.

The *object equation* has been introduced in Section 4.3.2 (Eq. 4.3.61) and describes the generation of the total field  $\tilde{u}(\underline{x}, \underline{x}_s, \omega)$  by the incident field  $\tilde{u}_{\text{inc}}(\underline{x}, \underline{x}_s, \omega)$  and the contrast:

$$(\mathcal{I} - \mathcal{G}_D \mathcal{X}) \tilde{u}(\underline{x}, \underline{x}_s, \omega) = \tilde{u}_{\text{inc}}(\underline{x}, \underline{x}_s, \omega). \quad (5.1.1)$$

The object equation can also be formulated in terms of the contrast sources  $\tilde{w}(\underline{x}, \omega)$  by application of the contrast operator  $\mathcal{X}$  defined in Eq. 4.3.60 to both sides:

$$(\mathcal{I} - \mathcal{X} \mathcal{G}_D) \tilde{w}(\underline{x}, \underline{x}_s, \omega) = \mathcal{X} \tilde{u}_{\text{inc}}(\underline{x}, \underline{x}_s, \omega). \quad (5.1.2)$$

The second equation describing the scattering is the *data equation* introduced in Section 4.2 (Eq. 4.2.18). It is used to calculate the receiver signals  $\tilde{f}(\underline{x}_r, \omega)$  for the given contrast sources  $\tilde{w}(\underline{x}, \omega)$ :

$$\tilde{f}(\underline{x}_r, \underline{x}_s, \omega) = \mathcal{G}_R \tilde{w}(\underline{x}, \underline{x}_s, \omega). \quad (5.1.3)$$

The generation of the scattered signals at the receiver positions is described by both the object and the data equation. Combination of these two equations leads to the following formal relation:

$$\tilde{f}(\underline{x}_r, \underline{x}_s, \omega) = \mathcal{G}_R (\mathcal{I} - \mathcal{X} \mathcal{G}_D)^{-1} \mathcal{X} \tilde{u}_{\text{inc}}(\underline{x}, \underline{x}_s, \omega). \quad (5.1.4)$$

If the contrast and the incident field are known, the object equation can be used to solve the forward problem as described in Section 4.3.2, and the receiver signals can be computed.

For the inverse imaging problem of determining the contrasts from the receiver signals, however, only the incident field  $\tilde{u}_{\text{inc}}(\underline{x}, \underline{x}_s, \omega)$  and the receiver signals  $\tilde{f}(\underline{x}_r, \omega)$  are assumed to be known. By writing out the contrast operator as a multiplication by the scattering potential  $\tilde{\Phi}(\underline{x}, \omega) = k_0^4 \chi(\underline{x})$ , it can be seen that there exists a nonlinear relationship between the contrast  $\chi(\underline{x})$  and the receiver signals:

$$\tilde{f}(\underline{x}_r, \underline{x}_s, \omega) = \mathcal{G}_R [\mathcal{I} - k_0^4 \chi(\underline{x}) \mathcal{G}_D]^{-1} k_0^4 \chi(\underline{x}) \tilde{u}_{\text{inc}}(\underline{x}, \underline{x}_s, \omega). \quad (5.1.5)$$

Hence, the problem cannot be solved in closed form, and direct linear inversion for the contrast is not possible. The Born approximation presented in the previous chapter relies on a linearised approximation of this equation:

$$[\mathcal{I} - k_0^4 \chi(\underline{x}) \mathcal{G}_D]^{-1} \approx \mathcal{I} \quad (5.1.6)$$

$$\tilde{f}(\underline{x}_r, \underline{x}_s, \omega) \approx \mathcal{G}_R k_0^4 \chi(\underline{x}) \tilde{u}_{\text{inc}}(\underline{x}, \underline{x}_s, \omega). \quad (5.1.7)$$

It is evident that this approximation is useful only if the contrasts  $\chi(\underline{x})$  are small. Furthermore, it should be noted that the effect of the operator term  $k_0^4 \chi(\underline{x}) \mathcal{G}_D$  cannot be neglected for higher frequencies. In the previous chapter, it has been shown that such an approximation results in additional ‘noise’ in the image due to the part of the data that cannot be explained by the simplified model of the Born approximation. By taking multiple scattering into account, the level of noise and artefacts in the image is expected to decline.

Another view of the capabilities of this approach is obtained by regarding the object equation as a regulariser for the data equation. Hence, the obtained solutions for the contrast sources and the contrast are expected not only to explain the measurement data at the receiver positions, but also to be consistent with the object equation, i.e., be explainable by multiple scattering in the object domain. In the following, approaches for solving both data and object equation will be discussed.

## 5.2 Iterative linear inversion

As a first approximation, the nonlinear imaging problem given by Eq. 5.1.5 can be tackled by computation of a series of linearised inversions [Wirgin 2002].

The iterative linear inversion starts out from an estimate of the contrast using the Born approximation. In the simplest case, this estimate can be obtained by back-propagation. The scheme then consists of the alternating application of the following two operations:

- (1) Calculation of the total field based on the current estimate of the contrast. This can be achieved by application of Eq. 4.3.61:

$$\tilde{u}_{\text{est}}(\underline{x}, \underline{x}_s, \omega) = (\mathcal{I} - \mathcal{G}_D \mathcal{A})^{-1} \tilde{u}_{\text{inc}}(\underline{x}, \underline{x}_s, \omega). \quad (5.2.8)$$

The inversion is usually carried out by application of an iterative optimisation as described in Section 4.3.2.

- (2) Calculation of the contrast from the current estimate of the total field by application of the methods introduced in Section 4.3.6, formally expressed by the following equation:

$$\chi(\underline{x})_{\text{est}} = [k_0^4 \tilde{u}_{\text{est}}(\underline{x}, \underline{x}_s, \omega)]^{-1} \mathcal{G}_R^{-1} \tilde{f}(\underline{x}_r, \underline{x}_s, \omega). \quad (5.2.9)$$

This method has the major drawback of requiring the solution of the full forward scattering problem in every iteration. Alternatively, only an update of the total field according to the Neumann series presented in Section 4.3.2.1 can be performed in every iteration, such that one additional order of scattering is taken into account

[Van den Berg 2002]. Equation 5.2.8 is then replaced by the following update scheme for the  $n$ th iteration:

$$\tilde{u}_{\text{est},n}(\underline{x}, \underline{x}_s, \omega) = \tilde{u}_{\text{inc}}(\underline{x}, \underline{x}_s, \omega) + \mathcal{G}_D \mathcal{X} \tilde{u}_{\text{est},n-1}(\underline{x}, \underline{x}_s, \omega). \quad (5.2.10)$$

However, the Neumann series is known to converge slowly for strong scattering or higher frequencies [Tomio 1995], which are just the cases in which the inclusion of multiple scattering should provide results superior to the Born approximation.

### 5.3 Contrast source inversion

A more promising approach is given by the simultaneous solution of the object and the data equation. This idea has been used for the *modified gradient approach* developed by Kleinman and Van den Berg [Kleinman 1992], for which the error in the contrast and the unknown wave field are minimised. Since 1997, the modified gradient approach has been superseded by the method of *contrast source inversion* (CSI), which could be shown to perform better [Van den Berg 1997]. In the contrast source inversion approach, an error functional is minimised with respect to both the contrast and the contrast sources.

A general error functional can be obtained by defining the residual for the receivers with index  $R$  using the data equation

$$\tilde{r}_R(\underline{x}_r, \underline{x}_s, \omega) = \tilde{f}(\underline{x}_r, \underline{x}_s, \omega) - \mathcal{G}_R \tilde{w}(\underline{x}, \underline{x}_s, \omega), \quad (5.3.11)$$

and the residual for the domain with index  $S$  using the object equation:

$$\begin{aligned} \tilde{r}_S(\underline{x}, \underline{x}_s, \omega) &= k_0^4(\omega) \chi(\underline{x}) \tilde{u}(\underline{x}, \underline{x}_s, \omega) - \tilde{w}(\underline{x}, \underline{x}_s, \omega) \\ &= k_0^4(\omega) \chi(\underline{x}) \tilde{u}_{\text{inc}}(\underline{x}, \underline{x}_s, \omega) - \tilde{w}(\underline{x}, \underline{x}_s, \omega) + k_0^4(\omega) \chi(\underline{x}) \mathcal{G}_D \tilde{w}(\underline{x}, \underline{x}_s, \omega). \end{aligned} \quad (5.3.12)$$

Information at different frequencies is equally taken into account in the standard CSI scheme, and information obtained at different frequencies is considered equally important as information gained by illuminating the scattering object using sources from different directions [Abubakar 2003]. However, in the derivation of the equations for backpropagation in Section 4.2.6, it was shown that the imaging problem for flexural waves is highly frequency-dependent, and that this dependency has to be taken into account in order to ensure the proper weighting of the information that is present at different frequencies.

Therefore, it is chosen to define the following objective function, similar to Bloemenkamp et al. [Bloemenkamp 2001]:

$$E = \frac{1}{N_\omega} \sum_{\omega=\omega_1}^{\omega_N} \tilde{\eta}_R(\omega) \|\tilde{r}_R(\underline{x}_r, \underline{x}_s, \omega)\|_R^2 + \frac{1}{N_\omega} \sum_{\omega=\omega_1}^{\omega_N} \tilde{\eta}_S(\omega) \|\tilde{r}_S(\underline{x}, \underline{x}_s, \omega)\|_S^2. \quad (5.3.13)$$

In this equation, the summation is taken over a discrete number  $N_\omega$  of frequencies in the range  $\omega_1 \dots \omega_N$ .

The normalisations  $\tilde{\eta}_R(\omega)$  and  $\tilde{\eta}_S(\omega)$  have been chosen in such a way that both terms are equal to one for  $\tilde{w}(\underline{x}, \underline{x}_s, \omega) = 0$ :

$$\tilde{\eta}_R(\omega) = \left( \left\| \tilde{f}(\underline{x}_r, \underline{x}_s, \omega) \right\|_R^2 \right)^{-1}, \quad (5.3.14)$$

$$\tilde{\eta}_S(\omega) = \left( \left\| k_0^4(\omega) \chi(\underline{x}) \tilde{u}_{\text{inc}}(\underline{x}, \underline{x}_s, \omega) \right\|_S^2 \right)^{-1}. \quad (5.3.15)$$

In the remainder of this section, it is decided to drop the explicit dependencies of the variables as well as the tilde indicating operation in Fourier space for the sake of improved readability. Since multiplication by the number of frequencies  $N_\omega$  used in the inversion does not change the extrema, the error functional can be reformulated in the following form:

$$E = E_R + E_S, \quad (5.3.16)$$

with

$$E_R = \sum_{\omega=\omega_1}^{\omega_N} \frac{\|f - \mathcal{G}_R w\|_R^2}{\|f\|_R^2} = \sum_{\omega=\omega_1}^{\omega_N} \eta_R \|f - \mathcal{G}_R w\|_R^2, \quad (5.3.17)$$

$$E_S = \sum_{\omega=\omega_1}^{\omega_N} \frac{\|k_0^4 \chi u_{\text{inc}} - w + k_0^4 \chi \mathcal{G}_D w\|_S^2}{\|k_0^4 \chi u_{\text{inc}}\|_S^2} = \sum_{\omega=\omega_1}^{\omega_N} \eta_S \|k_0^4 \chi u_{\text{inc}} - w + k_0^4 \chi \mathcal{G}_D w\|_S^2. \quad (5.3.18)$$

The first term will be referred to as the *data error*  $E_R$ , while the second term represents the *object error*  $E_S$ . The joint minimisation of these error terms can be achieved by application of a nonlinear conjugate gradient scheme, a general representation of which is presented in Appendix F.3.

In every iteration, the cost function is first minimised with respect to the contrast sources  $\tilde{w}$  while keeping the current estimate of the contrast  $\chi$  constant. An estimate of the field  $u$  is then obtained, followed by an update of the contrast  $\chi$ .

It is evident that the contrast cannot be initialised to zero due to its presence in the denominator of Eq. 5.3.18. Therefore, the result obtained by backpropagation of the receiver data under the Born approximation as discussed in Section 4.2.6 is used as a starting value for the contrast sources, from which a first estimate of the

contrast and the field are readily obtained:

$$w_0 = \frac{\left\| \mathcal{G}_R^\dagger f \right\|_S^2}{\left\| \mathcal{G}_R \mathcal{G}_R^\dagger f \right\|_R^2} \mathcal{G}_R^\dagger f, \quad (5.3.19)$$

$$\chi_0 = \frac{1}{\Omega} \int_{-\infty}^{\infty} \frac{\sum_{s=1}^{N_s} w u^*}{k_0^4 \sum_{s=1}^{N_s} |u|^2} d\omega, \quad \text{with } \Omega = \int_{-\infty}^{\infty} d\omega, \quad (5.3.20)$$

$$u_0 = u_{\text{inc}} + G_D w_0. \quad (5.3.21)$$

### ■ 5.3.1 Update of the contrast sources

The gradient  $g$  of the cost function with respect to the contrast sources  $w$  is given by the following equation for the  $n$ th iteration:

$$g_n = \frac{\partial E_n}{\partial w} = -2\eta_{R,n-1} \mathcal{G}_R^\dagger r_{R,n-1} - 2\eta_{S,n-1} \left[ r_{S,n-1} - \mathcal{G}_D^\dagger (\chi_{n-1}^* r_{S,n-1}) \right]. \quad (5.3.22)$$

It is chosen to make use of the Polak-Ribière search direction  $d$ , which is determined from the gradient  $g$  as follows [Kelley 1995]:

$$d_0 = 0, \quad (5.3.23)$$

$$d_n = g_n + \frac{\langle g_n, g_n - g_{n-1} \rangle_S}{\|g_{n-1}\|_S^2} d_{n-1} \quad \text{for } n > 0. \quad (5.3.24)$$

The optimal step size  $\alpha$  must minimise the cost functional  $E$  for a given search direction  $d$ :

$$E(w + \alpha d_n) = \sum_{\omega=\omega_1}^{\omega_N} \left( \eta_R \|r_{R,n-1} - \alpha \mathcal{G}_R d_n\|_R^2 + \eta_S \|r_{S,n-1} + \alpha (k_0^4 \chi \mathcal{G}_D d_n - d_n)\|_S^2 \right). \quad (5.3.25)$$

The gradient with respect to  $\alpha$  is given by the following expression:

$$\begin{aligned} \frac{\partial E(w + \alpha d_n)}{\partial \alpha} &= \sum_{\omega=\omega_1}^{\omega_N} \eta_R \left( -2\text{Re} \langle r_{R,n-1}, \mathcal{G}_R d_n \rangle_R + 2\alpha \|\mathcal{G}_R d_n\|_R^2 \right) \\ &+ \sum_{\omega=\omega_1}^{\omega_N} \eta_S \left( 2\text{Re} \langle r_{S,n-1}, k_0^4 \chi \mathcal{G}_D d_n - d_n \rangle_S + 2\alpha \|k_0^4 \chi \mathcal{G}_D d_n - d_n\|_S^2 \right). \end{aligned} \quad (5.3.26)$$

The optimal step size  $\alpha$  is obtained by requiring the gradient to be zero:

$$\alpha = \frac{\eta_R \operatorname{Re} \langle r_{R,n-1}, \mathcal{G}_R d \rangle_R + \eta_S \operatorname{Re} \langle r_{S,n-1}, d - k_0^4 \chi \mathcal{G}_D d \rangle_S}{\eta_R \|\mathcal{G}_R d\|_R^2 + \eta_S \|d - k_0^4 \chi \mathcal{G}_D d\|_S^2}. \quad (5.3.27)$$

This completes the description of the contrast source update. Once the contrast sources  $w$  are known, the current estimate of the field  $u$  can be updated:

$$u_n = u_{\text{inc}} + \mathcal{G}_D w_n. \quad (5.3.28)$$

### ■ 5.3.2 Update of the contrast

The second important step in every iteration of the CSI method is the update of the contrast  $\chi$ , which can be performed in different ways. The simplest approach is the calculation of the contrast  $\chi$  that minimises the residual of the object equation, i.e., the numerator of the object error:

$$E_\chi = \|k_0^4 u_n \chi - w_n\|_{S,\omega}^2. \quad (5.3.29)$$

Minimisation of this function results in an estimate of the contrast based on the current estimate of the field and contrast sources analogue to Eq. 4.3.73 in the previous chapter. Taking the appropriate weighting of different frequencies into account as discussed in Section 4.3.4 and Appendix E, the estimate of the contrast in the least-squares sense is obtained using the following equation (Eq. E.5):

$$\chi_{n,\text{LS}} = \frac{1}{\Omega} \int_{-\infty}^{\infty} \frac{\sum_{s=1}^{N_s} w_n u_n^*}{k_0^4 \sum_{s=1}^{N_s} |u_n|^2} d\omega, \quad \text{with } \Omega = \int_{-\infty}^{\infty} d\omega. \quad (5.3.30)$$

An equivalent formulation was used in the original contrast source inversion method due to its simplicity [Van den Berg 1997]. However, it does not account for the fact that the contrast is also contained in the denominator of the object error functional  $E_S$  as can be seen from Eq. 5.3.18.

A more sophisticated approach is thus given by taking the entire object error term  $E_S$  into account [Van den Berg 1999]. To this end, an additional minimisation step with respect to the contrast  $\chi$  is performed to obtain a second update for the contrast. The update direction  $d_{\chi,n}$  is thereby taken from the contrast estimate  $\chi_{n-1}$  of the previous iteration into the direction indicated by the least-squares estimate  $\chi_{n,\text{LS}}$  of

Eq. 5.3.30:

$$\begin{aligned}
 d_{\chi,n} &= \sum_{\omega=\omega_1}^{\omega_N} \frac{\sum_{s=1}^{N_s} w_n u_n^*}{\sum_{s=1}^{N_s} k_0^4 |u_n|^2} - \chi_{n-1} \\
 &= \sum_{\omega=\omega_1}^{\omega_N} \frac{\sum_{s=1}^{N_s} (k_0^4 u_n \chi_{n-1} - w_n) u_n^*}{\sum_{s=1}^{N_s} k_0^4 |u_n|^2}.
 \end{aligned} \tag{5.3.31}$$

Note that the term in parentheses represents the object residual from the previous iteration. The denominator can thus be interpreted as a preconditioning of this search direction [Van den Berg 1999].

Whereas Van den Berg suggests an updating scheme based on the Polak-Ribière conjugate gradient directions, a different approach is chosen in this work. The usage of conjugate directions seems appropriate if the contrast is updated only by the second minimisation step with direction  $d_{\chi,n}$ . However, due to the fact that a first update of the contrast is obtained from Eq. 5.3.30 in every iteration, the usage of conjugate directions in a subsequent step has been found to have only limited benefit. Therefore, a simple line search for a minimum along the direction  $d_{\chi,n}$  is performed.

The optimal step size  $\alpha_\chi$  must minimise the object error  $E_S$  for this given search direction:

$$E_S(\chi_{n,LS} + \alpha_\chi d_{\chi,n}) = \sum_{\omega=\omega_1}^{\omega_N} \frac{\|k_0^4(\chi_{n,LS} + \alpha_\chi d_{\chi,n})u_n - w_n\|_S^2}{\|k_0^4(\chi_{n,LS} + \alpha_\chi d_{\chi,n})u_{inc}\|_S^2}. \tag{5.3.32}$$

Since the optimal value for  $\alpha_\chi$  cannot be determined analytically, Brent's method for minimisation without derivatives is applied [Brent 2002], an implementation of which was provided by Press et al. [Press 1996]. After determination of the step size  $\alpha_\chi$ , the second update of the contrast can be carried out:

$$\chi_n = \chi_{n,LS} + \alpha_\chi d_{\chi,n}. \tag{5.3.33}$$

As in Chapter 4, examples of the performance of the methods presented will be given after introducing all relevant approaches. Section 5.4 contains demonstrations of the capabilities of contrast source inversion in comparison to imaging results under the Born approximation presented in Section 4.3.7.

### ■ 5.3.3 Regularisation by total variation

Since the inclusion of multiple scattering constitutes a physically more accurate model of the behaviour of the plate, it is able to explain the measured data bet-

ter than the Born approximation used in the previous chapter. It has already been pointed out that the imaging problem is implicitly regularised by concurrent minimisation of both data and object equation, thereby making use of the imaging model including multiple scattering. However, the contrast source inversion method can further be stabilised and improved by applying additional regularisation. The approach of using total variation as a multiplicative constraint, which has proved to be useful under the Born approximation, can also be expected to be beneficial in this context. The helpfulness of total variation as regularisation constraint for contrast source inversion has been confirmed by Van den Berg et al. [Van den Berg 1999], with later improvements of the method given by [Van den Berg 2003] and [Abubakar 2005].

The inclusion of a total variation constraint requires modification of the contrast source inversion scheme. The total error to be minimised is given by the following expression:

$$E(w, \chi) = \left[ E_R(w) + E_S(w, \chi) \right] \times E_{\text{reg}}(\chi), \quad (5.3.34)$$

with  $E_{\text{reg}}$  being the multiplicative weighted  $L^2$ -norm regulariser of the contrast as given by Eq. 4.3.111 introduced in Section 4.3.6.2.

It can be seen that the multiplicative regularisation factor is only influenced by the contrast  $\chi$ , not by the contrast sources  $w$ . Therefore, the extra regularisation does not have to be taken into account when updating the contrast sources, and this first step discussed in Section 5.3.1 remains unaltered.

By analogy to the basic contrast source inversion scheme, the contrast is subsequently updated in two steps:

- (1) A least-squares estimate  $\chi_{n,\text{LS}}$  of the contrast is obtained from Eq. 5.3.30.
- (2) A second update is performed in order to minimise the error functional  $E(w, \chi)$ .

For the latter step, minimisation of the entire error functional is required, for which the gradient of  $E(w, \chi)$  with respect to  $\chi$  provides the search direction:

$$d_{\chi,\text{TV}} = \frac{\partial E(w, \chi)}{\partial \chi} = \frac{\partial E_S(w, \chi)}{\partial \chi} E_{\text{reg}}(\chi) + \left[ E_R(w) + E_S(w, \chi) \right] \frac{\partial E_{\text{reg}}(\chi)}{\partial \chi}. \quad (5.3.35)$$

Since this minimisation is carried out with the least-squares estimate  $\chi_{n,\text{LS}}$  as a starting point, the object error can be assumed to have already been minimised with respect to the contrast:

$$\left. \frac{\partial E_S(w, \chi)}{\partial \chi} \right|_{\chi=\chi_{n,\text{LS}}} = 0. \quad (5.3.36)$$

The search direction can thus be simplified:

$$d_{\chi,\text{TV}} = \left. \frac{\partial E(w, \chi)}{\partial \chi} \right|_{\chi=\chi_{n,\text{LS}}} = \frac{E_{\text{reg}}(\chi)}{\partial \chi}. \quad (5.3.37)$$

Van den Berg et al. suggest a preconditioned variation of this update direction [Van den Berg 2003], which has, however, not proved to be beneficial for the simulations carried out in this work.

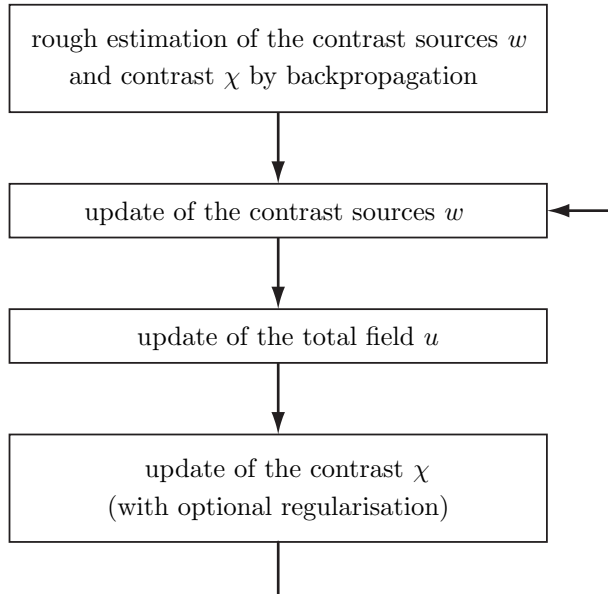
The optimal step size  $\alpha_{\chi,TV}$  cannot be calculated analytically and is, therefore, determined numerically using Brent's method [Brent 2002] by minimising the following expression:

$$\begin{aligned} E(w, \chi_{n,LS} + \alpha_{\chi,TV} d_{\chi,TV}) \\ = \left[ E_R(w) + E_S(w, \chi_{n,LS} + \alpha_{\chi,TV} d_{\chi,TV}) \right] \times E_{\text{reg}}(\chi_{n,LS} + \alpha_{\chi,TV} d_{\chi,TV}). \end{aligned} \quad (5.3.38)$$

Subsequently, the regularised update of the contrast is readily obtained:

$$\chi_n = \chi_{n,LS} + \alpha_{\chi,TV} d_{\chi,TV}. \quad (5.3.39)$$

Figure 5.1 gives an overview of the full contrast source inversion scheme with optional regularisation.




---

**Figure 5.1:** Overview of the contrast source inversion scheme.

---

## 5.4 Examples and discussion

The simulation examples introduced in Section 4.3.7 will in the following be used to assess the result achieved by the inclusion of multiple scattering in the imaging model. Figure 5.2 presents the images obtained with full circular coverage by sources and receivers, analogous to Fig. 4.34 in Chapter 4. The imaging results for limited coverage with a semicircle and a quarter of a circle are shown in Fig. 5.3 and Fig. 5.4, respectively. As a last example, the images obtained for two point-like scatterers with full circular coverage by sources and receivers are shown in Fig. 5.5.

First of all, it can be seen that contrast source inversion is able to recover the structure to be imaged by using only a single frequency if the coverage by sources and receivers is sufficient as illustrated in Fig. 5.2 in the case of full circular coverage. The usage of multiple frequencies provides additional robustness, which is especially needed if the object is illuminated and imaged from only one side (Figs. 5.3 and 5.4).

In comparison to imaging under the Born approximation as presented in the previous chapter, it can be stated that contrast source inversion without additional regularisation is able to obtain images with less noise and artefacts than Born inversion. It turns out that the artefacts in the images obtained by Born inversion are actually due to the multiple scattering between the defects; the effect not taken into account by the Born approximation shows up as ‘noise’ in the images. The more sophisticated model of contrast source inversion can explain the measured data better; it produces images of higher signal-to-noise ratio.

In all examples shown, it can be seen that the results obtained by contrast source inversion are comparable to those generated by Born inversion with minimum total variation as a regularisation constraint. However, the crucial difference between these images lies in their interpretation: whereas Born inversion with regularisation shapes the resulting image to comply to an a priori model of expected form, contrast source inversion uses actual physical evidence from the measurements to reconstruct the field variables and generate an image of inhomogeneities. This means that the result obtained by contrast source inversion does not depend on assumptions on the expected structure of the image; the chance of an incorrect interpretation is thus minimised by using a more sophisticated imaging model including multiple scattering.

Furthermore, it can be seen that remaining artefacts due to receiver noise in the image obtained by contrast source inversion can be damped by combining contrast source inversion with minimum total variation as additional regularisation constraint.

With respect to the purpose of pure detection of defects, it could be argued that imaging under the Born approximation is sufficient and the additional computational burden of contrast source inversion is unnecessary. In the end, almost all of the

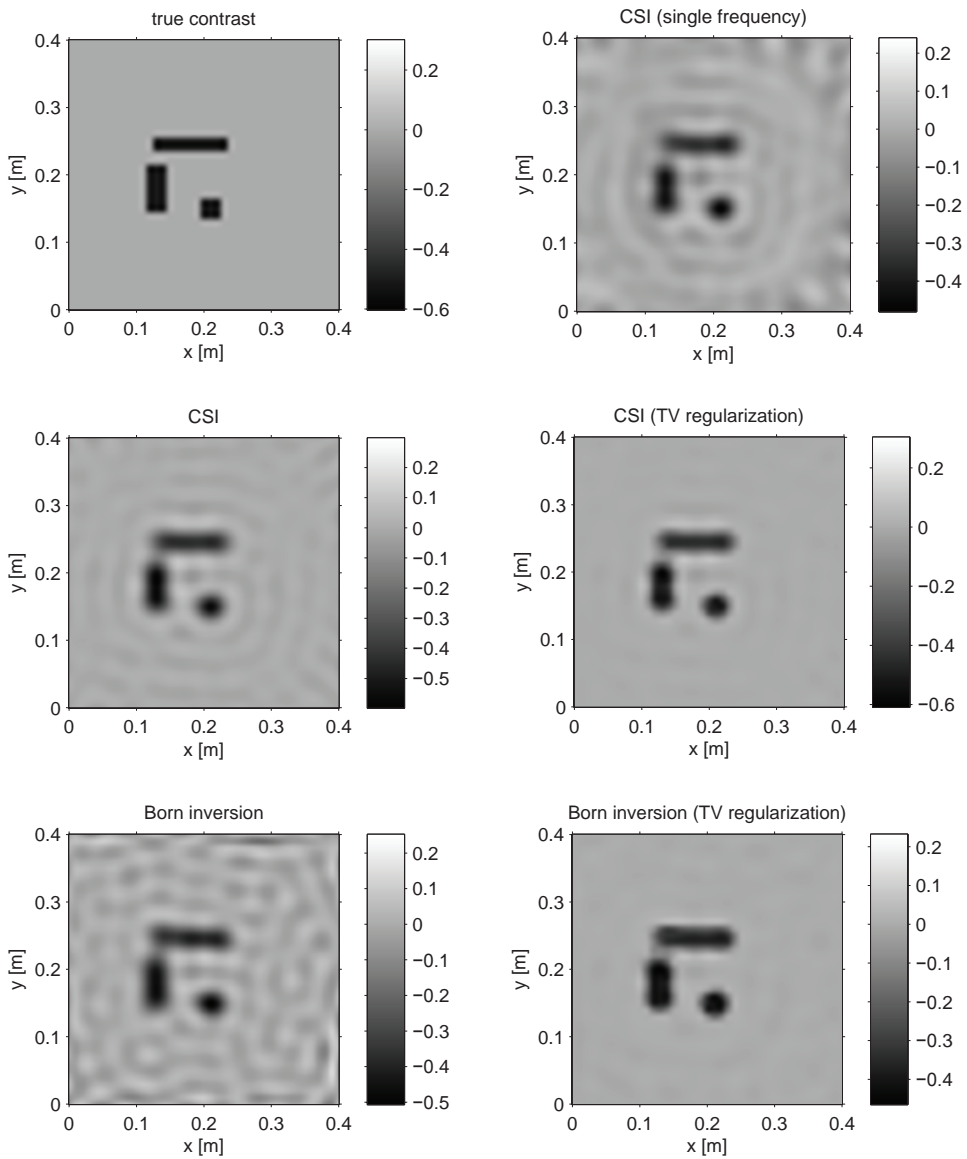


**Figure 5.2:** Imaging results for the setup shown in Fig. 4.32 with full circular coverage by sources and receivers, compare also to Fig. 4.34.

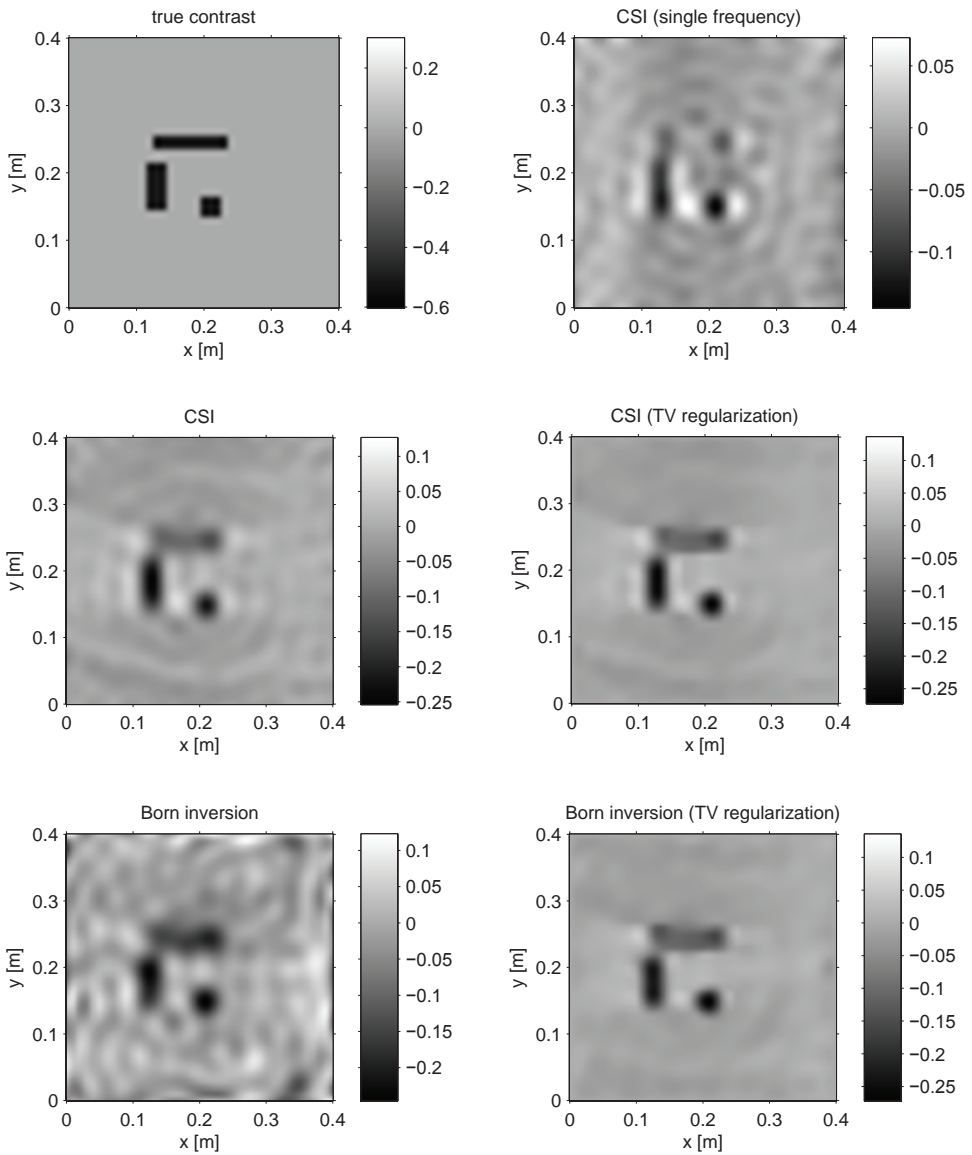


**Figure 5.3:** Imaging results for the setup shown in Fig. 4.32 using sources and receivers only on the right-hand side, compare also to Fig. 4.35.

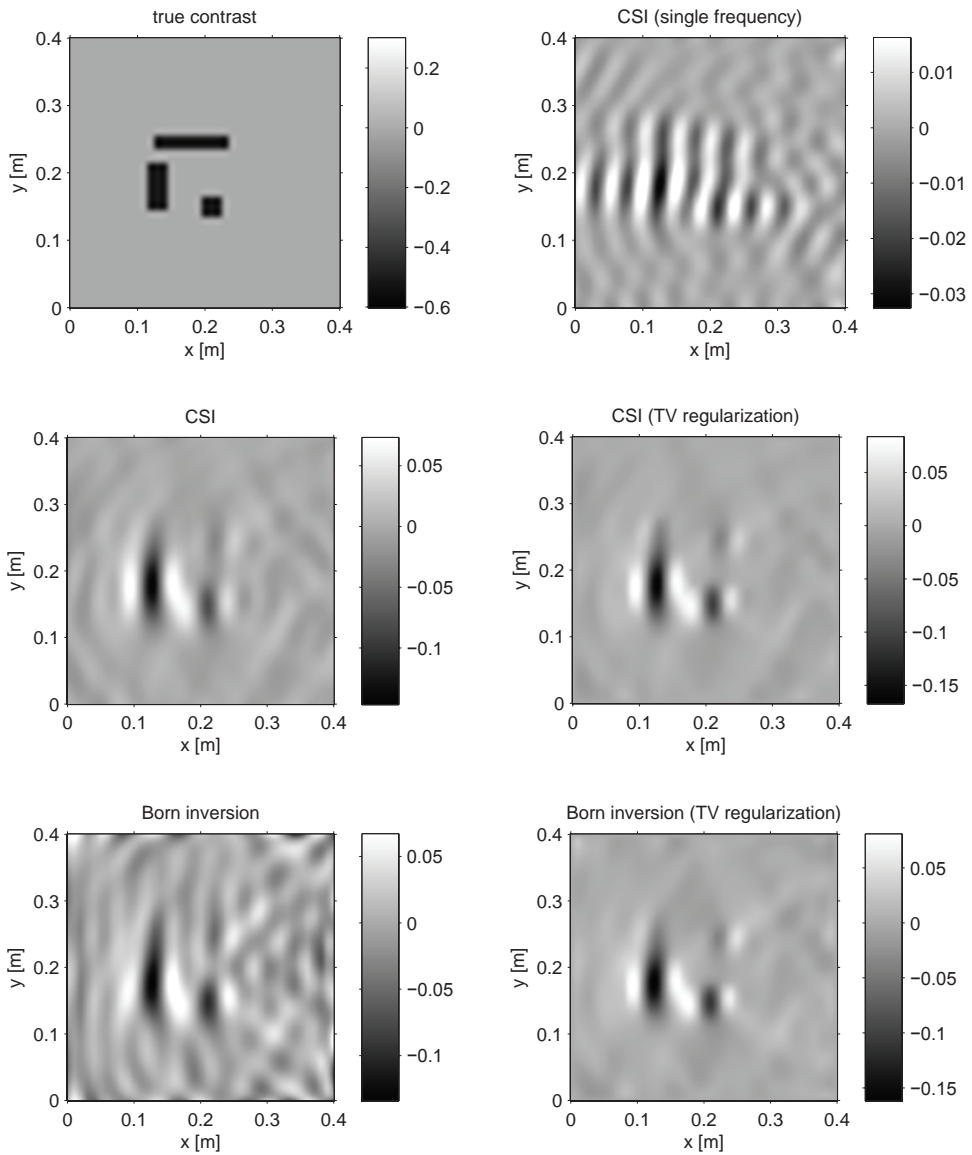


**Figure 5.4:** Imaging results for the setup shown in Fig. 4.32 with sources and receivers positioned only within a quarter of a circle to the right of the object, compare also to Fig. 4.36.

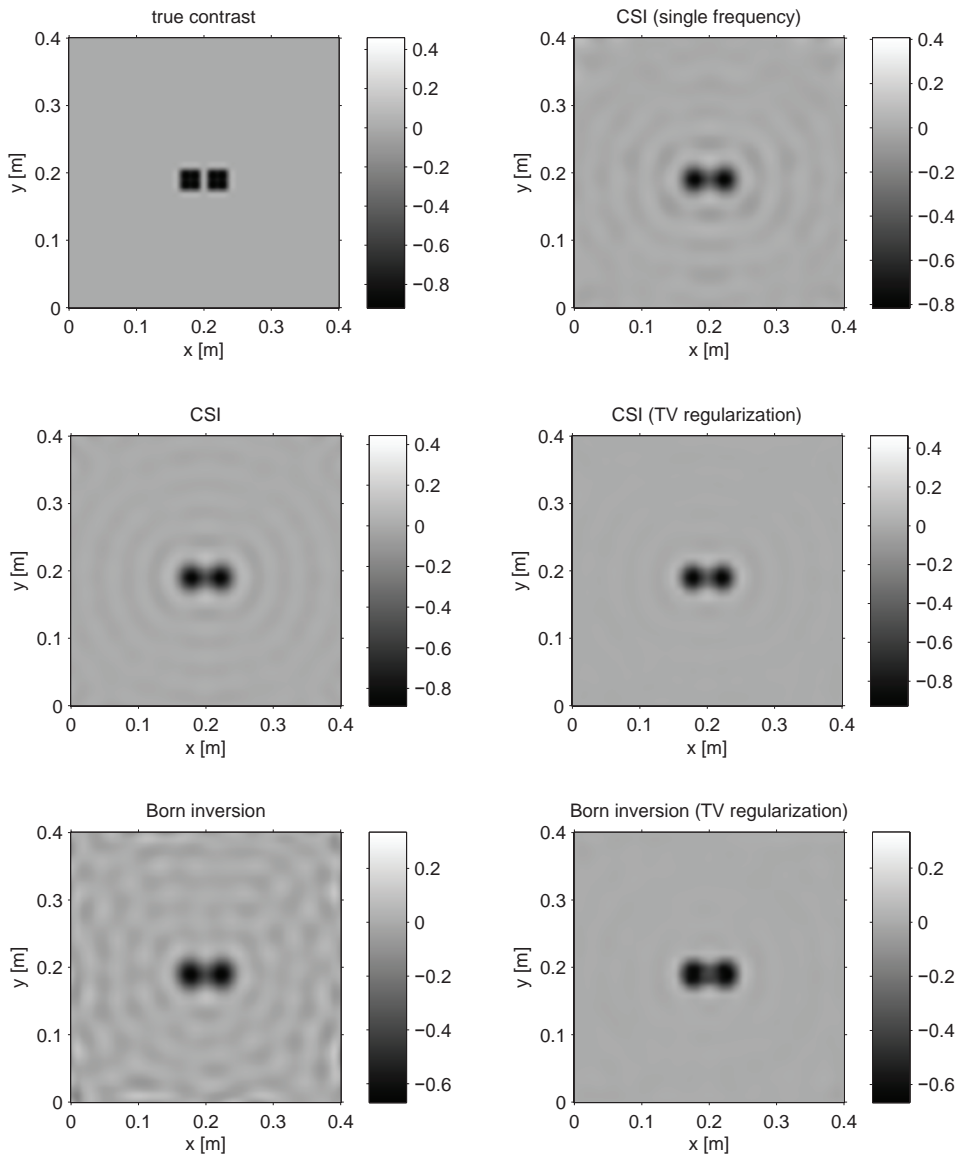


**Figure 5.5:** Imaging results for two point-like scatterers as shown in Fig. 4.33 with full circular coverage by sources and receivers, compare also to Fig. 4.37.

images show that the presence of defects is appropriately indicated. However, it becomes also evident that the imaging model including multiple scattering has the ability to resolve complex defect constellations with higher resolution. Furthermore, it should be noted that contrast source inversion is needed in order to retrieve the size and *severity* of the defects.

Figure 5.5 presents such a situation, in which only contrast source inversion is able to estimate the strength of the scatterers correctly as can be seen from the different colour scales of the results obtained by different methods. Hence, a good estimate of the severity of the defect requires an imaging model which takes multiple scattering into account. However, it should be noted that sufficient angular coverage by the transducers is needed for this purpose as well. Otherwise, the severity of the defects is underestimated as can be seen in Figs. 5.3 and 5.4.

## 5.5 Modelling of finite plates

Analogously to Section 4.4, it is necessary to investigate how the techniques derived above can be applied to finite plates. An adaptation is most easily achieved by employing the Green's function of the finite plate.

### ■ 5.5.1 Adaptation of the incident field

The Green's function for the finite plate does not necessarily have to be used for the calculation of both the incident and the scattered field. As a first approximation, the Green's function of the finite plate can thus be applied to determine only the incident field, exactly as in the case of imaging in finite plates under the Born approximation presented in the previous chapter. This way, the scattering of the boundary reflections by a material inhomogeneity is taken into account. However, the reflections of the scattered field at the boundaries of the plate are neglected.

### ■ 5.5.2 Usage of the Green's function for finite plates

Assuming that the Green's function of the plate is known, the calculation of the incident field due to sources at arbitrary positions on the plate is straightforward. The usage of the Green's function for the calculation of the scattering can, however, pose a problem: the Green's function in finite plates depends on the position of excitation as shown in Section 4.4.1. In a straightforward implementation, the operator  $\mathcal{G}_D$  in the object equation (Eq. 5.1.1) would require the storage of plate responses  $\tilde{G}(\underline{x}, \underline{x}_0, \omega)$  to excitation at all possible points  $\underline{x}_0$  in the domain to be imaged. This approach would pose considerable memory requirements, even for relatively small domains.

Nevertheless, it might be possible to use the precomputed modal shapes  $\xi_m(\mathbf{x})$  of the plate. This idea requires the storage of modal shapes for a number of eigenfrequencies. Especially in the case of low damping, the number of relevant eigenfrequencies can be expected to be significantly lower than the number of points in the discretised domain. A disadvantage is the fact that the Green's function has to be computed 'on the fly', which is anticipated to slow down the contrast source inversion approach significantly. Further decrease in speed has to be expected due to the fact that the operator  $\mathcal{G}_D$  represents a position-dependent convolution operator, which can no longer be implemented by application of Fourier transforms.

### ■ 5.5.3 Modelling of plate boundaries by the contrast

An alternative option is the inclusion of the boundaries in the contrast source inversion itself. The boundaries of a plate can be modelled as a distribution of discontinuities in the material. It would then be sufficient to create a discontinuity in the contrast in order to model a boundary and generate a reflection.

Therefore, the following approach has been tested:

- The imaging domain is chosen large enough to include the plate in its entirety.
- The contrast is set to a high value for samples in the imaging domain that are outside the plate.
- The contrast source inversion scheme is applied with the contrast values outside the plate held fixed.

Due to the values of high contrast outside the plate, the field is expected to be trapped between these artificially created boundaries. Outside the plate, the field decreases rapidly towards zero due to high contrast values.

First of all, the question arises what contrast values have to be chosen in order to generate a full reflection. In theory, the contrast outside the plate is infinite. For practical cases, the contrast required to generate a reflection with a reflection coefficient close to one must be expected to be several orders of magnitudes larger than the contrasts of inhomogeneities within the plate to be imaged.

Unfortunately, it turns out that this approach cannot be realised in a straightforward way. Even if the boundary contrast is assumed to be known in terms of position and strength and kept fixed while performing contrast source inversion, the difference in magnitude between the boundary contrast and possible inhomogeneities within the plate prevents the method of contrast source inversion from finding a useful optimum [Hörchens 2009]. It is thus either possible to detect the boundaries at the price of losing sensitivity for small defects, or to image the defects without being able to model the boundaries by a high contrast.

#### ■ 5.5.4 Extension of contrast source inversion for an inhomogeneous background medium

Nevertheless, there exists another possible approach of including the boundaries in cases in which the dimensions of the plate under investigation are known. The original contrast source inversion method based on the integral equations with a homogeneous background medium has recently been extended by Abubakar et al. to deal with an inhomogeneous background medium [Abubakar 2008]. In this approach, the inhomogeneity in the background medium is included by determining the Green's function from a finite difference scheme, which is then combined with contrast source inversion.

With respect to the intended application for flexural wave fields in plates, the finite difference scheme can be used to model the plate of finite extent and calculate its response to excitation, thereby including the boundary reflections. In contrast to the original proposal by Abubakar et al. [Abubakar 2008], the usage of perfectly matched layers is not required since the reflections at the boundaries of the modelled domain are explicitly desired.

While being more promising than the modelling of the boundary reflections by high contrast values, this approach lacks the ability to retrieve the position of the boundaries from the measurement itself.

#### ■ 5.5.5 Recommendations for further research

The inclusion of boundary reflections into the imaging model is of interest for imaging both under and beyond the Born approximation. If the structures to be inspected are of simple shape, such as polygonal plates, for instance, the mirror image source model might be sufficient to include the effects of boundary reflections in the imaging model with only a low number of parameters to be estimated. In this case, these unknown parameters describe the position and conditions of the boundaries. It can be assumed that properties of the boundaries can be determined independently of the possible inhomogeneities, such that the estimation of the boundaries can be carried out as a separate procedure by inversion of the measured data. This approach enables the usage of retrieved positions for the imaging of the object under investigation in a subsequent step.

Adaptivity of the boundary estimation to completely arbitrary shapes is an interesting goal in terms of the achievable flexibility for different applications. However, this approach requires a suitable parametric description of the boundaries. The number of unknown parameters should be kept as small as possible to facilitate a reliable estimate. Therefore, the usage of prior knowledge, for instance the rough shape of the boundary, is recommended.

## 5.6 Summary

In this chapter, methods for imaging beyond the Born approximation have been presented. The inclusion of multiple scattering has been shown to provide improved imaging results with higher resolution, albeit at a significant computational effort in comparison to techniques presented in Chapter 4.

An important difference with respect to imaging under the Born approximation based on regularised inversion is the fact that imaging results obtained using contrast source inversion are based on a sophisticated physical model including multiple scattering and do not depend on arbitrary additional regularisation. The image is thus to a greater extent based on evidence from the measured data rather than on prior knowledge of the structure to be expected.

The inclusion of the reflections generated by the boundaries forms a useful extension to the imaging procedure. The problem of estimating the boundary positions and properties directly from measurements has been proposed for future research.



# Conclusions and outlook

*If I'd asked people what they wanted,  
they would have asked for a better horse.*

(Henry Ford, 1863 – 1947)

In this thesis, the equations governing the propagation of flexural waves in beams and plates have been used to derive methods for the analysis of dispersive wave fields. Emphasis has been put on approaches for imaging of flexural wave fields. To this end, well-established techniques from fields such as seismics, medical acoustics, radar imaging, material inspection and room acoustics have been combined with past and current research on the analysis of dispersive wave fields.

## 6.1 Conclusions

The direct analysis of flexural wave fields is hampered by the effects of dispersion, which affect the resolution and the separability of different wave fronts adversely. With respect to this problem, the methods for dispersion removal presented in Chapter 3 can be regarded as preliminary tools allowing for separate assessment of different events in the wave field, enabling the extraction of primary and secondary wave fronts as well as the rough characterisation of discontinuities in the object under investigation.

In this context, the dispersion relation has served as a model which can be applied to perform a transformation from a temporal to a dispersion-free spatial representation of the wave field via the spectral domain. As a central result, it has been shown that the requirements for optimal resolution with respect to sampling and desired spectrum are dictated by the spatial output of the presented methods. These requirements can be transferred to the temporal input signals by means of the dispersion relation, leading to (possibly) counterintuitive demands such as non-equidistant sampling or non-white spectral characteristics. In essence, the medium determines the methods for its analysis. Furthermore, approaches for the estimation of unknown parameters based on a resolution criterion have been presented.

In Chapter 4, the view has been extended from information available at a single point to the possibilities of array-based imaging. Starting out from a systematic analysis of the resolution obtained by imaging methods under the Born approximation, a tightened sampling criterion for finite arrays has been derived. Both the propagation medium and the array have been shown to act as spectral filters limiting the obtainable resolution. The ill-posedness of the imaging problem is circumvented by several standard methods for imaging. However, the solution of the inverse problem is expected to exploit optimally the possibilities available within the physical resolution limit. In this context, stabilisation and regularisation form indispensable tools to tackle the ill-posedness and obtain useful results, in which noise and artefacts do not disturb the features of interest. Whereas sparse regularisation is rather biased, the total variation constraint has proved useful in a number of experiments.

Furthermore, it has been shown how the choice of the frequencies used in the image formation and the array aperture can be combined to cover the wavenumber spectrum containing information about the object under investigation optimally. In addition, suggestions for the extension of the imaging methods for usage on finite plates have been presented. The incorporation of reflections from the plate boundaries is expected to broaden the range of possible applications.

In Chapter 5, it has been shown that the inclusion of multiple scattering has the potential of increasing the available resolution. To this end, a simplified scalar scattering model has been used in the inverse scattering problem. The scattering model is closer to reality than the Born approximation. Therefore, it can explain the observed data better. Whereas inversion under the Born approximation has to be combined with regularisation to suppress noise-like artefacts due to the neglecting of multiple scattering, inversion beyond the Born approximation can make use of this information and actually apply it to increase the quality of the obtained image, in terms of both resolution and noise level.

While all results have been presented for flexural wave fields, it should be noted that most of the findings are directly applicable to dispersive wave fields in general, thereby providing a framework that can, for instance, be used for imaging with other types of guided waves than only the flexural mode.

## 6.2 Recommendations for further research

Based on the current state of the art and the results presented in this work, the following recommendations for further research can be made:

- **Forward and inverse transformation for dispersion removal**

The procedure for dispersion removal presented in Section 3.4 should be complemented with an analogous inverse transformation. This way, the method for dispersion removal can be used to separate and extract single events from

the wave field. Application of the inverse transform provides a wave field containing only the desired events in their original dispersive state. Subsequently, imaging methods can be applied.

- **Extensions for imaging in finite plates**

The methods for imaging in finite plates presented in Section 4.4 and Section 5.5 require further extension. It would be desirable to estimate the position of the boundaries and the boundary conditions from measurements, along with an image of discontinuities present in the plate. This way, the conditions of the structure under investigation can be determined in detail. Furthermore, the information on the boundaries can be used for the modelling of the reflections to be expected.

- **Derivation of an advanced scattering model**

The scattering model derived in Section 2.5.3 assumes the bending stiffness to be constant and allows only for the variation of the mass density. If this approximation is abandoned, it should be possible to obtain results that provide better quantitative information on local deviations of material parameters. However, the effort for modelling and inversion increases significantly.

- **Applications to other types of guided waves**

Most of the methods presented in this thesis can directly be applied for the analysis and imaging of other kinds of dispersive waves, such as the general family of Lamb waves in plates. Similar kinds of dispersive waves can also be found in shells and cylindrical structures, such as curved encasements and pipelines. The derived methods can be applied to these structures by adaptation of the Green's function and the dispersion relation. For curved surfaces, the orthotropic character of the propagation is expected to pose additional challenges. Further possible extensions are given by application to inhomogeneous materials such as wood or laminated composites. Nevertheless, this short list of possible structural shapes and materials illustrates the potential of the derived methods for industrial applications.

## 6.3 Outlook

From the current research on dispersive waves and imaging methods, several trends can be observed:

- **Improved modelling of wave fields**

The complexity and accuracy of models for the generation, propagation and reception of dispersive waves has steadily increased over the last centuries. An improvement in modelling, for instance by including multiple scattering, helps to increase the achievable resolution in imaging. On the other hand, the

degree of accuracy required for an image is determined by the application. In general, a balance must be found between the effort and the achieved result. The present work indicates that there is still more potential to be exploited.

- **Higher resolution due to improved inverse methods in imaging**

To a great extent, the imaging methods applied for non-destructive inspection in the industry are based on backpropagation or similar techniques due to the simplicity and inherent robustness. Imaging by inversion can and will be accepted only if the result is stable, accurate and reproducible. From this perspective, the combination of inversion and total variation is promising.

- **Improved visualisation of detection results**

Whereas it is expected that an expert will be needed to operate the imaging equipment properly, the visualisation of the measured data and the formation of an image of the medium under investigation will continue to approach a level of photographic representation that can easily be interpreted. This trend has become more pronounced over the past decades. However, there are still many applications in which the position of inhomogeneities is determined based on visual representations of signal amplitude over travel time or distance to receivers. In the end, the representation of discontinuities as an image is expected to prevail, simply due to the minimised risk of misinterpretation by the human observer.

With such an amount of work left to do and so many unexplored ideas in mind, it is only fortunate that imaging is a true interdisciplinary problem, and that it can be expected that the cross-fertilisation of different disciplines, as observed in the past and extensively used for the work presented in this thesis, will also help the evolution of future developments.

# A

## Fourier transform

The conventions used for temporal and spatial Fourier transforms are defined in this appendix.

### A.1 Fourier transforms with respect to time

The forward Fourier transform from time domain to frequency domain is given by the following expression:

$$\tilde{u}(\omega) = \mathcal{F}[u(t)] = \int_{-\infty}^{\infty} u(t)e^{-j\omega t} dt, \quad (\text{A.1})$$

with the inverse transform to the time domain being defined as:

$$u(t) = \mathcal{F}^{-1}[\tilde{u}(\omega)] = \frac{1}{2\pi} \int_{-\infty}^{\infty} \tilde{u}(\omega)e^{j\omega t} d\omega. \quad (\text{A.2})$$

### A.2 Fourier transforms with respect to space

For the Fourier transform from the spatial to the wavenumber domain, the complex conjugate of the exponential kernel is used. This convention ensures that waves can travel into the positive directions along space axes [Claerbout 2009]. As an example, the field by a point source situated at the origin of the coordinate system with source signal  $S(t)$  is taken, which is observed at a certain point in time  $t_0$  and distance from the source  $x_0$ . Neglecting any damping, the observed field can be written in the following form:

$$p(x_0, t_0, t) = S\left(t - \frac{x_0}{c} + t_0\right), \quad (\text{A.1})$$

with  $c$  being the speed of propagation. If the point of observation is moved away from the source ( $x_1 > x_0$ ) without changing the time of observation, the source signal

observed at this new point  $x_1$  was released *earlier* by the source than the signal observed at the first observation point  $x_0$ . However, if the position of observation is kept constant and a later point in time ( $t_1 > t_0$ ) is chosen, a *later* part of the source signal is registered. Therefore, the choice of using different signs for time and space in the above equation is physically motivated. The kernels of the Fourier transforms for spatio-temporal analysis are chosen equivalently.

The spatial Fourier transformation is presented for the two-dimensional case:

$$\tilde{u}(k_x, k_y) = \mathcal{F}[u(x, y)] = \iint_{-\infty}^{\infty} u(x, y) e^{j(k_x x + k_y y)} dx dy, \quad (\text{A.2})$$

with the associated inverse transform given by the following equation:

$$u(x, y) = \mathcal{F}^{-1}[\tilde{u}(k_x, k_y)] = \frac{1}{(2\pi)^2} \iint_{-\infty}^{\infty} \tilde{u}(k_x, k_y) e^{-j(k_x x + k_y y)} dk_x dk_y. \quad (\text{A.3})$$

# B

## Derivation of the Green's functions

### B.1 Green's function for the one-dimensional wave equation

The one-dimensional Helmholtz equation for flexural waves is given by [Cremer 2005]:

$$\frac{\partial^4 u}{\partial x^4} - k_B^4 u = 0, \quad (\text{B.1})$$

with the wavenumber  $k_B$  for a beam defined as

$$k_B = \sqrt{\omega} \sqrt[4]{\frac{m'}{B'}}. \quad (\text{B.2})$$

The Green's function  $G(x_0, x, t)$  can be determined using the following inhomogeneous equation:

$$\frac{\partial^4}{\partial x^4} G(x, x_0, t) - k_B^4 G(x, x_0, t) = \delta(x - x_0). \quad (\text{B.3})$$

Application of a spatial Fourier transform (see appendix A) leads to the following representation in the wavenumber-frequency domain:

$$(k_x^4 - k_B^4) \tilde{G}(k_x, x_0, \omega) = e^{jk_x x_0}. \quad (\text{B.4})$$

Hence, the Green's function is given by the following expression:

$$\tilde{G}(k_x, x_0, \omega) = \frac{e^{jk_x x_0}}{k_x^4 - k_B^4} = \frac{e^{jk_x x_0}}{2k_B^2} \left( \frac{1}{k_x^2 - k_B^2} - \frac{1}{k_x^2 + k_B^2} \right). \quad (\text{B.5})$$

In the next step, an inverse spatial Fourier transform is applied:

$$\tilde{G}(x, x_0, \omega) = \frac{1}{4\pi k_B^2} \left[ \int_{-\infty}^{\infty} \frac{e^{-jk_x \Delta x}}{(k_x + k_B)(k_x - k_B)} dk_x - \int_{-\infty}^{\infty} \frac{e^{-jk_x \Delta x}}{(k_x - jk_B)(k_x + jk_B)} dk_x \right], \quad (\text{B.6})$$

with  $\Delta x = |x - x_0|$  representing the distance to the source point, thereby making use of the symmetry of the problem.

The integrals can be solved by contour integration using Cauchy's integral formula [Griffiths 2005]. The contours are chosen as shown in Fig. B.1.

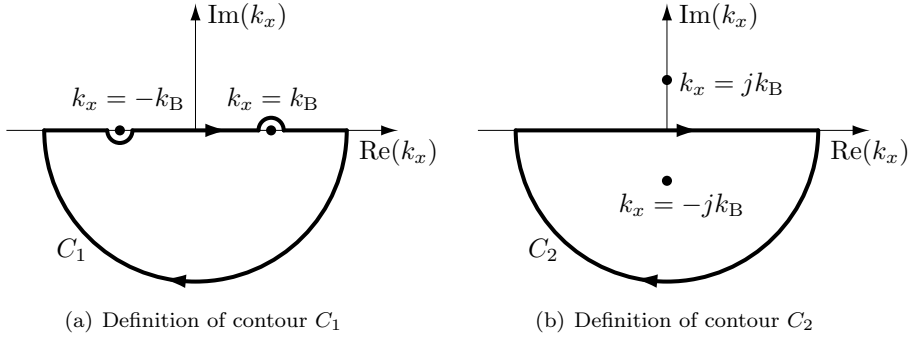


**Figure B.1:** Contours for the integrals of Eq. B.7.

Eq. B.6 can therefore be rewritten:

$$\tilde{G}(x, x_0, \omega) = \frac{1}{4\pi k_B^2} \left[ \oint_{C_1} \frac{e^{-jk_x \Delta x}}{(k_x + k_B)(k_x - k_B)} dk_x - \oint_{C_2} \frac{e^{-jk_x \Delta x}}{(k_x - jk_B)(k_x + jk_B)} dk_x \right]. \quad (\text{B.7})$$

Application of the residue theorem leads to:

$$\tilde{G}(x, x_0, \omega) = \frac{j}{2k_B^2} \left( -\frac{e^{-jk_B \Delta x}}{2k_B} - \frac{e^{-k_B \Delta x}}{2jk_B} \right). \quad (\text{B.8})$$

The one-dimensional Green's function consisting of a propagating and an evanescent part is therefore given by:

$$\tilde{G}(x, x_0, \omega) = -\frac{1}{4k_B^3} (je^{-jk_B \Delta x} + e^{-k_B \Delta x}). \quad (\text{B.9})$$

## B.2 Green's function for the two-dimensional wave equation

The Helmholtz equation for flexural waves in a plate is given by the following expression [Cremer 2005]:

$$\nabla^4 u + \frac{m''}{B''} \frac{\partial^2 u}{\partial t^2} = 0. \quad (\text{B.1})$$

The Green's function  $G(\underline{x}, \underline{x}_0, t)$  is the solution to the following inhomogeneous equation:

$$\nabla^4 G(\underline{x}, \underline{x}_0, t) - k_P^4 G(\underline{x}, \underline{x}_0, t) = \delta(\underline{x} - \underline{x}_0), \quad (\text{B.2})$$

with  $\underline{x}_0 = (x_0, y_0)^T$  being the position of the source.

The wavenumber for plates  $k_P$  is given by

$$k_P = \sqrt{\omega} \sqrt[4]{\frac{m''}{B''}}. \quad (\text{B.3})$$

Application of a two-dimensional spatial Fourier transform leads to the following representation in the wavenumber-frequency domain:

$$\left[ (k_x^2 + k_y^2)^2 - k_P^4 \right] \tilde{\tilde{G}}(\underline{k}, \underline{x}_0, \omega) = e^{j\underline{k} \cdot \underline{x}_0}, \quad (\text{B.4})$$

with  $\underline{k} = (k_x, k_y)^T$ .

Hence, the Green's function is given by the following expression:

$$\tilde{\tilde{G}}(\underline{k}, \underline{x}_0, \omega) = \frac{e^{j\underline{k} \cdot \underline{x}_0}}{(k_x^2 + k_y^2)^2 - k_P^4}. \quad (\text{B.5})$$

Splitting of the denominator leads to:

$$\tilde{\tilde{G}}(\underline{k}, \underline{x}_0, \omega) = \frac{e^{j\underline{k} \cdot \underline{x}_0}}{2k_P^2} \left( \frac{1}{k_x^2 + k_y^2 - k_P^2} - \frac{1}{k_x^2 + k_y^2 + k_P^2} \right). \quad (\text{B.6})$$

In the next step, an inverse spatial Fourier transform is applied:

$$\tilde{G}(\underline{x}, \underline{x}_0, \omega) = \frac{1}{8(\pi k_P)^2} \left[ \iint_{-\infty}^{\infty} \frac{e^{-j\underline{k} \cdot (\underline{x} - \underline{x}_0)}}{k_x^2 + k_y^2 - k_P^2} dk_x dk_y - \iint_{-\infty}^{\infty} \frac{e^{-j\underline{k} \cdot (\underline{x} - \underline{x}_0)}}{k_x^2 + k_y^2 + k_P^2} dk_x dk_y \right]. \quad (\text{B.7})$$

The integrals with  $k_y$  as integration variable can be solved by contour integration [Griffiths 2005]. The contours are chosen as shown in Fig. B.2.

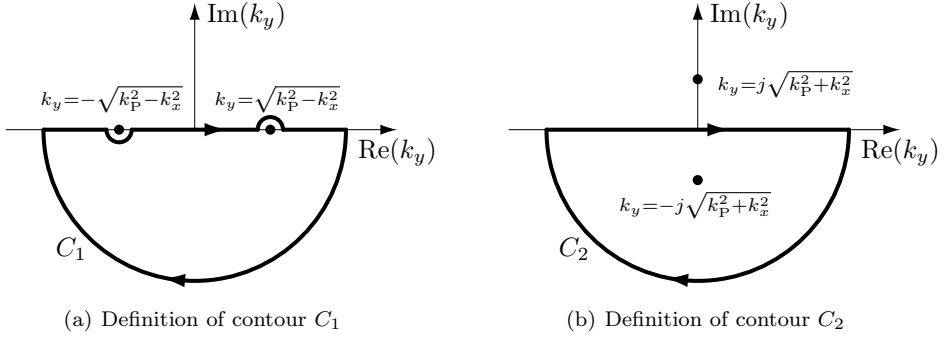


**Figure B.2:** Contours for the integrals of Eq. B.7.

Eq. B.7 can thus be rewritten:

$$\tilde{G}(\underline{x}, \underline{x}_0, \omega) = \frac{1}{8(\pi k_P)^2} \left[ \int_{-\infty}^{\infty} \oint_{C_1} \frac{e^{-j\mathbf{k} \cdot (\underline{x} - \underline{x}_0)}}{k_x^2 + k_y^2 - k_P^2} dk_y dk_x - \int_{-\infty}^{\infty} \oint_{C_2} \frac{e^{-j\mathbf{k} \cdot (\underline{x} - \underline{x}_0)}}{k_x^2 + k_y^2 + k_P^2} dk_y dk_x \right]. \quad (\text{B.8})$$

Application of the residue theorem leads to:

$$\tilde{G}(\underline{x}, \underline{x}_0, \omega) = \frac{j}{4\pi k_P^2} \left[ - \int_{-\infty}^{\infty} \frac{e^{-jk_x(x-x_0) - j\sqrt{k_P^2 - k_x^2}(y-y_0)}}{2\sqrt{k_P^2 - k_x^2}} dk_x - \int_{-\infty}^{\infty} \frac{e^{-jk_x(x-x_0) - \sqrt{k_P^2 + k_x^2}(y-y_0)}}{2j\sqrt{k_P^2 + k_x^2}} dk_x \right]. \quad (\text{B.9})$$

A number of substitutions are carried out in order to rewrite the integrals according to Fokkema and Van den Berg [Fokkema 1993]. The following substitutions are performed for the first integral in Eq. B.9:

$$k_x = k_P \cos(\theta - j\Psi) \quad (\text{B.10a})$$

$$dk_x = jk_P \sin(\theta - j\Psi) d\Psi \quad (\text{B.10b})$$

$$\sqrt{k^2 - k_x^2} = k_P \sin(\theta - j\Psi). \quad (\text{B.10c})$$

The following substitutions are performed for the second integral in Eq. B.9:

$$k_x = -jk_P \cos(\theta - j\Psi) \quad (\text{B.11a})$$

$$dk_x = k_P \sin(\theta - j\Psi) d\Psi \quad (\text{B.11b})$$

$$\sqrt{k^2 + k_x^2} = k_P \sin(\theta - j\Psi). \quad (\text{B.11c})$$

Furthermore, these substitutions are carried out for both integrals of Eq. B.9:

$$x - x_0 = \Delta x \cos(\theta) \quad (\text{B.12a})$$

$$y - y_0 = \Delta x \sin(\theta) \quad (\text{B.12b})$$

$$\text{with } \Delta x = \sqrt{(x - x_0)^2 + (y - y_0)^2}. \quad (\text{B.12c})$$

Eq. B.9 is then rewritten as

$$\tilde{G}(\underline{x}, \underline{x}_0, \omega) = \frac{1}{8\pi k_P^2} \left[ \int_{-\infty}^{\infty} d\Psi e^{-jk_P \Delta x \cosh(\Psi)} - \int_{-\infty}^{\infty} d\Psi e^{-k_P \Delta x \cosh(\Psi)} \right], \quad (\text{B.13})$$

for which the following identity has been used:

$$\cosh(\Psi) = \cos(j\Psi) = \cos(\theta - j\Psi) \cos(\theta) + \sin(\theta - j\Psi) \sin(\theta). \quad (\text{B.14})$$

The integrals of Eq. B.13 can be written as Hankel functions, see section B.3. Therefore, the two-dimensional Green's function is given by the following expression consisting of a propagating and an evanescent part:

$$\tilde{G}(\underline{x}, \underline{x}_0, \omega) = -\frac{j}{8k_P^2} \left[ H_0^{(2)}(k_P \Delta x) - H_0^{(2)}(-jk_P \Delta x) \right]. \quad (\text{B.15})$$

### B.3 Integral representation of the Hankel function of the second kind

According to Abramowitz en Stegun [Abramowitz 1964], the modified Bessel function  $K_0(k\Delta x)$  can be represented by the following integral:

$$K_0(k\Delta x) = \int_0^{\infty} d\Psi e^{-k\Delta x \cosh(\Psi)}. \quad (\text{B.1})$$

Exploiting the symmetry of the integrand, the integral can be extended:

$$K_0(k\Delta x) = \frac{1}{2} \int_{-\infty}^{\infty} d\Psi e^{-k\Delta x \cosh(\Psi)}. \quad (\text{B.2})$$

Using the relations between the modified Bessel function  $K_0(k\Delta x)$  and the Hankel function of the second kind  $H_0^{(2)}(k\Delta x)$  [Abramowitz 1964],

$$K_0(k\Delta x) = -\frac{j\pi}{2} H_0^{(2)}(-jk\Delta x), \quad (\text{B.3})$$

the following integral representations can be obtained for the Hankel function of the second kind:

$$H_0^{(2)}(k\Delta x) = -\frac{1}{j\pi} \int_{-\infty}^{\infty} d\Psi e^{-jk\Delta x \cosh(\Psi)}, \quad (\text{B.4})$$

$$H_0^{(2)}(-jk\Delta x) = -\frac{1}{j\pi} \int_{-\infty}^{\infty} d\Psi e^{-k\Delta x \cosh(\Psi)}. \quad (\text{B.5})$$

## Inverse Fourier transformation of a distance-dependent matched filter

This appendix deals with the derivation of a time domain representation of the distance-dependent matched filter given in Section 3.3:

$$q(x) = \int_{-\infty}^{\infty} \tilde{F}_D(x, \omega) \tilde{u}(\omega) d\omega. \quad (\text{C.1})$$

First, the distance-dependent filter function  $\tilde{F}_D(x, \omega)$  as given in Eq. 3.3.13 is inserted and the input signal  $\tilde{u}(\omega)$  is replaced by the Fourier transform of its time domain counterpart:

$$q(x) = \int_{-\infty}^{\infty} e^{j\frac{\sqrt{\omega}}{A}x} \int_{-\infty}^{\infty} u(t) e^{-j\omega t} dt d\omega. \quad (\text{C.2})$$

A similar integration problem has been solved by Margrave in the context of time-variant convolution [Margrave 1998]. The order of integration can be changed under the assumption that the integrand is continuous and that the Fourier transform converges. It is assumed that these prerequisites are met, such that Eq. C.2 can be rewritten in the following form:

$$q(x) = \int_{-\infty}^{\infty} u(t) \left( \int_{-\infty}^{\infty} e^{j\frac{\sqrt{\omega}}{A}x} e^{-j\omega t} d\omega \right) dt. \quad (\text{C.3})$$

Using the substitution  $\tau = -t$ , the term in parentheses can be written as an inverse Fourier transform:

$$q(x) = -2\pi \int_{-\infty}^{\infty} u(-\tau) \left( \frac{1}{2\pi} \int_{-\infty}^{\infty} e^{j\frac{\sqrt{\omega}}{A}x} e^{j\omega\tau} d\omega \right) d\tau. \quad (\text{C.4})$$

Carrying out this inverse Fourier transform and substituting again  $t = -\tau$ , the term in parentheses reduces to the dispersive wavelet  $W(x, t)$  defined in Section 3.1:

$$q(x) = 2\pi \int_{-\infty}^{\infty} u(t) W(x, t) dt. \quad (\text{C.5})$$

The presence of a source at distance  $x$  is thus determined by correlating the input signal  $u(t)$  with the dispersive wavelet for this specific distance.

# Forward and adjoint operators for acoustical imaging

## D.1 Definition of the spaces

In order to present the operators for acoustical imaging and derive their adjoints, some inner product spaces have to be defined first.

The *contrast space*  $X$  is the space of spatial coordinates  $\underline{x}$  with the following inner product:

$$\langle a(\underline{x}), b(\underline{x}) \rangle_X = \int_{-\infty}^{\infty} a(\underline{x}) b^*(\underline{x}) d\underline{x}. \quad (\text{D.1})$$

The form of the *source space*  $S$  depends on the context:

- For the imaging of a continuous distribution of sources as described in Section 4.2, it is equivalent to the contrast space  $X$  defined above.
- For the imaging of a distribution of scatterers illuminated by different discrete sources, the source space  $S$  is the space of spatial coordinates  $\underline{x}$  and sources  $s$  with the following inner product:

$$\langle a(\underline{x}, \underline{x}_s), b(\underline{x}, \underline{x}_s) \rangle_S = \sum_{s=1}^{N_s} \int_{-\infty}^{\infty} a(\underline{x}, \underline{x}_s) b^*(\underline{x}, \underline{x}_s) d\underline{x}. \quad (\text{D.2})$$

Analogously, the *receiver space*  $R$  can have two forms depending on the context:

- For the imaging of a continuous distribution of sources as described in Section 4.2, the receiver space simply extends over all receivers and has the following inner product:

$$\langle a(\underline{x}_r), b(\underline{x}_r) \rangle_R = \sum_{r=1}^{N_r} a(\underline{x}_r) b^*(\underline{x}_r). \quad (\text{D.3})$$

- For the imaging of a distribution of scatterers illuminated by different discrete sources, the receiver space is the space of receivers  $r$  and sources  $s$  with the following inner product:

$$\langle a(\underline{x}_r, \underline{x}_s), b(\underline{x}_r, \underline{x}_s) \rangle_R = \sum_{r=1}^{N_r} \sum_{s=1}^{N_s} a(\underline{x}_r, \underline{x}_s) b^*(\underline{x}_r, \underline{x}_s). \quad (\text{D.4})$$

The inner products defined above can be extended to include all frequencies by adding the index  $\omega$ . For instance, for the receiver space, the following notation is used:

$$\left\langle \tilde{a}(\underline{x}_r, \underline{x}_s, \omega), \tilde{b}(\underline{x}_r, \underline{x}_s, \omega) \right\rangle_{R, \omega} = \int_{-\infty}^{\infty} \sum_{r=1}^{N_r} \sum_{s=1}^{N_s} \tilde{a}(\underline{x}_r, \underline{x}_s, \omega) \tilde{b}^*(\underline{x}_r, \underline{x}_s, \omega) d\omega. \quad (\text{D.5})$$

## D.2 Contrast source operator

The operator  $\mathcal{C}$  determines the contrast sources for a given field  $\tilde{u}(\underline{x}, \underline{x}_s, \omega)$  and contrast  $\chi(\underline{x})$ .

The forward operator is given by the following equation:

$$\tilde{w}(\underline{x}, \underline{x}_s, \omega) = k_0^4 \tilde{u}(\underline{x}, \underline{x}_s, \omega) \chi(\underline{x}) = \tilde{S}(\omega) \tilde{G}(\underline{x}, \underline{x}_s, \omega) \tilde{\Phi}(\underline{x}, \omega) = \mathcal{C} \chi(\underline{x}). \quad (\text{D.1})$$

The adjoint operator  $\mathcal{C}^\dagger$  is derived from the inner product of the forward operator and its result [Claerbout 2009].

$$\begin{aligned} \langle \mathcal{C} \chi(\underline{x}), \tilde{w}(\underline{x}, \underline{x}_s, \omega) \rangle_{S, \omega} &= \int_{-\infty}^{\infty} \int_{-\infty}^{\infty} \tilde{S}(\omega) \sum_{s=1}^{N_s} \tilde{w}^*(\underline{x}, \underline{x}_s, \omega) k_0^4 \tilde{u}(\underline{x}, \underline{x}_s, \omega) \chi(\underline{x}) d\omega d\underline{x} \\ &= \int_{-\infty}^{\infty} \chi(\underline{x}) \int_{-\infty}^{\infty} k_0^4 \tilde{S}(\omega) \sum_{s=1}^{N_s} \tilde{u}(\underline{x}, \underline{x}_s, \omega) \tilde{w}^*(\underline{x}, \underline{x}_s, \omega) d\omega d\underline{x} \\ &= \langle \mathcal{C}^\dagger \tilde{w}(\underline{x}, \underline{x}_s, \omega), \chi(\underline{x}) \rangle_X. \end{aligned} \quad (\text{D.2})$$

This leads to the following adjoint operator  $\mathcal{C}^\dagger$ , assuming that the wavenumber  $k_0$  is real:

$$\mathcal{C}^\dagger \tilde{w}(\underline{x}, \underline{x}_s, \omega) = \int_{-\infty}^{\infty} k_0^4 \tilde{S}^*(\omega) \sum_{s=1}^{N_s} \tilde{u}^*(\underline{x}, \underline{x}_s, \omega) \tilde{w}(\underline{x}, \underline{x}_s, \omega) d\omega. \quad (\text{D.3})$$

### D.3 Measurement operator

The measurement operator  $\mathcal{G}_R$  introduced in Section 4.2 performs a mapping from the contrast sources  $\tilde{w}(\underline{x}, \underline{x}_s, \omega)$  to the receiver signals  $\tilde{f}(\underline{x}_r, \underline{x}_s, \omega)$ . This operator can also be used to model the measurement of signals from a distribution of primary sources. In this case, the dependency on  $s$  can simply be omitted.

The forward measurement operator is given by the following equation:

$$\tilde{f}(\underline{x}_r, \underline{x}_s, \omega) = \int_{-\infty}^{\infty} \tilde{G}(\underline{x}_r, \underline{x}, \omega) \tilde{w}(\underline{x}, \underline{x}_s, \omega) d\underline{x} = \mathcal{G}_R \tilde{w}(\underline{x}, \underline{x}_s, \omega). \quad (\text{D.1})$$

The adjoint operator is derived from the inner product:

$$\begin{aligned} & \left\langle \mathcal{G}_R \tilde{w}(\underline{x}, \underline{x}_s, \omega), \tilde{f}(\underline{x}_r, \underline{x}_s, \omega) \right\rangle_{R, \omega} \\ &= \sum_{s=1}^{N_s} \sum_{r=1}^{N_r} \int_{-\infty}^{\infty} \tilde{f}^*(\underline{x}_r, \underline{x}_s, \omega) \int_{-\infty}^{\infty} \tilde{G}(\underline{x}_r, \underline{x}, \omega) \tilde{w}(\underline{x}, \underline{x}_s, \omega) d\underline{x} d\omega \\ &= \int_{-\infty}^{\infty} \int_{-\infty}^{\infty} \sum_{s=1}^{N_s} \tilde{w}(\underline{x}, \underline{x}_s, \omega) \sum_{r=1}^{N_r} \tilde{G}(\underline{x}_r, \underline{x}, \omega) \tilde{f}^*(\underline{x}_r, \underline{x}_s, \omega) d\underline{x} d\omega \\ &= \left\langle \tilde{w}(\underline{x}, \underline{x}_s, \omega), \mathcal{G}_R^\dagger \tilde{f}(\underline{x}_r, \underline{x}_s, \omega) \right\rangle_{S, \omega}. \end{aligned} \quad (\text{D.2})$$

Hence, the adjoint operator  $\mathcal{G}_R^\dagger$  has the following form:

$$\mathcal{G}_R^\dagger \tilde{f}(\underline{x}_r, \underline{x}_s, \omega) = \sum_{r=1}^{N_r} \tilde{G}^*(\underline{x}_r, \underline{x}, \omega) \tilde{f}(\underline{x}_r, \underline{x}_s, \omega). \quad (\text{D.3})$$

### D.4 Born measurement operator

#### ■ D.4.1 Born measurement operator in space-frequency domain

The Born measurement operator  $\mathcal{G}_X$  provides the receiver signals  $\tilde{f}(\underline{x}_r, \underline{x}_s, \omega)$  for a given contrast function  $\chi(\underline{x})$  and known incident field  $\tilde{u}_{\text{inc}}(\underline{x}, \underline{x}_s, \omega)$  under the Born approximation.

$$\tilde{f}(\underline{x}_r, \underline{x}_s, \omega) = k_0^4 \int_{-\infty}^{\infty} \tilde{G}(\underline{x}_r, \underline{x}, \omega) [\tilde{u}_{\text{inc}}(\underline{x}, \underline{x}_s, \omega) \chi(\underline{x})] d\underline{x} = \mathcal{G}_X \chi(\underline{x}). \quad (\text{D.1})$$

The adjoint operator is derived by forming the inner product of the operator result and the receiver signals:

$$\begin{aligned}
& \left\langle \mathcal{G}_X \chi(\underline{x}), \tilde{f}(\underline{x}_r, \underline{x}_s, \omega) \right\rangle_{R, \omega} \\
&= \sum_{s=1}^{N_s} \sum_{r=1}^{N_r} \int_{-\infty}^{\infty} \tilde{f}^*(\underline{x}_r, \underline{x}_s, \omega) \int_{-\infty}^{\infty} \tilde{G}(\underline{x}_r, \underline{x}, \omega) [k_0^4 \tilde{u}_{\text{inc}}(\underline{x}, \underline{x}_s, \omega) \chi(\underline{x})] \, d\underline{x} \, d\omega \\
&= \int_{-\infty}^{\infty} \chi(\underline{x}) \int_{-\infty}^{\infty} k_0^4 \sum_{s=1}^{N_s} \tilde{u}_{\text{inc}}(\underline{x}, \underline{x}_s, \omega) \sum_{r=1}^{N_r} \tilde{G}(\underline{x}_r, \underline{x}, \omega) \tilde{f}^*(\underline{x}_r, \underline{x}_s, \omega) \, d\omega \, d\underline{x} \\
&= \left\langle \chi(\underline{x}), \mathcal{G}_X^\dagger \tilde{f}(\underline{x}_r, \underline{x}_s, \omega) \right\rangle_X.
\end{aligned} \tag{D.2}$$

Under the assumption that the wavenumber  $k_0$  is real, it can be seen that the adjoint operator  $\mathcal{G}_X^\dagger$  has the following form:

$$\mathcal{G}_X^\dagger \tilde{f}(\underline{x}_r, \underline{x}_s, \omega) = \int_{-\infty}^{\infty} k_0^4 \sum_{s=1}^{N_s} \tilde{u}_{\text{inc}}^*(\underline{x}, \underline{x}_s, \omega) \sum_{r=1}^{N_r} \tilde{G}^*(\underline{x}_r, \underline{x}, \omega) \tilde{f}(\underline{x}_r, \underline{x}_s, \omega) \, d\omega. \tag{D.3}$$

#### ■ D.4.2 Born measurement operator in wavenumber-frequency domain

The transformation of the Born measurement operator to the wavenumber-frequency domain is used to determine the achievable resolution for given array setups:

$$\tilde{f}(\underline{x}_r, \underline{x}_s, \omega) = \mathcal{G}_X \tilde{\chi}(\underline{k}) = k_0^4 \int_{-\infty}^{\infty} e^{-j\underline{k} \cdot \underline{x}_r} \tilde{\tilde{G}}(\underline{k}, \omega) \left[ \tilde{u}_{\text{inc}}(\underline{k}_1 - \underline{k}, \underline{x}_s, \omega) * \tilde{\chi}(\underline{k}) \right] \, d\underline{k}. \tag{D.4}$$

By writing out the incident field in terms of source positions, Green's function and

spectrum, the following re-arrangements can be made:

$$\begin{aligned}
\tilde{f}(\underline{x}_r, \underline{x}_s, \omega) &= \mathcal{G}_X \tilde{\chi}(\underline{k}) \\
&= k_0^4 \int_{-\infty}^{\infty} \tilde{\tilde{G}}(\underline{k}, \omega) \left\{ \left[ \tilde{S}(\omega) \tilde{\tilde{G}}(\underline{k}, \omega) e^{j\underline{k} \cdot \underline{x}_s} \right] * \tilde{\chi}(\underline{k}) \right\} d\underline{k} \\
&= k_0^4 \tilde{S}(\omega) \int_{-\infty}^{\infty} \tilde{\tilde{G}}(\underline{k}_1, \omega) e^{-j\underline{k}_1 \cdot \underline{x}_r} \int_{-\infty}^{\infty} \tilde{\tilde{G}}(\underline{k}_1 - \underline{k}, \omega) e^{j(\underline{k}_1 - \underline{k}) \cdot \underline{x}_s} \tilde{\chi}(\underline{k}) d\underline{k} d\underline{k}_1 \\
&= k_0^4 \tilde{S}(\omega) \int_{-\infty}^{\infty} \tilde{\chi}(\underline{k}) \int_{-\infty}^{\infty} \tilde{\tilde{G}}(\underline{k}_1, \omega) e^{-j\underline{k}_1 \cdot \underline{x}_r} \tilde{\tilde{G}}(\underline{k} - \underline{k}_1, \omega) e^{-j(\underline{k} - \underline{k}_1) \cdot \underline{x}_s} d\underline{k}_1 d\underline{k} \\
&= k_0^4 \tilde{S}(\omega) \int_{-\infty}^{\infty} \tilde{\chi}(\underline{k}) \left\{ \left[ \tilde{\tilde{G}}(\underline{k}, \omega) e^{-j\underline{k} \cdot \underline{x}_r} \right] * \left[ \tilde{\tilde{G}}(\underline{k}, \omega) e^{-j\underline{k} \cdot \underline{x}_s} \right] \right\} d\underline{k},
\end{aligned} \tag{D.5}$$

with the asterisk denoting two-dimensional convolution in the wavenumber domain.

For the above derivation, the symmetry of Green's function has been used:

$$\tilde{\tilde{G}}(\underline{k}, \omega) = \tilde{\tilde{G}}(-\underline{k}, \omega). \tag{D.6}$$

In a subsequent step, the inner product is formed in order to derive the form of the adjoint operator:

$$\begin{aligned}
&\left\langle \mathcal{G}_X \tilde{\chi}(\underline{k}), \tilde{f}(\underline{x}_r, \underline{x}_s, \omega) \right\rangle_{R, \omega} \\
&= \sum_{s=1}^{N_s} \sum_{r=1}^{N_r} \int_{-\infty}^{\infty} \tilde{f}^*(\underline{x}_r, \underline{x}_s, \omega) k_0^4 \tilde{S}(\omega) \int_{-\infty}^{\infty} \tilde{\chi}(\underline{k}) \tilde{\tilde{\Psi}}(\underline{k}, \underline{x}_r, \underline{x}_s, \omega) d\underline{k} d\omega \\
&= \int_{-\infty}^{\infty} \tilde{\chi}(\underline{k}) \int_{-\infty}^{\infty} k_0^4 \tilde{S}(\omega) \sum_{s=1}^{N_s} \sum_{r=1}^{N_r} \tilde{f}^*(\underline{x}_r, \underline{x}_s, \omega) \tilde{\tilde{\Psi}}(\underline{k}, \underline{x}_r, \underline{x}_s, \omega) d\omega d\underline{k},
\end{aligned} \tag{D.7}$$

with  $\tilde{\tilde{\Psi}}(\underline{k}, \underline{x}_r, \underline{x}_s, \omega)$  being the image decomposition filter defined by Eq. 4.3.78 and repeated here for convenience:

$$\tilde{\tilde{\Psi}}(\underline{k}, \underline{x}_r, \underline{x}_s, \omega) = \left[ \tilde{\tilde{G}}(\underline{k}, \omega) e^{-j\underline{k} \cdot \underline{x}_r} \right] * \left[ \tilde{\tilde{G}}(\underline{k}, \omega) e^{-j\underline{k} \cdot \underline{x}_s} \right]. \tag{D.8}$$

For real wavenumbers  $k_0$ , the adjoint is thus given by the following expression:

$$\begin{aligned}
& \mathcal{G}_X^\dagger \tilde{f}(\underline{x}_r, \underline{x}_s, \omega) \\
&= \int_{-\infty}^{\infty} k_0^4 \tilde{S}^*(\omega) \sum_{s=1}^{N_s} \sum_{r=1}^{N_r} \tilde{f}(\underline{x}_r, \underline{x}_s, \omega) \tilde{\Psi}^*(\underline{k}, \underline{x}_r, \underline{x}_s, \omega) d\omega \\
&= \int_{-\infty}^{\infty} k_0^4 \tilde{S}^*(\omega) \sum_{s=1}^{N_s} \sum_{r=1}^{N_r} \tilde{f}(\underline{x}_r, \underline{x}_s, \omega) \left\{ \left[ \tilde{G}^*(\underline{k}, \omega) e^{j\underline{k} \cdot \underline{x}_r} \right] * \left[ \tilde{G}^{*\dagger}(\underline{k}, \omega) e^{j\underline{k} \cdot \underline{x}_s} \right] \right\} d\omega.
\end{aligned} \tag{D.9}$$

### ■ D.4.3 Forward scattering operator

The forward scattering operator describes the relation between incident and total field. It is used for the calculation of the total field in the case that the scattering contrast is known:

$$\tilde{u}_{\text{inc}}(\underline{x}, \underline{x}_s, \omega) = (\mathcal{I} - \mathcal{G}_D \mathcal{X}) \tilde{u}(\underline{x}, \underline{x}_s, \omega). \tag{D.10}$$

The adjoint of the forward scattering operator can easily be seen to have the following form:

$$(\mathcal{I} - \mathcal{G}_D \mathcal{X})^\dagger \tilde{u}_{\text{inc}}(\underline{x}, \underline{x}_s, \omega) = \left( \mathcal{I} - \mathcal{X}^\dagger \mathcal{G}_D^\dagger \right) \tilde{u}_{\text{inc}}(\underline{x}, \underline{x}_s, \omega). \tag{D.11}$$

## Estimation of the contrast

The contrast is related to the contrast sources  $\tilde{w}(\underline{x}, \underline{x}_s, \omega)$  and the field  $\tilde{u}(\underline{x}, \underline{x}_s, \omega)$  by the following equation:

$$\tilde{w}(\underline{x}, \underline{x}_s, \omega) = k_0^4(\omega) \tilde{u}(\underline{x}, \underline{x}_s, \omega) \chi(\underline{x}). \quad (\text{E.1})$$

If the contrast sources and the field are known, the contrast can be estimated by minimising the following error functional:

$$E[\chi(\underline{x})] = \int_{-\infty}^{\infty} \int_{-\infty}^{\infty} \frac{\sum_{s=1}^{N_s} |\tilde{w}(\underline{x}, \underline{x}_s, \omega) - k_0^4(\omega) \tilde{u}(\underline{x}, \underline{x}_s, \omega) \chi(\underline{x})|^2}{\sum_{s=1}^{N_s} |k_0^4(\omega) \tilde{u}(\underline{x}, \underline{x}_s, \omega)|^2} d\underline{x} d\omega, \quad (\text{E.2})$$

$$\chi(\underline{x})_{\text{est}} = \arg \min_{\chi(\underline{x})} E[\chi(\underline{x})]. \quad (\text{E.3})$$

The weighting by  $\|k_0^4(\omega) \tilde{u}(\underline{x}, \underline{x}_s, \omega)\|_S^2$  is used in order to ensure that the information present at different frequencies is equally taken into account.

Differentiation with respect to the contrast  $\chi(\underline{x})$  leads to the following gradient:

$$\begin{aligned} \frac{\partial E[\chi(\underline{x})]}{\partial \chi(\underline{x})} &= \int_{-\infty}^{\infty} \frac{\sum_{s=1}^{N_s} \left[ -2k_0^4(\omega) \tilde{w}(\underline{x}, \underline{x}_s, \omega) \tilde{u}^*(\underline{x}, \underline{x}_s, \omega) + 2k_0^8(\omega) \chi(\underline{x}) |\tilde{u}(\underline{x}, \underline{x}_s, \omega)|^2 \right]}{\sum_{s=1}^{N_s} k_0^8(\omega) |\tilde{u}(\underline{x}, \underline{x}_s, \omega)|^2} d\omega \\ &= \int_{-\infty}^{\infty} \frac{\sum_{s=1}^{N_s} -2\tilde{w}(\underline{x}, \underline{x}_s, \omega) \tilde{u}^*(\underline{x}, \underline{x}_s, \omega)}{\sum_{s=1}^{N_s} k_0^4(\omega) |\tilde{u}(\underline{x}, \underline{x}_s, \omega)|^2} d\omega + \int_{-\infty}^{\infty} 2\chi(\underline{x}) d\omega. \end{aligned} \quad (\text{E.4})$$

The minimum is obtained by setting the gradient equal to zero:

$$\chi(\underline{x}) = \frac{1}{\Omega} \int_{-\infty}^{\infty} \frac{\sum_{s=1}^{N_s} \tilde{w}(\underline{x}, \underline{x}_s, \omega) \tilde{u}^*(\underline{x}, \underline{x}_s, \omega)}{k_0^4(\omega) \sum_{s=1}^{N_s} |\tilde{u}(\underline{x}, \underline{x}_s, \omega)|^2} d\omega, \quad (\text{E.5})$$

with the constant  $\Omega$  representing the spectral bandwidth:

$$\Omega = \int_{-\infty}^{\infty} d\omega. \quad (\text{E.6})$$

For a discrete implementation with  $N_\omega$  frequencies  $\omega_1 \dots \omega_N$ , one obtains:

$$\chi(\underline{x}) = \frac{1}{N_\omega} \sum_{\omega=\omega_1}^{\omega_N} \frac{\sum_{s=1}^{N_s} \tilde{w}(\underline{x}, \underline{x}_s, \omega) \tilde{u}^*(\underline{x}, \underline{x}_s, \omega)}{k_0^4(\omega) \sum_{s=1}^{N_s} |\tilde{u}(\underline{x}, \underline{x}_s, \omega)|^2}. \quad (\text{E.7})$$

# Conjugate gradient schemes

## F.1 Linear conjugate gradient scheme

A linear conjugate gradient scheme obtains a least-squares solution to the problem:

$$\mathcal{L}x = b. \quad (\text{F.1})$$

This can be done by solving the normal equations:

$$\mathcal{L}^\dagger \mathcal{L}x = \mathcal{L}^\dagger b. \quad (\text{F.2})$$

In this work, linear imaging problems, such as imaging under the Born approximation, are tackled using a linear conjugate gradient scheme applied to the normal equations. The following conjugate gradient scheme is adopted from Fokkema and Van den Berg [Fokkema 1993]. For the sake of clear arrangement, it is presented on the next page.

## F.2 BI-CGSTAB

BI-CGSTAB is an improved and stabilised version of the bi-conjugate gradient method developed by Van der Vorst [Van der Vorst 1992]. The algorithm has superior convergence properties compared to the conjugate gradient method without preconditioning. Furthermore, it only requires the forward operator in order to solve a system of linear equations in the form of:

$$\mathcal{L}x = b. \quad (\text{F.1})$$

The BI-CGSTAB scheme is presented on page 191. In the present work, it is applied to solve the forward scattering problem, i.e., to calculate the receiver signals in simulations including multiple scattering.

**Linear conjugate gradient scheme for the normal equations (CGNE)**

```

 $x = 0$  // start from zero to obtain pseudo-inverse solution
 $r = b - \mathcal{L}x$  // calculate residual
 $\eta = \|b\|^2$ 
 $F_0 = \|r\|^2 / \eta$ 
 $d = \mathcal{L}^\dagger r$  // determine starting direction
 $A_n = \text{Re} \langle r, \mathcal{L}d \rangle$ 
 $\alpha = \frac{A_n}{\|\mathcal{L}d\|^2}$  // calculate step size
 $x = x + \alpha d$  // take step
 $r = b - \mathcal{L}x$  // update residual
for  $n = 1$  to  $N$ 
     $g = \mathcal{L}^\dagger r$  // calculate gradient
     $A_n = \text{Re} \langle r, \mathcal{L}g \rangle$ 
     $d = g + \frac{A_n}{A_{n-1}} d$  // determine conjugate direction
     $\alpha = \frac{A_n}{\|\mathcal{L}d\|^2}$  // calculate step size and take step
     $x = x + \alpha d$ 
     $r = b - \mathcal{L}x$  // update residual
     $F_n = \frac{\|r\|^2}{\eta}$ 
    if ( $F_n < \epsilon$ ) exit // exit if error is small enough
end

```

**BI-CGSTAB scheme**

```
 $r = b - \mathcal{L}x$   
 $d = r$   
 $\rho_0 = 1$   
 $\alpha = 1$   
 $\omega = 1$   
 $v = 0$   
 $p = 0$   
for  $n = 1$  to  $N$   
   $\rho_n = \langle r, d \rangle$   
   $F_n = |\rho|$   
  if ( $F_n < \epsilon$ ) exit  
   $\beta = \frac{\rho_n \alpha}{\rho_{n-1} \omega}$   
   $p = r + \beta(p - \omega v)$   
   $v = \mathcal{L}p$   
   $\alpha = \frac{\rho}{\langle v, d \rangle}$   
   $s = r - \alpha v$   
   $t = \mathcal{L}s$   
   $\omega = \frac{\langle s, t \rangle}{\|t\|^2}$   
   $x = x + \alpha p + \omega s$   
   $r = s - \omega t$   
end
```

### F.3 Nonlinear conjugate gradient scheme

A nonlinear conjugate gradient scheme can be used to minimise a possibly nonlinear error functional in the form of:

$$F = \|r(x)\|^2, \quad (\text{F.1})$$

for which the minimisation is carried out with respect to  $x$ . In this work, modified versions of a nonlinear conjugate gradient scheme are used for imaging beyond the Born approximation, i.e., imaging including multiple scattering.

#### Nonlinear conjugate gradient scheme

```

 $x_0 = 0$  // start from zero
 $F_0 = \|r(x_0)\|^2$ 
 $d_0 = 0$ 
for  $n = 1$  to  $N$ 
     $g = \frac{\partial F(x_{n-1})}{\partial x}$  // calculate gradient
     $d_n = g_n + \frac{\langle g_n, g_n - g_{n-1} \rangle}{\|g_{\chi, n-1}\|_S^2} d_{n-1}$  // determine Polak-Ribière direction
     $\alpha = \arg \min_{\alpha} F(x_{n-1} + \alpha d_n)$  // calculate step size and take step
     $x_n = x_{n-1} + \alpha d_n$ 
     $F_n = \|r(x_n)\|^2$ 
    if ( $F_n < \epsilon$ ) exit // exit if error is small enough
end

```

# G

## Experiments

### *TIMING TOAST*

*There's an art of knowing when.*

*Never try to guess.*

*Toast until it smokes and then  
twenty seconds less.*

(Piet Hein, 1905 – 1996)

In this appendix, the experiments performed to acquire the measurement datasets used in this work are described.

### **G.1 Measurements on a 2 mm steel plate**

The measurement setup for the dataset obtained from a 2 mm steel plate is shown in Fig. G.1. The plate is supported by four nails placed at the corners. It is set into vibration by a steel bullet dropped from a chute. The chute can be moved in order to vary the position of excitation. The movement of the plate is picked up by an accelerometer (Brüel & Kjær type 4371) mounted on a fixed position using double-sided adhesive tape.

The dimensions of the plate and the excitation and measurement positions are shown in Fig. G.2. Over the width of the plate, 161 different excitation points are used. A sampling frequency of 100 kHz is chosen.

In order to determine the moment of impact accurately, a laser vibrometer is pointed close to the point of excitation and moved along with the chute, thereby providing a signal which can be used to synchronise different measurements for processing.

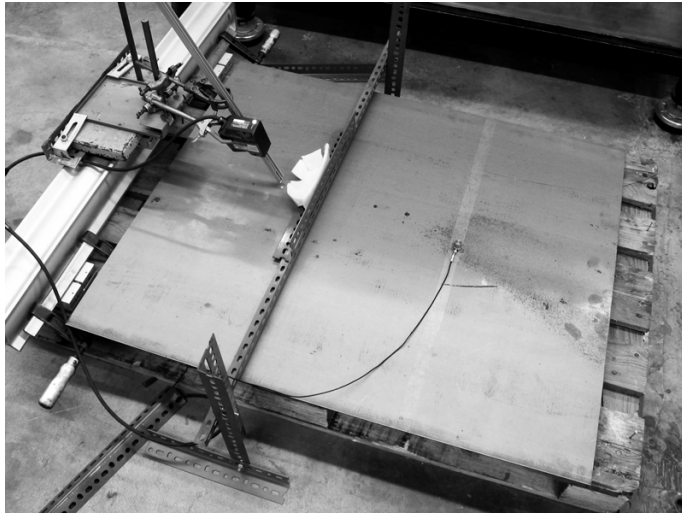


**Figure G.1:** Setup of the steel plate measurement.

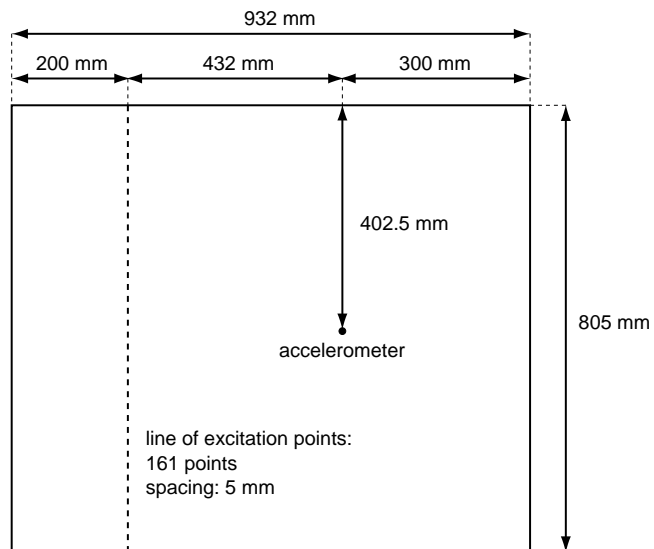


**Figure G.2:** Positions of the excitation and measurement points.

## G.2 Measurements on a 4 mm iron beam

Figure G.3 depicts the measurement setup for an iron beam of 2 metres length with a thickness of 4 mm and a width of 20 mm. The beam is positioned with the slender side down. It is supported by foam rubber at the outer ends, thereby only slightly damped. A shaker (Brüel & Kjær type 4810) is positioned at 50 cm from the end of the beam and coupled using a permanent magnet. The normal velocity of the beam is measured using a laser Doppler vibrometer positioned at a distance of approximately 4 metres from the beam.



**Figure G.3:** Setup of the iron beam measurement.

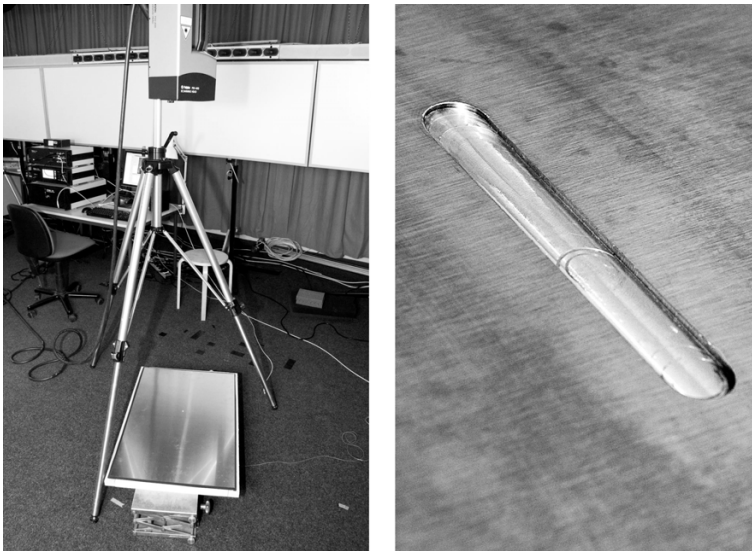
A schematic view of the beam and its excitation point is given in Fig. G.4.



**Figure G.4:** Illustration of the beam setup showing the point of excitation.

### G.3 Measurements on a 3 mm aluminium plate

In order to apply the imaging algorithms for defect detection, measurements were taken on an aluminium plate of 3 mm thickness. Figure G.5 presents the measurement setup with the laser Doppler vibrometer positioned above the plate and a photograph of the artificial defect in the plate. This defect is a slit of 10 mm width and 70 mm length produced by milling, locally reducing the plate thickness to 2 mm.



---

**Figure G.5:** Setup of the aluminium plate measurement (left); photograph of the slit created by milling representing a defect of 1 mm depth (right).

---

The boundaries of the plate are supported by a frame with foam rubber strips attached. The exact position of the excitation source (Brüel & Kjær shaker type 4810), the artificial defect, and the line on which measurements of the surface normal velocity are taken, are shown in Fig. G.6. There are 49 measurement points with a spacing of 1 cm.

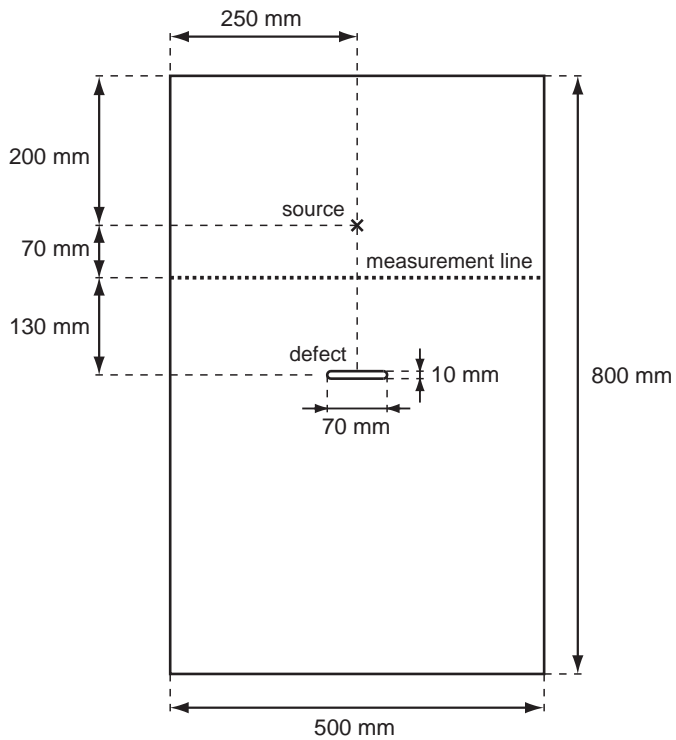


**Figure G.6:** Technical drawing of the 3 mm aluminium plate showing the point of excitation, the position of the line on which measurements are taken, and the location of the artificial defect.



# Notation, symbols and acronyms

## H.1 Variables

symbol	meaning
$a$	aperture of a linear array
$b$	width of a beam
$b_{\text{TV}}$	weighting function for total variation regularisation
$c$	phase velocity
$c_{\text{gr}}$	group velocity
$d$	distance between receivers / conjugate gradient search direction
$f$	frequency
$\tilde{f}$	receiver signals
$g$	function for the derivation of the reflection coefficient / gradient
$h$	height of a beam/plate
$j$	imaginary unit
$k$	wavenumber
$k_{\text{B}}$	wavenumber (beam)
$k_{\text{P}}$	wavenumber (plate)
$m'$	mass per unit length (beam)
$m''$	mass per unit area (plate)
$n$	noise signal / iteration number
$p$	probability distribution
$q$	dispersion-free representation of the wave field

$r$	receiver index
$r_R/r_S$	residual in the receiver / source space
$s$	source index
$t$	time
$u$	normal displacement of the plate
$v$	normal velocity
$w$	contrast sources
$x$	spatial coordinate (in-plane)
$y$	spatial coordinate (in-plane)
$z$	spatial coordinate (out-of-plane)
$\Delta x$	distance between point of excitation and point of observation
$A$	dispersion constant
$B$	bending stiffness
$B'$	bending stiffness in a beam
$B''$	bending stiffness in a plate
$C$	coefficient of a wave field component at a boundary
$D$	dispersion factor
$E$	Young modulus / error functional
$F$	force
$F_D$	dispersion removal filter
$F_1, F_2$	spectral filters in the wavenumber-frequency domain
$G$	Green's function
$I'$	area moment of inertia (beam)
$I''$	area moment of inertia (plate)
$M$	bending moment
$N$	arbitrary integer
$N_r$	number of receivers
$N_s$	number of sources
$N_\omega$	number of discrete frequencies
$Q$	plate thickness ratio at a cross-sectional change
$R$	reflection coefficient
$R_{ev}$	reflection coefficient (evanescent field)
$\tilde{\tilde{R}}$	spectrum describing the resolution
$S$	source wavelet / spectrum / distribution
$S_x$	spatial wavelet / wavenumber spectrum
$V$	area of the imaging domain
$W$	wavelet
$Y$	point mobility

$\alpha$	optimal step size for minimisation of a function
$\beta$	small positive constant for total variation regularisation
$\gamma$	regularisation parameter
$\delta$	Dirac delta function
$\epsilon$	small positive stabilisation constant
$\zeta$	auxiliary variable for sparse regularisation
$\eta$	damping coefficient
$\eta_R/\eta_S$	normalisation factors for source and receiver space
$\theta$	angle
$\lambda$	wavelength
$\mu$	dispersion model parameter
$\nu$	Poisson constant
$\xi$	modal shape
$\rho$	mass density
$\sigma$	axial stress
$\sigma_i$	eigenvalue
$\sigma_n$	variance of a normal distribution
$\sigma_\chi$	parameter for sparse regularisation
$\tau$	time shift
$\varphi$	angle of rotation (beam element, chapter 2)
$\chi$	contrast
$\psi$	Fourier transform of the receiver positions
$\omega$	angular frequency
$\Phi$	scattering potential
$\Psi$	spectral filter for a source-receiver combination
$\Omega$	bandwidth

## H.2 Special functions

$H$	Heaviside step function
$H_0^{(2)}$	zeroth order Hankel function of the second kind
$J_0$	zeroth order Bessel function
$K_0$	zeroth order modified Bessel function of the second kind

## H.3 Mathematical operations

$\text{Re}$	real part of a complex variable
$a^*$	complex conjugate of $a$
$\underline{a}^T$	transpose of vector $\underline{a}$
$\mathcal{A}^\dagger$	hermitian adjoint of operator $\mathcal{A}$
$\text{sgn}$	sign operator
$\text{arg min}$	argument of the minimum
$\lim$	limit

### ■ H.3.1 Operators

$\mathcal{F}$	Fourier transform
$\mathcal{G}$	Green operator
$\mathcal{G}_D$	Green operator in the source space (mapping from the source space onto itself)
$\mathcal{G}_R$	Green operator for the receivers (mapping from the source space to receiver space)
$\mathcal{G}_X$	Green operator under the Born approximation (mapping from the source space to receiver space)
$\mathcal{H}$	Helmholtz operator
$\mathcal{I}$	identity operator
$\mathcal{L}$	general operator
$\mathcal{Q}$	sparseness operator
$\mathcal{R}$	resolution operator
$\mathcal{S}$	operator performing multiplication by eigenvalues
$\mathcal{T}$	time shift operator
$\mathcal{U}$	unitary operator
$\mathcal{X}$	contrast operator

## H.4 Indices, subscripts

B	for bars/beams
P	for plates
Born	within the Born approximation
LS	least-squares
TV	total variation
adj	adjoint solution
back	backpropagation
est	estimated
ev	evanescent
inc	incident
reg	regularisation
$r$	receiver index
$s$	source index
sc	scattered
$x$	with respect to the x-coordinate
$y$	with respect to the y-coordinate
$z$	with respect to the z-coordinate
$\chi$	with respect to the contrast $\chi$

## H.5 Representation of variables in frequency and wavenumber space

$\tilde{a}$	variable $a$ in one-dimensional Fourier space (wavenumber or frequency domain)
$\tilde{\tilde{a}}$	variable $a$ in two-dimensional Fourier space (two-dimensional wavenumber or wavenumber-frequency domain)
$\tilde{\tilde{\tilde{a}}}$	variable $a$ in three-dimensional Fourier space (three-dimensional wavenumber-frequency domain)

## H.6 Matrices and vectors

$\underline{a}$	vector $\underline{a}$
$\underline{x}$	two-dimensional position vector $\underline{x} = (x, y)^T$
$\underline{\underline{A}}$	matrix $\underline{\underline{A}}$

## H.7 Spaces, norms and inner products

$L^0$	$L^0$ -norm
$L^1$	$L^1$ -norm
$L^2$	$L^2$ -norm
$L^p$	$L^p$ -norm
$R$	receiver space (space over $\underline{x}$ , $r$ , and optionally $s$ )
$S$	source space (space over $\underline{x}$ and optionally $s$ )
$X$	contrast space (space over $\underline{x}$ )
$\ \cdot\ _R$	norm over space $R$
$\langle \cdot, \cdot \rangle_R$	inner product over space $R$

## H.8 Acronyms

CG	conjugate gradient
CGNE	conjugate gradient scheme applied to the normal equations
CSI	contrast source inversion
IRLS	iteratively reweighted least-squares
SVD	singular value decomposition
TSVD	truncated singular value decomposition
TV	total variation

# Bibliography

---

- [Abramowitz 1964] Milton Abramowitz and Irene A. Stegun: *Handbook of mathematical functions with formulas, graphs, and mathematical tables*. US National Bureau of Standards, Washington, 1964.
- [Abubakar 2003] Aria Abubakar, Peter M. van den Berg and Jacob T. Fokkema: Time-lapse TM-polarization electromagnetic imaging. *Subsurface Sensing Technologies and Applications*, 4 (1), p. 117–135, 2003.
- [Abubakar 2004] A. Abubakar, P. M. van den Berg et al.: A multiplicative regularization approach for deblurring problems. *IEEE Transactions on Image Processing*, 13 (11), p. 1524–1532, 2004.
- [Abubakar 2005] Aria Abubakar, Tarek M. Habashy et al.: The diagonalized contrast source approach: an inversion method beyond the Born approximation. *Inverse Problems*, 21, p. 685–702, 2005.
- [Abubakar 2008] A. Abubakar, W. Hu et al.: A contrast source inversion method for reconstructing objects in an inhomogeneous background medium. *IEEE Antennas and Propagation Society International Symposium*, San Diego, California, USA, p. 1–4, 2008.
- [Alleyne 1991a] D. Alleyne and P. Cawley: A two-dimensional Fourier transform method for the measurement of propagating multimode signals. *Journal of the Acoustical Society of America*, 89 (3), p. 1159–1168, 1991.

- [Alleyne 1991b] David N. Alleyne: *The nondestructive testing of plates using ultrasonic Lamb waves*. PhD thesis, University of London, 1991.
- [Arfken 1985] G. B. Arfken and H. J. Weber: *Mathematical methods for physicists*. Academic Press, New York, 1985.
- [Aster 2005] Richard C. Aster, Brian Borchers and Clifford H. Thurber: *Parameter estimation and inverse problems*. Elsevier Academic Press, Amsterdam, 2005.
- [Auld 1973] B. A. Auld: *Acoustic fields and waves in solids*. Wiley Interscience, New York, 1973.
- [Bailey 2004] D. Bailey, W. Allen and S. Demidenko: Spectral warping revisited. *Proceedings of the Second IEEE International Workshop on Electronic Design, Test and Applications*, p. 23–28, 2004.
- [Berkhout 1974] A. J. Berkhout: Related properties of minimum-phase and zero-phase time functions. *Geophysical Prospecting*, 22 (4), p. 683–709, 1974.
- [Berkhout 1977] A. J. Berkhout: Least-squares inverse filtering and wavelet deconvolution. *Geophysics*, 42, p. 1369–383, 1977.
- [Berkhout 1980] A. J. Berkhout, D. De Vries and M. M. Boone: A new method to acquire impulse responses in concert halls. *The Journal of the Acoustical Society of America*, 68 (1), p. 179–183, 1980.
- [Berkhout 1984] A. J. Berkhout: *Seismic resolution: a quantitative analysis of resolving power of acoustical echo techniques*, volume 12. Geophysical Press, London, 1984.
- [Berkhout 1987] A. J. Berkhout: *Applied seismic wave theory*. Elsevier, New York, 1987.
- [Berkhout 2007] A. J. Berkhout, D. de Vries and M. C. Brink: Array technology for bending wave field analysis in constructions. *Journal of Sound and Vibration*, 300 (1-2), p. 25–42, 2007.
- [Bertero 1998] Mario Bertero and Patricia Boccacci: *Introduction to inverse problems in imaging*. Institute of Physics Publishing, Bristol, 1998.

- [Beylkin 1985] G. Beylkin, M. Oristaglio and D. Miller: Spatial resolution of migration algorithms. In: *Acoustical Imaging*, edited by A.J. Berkhout, J. Ridder and L.F. van der Wal, p. 155–168, Springer, New York, 1985.
- [Bishop 2006] Christopher M. Bishop: *Pattern recognition and machine learning*. Springer New York, 2006.
- [Bleistein 2001] Norman Bleistein, Jack K. Cohen and John W. Stockwell: *Mathematics of multidimensional seismic imaging, migration, and inversion*. Springer, New York, 2001.
- [Bloemenkamp 2001] Richard F. Bloemenkamp, Aria Abubakar and Peter M. van den Berg: Inversion of experimental multi-frequency data using the contrast source inversion method. *Inverse Problems*, 17, p. 1611–1622, 2001.
- [Blomgren 2002] Peter Blomgren, George Papanicolaou and Hongkai Zhao: Super-resolution in time-reversal acoustics. *The Journal of the Acoustical Society of America*, 111 (1), p. 230–248, 2002.
- [Born 1999] Max Born and Emil Wolf: *Principles of optics*, 7th edition. Cambridge University Press, 1999.
- [Boussinesq 1885] J. Boussinesq: *Application des potentiels a l'etude de l'equilibre et du mouvement des solides elastiques*. Gauthier-Villars, Paris, 1885.
- [Bracewell 2003] Ronald Newbold Bracewell: *Fourier analysis and imaging*. Kluwer Academic / Plenum Publishers, New York, 2003.
- [Brent 2002] Richard P. Brent: *Algorithms for minimization without derivatives*. Dover Publications, 2002.
- [Brinkmeyer 1990] E. Brinkmeyer and R. Ulrich: High-Resolution OCSR in dispersive waveguides. *Electronics Letters*, 26 (6), p. 413–414, 1990.
- [Büssow 2008a] Richard Büssow: Applications of the flexural impulse response functions in the time domain. *Acta Acustica united with Acustica*, 94, p. 207–214, 2008.
- [Büssow 2008b] Richard Büssow: Bending wavelet for flexural impulse response. *The Journal of the Acoustical Society of America*, 123 (4), p. 2126–2135, 2008.

- [Calvetti 2000] D. Calvetti, S. Morigi et al.: Tikhonov regularization and the L-curve for large discrete ill-posed problems. *Journal of computational and applied mathematics*, 123 (1-2), p. 423–446, 2000.
- [Chaigne 2007] Antoine Chaigne: Structural acoustics and vibration. In: *Springer Handbook of Acoustics*, edited by Thomas D. Rossing, Springer, New York, 2007.
- [Chen 1998] Fu-Chiarng Chen and Weng C. Chew: Experimental verification of super resolution in nonlinear inverse scattering. *Applied Physics Letters*, 72 (23), p. 3080–3082, 1998.
- [Claerbout 2009] Jon F. Claerbout: *Basic Earth Imaging*. Stanford University, 2009, Electronic book, URL: <http://sepwww.stanford.edu/sep/prof/bei6.2009.pdf>, accessed September 22, 2009.
- [Courjon 1994] D. Courjon and C. Bainier: Near field microscopy and near field optics. *Reports on Progress in Physics*, 57, p. 989–1028, 1994.
- [Cremer 2005] L. Cremer, M. Heckl and B.A.T. Petersson: *Structure-borne sound*, third edition. Springer, Berlin, 2005.
- [Cuenca 2009] J. Cuenca, F. Gautier and L. Simon: The image source method for calculating the vibrations of simply supported convex polygonal plates. *Journal of Sound and Vibration*, 322 (4-5), p. 1048–1069, 2009.
- [Cui 2004] Tie J. Cui, Weng C. Chew et al.: Study of resolution and super resolution in electromagnetic imaging for half-space problems. *IEEE Transactions on Antennas and Propagation*, 52 (6), p. 1398–1411, 2004.
- [Davies 2005] J. Davies, F. Simonetti et al.: Review of synthetically focused guided wave imaging techniques with application to defect sizing. *Review of Progress in Quantitative Nondestructive Evaluation*, p. 142–149, 2005.
- [De Hoop 1995] A. T. de Hoop: *Handbook of radiation and scattering of waves*. Academic Press, London, 1995.
- [De Vries 1984] Diemer de Vries: *Velocity analysis based on minimum entropy*. PhD thesis, Delft University of Technology, 1984.
- [Debnath 2005] Lokenath Debnath and Piotr Mikuśiński: *Hilbert spaces with applications*, third edition. Elsevier, Amsterdam, 2005.

- [Donoho 2006] David L. Donoho: Compressed sensing. *IEEE Transactions on Information Theory*, 52 (4), p. 1289–1306, 2006.
- [Donoho 2008] David L. Donoho and Yaakov Tsaig: Fast solution of  $L_1$ -norm minimization problems when the solution may be sparse. *IEEE Transactions on Information Theory*, 54 (11), p. 4789–4812, 2008.
- [Ertürk 2002] Hakan Ertürk, Ofodike A. Ezekoye and John R. Howell: Comparison of three regularized solution techniques in a three-dimensional inverse radiation problem. *Journal of Quantitative Spectroscopy and Radiative Transfer*, 73 (2–5), p. 307–316, 2002.
- [Ewald 1969] P. P. Ewald: Introduction to the dynamical theory of X-ray diffraction. *Acta Crystallographica Section A: Crystal Physics, Diffraction, Theoretical and General Crystallography*, 25 (1), p. 103–108, 1969.
- [Fahy 1985] Frank Fahy: *Sound and structural vibration: radiation, transmission and response*. Academic Press, London, 1985.
- [Fokkema 1993] Jacob T. Fokkema and Peter M. van den Berg: *Seismic Applications of Acoustic Reciprocity*. Elsevier, Amsterdam, 1993.
- [Francoeur 2008] Dany Francoeur and Alain Berry: Time reversal of flexural waves in a beam at audible frequency. *The Journal of the Acoustical Society of America*, 124 (2), p. 1006–1017, 2008.
- [Gelius 2000] Leiv-J. Gelius and Isabelle Lecomte: The resolution function in linearized Born and Kirchhoff inversion. In: *Methods and applications of inversion*, p. 129–141, Springer, Berlin, 2000.
- [Golub 1989] Gene H. Golub and Dianne P. O’Leary: Some history of the conjugate gradient and Lanczos algorithms: 1948-1976. *SIAM review*, 31 (1), p. 50–102, 1989.
- [Graff 1975] Karl F. Graff: *Wave motion in elastic solids*. Oxford University Press, London, 1975.
- [Greffet 1997] Jean-Jacques Greffet and Rémi Carminati: Image formation in near-field optics. *Progress in surface science*, 56 (3), p. 133–237, 1997.
- [Griffiths 2005] David J. Griffiths: *Introduction to quantum mechanics*, second edition. Pearson Prentice Hall, Upper Saddle River, 2005.

- [Hadamard 1923] Jacques Hadamard: *Lectures on Cauchy's problem in linear partial differential equations*. Dover Publications, Mineola, 1923, reprinted 2003.
- [Hanke 1995] Martin Hanke: *Conjugate gradient type methods for ill-posed problems*. Longman Scientific & Technical, Harlow, 1995.
- [Hansen 1987] Per C. Hansen: The truncated SVD as a method for regularization. *BIT Numerical Mathematics*, 27 (4), p. 534–553, 1987.
- [Hansen 1998] Per C. Hansen: *Rank-deficient and discrete ill-posed problems: numerical aspects of linear inversion*. Society for Industrial and Applied Mathematics, Philadelphia, 1998.
- [Hendee 2002] W. R. Hendee and E. R. Ritenour: *Medical imaging physics*, fourth edition. John Wiley and Sons, New York, 2002.
- [Hestenes 1975] Magnus R. Hestenes: Pseudoinverses and conjugate gradients. *Communications of the ACM*, 18 (1), p. 40–43, 1975.
- [Hong 2005] Jin-Chul Hong, Kyung H. Sun and Yoon Y. Kim: Dispersion-based short-time Fourier transform applied to dispersive wave analysis. *The Journal of the Acoustical Society of America*, 117 (5), p. 2949–2960, 2005.
- [Hörchens 2009] Lars Hörchens and Diemer de Vries: Imaging using scattering of flexural waves. *9th International Conference on Theoretical and Computational Acoustics*, Dresden, 2009.
- [Kac 1966] Mark Kac: Can one hear the shape of a drum? *The American Mathematical Monthly*, 73 (4), p. 1–23, 1966.
- [Karvanen 2003] Juha Karvanen and Andrzej Cichocki: Measuring sparseness of noisy signals. *4th International Symposium on Independent Component Analysis and Blind Signal Separation (ICA2003)*, Nara, Japan, p. 125–130, 2003.
- [Kelley 1995] C. T. Kelley: *Iterative methods for linear and nonlinear equations*. Society for Industrial and Applied Mathematics, Philadelphia, 1995.
- [Kleinman 1992] Ralph E. Kleinman and Peter M. van den Berg: A modified gradient method for two-dimensional problems in tomography. *Journal of Computational and Applied Mathematics*, 42 (1), p. 17–35, 1992.

- [Kohlhaas 1991] A. Kohlhaas, C. Fromchen and E. Brinkmeyer: High-resolution OCDR for testing integrated-optical waveguides: dispersion-corrupted experimental data corrected by a numerical algorithm. *Journal of Lightwave Technology*, 9 (11), p. 1493–1502, 1991.
- [Kuster 2004] Martin Kuster, Diemer de Vries et al.: Acoustic imaging in enclosed spaces: Analysis of room geometry modifications on the impulse response. *The Journal of the Acoustical Society of America*, 116 (4), p. 2126–2137, 2004.
- [Lamb 1889] Horace Lamb: On the flexure of an elastic plate. *Proceedings of the London Mathematical Society*, 21 (360), p. 70–90, 1889.
- [Langenberg 2002] Karl J. Langenberg: Linear scalar inverse scattering. In: *Scattering and inverse scattering in pure and applied science*, edited by Roy Pike and Pierre Sabatier, p. 121–141, Academic Press, London, 2002.
- [Leissa 1969] Arthur W. Leissa: *Vibration of plates*. Scientific and Technical Information Division, NASA, Washington, 1969.
- [Margrave 1998] G. F. Margrave: Theory of nonstationary linear filtering in the Fourier domain with application to time-variant filtering. *Geophysics*, 63 (1), p. 244–259, 1998.
- [Mead 1982] D.J. Mead: Structural wave motion. In: *Noise and vibration*, edited by R.G. White and J.G. Walker, p. 207–226, Ellis Horwood Ltd., Chichester, 1982.
- [Mindlin 1951] Raymond D. Mindlin: Influence of rotatory inertia and shear on flexural motions of isotropic, elastic plates. *Journal of Applied Mechanics*, 181951.
- [Nagy 2003] J. G. Nagy and K. M. Palmer: Steepest descent, CG, and iterative regularization of ill-posed problems. *BIT Numerical Mathematics*, 43 (5), p. 1003–1017, 2003.
- [Niethammer 2000] M. Niethammer, L. J. Jacobs et al.: Time-frequency representation of Lamb waves using the reassigned spectrogram. *Journal of the Acoustical Society of America*, 107 (5), p. 19–24, 2000.
- [Oppenheim 1971] A. Oppenheim, D. Johnson and K. Steiglitz: Computation of spectra with unequal resolution using the fast Fourier transform. *Proceedings of the IEEE*, 59 (2), p. 299–301, 1971.

- [Oppenheim 1972] A. V. Oppenheim and D. H. Johnson: Discrete representation of signals. *Proceedings of the IEEE*, 60 (6), p. 681–691, 1972.
- [Pierce 1989] Allan D. Pierce: *Acoustics: an introduction to its physical principles and applications*. Acoustical Society of America, Melville, 1989.
- [Porter 2007] R. Porter and D. V. Evans: Diffraction of flexural waves by finite straight cracks in an elastic sheet over water. *Journal of Fluids and Structures*, 23 (2), p. 309–327, 2007.
- [Pörtzgen 2007] Niels Pörtzgen: *Imaging of defects in girth welds using inverse wave field extrapolation of ultrasonic data*. PhD thesis, Delft University of Technology, 2007.
- [Prada 1994] Claire Prada and Mathias Fink: Eigenmodes of the time reversal operator: A solution to selective focusing in multiple-target media. *Wave motion*, 20, p. 151–163, 1994.
- [Press 1996] William H. Press, Saul A. Teukolsky et al.: *Numerical recipes in Fortran 90*. Cambridge University Press, Cambridge, 1996.
- [Prosser 1999] W. H. Prosser, M. D. Seale and B. T. Smith: Time-frequency analysis of the dispersion of Lamb modes. *The Journal of the Acoustical Society of America*, 105 (5), p. 2669–2676, 1999.
- [Rayleigh 1878] John William Strutt, Baron Rayleigh: *The Theory of Sound*, volume 2, second edition. Dover Publications, New York, 1878, reprinted 1945.
- [Reddy 1999] J.N. Reddy: *Theory and analysis of elastic plates*. Taylor & Francis, Philadelphia, USA, 1999.
- [Reissner 1945] Eric Reissner: The effect of transverse shear deformation on the bending of elastic plates. *Journal of Applied Mechanics*, 12 (A), p. 69–77, 1945.
- [Riley 1997] Kenneth F. Riley, Michael P. Hobson and Stephen J. Bence: *Mathematical methods for physics and engineering*. Cambridge University Press, Cambridge, 1997.
- [Robinson 1985] Enders A. Robinson: Seismic time-invariant convolutional model. *Geophysics*, 50 (12), p. 2742–2752, 1985.
- [Robinson 1987] Enders Robinson and Dean Clark: Basic seismology 2 – A wave at a boundary; reflection, transmission/refraction, and diffraction. *The Leading Edge*, 6 (9), p. 38–42, 1987.

- [Robinson 2008] Enders A. Robinson and Sven Treitel: *Digital imaging and deconvolution: the ABCs of seismic exploration and processing*. Society of Exploration Geophysicists, Tulsa, 2008.
- [Rudin 1992] Leonid Rudin, Stanley Osher and Emad Fatemi: Nonlinear total variation based noise removal algorithms. *Physica D*, 60 (1–4), p. 259–268, 1992.
- [Sacchi 1995] Mauricio D. Sacchi and Tadeusz J. Ulrych: High-resolution velocity gathers and offset space reconstruction. *Geophysics*, 60 (4), p. 1169–1177, 1995.
- [Sacchi 1998] Mauricio D. Sacchi, Tadeusz J. Ulrych and Colin J. Walker: Interpolation and extrapolation using a high-resolution discrete Fourier transform. *IEEE Transactions on Signal Processing*, 46 (1), p. 31–38, 1998.
- [Saks 1937] Stanisław Saks: *Theory of the integral*, second revised edition. Monografie Matematyczne, Warsaw, 1937.
- [Sava 2006] Paul Sava and Sergey Fomel: Time-shift imaging condition in seismic migration. *Geophysics*, 71 (6), p. S209–S217, 2006.
- [Scales 1988] John A. Scales, Adam Gersztenkorn and Sven Treitel: Fast  $L_p$  solution of large, sparse, linear systems: Application to seismic travel time tomography. *Journal of Computational Physics*, 75 (2), p. 314–333, 1988.
- [Shannon 1949] Claude E. Shannon: Communication in the presence of noise. *Proceedings of the Institute of Radio Engineers*, 37 (1), p. 10–21, 1949.
- [Sibul 1995] Leon H. Sibul: Array processing and generalized inverses. *29th Asilomar Conference on Signals, Systems and Computers*, p. 438, 1995.
- [Sicard 2002] René Sicard, Jacques Goyette and Djamel Zellouf: A SAFT algorithm for Lamb wave imaging of isotropic plate-like structures. *Ultrasonics*, 39 (7), p. 487–494, 2002.
- [Simonetti 2006] F. Simonetti: Multiple scattering: The key to unravel the subwavelength world from the far-field pattern of a scattered wave. *Physical Review E*, 73 (036619)2006.
- [Stöckmann 2007] H.-J. Stöckmann: Chladni meets Napoleon. *European Physical Journal Special Topics*, 145, p. 15–23, 2007.

- [Stolt 1978] R. H. Stolt: Migration by Fourier transform. *Geophysics*, 43 (1), p. 23, 1978.
- [Strang 1988] Gilbert Strang: *Linear algebra and its applications*, third edition. Harcourt Brace Jovanovich, Orlando, Florida, 1988.
- [Szilard 2004] Rudolph Szilard: *Theories and applications of plate analysis*. John Wiley & Sons, Hoboken, New Jersey, USA, 2004.
- [Tarantola 1988] A. Tarantola: Theoretical background for the inversion of seismic waveforms including elasticity and attenuation. *Pure and Applied Geophysics*, 128 (1), p. 365–399, 1988.
- [Tarantola 2005] Albert Tarantola: *Inverse problem theory and methods for model parameter estimation*. Society for Industrial and Applied Mathematics, Philadelphia, 2005.
- [Timoshenko 1959] S. Timoshenko and S. Woinowsky-Krieger: *Theory of plates and shells*, second edition. McGraw-Hill, New York, USA, 1959.
- [Tomio 1995] Lauro Tomio and Sadhan K. Adhikari: Iterative numerical solution of scattering problems. *Chemical Physics Letters*, 241 (4), p. 477–483, 1995.
- [Trad 2003] Daniel Trad, Tadeusz J. Ulrych and Mauricio D. Sacchi: Latest views of the sparse Radon transform. *Geophysics*, 68 (1), p. 386–399, 2003.
- [Van den Berg 1997] Peter M. van den Berg and Ralph E. Kleinman: A contrast source inversion method. *Inverse Problems*, 13, p. 1607–1620, 1997.
- [Van den Berg 1999] P. M. van den Berg, A. L. van Broekhoven and A. Abubakar: Extended contrast source inversion. *Inverse Problems*, 15, p. 1325–1344, 1999.
- [Van den Berg 2002] Peter M. van den Berg: Nonlinear scalar inverse scattering: algorithms and applications. In: *Scattering and inverse scattering in pure and applied science*, edited by Roy Pike and Pierre Sabatier, p. 142–161, Academic Press, London, 2002.
- [Van den Berg 2003] Peter M. van den Berg, Aria Abubakar and Jacob T. Fokkema: Multiplicative regularization for contrast profile inversion. *Radio Science*, 38 (2, 8022)2003.

- [Van den Berg 2010] Peter M. van den Berg and Aria Abubakar: Optical microscopy imaging using the contrast source inversion method. *Journal of Modern Optics*, first published on 4 January 2010, p. 1–9, 2010.
- [Van der Vorst 1992] Henk A. van der Vorst: Bi-CGSTAB: A fast and smoothly converging variant of Bi-CG for the solution of nonsymmetric linear systems. *SIAM Journal on Scientific and Statistical Computing*, 13 (2), p. 631–644, 1992.
- [Van der Vorst 2003] Henk A. van der Vorst: *Iterative Krylov methods for large linear systems*. Cambridge University Press, Cambridge, 2003.
- [Van Dongen 2007] Koen W. A. van Dongen and William M. D. Wright: A full vectorial contrast source inversion scheme for three-dimensional acoustic imaging of both compressibility and density profiles. *The Journal of the Acoustical Society of America*, 121 (3), p. 1538–1549, 2007.
- [Wang 2005] Chun H. Wang and Fu-Kuo K. Chang: Scattering of plate waves by a cylindrical inhomogeneity. *Journal of Sound and Vibration*, 282 (1-2), p. 429–451, 2005.
- [Wei 2009] Liang Wei, Zuo-ying Huang and Que Pei-wen: Sparse deconvolution method for improving the time-resolution of ultrasonic NDE signals. *NDT&E international*, 42 (5), p. 430–434, 2009.
- [Wiener 1964] Norbert Wiener: *Extrapolation, interpolation, and smoothing of stationary time series*, First paperback edition. MIT Press, Cambridge, Massachusetts, 1964.
- [Wiggins 1978] Ralph A. Wiggins: Minimum entropy deconvolution. *Geophysical Research Letters*, 16 (1-2), p. 21–35, 1978.
- [Wilcox 2001a] P. Wilcox, M. Lowe and P. Cawley: The effect of dispersion on long-range inspection using ultrasonic guided waves. *NDT&E international*, 34 (1), p. 1–9, 2001.
- [Wilcox 2001b] P.D. Wilcox, M.J.S. Lowe and P. Cawley: A signal processing technique to remove the effect of dispersion from guided wave signals. *Review of Progress in Quantitative Nondestructive Evaluation*, p. 555–562, 2001.
- [Wilcox 2002] P. Wilcox: Guided wave beam steering from omnidirectional transducer arrays. *Review of Progress in Quantitative Nondestructive Evaluation*, p. 761, 2002.

- 
- [Wilcox 2003] P. D. Wilcox: A rapid signal processing technique to remove the effect of dispersion from guided wave signals. *IEEE Transactions on Ultrasonics, Ferroelectrics and Frequency Control*, 50 (4), p. 419–427, 2003.
- [Williams 1999] Earl G. Williams: *Fourier acoustics: sound radiation and nearfield acoustical holography*. Academic Press, San Diego, 1999.
- [Wirgin 2002] Armand Wirgin: Acoustical imaging: classical and emerging methods for applications in macrophysics. In: *Scattering and inverse scattering in pure and applied science*, edited by Roy Pike and Pierre Sabatier, p. 95–120, Academic Press, London, 2002.
- [Wolf 1969] Emil Wolf: Three-dimensional structure determination of semi-transparent objects from holographic data. *Optics Communications*, 1 (4), p. 153–156, 1969.
- [Wolf 1998] Emil Wolf and John T. Foley: Do evanescent waves contribute to the far field? *Optics letters*, 23 (1), p. 16–18, 1998.
- [Zakharia 2000] M. E. Zakharia and P. Chevret: Neural network approach for inverting velocity dispersion; application to sediment and to sonar target characterization. *Inverse Problems*, 16 (6), p. 1693–1708, 2000.
- [Zwartjes 2005] Paul M. Zwartjes: *Fourier reconstruction with sparse inversion*. PhD thesis, Delft University of Technology, 2005.

# Summary

---

## Imaging of material inhomogeneities with flexural waves

The detection of inhomogeneities in plates or plate-like structures constitutes a major problem in the field of non-destructive testing. For a few decades, classical techniques based on X-ray radiography have – as far as possible – been complemented and replaced by the usage of vibrations or acoustical waves due to the fact that these are less dangerous and enable the utilisation of diffraction. The local material thickness is thereby often measured using bulk waves. To this end, an excitation source and a receiver are used to scan the plate in order to detect the position of inhomogeneities. As an alternative to this time-consuming process, *guided waves* propagating along the plate have been a matter of research for more than thirty years. This wave type allows for the inspection of a plate region from remote locations using only a limited number of source and receiver points.

This thesis focuses on the improvement of techniques for the detection and visualisation of inhomogeneities in plate-like structures using flexural waves, one specific member of the family of guided waves. In order to retrieve reliable information about the position and strength of sources and scatterers in flexural wave fields, it is necessary to deal with the effects of dispersion. Compensation for these effects is possible if the material parameters are known or can be estimated from measured data.

Well-known methods from the field of seismics and acoustics can then be applied to estimate the wave field at different points than the measured ones. A key objective of the present work is the development and comparison of methods for generating an image, i.e., a map disclosing the positions of sources or material inhomogeneities.

It is shown that the dispersive properties of the wave field dictate the conditions needed to apply the developed methods for detection and imaging in an optimal way: the spectrum of the excitation source, the temporal and spatial sampling of the wave field as well as the processing routines have to be adapted to the dispersion characteristics.

Several approaches for the generation of an image from measured data are derived and compared. These approaches are based on a forward model describing the influence of sources and inhomogeneities on the receiver signals. Whereas direct methods such as backpropagation offer a quick estimate, higher resolution of the obtained image can be achieved by inversion of this forward model. If this forward model is based on the Born approximation, i.e., includes only first-order scattering, additional regularisation is needed to obtain stable and useful imaging results. Two possible regularisation methods are presented: regularisation by a sparseness constraint and multiplicative regularisation by minimum total variation. Whereas the sparseness assumption can help to achieve superior resolution, minimisation of the total variation provides a tool that is less presumptive about the structure of the image.

The application of the imaging methods to finite plates is discussed and demonstrated on simulation and measurement examples. It is shown that the inclusion of boundary reflections in the imaging model poses an additional challenge. The estimation of the positions and properties of the boundaries is proposed as a topic for future research.

When abandoning the Born approximation, the inclusion of multiple scattering in the imaging model relaxes the requirement of regularisation being applied to the inversion. The image generated by this more sophisticated physical model can to a greater extent be based on evidence from the data and does not have to rely on assumptions on the typical image structure to be expected. To this end, the *contrast source inversion* approach has been adapted to deal with flexural wave fields at multiple frequencies. While being significantly more complex than methods relying on the Born approximation, this approach has the advantage of providing not only qualitative, but also quantitative information on the inhomogeneities, thereby allowing for better assessment of the severity of a defect from the obtained image. This way, more reliable decisions on required actions with respect to industrial installations can be made, and costs can be reduced.

# Samenvatting

---

## Het afbeelden van inhomogeniteiten in materialen met behulp van buiggolven

De detectie van inhomogeniteiten in platen of plaatachtige structuren vormt een centraal probleem op het gebied van niet-destructief materiaalonderzoek. Klassieke technieken gebaseerd op radiologie zijn daarbij – voor zover mogelijk – tijdens de afgelopen decennia aangevuld of vervangen door het gebruik van trillingen of akoestische golven omdat deze minder gevaarlijk zijn en het gebruik van diffractie mogelijk maken. Vaak wordt bij deze aanpak de lokale materiaaldikte met behulp van compressie- of schuifgolven gemeten. Daarbij worden een trillingsbron en een ontvanger over de te onderzoekende plaat bewogen om zo de locatie van inhomogeniteiten op te sporen. Als alternatief voor dit tijdrovend proces wordt al sinds meer dan dertig jaar ook onderzoek gedaan aan zogenaamde *guided waves* die zich langs een plaat voortplanten. Dit golftype maakt het mogelijk om een onderdeel van een plaat op afstand te inspecteren waarbij maar van een beperkt aantal bronnen en ontvangers gebruik gemaakt wordt.

Dit proefschrift richt zich op het verbeteren van technieken voor het opsporen en visualiseren van inhomogeniteiten in plaatvormige structuren met behulp van buiggolven, een specifiek type golf uit de groep van *guided waves*. Om betrouwbare informatie over de positie en sterkte van bronnen en verstrooiende objecten in buiggolfvelden te extraheren, is het noodzakelijk om de effecten van dispersie goed aan te pakken. Compensatie voor deze effecten is mogelijk in het geval dat de materiaalparameters bekend zijn of uit de gemeten gegevens kunnen worden geschat.

Vervolgens kunnen bekende aanpakken uit de seismiek en de akoestiek worden toegepast om het golfveld in andere dan de gemeten punten te schatten. De focus van dit onderzoek is gericht op de ontwikkeling en vergelijking van methodes voor het genereren van een afbeelding, d.w.z. een kaart waarop de posities van bronnen of inhomogeniteiten van het materiaal zichtbaar zijn. Er wordt aangetoond dat de dispersieve eigenschappen van het golfveld de voorwaarden bepalen voor het toepassen van de ontwikkelde technieken voor het detecteren en maken van een afbeelding: het spectrum van de excitatie, de temporele en ruimtelijke bemonstering van de golfvelden en de verwerkingsroutines moeten aan de karakteristiek van dispersie worden aangepast.

Meerdere aanpakken voor het genereren van een afbeelding op basis van meetgegevens worden afgeleid en vergeleken. Deze zijn gebaseerd op een voorwaarts model dat beschrijft hoe de gemeten signalen door bronnen en inhomogeniteiten worden beïnvloed. Directe methodes zoals terugpropagatie bieden een snelle schatting, terwijl met de inversie van het voorwaartse model een hogere resolutie kan worden behaald. Indien dit model op de Born benadering is gebaseerd en dus alleen eerste orde verstrooiing meeneemt, is regularisatie noodzakelijk om een stabiel en bruikbaar resultaat te behalen. Twee mogelijke technieken voor regularisatie worden voorgesteld: regularisatie met schaarsheid als voorwaarde en multiplicatieve regularisatie gebaseerd op minimale totale variatie. Waar de veronderstelling van schaarsheid kan helpen om uitstekende resolutie te bereiken, vormt de minimalisatie van de totale variatie een techniek waarbij de verwachte structuur van de gegenereerde afbeelding een minder beperkende rol speelt.

De toepassing van technieken voor het maken van afbeeldingen op eindige platen wordt bediscussieerd en gedemonstreerd met behulp van voorbeelden van simulaties en metingen. Het meenemen van de reflecties van de randen bij het maken van een afbeelding vormt een extra uitdaging. Het schatten van de posities en eigenschappen van de randen wordt aanbevolen voor vervolgonderzoek.

Wanneer de Born benadering wordt opgegeven, hoeft er door het meenemen van meervoudige verstrooiing in het afbeeldingsmodel minder beroep te worden gedaan op de regularisatie die op de inversie wordt toegepast. De afbeelding die met behulp van dit verfijnd model is verkregen kan sterker op de daadwerkelijke meetgegevens zijn gebaseerd en is niet noodzakelijk aangewezen op veronderstellingen van de typische structuur van een afbeelding. Met oog op dit doel is de *contrast source inversion* methode aangepast om met buiggolfvelden om te kunnen gaan als er informatie voor meerdere frequenties beschikbaar is. De resulterende aanpak is duidelijk complexer dan technieken die zijn gebaseerd op de Born benadering. Een voordeel ervan is echter dat niet alleen kwalitatieve, maar ook kwantitatieve informatie over de inhomogeniteiten wordt verkregen, waardoor een betere inschatting van de ernst van een defect op basis van de resulterende afbeelding mogelijk is. Op deze manier zijn betrouwbaardere beslissingen over noodzakelijke acties voor industriële installaties mogelijk en kunnen kosten worden bespaard.

# Curriculum vitae

---

Lars Hörchens was born in Mönchengladbach, Germany, on December 7, 1979. He attended secondary school at the Gymnasium Odenkirchen in Mönchengladbach and received his 'Abitur' in 1999. After 13 months of civil service, he started studying 'Medientechnologie' (Media Technology) at Ilmenau University of Technology, Germany, in 2000. From October 2003 to March 2004, he spent an industrial placement as part of his studies at Canon Research Europe in Bracknell, United Kingdom, where he worked on coding and compression of speech recognition results represented by lattice structures. In November 2005, he graduated from Ilmenau University of Technology with a thesis on the segmentation of video sequences for compositing applications. He received his 'Diplom' (equivalent to an MSc title) with distinction.



Following an invitation by his later supervisor, he joined the Laboratory of Acoustical Imaging and Sound Control at Delft University of Technology, where he conducted the work that led to this PhD thesis. Currently, he is employed at the same group as a postdoctoral researcher, extending the methods for the analysis of flexural wave fields with respect to sound radiation and optimised damping of vibrations for applications in the fields of building acoustics and industrial product design.



# Acknowledgements

---

For someone whose daily working routine consists of using three languages, it is only natural to use all three of them to acknowledge the people contributing to the writing of this thesis in many different ways.

Allereerst wil ik mijn promotor Dries Gisolf alsmede mijn begeleider Diemer de Vries bedanken. Dries wil ik vooral bedanken voor het in de gaten houden van de grote lijnen en het bewaken van het proces dat uiteindelijk tot een proefschrift moest leiden. Zijn inhoudelijke inbreng, met name de discussie over contrast source inversion, heeft duidelijk tot de finale vorm van dit boek bijgedragen. Diemer wil ik bedanken voor de uitnodiging (“het inladen”) om voor mijn promotie naar Delft te komen en zijn begeleiding met inhoudelijke en morele steun in de afgelopen vier jaar. Ook de open en diepgaande gesprekken heb ik zeer op prijs gesteld, evenals de ontspannen gesprekken, reizen of etentjes tijdens conferenties. Het was fijn om naast mijn eigen onderzoek ook nog aan andere projecten mee te kunnen doen en ervaringen op te doen waarvan er vele uiteindelijk bij het schrijven van dit proefschrift van pas kwamen. Ook al was dit soms tijdrovend, ik hoop er toch een hoop van te hebben opgestoken, en dan niet alleen op wetenschappelijk gebied.

Mijn dank gaat uit naar STW voor de financiële ondersteuning van het project. De leden van de STW gebruikerscommissie wil ik bedanken voor hun interesse en hun inbreng bij onze halfjaarlijkse vergaderingen.

Casper Wassink, Niels Pörtzgen, Khalid Chougrani en Bert de Waal van Applus RTD wil ik bedanken voor discussies en demonstraties met betrekking tot niet-destructief materiaalonderzoek.

Maarten Bakker bedank ik voor de mogelijkheid om bij de faculteit lucht- en ruimtevaart de eerste plaatmetingen te kunnen doen en de vrijheid die ik daarbij kreeg

(“kijk maar wat je nodig hebt”). Ik zal de knikker zo snel niet vergeten.

Nevertheless, I am happy that it was possible to acquire a shared scanning laser vibrometer setup together with the department Precision and Microsystems Engineering at the 3mE faculty. I thank Prof. Daniel Rixen for his cooperation and Muammer Ozbek for his practical support.

Mijn dank gaat verder uit naar Joost Bloom van TNO voor de discussies over technieken voor de detectie van defecten in pijpleidingen en de rondleiding bij TNO. Frans Biegstraaten van TNO wil ik bedanken voor de ondersteuning bij de metingen door het uitlenen van meetapparatuur.

Peter van den Berg bedank ik voor de discussies over contrast source inversion en multiplicatieve regularisatie, vooral voor zijn geduld om alle details uit te leggen en zijn onuitputtelijke voorraad aan kladpapier.

Koen van Dongen heeft me ondanks zijn drukke werkzaamheden als beginnend docent geholpen om naast contrast source inversion en totale variatie ook het bepalen van adjoints met behulp van inwendige producten te begrijpen, zonder die dit proefschrift ook zeker niet mogelijk was geweest.

Rinus Boone wil ik bedanken voor zijn hulp bij vragen op akoestisch gebied, gezellige dagen op conferenties en zijn bereidheid het projectleiderschap over te nemen.

Zoals vrijwel iedereen in onze sectie zou ik verloren geweest zijn zonder Henry, die steeds als helpende hand bij hard- en softwareproblemen, het vergaren van meetapparatuur, het beantwoorden van ‘waar-krijg-ik-dit-vandaan-vragen’ en een heleboel andere technische kwesties beschikbaar was.

Op niet-wetenschappelijk vlak werd deze functie vervuld door Margaret, die (bijna) zonder zeuren van alles voor me uitzocht: het boeken van reizen, indienen van declaraties, voeren van verfrissende telefoongesprekken met de personeelsafdeling en duizend andere kleine organisatorische vragen. Margaret moet ik echter vooral bedanken voor haar poging tot omscholing van mijn “deutsche Gründlichkeit” naar Nederlandse gezelligheid. Dankzij haar weet ik dat je na het nuttigen van een portie kibbeling niet meer dan één tompouce moet eten, ook niet op Koninginnedag.

Mijn kamergenoten wil ik bedanken voor de prettige sfeer: Bouchaib, Jan, Anton, Jasper en Joost. Met Anton en Jasper heb ik de meeste tijd doorgebracht, een groot aantal gezellige dagen met metingen, op conferenties, gedeelde hotelkamers en uiteraard ook op TU. Tot de prettige sfeer bijgedragen hebben natuurlijk ook de andere collega’s en de lunch groep.

Meinen Eltern möchte ich danken für ihre Unterstützung und das Mitfiebern während der letzten doch etwas schwierigeren Zeit, bis endlich alles geschafft war.

Tenslotte wil ik Ingeborg bedanken voor al haar steun en geduld. Het is nu echt af.